A Study on the Strain-Rate- and Stress-State-Dependent Behavior of Advanced Ceramics: Experimental Mechanics and Multiscale Simulations

by

Zahra Zaiemyekeh

A thesis submitted in partial fulfillment of the requirements for the degree of

Doctor of Philosophy

Department of Mechanical Engineering
University of Alberta

Abstract

Design and development of better-performing ceramic structures are vital in industry-driven applications where a wide range of strain rates and stress states are induced in the material (e.g., impact events). Accordingly, this thesis investigates the strain-rate- and stress-state-dependent behavior of advanced alumina ceramics through combined experimental mechanics and multiscale numerical approaches. Experimentally, the effect of the strain-rate and stress state on the failure response of alumina ceramics was explored by designing and testing cuboidal, angled, and flattened Brazilian disc (FBD) specimens to induce compression, shear-compression, and tensile stress states in the material, respectively. Experimental testing was equipped with ultra-high-speed imaging coupled with digital image correlation (DIC) to achieve the full-filed strains and capture the failure initiation and propagation sites. The material microstructure was characterized by state-of-the-art diagnostics to inform the multi-scale models in terms of grain size distribution, porosity, and grain crystallographic orientations. Finite element (FE) models of the macroscale experiments were developed to provide a better insight into the failure progression in the material by quantifying the history of damage. A rate-dependent viscosity regularized version of the phenomenological Johnson-Holmquist-2 (JH2) material model (i.e., the JH2-V model) was implemented through a VUMAT subroutine in Abaqus FE software. Once validated, the model was exercised to quantitatively analyze the damage initiation and growth in the material to provide insights into the role of stress state on the failure response of alumina ceramics at the macroscale. Next, polycrystalline-based representative volume elements (RVEs) of the additively manufactured (AM)

alumina ceramics were generated using Neper software based on the data captured through the microstructural characterization. To account for the transgranular failure mechanism, the grains were constitutively modeled by the developed JH2-V model, and the grain boundaries were modeled by the bi-linear cohesive zone model (CZM) approach to account for the intergranular failure mechanism. Upon validation with the experimental data, the micromechanical model was leveraged to quantify the history of failure mechanisms, which is challenging to unravel by in-situ experimental approaches, particularly for brittle materials. The model was used to study the effect of microstructural features (e.g., porosity, grain orientations, and grain boundary properties) on the macroscale response of the AM alumina. The novelty and importance of this thesis stem from (a) Building on the limited previous studies, in light of the expansion in the application of AM ceramic structures as a potential replacement for conventionally made ones, this thesis experimentally investigates the mechanical performance of AM alumina ceramics across different stress states and strain rates, providing implications for model development and design of AM ceramic structures with tailored mechanical performance. (b) This work develops an experimentally validated microstructure-based FE modeling framework to explore the relationships between the microstructure and macroscale response of AM ceramics, which lays the foundation for developing machine learning (ML)-based surrogate models and ML-assisted cross-scale simulations to accelerate the design and optimization of AM ceramic structures that perform better.

Preface

Chapter 2 of this thesis has been published as **Z. Zaiemyekeh**, H. Li, S. Sayahlatifi, M. Ji, J. Zheng, D.L. Romanyk, and J.D. Hogan, "Computational finite element modeling of stress-state-and strain-rate-dependent failure behavior of ceramics with experimental validation," Ceramics International (2023), vol. 49, 13878-13895. As the first author, I was responsible for conceptualization, experiments, investigation, software, simulations, validation, data analysis and visualization, and writing the original draft. H. Li assisted with experiments and contributed to manuscript editing. S. Sayahlatifi assisted with methodology, validation, and software, and contributed to manuscript editing. M. Ji assisted with the experiments. J. Zheng assisted with the experiments, and investigation, and contributed to manuscript editing. Dan L. Romanyk supervised the research and was involved with concept formation, manuscript reviewing, and editing. J.D. Hogan supervised the research, acquired funding, and was involved with concept formation, manuscript reviewing, and editing.

Chapter 3 of this thesis has been published as **Z. Zaiemyekeh**, H. Li, D.L. Romanyk, and J.D. Hogan, "Strain-rate-dependent behavior of additively manufactured alumina ceramics: Characterization and mechanical testing," Journal of Materials Research and Technology (2024), vol. 28, 3794-3804. As the first author, I was responsible for conceptualization, conducting experiments and data collection, data analysis and visualization, investigation, and writing the original draft. H. Li assisted with experiments and contributed to manuscript editing. D.L. Romanyk supervised the research and was involved with concept formation, manuscript reviewing, and

editing. J.D. Hogan supervised the research, acquired funding, and was involved with concept formation, manuscript reviewing, and editing.

Chapter 4 of this thesis has been published as **Z. Zaiemyekeh**, S. Sayahlatifi, D.L. Romanyk, and J.D. Hogan, "Understanding the effect of microstructure on the failure behavior of additively manufactured Al_2O_3 ceramics: 3D micromechanical modeling," Materials and Design (2024). As the first author, I was responsible for conceptualization, conducting experiments and analyzing the data, developing the model, designing and performing numerical simulations, analyzing results, and writing the original draft. S. Sayahlatifi assisted with the methodology, validation, and software, and contributed to manuscript editing. D.L. Romanyk supervised the research and was involved with concept formation, manuscript reviewing, and editing. J.D. Hogan supervised the research, acquired funding, and was involved with concept formation, manuscript reviewing, and editing.

Chapter 5 of this thesis has been submitted to Ceramics International for peer review publication as **Z. Zaiemyekeh**, M. Rezasefat, Y. Kumar, S. Sayahlatifi, J. Zheng, H. Li, D.L. Romanyk, and J.D. Hogan, "On the role of stress state in the failure behavior of alumina ceramics via stereolithography: Quasi-static and dynamic loading," As the first author, I was responsible for conceptualizing and methodology, conducting experiments, analyzing data, visualization, and Writing the original draft. M. Rezasefat assisted with the experiments and contributed to manuscript editing. Y. Kumar assisted with the experiments. S. Sayahlatifi assisted with the experiments and contributed to manuscript editing. H. Li assisted with the experiments and contributed to manuscript editing. D.L. Romanyk supervised the research and was involved with concept formation manuscript reviewing, and editing. J.D. Hogan supervised the research, acquired funding, and was involved with concept formation, manuscript reviewing, and editing.

Acknowledgements

I am profoundly grateful to my supervisors, Prof. James D. Hogan and Prof. Dan L. Romanyk, for their exceptional guidance, unwavering support, and encouragement throughout my doctoral journey. Your insightful advice, extensive knowledge, and continuous motivation were crucial in the completion of this research. I deeply appreciate your dedication to my academic and personal growth.

I would like to express my sincere gratitude to my final exam committee members Prof. Mihaela Vlasea, Prof. Osezua Ibhadode, Prof. Xiaodong Wang, and Prof. Mostafa Yakout. Their thorough review, and constructive, and insightful suggestions have greatly refined and elevated the quality of this thesis. I deeply appreciate their time and effort in evaluating my work and providing valuable feedback.

I would also like to extend my heartfelt thanks to my group mates at the Centre for Design of Advanced Materials (CDAM). Their friendship and collaboration have been indispensable throughout this journey. Our discussions and shared experiences have made this journey productive and enjoyable.

Above all, I am deeply grateful to my beloved parents (Manoochehr and Nahid) and husband (Saman) for their unconditional love, support, and encouragement throughout this journey. Their belief in me has been a constant source of strength and motivation. I am also truly thankful to my brothers (Amir and Hamid) for their encouragement, companionship, and unwavering belief in my abilities.

Table of Contents

List of Tables

List of Figures

Chapter 1

Introduction

1.1 Motivation

High hardness, high strength-to-weight ratio, and good thermal and chemical stability have made advanced ceramics (e.g., Al_2O_3 [1], SiC [2], and B_4C [3]) attractive for use in different industrial sectors (e.g., defense [4], health [5] and aerospace [6]), where the material may be subjected to a range of complex loading conditions such as extreme pressure (e.g., shock [7]), high strain rate loading [8], and high temperatures [9]. Design and development of longer-lasting ceramic structures are vital in industry-driven applications where a wide range of stress states and strain rates are induced in the material [10, 11], and this requires a comprehensive understanding of the mechanical properties and failure mechanisms [12, 13]. Once the microstructure-property-performance relationships are established, one can modify the manufacturing process to control the failure process of advanced ceramics via tailoring microstructures and mechanical properties. Among the many types of advanced ceramics, alumina (Al_2O_3) has been widely employed in impact applications (e.g., protection systems), owing to the cost-benefit ratio relative to other ceramics (e.g., boron carbide) and moderate mechanical properties [14, 15]. Conventional manufacturing (CM) processes of ceramics (e.g., dry pressing [16], and injection molding [17]) are complex, time-consuming, and need post-processing (i.e., machining) [18]. As such, additive manufacturing (AM) methods are gaining high popularity and progress for the fabrication of ceramic struc-

tures with flexibility in the design of complex-shaped geometries [19]. AM methods are based on using material deposition to fabricate 3D parts by adding material, usually layer-by-layer directly from computer-based models [20]. Among different AM methods (e.g., binder jetting [21], stereolithography (SLA) [22], and selective laser sintering (SLS) [23]), the SLA technique has been extensively used in recent years owing to high forming accuracy, high resolution, and high-quality surface finish when compared to other AM technologies [24, 25]. This thesis focuses on providing a comprehensive investigation of the strain-rate- and stress-state-dependent behavior of both CM and AM alumina ceramics through experimental mechanics and multiscale modeling approaches, having implications for the design of ceramic structures with tailored mechanical properties and failure behaviors.

In the literature on CM and AM alumina ceramics, many experimental studies have focused on investigating the strain-rate-dependent mechanical behavior of the material under uniaxial compression stress state [26–31], while limited efforts have been made to address the mechanical response of the material under tensile [32, 33] and combined loading conditions (e.g., compression-shear stress state) [30, 34]. Due to the brittleness of ceramic materials, the failure process, including the initiation and propagation of cracks, evolves in the order of microseconds under dynamic loading - for example, an average crack speed of 5.9 km/s was observed in the dynamic indirect tension tests at a strain rate range of 10 to 170 s^{-1} [7, 32]. Accordingly, to capture the failure process, advanced experimental methodologies are required (e.g., high-speed cameras to capture millions of frames per second [28, 29]). This thesis employs state-of-the-art experimental methodologies to study the effect of strain rate and stress state on the failure response of CM and AM alumina ceramics by designing and testing cuboidal, angled, and Flattened Brazilian Disc (FBD) specimens to induce a compression, compression–shear, and tensile stress state in the material, respectively, under different strain rates (e.g., 10^{-4} to 10^{3} s^{-1}) through coupling ultra-high-speed imaging and digital image correlation (DIC) analysis.

While experimental mechanics provides insights on the global measurement of mechanical properties and deformation mechanisms [26–28], computationally efficient models are needed to provide a fundamental understanding of the competition of different failure mechanisms, sensitivity of various underlying material parameters at much higher spatial and temporal resolutions and under conditions that are not readily accessible with experiments [35, 36], and the links between the microstructure and macroscale response of the material. To constitutively model ceramics, various constitutive models have been proposed in the literature [37–41], including phenomenological constitutive frameworks, (e.g., Johnson–Holmquist-I (JH1) [42], Johnson–Holmquist-II (JH2) [43], Johnson-Holmquist-Beissel (JHB) [44], Simha [45], Simons et al. [40, 46, 47]) and mechanism-based models (e.g., Rajendran and Grove [48, 49], Deshpande and Evans [50, 51], and Paliwal and Ramesh [52]). Among the phenomenological material models, models developed by Johnson and Holmquist (i.e., JH2) have been widely used to capture the response of ceramics under high strain rate loading conditions [4, 5, 14, 15, 36]. While the JH2 model is widely used for predicting ceramic behavior, there is still room for improvement in terms of mitigating the dependency of the model predictions on the mesh size and capturing the strain-rate- and stress-state-dependent failure behavior of ceramics. To do so, this thesis implements the JH2-V model proposed by Simons et al. [40, 46, 47], via a VUMAT subroutine in Abaqus software. In the JH2-V model, the hydrostatic tensile strength is dependent on the rate of equivalent plastic strain by introducing a viscosity parameter and this leads to a strain-rate-dependent yield function that allows mesh regularization in addition to capturing the strain-rate-dependent behavior of the ceramic material. In addition, the fracture strain formulation is revised and defined as a pressure-dependent failure strain formulation to better capture the asymmetry in the rate of damage growth under tension and compression stress states [46].

Building on these past studies on the ceramic materials [29, 30, 32, 40, 47], this thesis seeks to provide an in-depth investigation of the mechanical behavior and fail-

ure evolution/competition of both CM and AM Al_2O_3 ceramics across stress state and strain rates through a combination of experimental and multiscale numerical approaches, which has been rarely taken in the literature. Overall, this thesis will contribute to addressing gaps in the knowledge of stress-state- and strain-rate-dependent failure progression in advanced CM and AM alumina ceramics across length scales, governing the behavior of the material at structural scales, whose outcomes have implications for the design of better-performing and weight-optimized ceramic-based structures in a range of applications such as aerospace (e.g., engine components [53]) and defense (e.g., protection systems [54]). This thesis is presented in a paper-based format, where each chapter corresponds to a standalone research paper. Each paper provides a detailed background, including a comprehensive review of the relevant literature, specific to the subject being addressed. By structuring the thesis in this manner, the appropriate scientific context is directly integrated into each chapter, ensuring that the literature review aligns with the distinct objectives and findings of the individual studies.

1.2 Thesis Objectives

The overarching objectives of this thesis are to (a) Employ experimental mechanics approaches to provide high-fidelity qualitative and quantitative understandings of the failure initiation and propagation of AM alumina ceramics under different stress states and strain rates which are rarely investigated in the literature. (b) Providing insights into the correlations between the microstructure, the growth history of failure mechanisms, and the macroscale mechanical behavior of AM alumina by developing microstructure-based FE models. To achieve the objectives, experimentally, the microstructural features of the material (e.g., material composition, grain size distribution, and porosity) are characterized through scanning electron microscopy (SEM) equipped with energy dispersion spectroscopy (EDS), electron backscattered diffraction (EBSD), and X-Ray Microscopy (XRM). Following material characterization, the

stress-state-dependent behavior of the material is investigated by designing cuboidal, angled, and FBD specimens to induce uniaxial compression, shear-compression, and indirect tension stress states in the material, respectively, under a wide variety of strain rates (i.e., 10^{-4} s^{-1} to 10^{2} s^{-1}). Numerically, a VUMAT subroutine was developed in the ABAQUS software to implement the JH2-V material model proposed in Simons et al. [40, 47]. Next, EBSD-based polycrystalline representative volume element (RVE) models are generated using Neper software to develop a microstructure-informed FE model to inform on the microstructure-property-performance relationships of AM alumina ceramics. The micromechanical model is informed and validated by the outcomes from the experiments. Through this thesis, the objectives are accomplished by completing the following research goals:

1. Characterize the mechanical behavior of CM and AM alumina (i.e., hot-pressed Ceram Tec Alotech 98% and AM alumina by SLA method from Lithoz) under a wide variety of strain rates (i.e., 10^{-4} to 10^{2} s^{-1}) and stress states (i.e., compression, compression-shear, and tensile) through material testing system (MTS) 810 machine [28] and split-Hopkinson Pressure Bar (SHPB) [29] experiments coupled with high-speed imaging and DIC [26]. Quantitative measurements are conducted to obtain stress vs. strain responses, and lateral strain versus axial strain histories during the loading event to investigate how they evolve in a specified rate and loading path. Cuboid and angled specimens will be used to generate compression and compression-shear stress states in the material, while a tension-dominated stress state is induced through the FBD specimens. These experiments will be used to inform, parameterize, and validate the models developed in this thesis.

2. Ultra-high-speed imaging in the SHPB experiments will be used to observe the crack initiation and propagation in the material and the sequence of failure events. Regarding the limited measurements of this kind, observation of ini-

tiation and propagation of damage unravels new insights into the speed and mechanisms of crack growth. In addition, material characterization techniques such as SEM, EDS, EBSD, and XRM, will be employed to explore the microstructural characteristics of the material, such as the grain size distribution, chemical composition, grain morphologies, as well as post-mortem analysis of the fracture surfaces. These microstructural data sets will be linked with the macroscopic observations made in mechanical testing to better understand the stress-state- and strain-rate-dependent behaviors of the material in addition to being leveraged to develop microstructure-based models of the AM alumina.

3. Develop VUMAT subroutines in ABAQUS software to implement the phenomenological JH2-V model [46, 47]. This material model is a modification of the well-known JH2 model [43], by which the mesh dependency problem of the JH2 material model is improved. In this modified model, the hydrostatic tensile strength of the ceramic is linked with the equivalent plastic strain rate to account for the strain rate effect, and a pressure-dependent fracture strain formulation is also defined [47]. Next, the JH2-V material model is applied to model the behavior of the CM alumina ceramics at the macroscale by modeling the cuboidal, angled, and FBD specimens. Once validated with the corresponding experimental data, the developed modeling framework was leveraged for investigating the effect of bulking, regularization parameters of the JH2-V model, quantitative analysis of the damage initiation and growth in the material, and stress-state-dependent mesh sensitivity analysis for guiding higher scale modeling (e.g., impact events) [55].

4. Develop porous polycrystalline-based RVEs of AM alumina ceramics based on the grain size distribution, porosity, and crystallographic orientations from the SEM and EBSD analysis. To capture the transgranular failure mechanism grains are modeled by the JH2-V model, and grain boundaries are modeled

by a bi-linear traction-separation law via the CZM approach to capture the intergranular failure mechanism. The micromechanical model is validated by experimental stress-time curves and failure mechanisms observed in fractography analysis across strain rates. Once validated, by using Python scripting, the history of failure mechanisms, including intergranular and transgranular mechanisms is quantified to unravel the initiation and evolution of failure in the material. The validated model is leveraged to study the effect of microstructural features (e.g., grain orientations, porosity, grain boundary properties, and grain size) on the strain-rate-dependent structural behavior of the material. The multiscale numerical model is applied to inform on the correlations between the microstructure and macroscale response of the material, resulting in outcomes that are applicable to the design and development of ceramic materials with tailored mechanical properties (e.g., strength) [30, 56, 57].

1.3 Thesis Contributions

The main contributions of this thesis will be as follows:

- This thesis provides novel experimental quantitative and qualitative findings on the mechanical response of AM alumina ceramics under different stress states such as compression, combined shear-compression, and indirect tension across various strain rates. Building on the limited previous studies [30, 31, 58, 59], this thesis provides a comprehensive understanding of the material behavior through high-fidelity experiments coupled with the state-of-the-art diagnostics (e.g., DIC and ultra-high-speed imaging), which allows the development and validation of FE models to further explore the mechanical responses of the material subjected to various loading conditions.

- This thesis makes contributions in analyzing the quantitative damage initiation and growth in the materials at the macroscale across stress states and strain

rates through computational mechanics, which has primarily been addressed in previous studies by presenting qualitative time-resolved images.

- This thesis develops microstructure-based RVE models to correlate the microstructural characteristics of the AM ceramics (e.g., grain size, pore features, and interface properties), the progression of microscale failure mechanisms, and the macroscale response of the material (e.g., strength) to provide microstructure-property-performance relationships. Additionally, the current microstructure-informed model is the first of its kind that quantitatively unravels the evolution history of microscale failure mechanisms in AM ceramics, which are challenging to uncover experimentally by in-situ methodologies due to the brittle response. The outcomes of such a micromechanical model inform the design and optimization of AM ceramics with higher performance.

- This thesis will lay the foundation for training and developing microstructure-informed machine learning models [60–62] by the outcomes of the developed micromechanical model (e.g., generated datasets describing strength-porosity relationship) to enable autonomous prediction of the mechanical behavior of AM alumina ceramics accounting for microstructural features of the material. The impact of such a model originates from mitigating our reliance on expensive and time-consuming destructive testing, which eventually accelerates the process of material design and optimization.

1.4 Thesis Structure

This thesis is structured based on research published as journal articles presented as individual chapters in the following order:

- Chapter 1: "Introduction". This section discusses the background and motivation for investigating the strain-rate- and stress-state-dependent behavior

of advanced ceramics through a combination of experimental mechanics and multiscale simulation approaches.

- Chapter 2: "Computational finite element modeling of stress-state- and strain-rate-dependent failure behavior of ceramics with experimental validation". Published in *Ceramics International*, as **Zahra Zaiemyekeh**, Haoyang Li, Saman Sayahlatifi, Min Ji, Jie Zheng, Dan L. Romanyk, and James D. Hogan, 2023 [55]. This study investigates the stress-state- and strain-rate-dependent behavior of CeramTec ALOTEC 98% alumina (Al_2O_3) ceramics through an experimentally validated numerical approach. For constitutive modeling of the material, a VUMAT subroutine was developed in ABAQUS finite element (FE) software to implement a viscosity-regularized version of the phenomenological Johnson-Holmquist (JH2) material model (i.e., the JH2-V model for ceramics). Experimentally, the stress-state- and strain-rate-dependent failure response of the material was captured by designing and testing angled (i.e., compression-shear stress state) and flattened Brazilian disc (i.e., tensile stress state) specimens subjected to dynamic loading via SHPB setup, and the data was used to inform and validate the FE model. Once validated, the developed modeling framework was leveraged for investigating the effect of bulking, regularization parameters of the JH2-V model, quantitative analysis of the damage initiation and growth in the material, and stress-state-dependent mesh sensitivity analysis for providing guidance for higher scale modeling (e.g., impact events). The highlights of the paper are: 1) A new computational quantification approach was proposed to analyze damage initiation and growth in ceramics to provide a better understanding of the effect of shear on the failure response of the material, which has only been qualitatively addressed in previous studies by presenting time-resolved experimental images. 2) The investigation of the effect of mesh size across different stress states provided new guidelines to balance the computa-

tional cost and accuracy when the model is applied to higher-scale applications (e.g., impact loading).

- Chapter 3: "Strain-rate-dependent behavior of additively manufactured alumina ceramics: Characterization and mechanical testing". Published in the *Journal of Materials Research and Technology*, as **Zahra Zaiemyekeh**, Haoyang Li, Dan L. Romanyk, and James D. Hogan, 2024 [30]. This study investigates the microstructure and strain-rate-dependent behavior of additively manufactured (AM) alumina ceramics with two different printing orientations (POs) using the stereolithography method, which has been rarely studied in the literature. The strain-rate-dependent behavior and failure response of the AM alumina was studied under quasi-static and dynamic loading, where an ultra-highspeed camera coupled with digital image correlation (DIC) was used to visualize crack initiation/propagation processes and capture full-field strains. Additionally, the fracture surfaces were characterized by SEM to reveal the contributing micro failure mechanisms. Crack speed propagation in the AM alumina was measured and compared with conventionally made alumina ceramics across different strain rates. Lastly, the hardness of the current AM alumina ceramics was measured using the micro-indentation Vickers test and compared with those of the conventionally-made and other AM alumina counterparts in the literature. The highlights of the paper are: 1) The quasi-static and dynamic strength of our AM alumina was among the highest ones reported for AM alumina in the literature likely due to finer grain size confirmed by our EBSD characterization. 2) The POs were found to minimally affect the strength-strain-rate behavior while notably influencing the macro-scale failure pattern. 3) The crack speed propagation in AM alumina was found to be less than conventional counterparts due to a larger average pore size in the AM alumina. 4) The micro-indentation experiments showed that the hardness of the

AM material was independent of the PO. The current AM alumina represents a higher hardness compared to the other AM alumina ceramics in the literature and this was attributable to a higher relative density, smaller pore size, and a finer grain size. 5) This study provides novel data sets and new insights into the mechanical properties and failure behavior of AM alumina ceramics, and these have implications for the design of better-performing AM ceramics as promising future materials.

- Chapter 4: "Understanding the effect of microstructure on the failure behavior of additively manufactured Al_2O_3 ceramics: 3D micromechanical modeling". Published in *Materials and Design*, as **Zahra Zaiemyekeh**, Saman Sayahlatifi, Dan L. Romanyk, and James D. Hogan, 2024 [63]. In light of the expansion in popularity of additively manufactured (AM) ceramics due to their flexibility in the design of complex and multifunctional structures, the current work developed 3D microstructure-informed finite element (FE) models to study the failure behavior of AM Al_2O_3 ceramics under quasi-static ($\dot{\epsilon}$= 10^{-3} s^{-1}) and dynamic loading ($\dot{\epsilon}$= 690 s^{-1}). Porous polycrystalline-based representative volume elements (RVEs) of the material were reconstructed based on the grain size distribution, porosity, and crystallographic orientations from the SEM and EBSD analysis. Grains were modeled by a strain-rate-dependent constitutive model for brittle materials implemented by a VUMAT subroutine in Abaqus/FE solver, and grain boundaries were modeled by a bi-linear traction-separation law via the cohesive zone modeling (CZM) approach. Upon validation, by using Python scripting, the history of failure mechanisms, including intergranular and transgranular mechanisms was quantified to unravel the initiation and evolution of failure in the material. The validated model was leveraged to study the effect of grain orientations, porosity, grain boundary properties, and grain size on the strain-rate-dependent mechanical behavior of the material. The highlights

of the paper are: 1) The current microstructure-informed model is the first of its kind that quantitatively unravels the evolution history of microscale failure mechanisms in AM ceramics, which are challenging to uncover experimentally. 2) This study computationally correlates the microstructure, the progression of failure mechanisms, and the macroscale response of the material across strain rates whose outcomes inform the design of additively manufactured ceramics with higher performance.

- Chapter 5: "On the role of stress state in the failure behavior of alumina ceramics via stereolithography: Quasi-static and dynamic loading". Submitted to *Ceramics International*, as **Zahra Zaiemyekeh**, Mohammad Rezasefat, Yogesh Kumar, Saman Sayahlatifi, Jie Zheng, Haoyang Li, Dan L. Romanyk, and James D. Hogan, 2024. In light of the expansion in the application of ceramic structures by additive manufacturing, this study investigates the strain-rate- and stress-state-dependent behavior of additively manufactured (AM) alumina ceramics with three different printing orientations (POs) using the stereolithography method. The strain-rate-dependent behavior and failure response of the AM alumina were studied under shear-compression and tension stress states through the design of angled cuboids and flattened Brazilian discs, respectively, where an ultra-high-speed camera coupled with digital image correlation (DIC) was used to visualize crack initiation/propagation processes and capture full-field strains. The highlights of the paper are: 1) It was found that when the PO of AM specimens was perpendicular to the loading direction the material showed a higher strain-rate-dependent strength under both stress states, likely due to the layer-by-layer printing effect and how processing-induced microstructural defects across length scales contributed to the damage propagation. 2) It was found that the increase in shear strain induced a larger shear strain in the material, which resulted in the earlier initiation of damage, thereby lowering the

equivalent strength. 3) It was shown that the intergranular failure mechanism was dominated under quasi-static loading, while a combination of intergranular and transgranular mechanisms governed failure under dynamic loading. 4) The outcomes of this study, for the first time to the best of our knowledge, provide a comprehensive understanding of how strain-rate and stress state affect the failure behavior of AM alumina ceramics, and this has implications for the design and improvement of this novel AM material for environments including high strain-rate loading, such as aerospace and defense industries. Additionally, the datasets provided in this study are foundational for developing and validating microstructure-informed numerical models to be used for establishing microstructure property performance relationships applicable to material optimization.

- Chapter 6: "Conclusions & Future Work". Summarizes the key scientific outcomes of this research and outlines directions for future work. This chapter also highlights the list of all academic publications, resulting from this research program.

Chapter 2

Computational finite element modeling of stress-state-and strain-rate-dependent failure behavior of ceramics with experimental validation

Published as **Zahra Zaiemyekeh**, Haoyang Li, Saman Sayahlatifi, Min Ji, Jie Zheng, Dan L. Romanyk, James D. Hogan. "Computational finite element modeling of stress-state- and strain-rate-dependent failure behavior of ceramics with experimental validation", *Ceramics International*, 2023, 49, 13878–13895.

2.1 abstract

This study investigates the stress-state- and strain-rate-dependent behavior of CeramTec ALOTEC 98% alumina (Al_2O_3) ceramic through experimentally validated finite element (FE) modeling. As the constitutive material model, a rate-dependent viscosity-regularized phenomenological model (JH2-V model) was implemented through a VUMAT subroutine in ABAQUS software. The FE model was informed and validated with the data for indirect tension and compression-shear tests under dynamic rates both quantitatively (i.e., stress-strain histories and lateral strain-axial strain curves) and qualitatively (i.e., manifestation and accumulation of damage). The val-

idated model was leveraged to study the effect of the JH2-V model regularization parameters, mesh sensitivity, and bulking across different stress states. Additionally, by modeling the compression-shear specimen with different angles, the effect of shear on the material response was quantitatively investigated through the definition of a volumetric average damage parameter and shear strain history. Altogether, the outcomes of this study have implications for the computational design and development of ceramic-based structures in higher-scale applications (e.g., impact).

2.2 Introduction

Advanced ceramics have a wide range of applications (e.g., protection [64, 65] and aerospace [9, 66]) owing to their desirable mechanical properties, such as low density [14, 67], high compressive strength [2, 31], and high hardness [3, 68]. Under loading, the damage evolution in ceramics is a complex phenomenon involving various spatially and temporally evolving mechanical responses and deformation mechanisms, particularly at higher strain rates [35, 36]. To optimize the performance of advanced ceramics, it is important to consider the role of stress-state- and strain-rate-dependent behavior to better capture their failure phenomena [13, 69]. This study focuses on the alumina (Al_2O_3) ceramics due to the cost-benefit ratio relative to other ceramics (e.g., boron carbide) [14, 15] to provide a comprehensive investigation of the stress-state- and strain-rate-dependent behavior of the material through a combined experimental and numerical approach.

In the literature, the behavior of alumina ceramics has been mainly explored under a uniaxial compressive loading for both quasi-static and dynamic strain rates [26–29, 70–76]. For example, Lo et al. [27] performed quasi-static and dynamic uniaxial compression tests to characterize the mechanical response of an AD85 alumina ceramic. They found that variability in the mechanical properties was larger at quasi-static conditions compared to dynamic, and this is attributable to the activation of a higher number of pores at higher loading rates. In another study, the

dynamic macro-cracking and fragmentation process of alumina under uniaxial compression was studied by Wang et al. [14]. It was found that the compressive strength of alumina is almost insensitive to the low strain rate regimes, while it is significantly sensitive to higher strain rates ($\geq 250\ s^{-1}$). In contrast to many experimental studies exploring the uniaxial compressive behavior of alumina ceramics, limited efforts have been made to address the dynamic response of the material under tensile [32, 33] and combined loading conditions [34, 58, 77], where the effects of the stress state and loading rate on the mechanical properties and fracture mechanisms remain a field of interest. In this study, we seek to study the indirect tension and compression-shear response of Al_2O_3 ceramics to reveal the effect of stress state on failure response of the material.

To investigate the tensile and combined loading behavior of advanced ceramics, different methods have been proposed. The Brazilian disk (BD) [33, 59, 78] and the modified flattened Brazilian disk (FBD) [32, 79] experiments have been used in multiple studies as a typical indirect tension test to determine the tensile strength of brittle materials such as ceramics [32, 59] and rocks [80, 81]. To explore the shear-dominated behavior of brittle solids, hydraulic confinement techniques [82–84] and inclined specimen methods with a modified split-Hopkinson Pressure Bar (SHPB) system [85–87] have been employed in the previous studies. In a study by Du et al. [88], oblique cylindrical rock specimens with varying hydrostatic confining pressures were tested under different loading rates, and they found that by increasing the specimen inclination angle and the hydrostatic confining pressure, the failure pattern of the specimens changed from the tensile-dominated failure to shear-dominated failure. In a separate study by Xu et al. [85], angled rock specimens were used in the SHPB setup to achieve a combined compression-shear stress state, and it was found that all the inclined specimens exhibited a prominent shear-dominated failure accompanied by localized tensile damage. Based on previous studies [33, 59, 86, 87], the FBD and angled specimen are adopted in the current study to investigate the rate-dependent

tensile and compression-shear responses of the Al_2O_3 ceramics.

In addition to the experimental efforts, various constitutive models have been proposed to capture/describe the mechanical response of ceramic materials to obtain higher spatial and temporal resolutions. These models include phenomenological models (e.g., Johnson–Holmquist-I (JH1) [42], Johnson–Holmquist-II (JH2) [43], Johnson-Holmquist-Beissel (JHB) [44], Simha et al. [45], and Simons et al. [40, 47]), and mechanism-based material models (e.g., models by Rajendran and Grove [48, 49], Deshpande and Evans [50, 51], and Paliwal and Ramesh [52]). Among the phenomenological material models, the model developed by Johnson-Holmquist (i.e., JH2) [43], as a pressure dependent plasticity model, has been widely used to predict the response of ceramics under high strain rate loading conditions because of simplicity in implementation and applicability to a wide range of tests [15, 36, 89]. However, in a study by Simons et al. [47] indicated that damage initiation and propagation could be affected due to strain localization upon failure which is related to mesh characteristics in softening plasticity models (e.g., JH2 model). To improve the JH2 material model, Simons et al. [40, 47] proposed a regularized viscosity JH2 model (JH2-V). In the JH2-V model, the hydrostatic tensile strength was formulated as a function of the rate of equivalent plastic strain and a viscosity parameter to account for the strain-rate-dependent spall (hydrostatic tensile) strength of ceramics. This rate-dependent definition of tensile strength leads to a rate-dependent yield surface that helps to reduce strain localization [47, 90]. In addition, the fracture strain formulation was revised in the Simons et al. [40, 46] studies by defining pressure-dependent transition points to better capture the asymmetry in the rate of damage growth under tension and compression [40].

Motivated by previous efforts, this study investigates the stress-state- and strain-rate-dependent behavior of alumina ceramics under tensile and combined compression-shear stress states through an experimentally validated finite element (FE) framework with the JH2-V model incorporated. Experimentally, the effect of stress state on

failure response of alumina ceramics is explored by designing and testing angled specimens to induce a compression-shear stress state and FBD specimens to induce a tensile stress state in the material. The mechanical testing is carried out using a SHPB setup for dynamic strain rates in conjunction with ultra-high-speed imaging and digital image correlation (DIC). Computationally, the JH2-V model is implemented in ABAQUS software by using a VUMAT subroutine and is validated with experimental data. Once validated, the model is exercised to quantitatively analyze the damage initiation and growth with the presence of shear loading, and providing guidance for higher scale (e.g., impact events) in terms of element size selection. Ultimately, the outcomes of this study provide insights into the role of stress state (e.g., the presence of shear) on the failure response of Al_2O_3 ceramics that is applicable to the design of ceramic structures in a range of applications (e.g., impact [91, 92], and aerospace [66, 93]).

2.3 Experimental methodology

In this study, commercially available 98% purity alumina (Al_2O_3) from CeramTec, Germany, with a manufacturer-specified density of 3.9 g/cm^3, Young's modulus of 380 GPa, Poisson's ratio of 0.22, fracture toughness of 3.5 MPa$\sqrt{m}$, bending strength of 260 MPa, and average grain size of $\sim$ 1.85 μm was studied. For dynamic compression-shear experiments, cuboidal specimens with nominal dimensions of 3.5 mm $\times$ 2.3 mm $\times$ 2.7 mm, and a tilting angle of 5° were used. For indirect tension experiments, the FBD specimens with a diameter of 8 mm and thickness of 4 mm were fabricated. Fig. 2.1 (a) and (b) show the dimension and geometry of the specimens. In the FBD specimens, to facilitate the formation of a central crack and reduce shear strain, the thickness-to-diameter ratio was set to be 0.5 [32, 94], and two parallel flat ends were introduced to the specimen to reduce stress concentrations [94, 95]. The FBD samples used in this numerical study were fabricated based on the geometrical guidelines provided in the literature [96, 97] to increase the likelihood of the initiation of a

central crack and a successful FBD experiment [97]. In addition, a loading angle (i.e., 2α) is selected to be 20° following Griffith strength theory [98] to allow crack initiation at the center of the disk, and this loading angle was also used in previous studies [94, 98].

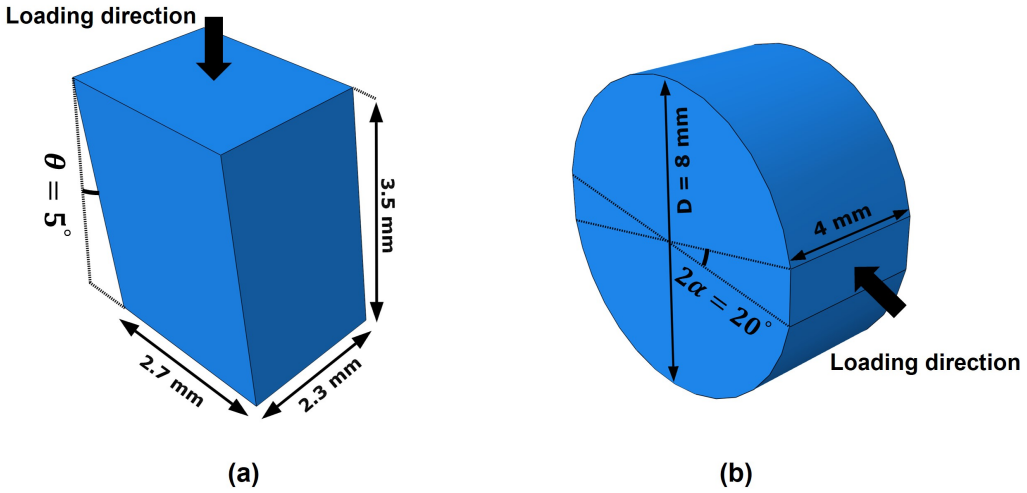

Fig. 2.1: (a) The geometry and dimensions of the angled ($\theta = 5°$) ceramic specimens designed to induce a compression-shear stress state in the material, and (b) The geometry and dimensions of the FBD ceramic specimens with flattened surfaces defined by 2α =20° designed to induce a tensile stress state in the material.

2.3.1 Material characterization

In the current study, the scanning electron microscopy (SEM) of the polished surface (mechanically polished down to 0.25 μm) of the as-received CeramTec 98% alumina ceramic coupled with an energy dispersive x-ray spectroscopy (EDS) was conducted to characterize the typical microstructure and the elemental composition of the material. Shown in Fig. 2.2 (a) is an SEM image of the material which is obtained using a Zeiss Sigma FESEM machine. Fig. 2.2 (b to f) shows the EDS map data which is post-processed using the Aztec software from Oxford Instruments. As seen, the alumina ceramic in this study is mainly composed of oxygen (weight and atomic percentages are 56.86% and 69.05%, respectively) and aluminum (weight and atomic percentage are 41.75% and 30.06%, respectively) mixed with traces of Mg, Si, and Ca which are

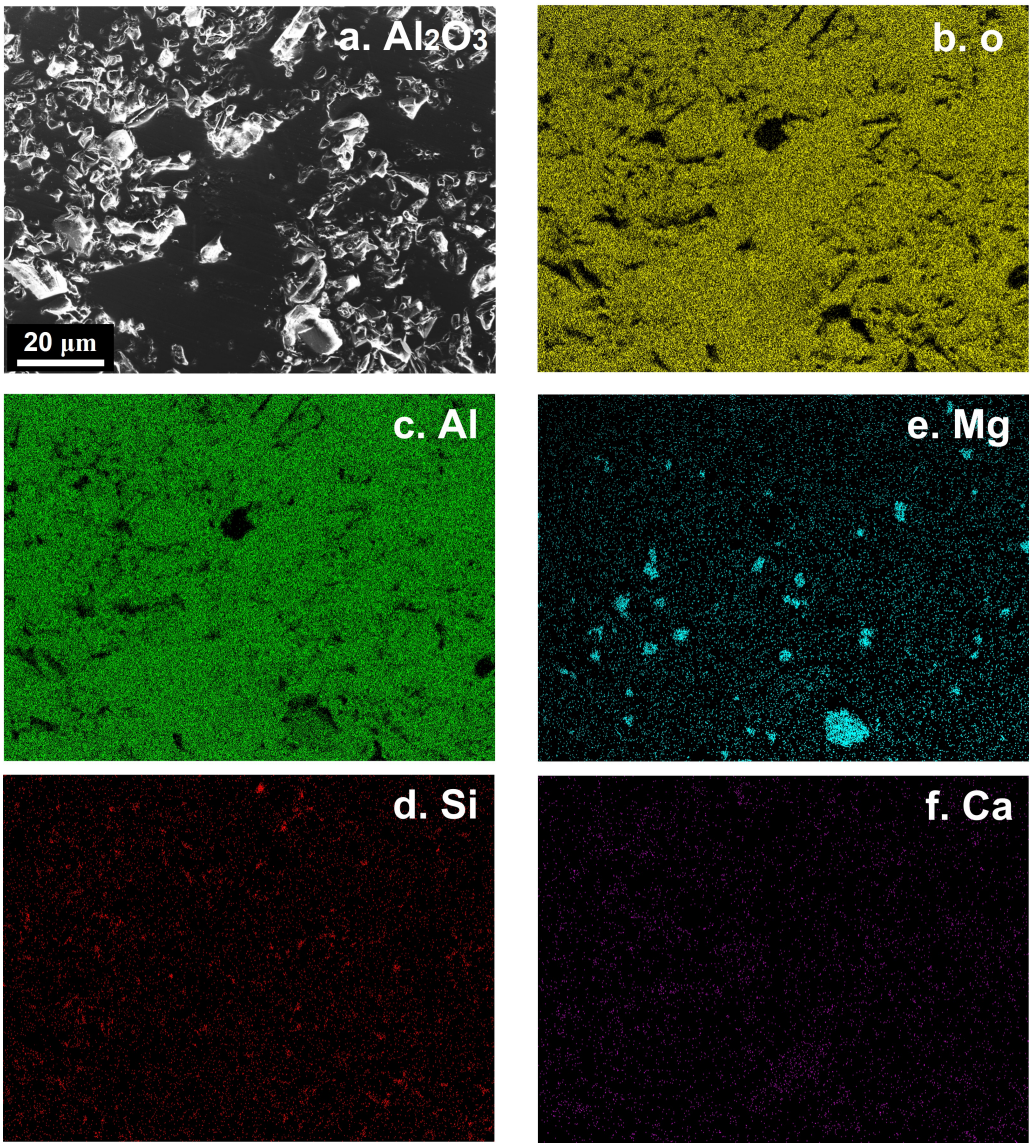

Fig. 2.2: SEM micrograph examining the microstructural features of the as-received material and EDS concentration mapping shows the distributions of selected elements. (a) SEM image of CeramTec alumina with 98 wt.% purity. (b) The distribution and concentration of O (atomic 69.05%, weight 56.86%) in the SEM image, show that it is present everywhere except for the dark spots. (c) Distribution and concentration of Al (atomic 30.6%, weight 41.75%) in the SEM image. (d) Distribution and concentration of Mg (atomic 0.43%, weight 0.35%). (e) Distribution and concentration of Si (atomic 0.3%, weight 0.43%). (f) Distribution and concentration of Ca (atomic 0.24%, weight 0.51%)

.

the consequence of fabrication process [99].

2.3.2 Mechanical testing set up

The dynamic indirect tension and compression-shear tests were conducted on a modified split-Hopkinson pressure bar (SHPB). The diameter of the incident and transmission bars was 12.7 mm with lengths of 1016 mm and 914 mm, respectively. The bars were made of hardened maraging steel (Service Steel America C-350) with density, elastic modulus, yield strength, and Poisson's ratio of 8080 kg/m^3, 200 GPa, 2.68 GPa, and 0.29, respectively. Shown in Fig. 2.3 is a schematic of the SHPB experimental setup. Two impedance-matched Ti-6Al-4V titanium alloy jacketed tungsten carbide (WC) platens with diameters the same as the bars were attached to the end of the incident and transmission bar to aid in re-distributing the loads, prevent indentation, and reduce stress concentration on the specimen. This setup has been used previously, and the results have been published [99, 100].

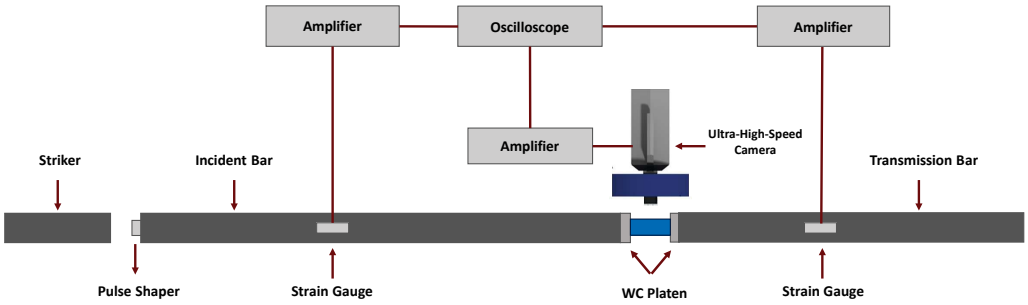

Fig. 2.3: The split-Hopkinson Pressure Bar (SHPB) experimental setup.

In the indirect tension experiments, the thicker specimen may lead to a secondary contact with the loading platens upon fracture, and this may result in the manifestation of a second peak on the recorded history of stress [32]. To avoid such an effect, no protection platens were used in the indirect tension tests. It is also worth noting that in the indirect tension experiments, the specimen was placed between the bars lubricated with high-pressure grease to reduce the frictional effect during loading, while in compression-shear tests no grease lubrication was applied to promote sufficient friction for shearing. In this SHPB setup, the data was collected with two strain

gauges (Micro 184 Measurements CEA- 13–250UN-350) attached to the bars. For the uniaxial compression-shear experiments, the transmission strain gauge signal, $\epsilon_t(t)$, was used to calculated the stress-time response $\sigma(t)$ [101]:

$$\sigma(t) = \frac{A_0}{A_s} E_0 \epsilon_t(t), \tag{2.1}$$

here, A_0 (m^2) and A_s (m^2) are the cross-sectional areas of the bar, and specimen, respectively; $\epsilon_t(t)$ is the transmitted strain-time history, and E_0 (N/m^2) is the elastic modulus of the bar material. For the indirect tension experiments, the tensile stress is calculated using the elasticity theory [102]:

$$\sigma_\theta = K \frac{2P}{\pi D t}, \tag{2.2}$$

where P, D, and t are the loading force applied to the specimen, diameter, and thickness of the disk, respectively. Here, K is a dimension coefficient as a function of the loading angle (i.e., 2α) of the flattened disk [103]. If $2\alpha = 0^\circ$ (i.e., conventional Brazilian disk), K is equal to 1, and if $2\alpha = 20^\circ$, K is approximated to 0.95 [102, 103].

In the dynamic experiments, pulse shapers were placed in front of the incident bar to provide a ramped signal, where the ramp pulse shape helps the ceramic specimen achieve stress equilibrium and constant strain rate during the high strain rate testing, as well as to filter the high-frequency component of the incident pulse [4, 104]. The indirect tension and compression-shear tests were conducted at strain rates ranging from 10 to 170 s^{-1} and 70 to 800 s^{-1}, respectively, through modifying the pulse shapers, and striker length. Table 2.1 summarizes the pulse shapers and lengths of strikers used in this study. To monitor the displacement and strain maps of the specimen during the experiments and to better visualize crack initiation and propagation, a Shimadzu HPV-X2 ultra-high-speed (UHS) camera images of speckled specimens coupled with DIC (VIC-2D V6, Correlated Solutions, Irmo, South Carolina, USA). The DIC analysis process used here follows that used in previous work, and the reader may refer to [32, 34] for further specific details. The stress-strain curves were obtained

by combining the average strain (the average strain was calculated by averaging across the area of interest (AOI) in the DIC analysis) profile with the stress profile generated from the data recorded by the strain gauge on the transmission bar by using Eq. (5.1) and Eq. (2.2). Lateral strain-axial strain curves were also generated using the DIC measurements.

Table 2.1: Pulse shaping characteristics used in dynamic loading (all dimensions are in mm).

Compression-shear experiments

Strain rate (s^{-1})	Material	Pulse shaper diameter	Thickness	Striker length
70 to 100	Tin	3.97	1.58	300
300 to 450	Thin HDPE	3.18	1.58	300
450 to 800	Thick HDPE	3.18	2.38	125

Indirect tension experiments

Strain rate (s^{-1})	Material	Pulse shaper diameter	Thickness	Striker length
10 to 20	Tin	3.97	1.58	300
25 to 40	Thin HDPE	3.97	1.58	300
90 to 170	Paper	3.97	0.5	125

Note. HDPE is the abbreviation for high-density polyethylene.

2.4 Numerical methodology

In this section, the theoretical framework of the JH2-V material model is first outlined, and the corresponding constants used in this study are given (Table 2.2). Next, the FE model of the SHPB setup is described to explore the behavior of Al_2O_3 ceramics under indirect tension and compression-shear stress states.

In the JH2-V model, as the first modification to the JH2 material model to accommodate the strain localization, the hydrostatic tensile strength was formulated as a function of the rate of equivalent plastic strain ($\dot{\epsilon}_P$) and a viscosity parameter (η). This strain-rate-dependent definition of tensile strength led to a strain-rate-dependent

yield function. In the JH2-V model, the strength is defined as an analytical functions of pressure and other parameters as [43, 47]:

$$\sigma^* = \sigma_i^* - D\left(\sigma_i^* - \sigma_f^*\right) \tag{2.3}$$

$$\sigma_i^* = A\left(P^* + T^*(\dot{\epsilon}_P)\right)^N \tag{2.4}$$

$$\sigma_f^* = B\left(P^*\right)^M \tag{2.5}$$

where σ^* is the normalized strength of the material, σ_i^* shows the normalized intact strength, σ_f^* represents the normalized fracture strength, D is the damage variable with a value between 0 and 1, A and N are intact strength constants, and B and M are fracture strength constants. Here, $\sigma^* = \frac{\sigma}{\sigma_{HEL}}$, $P^* = \frac{P}{P_{HEL}}$, $T^* = \frac{T}{P_{HEL}}$, and $\dot{\epsilon}^* = \frac{\dot{\epsilon}}{\dot{\epsilon}_0}$, where σ, σ_{HEL}, P, P_{HEL}, T, and $\dot{\epsilon}_P = \dot{\gamma}$ are the equivalent stress, equivalent stress at the Hugoniot elastic limit (HEL), actual hydrostatic pressure, pressure at the HEL, maximum tensile hydrostatic pressure tolerated by the material, and rate of the equivalent plastic strain, respectively.

Then, the hydrostatic tensile pressure $T(\dot{\epsilon_p})$ is defined as a mixed linear/logarithmic formulation [47]:

$$T(\dot{\epsilon}_p) = T(\dot{\lambda}) = \begin{cases} T_0 + \eta\dot{\lambda}, & \text{for } \dot{\lambda} < \dot{\lambda}_t \\ T_t(1 + \frac{\eta\dot{\lambda}_t}{T_t}(\ln\dot{\lambda}/\dot{\lambda}_t)), & \text{for } else \end{cases} \tag{2.6}$$

here, η is the viscosity constant, $\dot{\lambda}$ represents the rate of the plastic multiplier, T_0 is the reference rate-independent tensile strength parameter, T_t is a transition pressure ($T_t = T_0 + \eta\dot{\lambda}_t$), and $\dot{\lambda}_t$ represents the threshold rate for switching from the linear equation to logarithmic equation. Simons et al. [40, 46] found that by using a linear equation, the failure zone size in impact simulations increased rapidly with increasing loading rate, which is physically unrealistic. The logarithmic formulation is used to eliminate the rapid increase in the failure zone at high rate loading (i.e., $\dot{\lambda} \geq \dot{\lambda}_t$).

In addition, in the JH2-V model, the damage starts to accumulate once the yield function is met as shown in Eq. (2.7). The damage value is calculated based on incremental equivalent plastic strain accumulation ($\Delta\epsilon_p^{eff}$), as shown in Eq. (2.8):

$$\emptyset(\sigma, D, \dot{\lambda}) = \sigma_q - \sigma_{HEL}\sigma^* \tag{2.7}$$

$$D = \sum \frac{\Delta\epsilon_p^{eff}}{\epsilon_p^f} \tag{2.8}$$

where σ_q is the von Mises stress, and ϵ_p^f is the equivalent fracture plastic strain, which is defined by the tri-linear equivalent plastic strain formulation [40]:

$$\epsilon_p^f = \begin{cases} \epsilon_p^{min}, & p < p_t \\ \frac{p(\sigma)-p(t)}{p(c)-p(t)}(\epsilon_p^{max} - \epsilon_p^{min}) + \epsilon_p^{min}, & p_t < p < p_c, \ and \\ \epsilon_p^{max}, & p_c < p \end{cases} \tag{2.9}$$

here, for pressures below p_t and above p_c, a fixed minimum failure strain (ϵ_p^{min}) and a fixed maximum failure strain (ϵ_p^{max}) is assumed. For intermediate pressure values, the fracture strain is defined through linear interpolation. This formulation allows for independent control of damage rate under tensile and compressive loading [40, 46], which requires data (i.e., p_t, p_c, ϵ_p^{min}, and ϵ_p^{max}) on the transition points from a brittle to inelastic response of ceramics. Ceramic materials exhibit a brittle failure behavior under tension, and show inelastic deformation under high confining pressures [104]. Such inelastic deformation mechanisms have been also observed in brittle solids under shock compression [105–107]. This new formulation (Eq. (2.9)) allows to better account for such phenomena.

Lastly, to calculate pressure, a polynomial equation of state (EOS) represented by the relationship between hydrostatic pressure (P) and volumetric strain (μ) is defined as per Eq. (2.10) [43]. As the damage starts to accumulate, bulking manifests as an incremental pressure (ΔP) added to the EOS that is defined as per Eq. (2.11) [43, 108]. The value of ΔP varies from 0 when $D = 0$ to $\Delta P = \Delta P_{max}$ when $D = 1$. In this study, ΔP is calculated based on the conversion of internal elastic energy to potential internal energy owing to the decrease in shear and deviator stresses [43]:

$$P = \begin{cases} K_1\mu + K_2\mu^2 + K_3\mu^3 + \Delta P, & \text{if } \mu > 0 \\ K_1\mu, & \text{if } \mu \leq 0 \end{cases} \tag{2.10}$$

$$\Delta P_{t+\Delta t} = -K_1\mu_{t+\Delta t} + \sqrt{(K_1\mu_{t+\Delta t} + \Delta P_t)^2 + 2\mu K_1 \Delta U} \tag{2.11}$$

$$\Delta U = U_t - U_{t+\Delta t} \tag{2.12}$$

$$U = \frac{\sigma_y^2}{6G} \tag{2.13}$$

where K_1 is the bulk modulus, K_2 and K_3 represent EOS constants, and μ is the volumetric strain. The internal elastic energy is shown by U which is related to the equivalent plastic flow stress σ_y, the fraction of the elastic energy loss converted to potential hydrostatic energy is β, and G is the shear modulus. The elastic constants G and K, Young's modulus and Poisson's ratio were measured from the experimental stress-strain and lateral strain-axial strain curves (see Fig. 2.7), and then G and K were calculated with the theoretical relations between the elastic constants. The calibrated constants are the regularization parameters, including η and $\dot{\lambda}_t$. These parameters were changed within their feasible range proposed by Simons et al. [40, 47] to obtain the best match with the experimental stress-time curves and the pattern of damage initiation and propagation observed in ultra-high-speed camera images. The effect of these parameters is studied in detail in Fig. 2.8 and Fig. 2.9.

Summarized in Table 2.2 are the material constants of Al_2O_3 ceramic for the JH2-V model, which are mainly calibrated or obtained from previous studies [40, 109] and experiments in this current study. The model was implemented into ABAQUS via a VUMAT subroutine. For more details on the implementation of the JH2-V model, the reader is referred to 2.8.

2.4.1 Model description

In this study, the FE model was constructed for the entirety of the SHPB system, including the bars, the loading platens, and the specimens (see Section 2.3). The time step was set at 400 μs. The general contact algorithm was used where friction-less surface-to-surface contact was defined between the potential contacting surfaces of the FBD sample and the platen, given that these interfaces were lubricated in experiments to avoid inducing complex stress states. The same contact modeling

Table 2.2: The JH2-V constants used for Al_2O_3 ceramics.

Parameter	Value	Unit	Source
A	0.93	-	[109]
B	0.31	-	[109]
N	0.6	-	[109]
M	0.6	-	[109]
K_1	226	GPa	Current study
K_2	0	GPa	[109]
K_3	0	GPa	[109]
ρ	3900	kg/m^3	Current study
G	155	GPa	Current study
T	0.2	GPa	[40]
HEL	6.25	GPa	[40]
P_{HEL}	7.5	GPa	[40]
β	1	-	[40]
η	0.025	MPa·s	Calibrated in the current study
$\dot{\lambda}_t$	10000	s^{-1}	Calibrated in the current study
ϵ_p^{max}	0.496	-	[40]
ϵ_p^{min}	$1.5.10^{-4}$	-	[40]
p_c	3.02	GPa	[40]
p_t	-0.17	GPa	[40]

approach was applied to the compression-shear model, but a coefficient of friction of 0.06 [14] was considered for the interfaces between the sample and platens as no lubrication was applied in experiments to induce more tangential force and avoid surface sliding between the specimen and platens. To apply the load (see Fig. 2.4 (a)), the experimentally measured pressure pulse was applied on the cross-section of the modeled incident bar where the strain gauge was placed in the experiments.

Fig. 2.4 (b) shows the pressure pulse that was experimentally recorded through the strain gauge mounted on the incident bar; this pulse was used as the input to the model to induce the strain rate in the specimen. Shown in Fig. 2.4 (c) and (d) are the alignment of the FBD and angled specimens between the modeled bars and the WC platens, respectively. Upon a mesh convergence study (Fig. 2.13 (b), and (d)), the specimens were discretized by C3D8R element (continuum three dimensional 8 noded reduced integration element) with a size of 0.05 mm for angled specimen and 0.12 mm for FBD specimen, resulting in 173880 and 141636 elements, respectively. The incident bar, transmission bar, and WC platens were also discretized with C3D8R elements with a size of 1.5 mm, 1.5 mm, and 0.5 mm, leading to 33516, 46360 and 6400 elements, respectively. To reduce the run-time, the models were run on Compute Canada Graham cluster. For each simulation, four nodes (i.e., 128 cores) were employed and the corresponding computational times are summarized in Table 2.3.

2.5 Results and discussion

In this section, the results on the dynamic behavior of alumina ceramics under indirect tension and compression-shear loading are outlined for both the experiments and numerical simulations. As outlined in the previous section, the model predictions are validated with the experimental results both qualitatively (e.g., failure initiation and propagation process on the specimen surface) and quantitatively (e.g., stress versus strain and lateral strain versus axial strain responses of the material). Subsequently, the model is exercised to study the effect of the regularization parameters of the JH2-V material model (Section 2.5.2) and bulking phenomena (Section 2.5.3). The validated model is employed for studying the effect of shear on failure response of Al_2O_3 ceramics via quantitative analysis of the damage initiation and growth (Section 2.5.4), and provide guidance for higher-scale applications (e.g., impact) in terms of element size selection (Section 2.5.5).

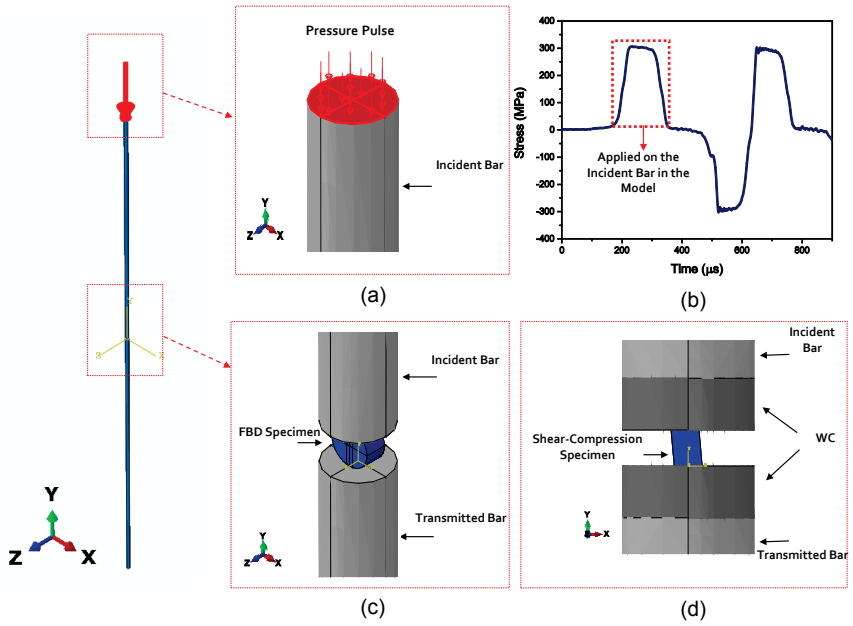

Fig. 2.4: 3D FE model of the SHPB setup used to simulate indirect tension and compression-shear experiments. (a) To simplify the model and decrease the run-time, the incident bar is only modeled between the location of the strain gauge toward the specimen, and the experimentally recorded stress-time pulse in the incident bar is applied as a pressure pulse on the cross-section of the modeled incident bar. (b) The subfigure shows the stress pulse in the incident bar measured through the strain gauge. The area in the red box is used as the input pressure pulse applied on the incident bar as shown in part (a). (c) and (d): The configuration of the indirect tension specimen and compression-shear specimen between the bars.

2.5.1 Experimental and numerical results for the mechanical behavior of Al_2O_3 ceramics under dynamic indirect tension and compression-shear loading

The predicted stress-time histories of the alumina ceramics under indirect tension loading at high strain rates (i.e., ranged from 10 to 10^2 s^{-1}) compared with the experimental results are summarized in Fig. 2.5 (a), (b), and (c). It is observed that, the predicted curves reasonably capture the experimentally measured ones, and the experimental trend of an increase in tensile strength with increasing strain rate is also reflected in the numerically predicted curves. Fig. 2.5 (d) shows the comparison between the predicted damage initiation and propagation (corresponding to numbered points in the Fig. 2.5 (b)) and the time-resolved images of crack propagation in the

specimen captured through the ultra-high-speed camera. Experiment-wise (see the first row of Fig. 2.5 (d)), it is observed that damage accumulates at the corners of the specimen in contact with the SHPB bars and starts to propagate along the center of the disk (from point 1 to point 2). At the onset of the peak stress (point 2), an axial primary crack appears at the center of the specimen, and this is followed by the initiation of secondary cracks at the edge of the specimen. Upon peak stress (point 3), multiple primary cracks are observed along the center of the specimen, and secondary circumferential cracks are generated at the edge of the specimen, and this failure process leads to an abrupt decrease in load sustaining capacity and catastrophic failure (point 4). The fracture pattern observed and predicted here has also been observed in previous studies on ceramic materials [110–112], indicating a valid FBD experiment. Numerically (see the second row of Fig. 2.5 (d)), the experimental failure process is reasonably reproduced. The damage first appears at the two interfaces due to stress concentrations and then starts to accumulate at the central area of the disk. Next, the element deletion process is triggered in the center-line of the disk, and this resembles the formation of the primary crack just before the peak stress. Note that the elements are deleted when the equivalent plastic strain at the integration points exceeds a critical value of 0.2, and this value has been used in previous numerical studies on alumina ceramics [89, 113]. The damage growth at the central area proceeds with the formation of secondary circumferential cracks at the edges which leads to the rapid decrease in the stress; both are consistent with experimental results (the first row of Fig. 2.5 (d)).

Similarly, the simulated stress-time histories of the alumina ceramics under compression-shear stress state at high strain rates (ranged from 10^2 to 10^3 s^{-1}) compared with the experimental results are illustrated in Fig. 2.6 (a), (b), and (c). In Fig. 2.6 (a), (b), and (c), the predicted shear strains are also compared with shear strains obtained by the DIC analysis. The experimental curves exhibit a softening regime before the peak stress, which is resulting from the initiation of axial cracks (see the time-resolved

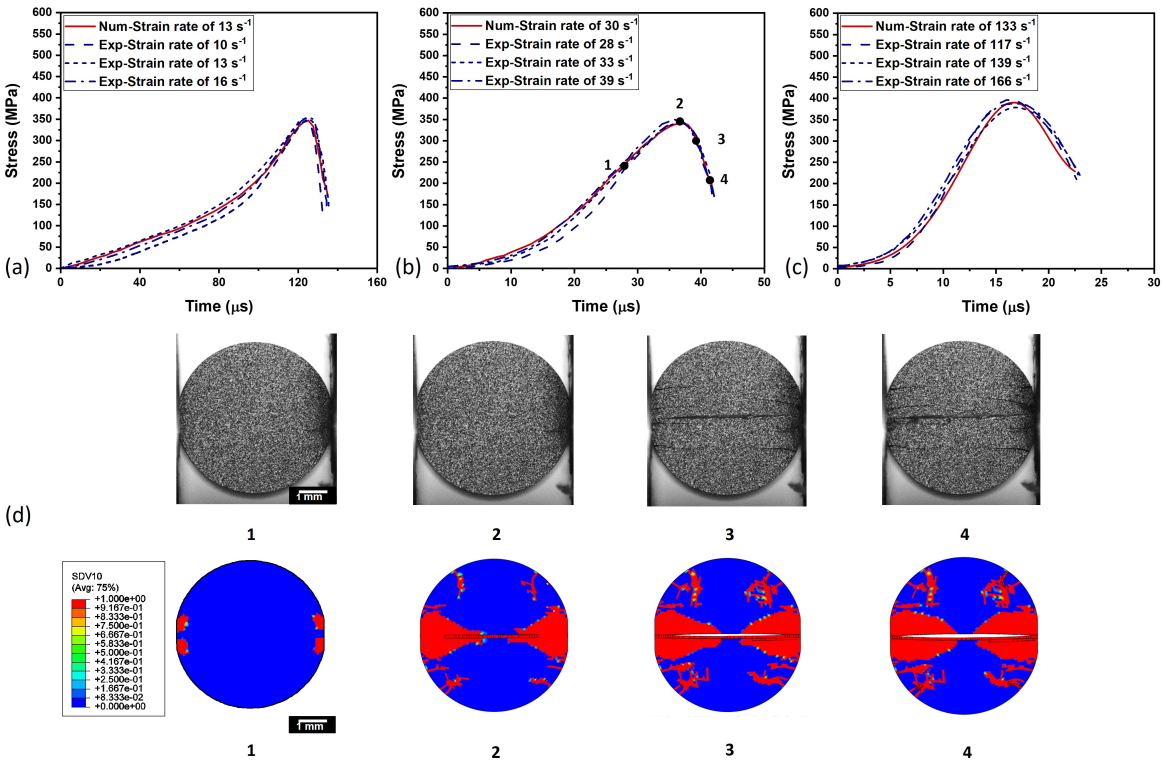

Fig. 2.5: The numerical (Num) and experimental (Exp) stress-time history of ceramic specimens under an indirect tension stress state with corresponding time-resolved images of crack propagation in the specimen captured through the ultra-high-speed camera. The numbered black points on the stress-time plot are selected to make a qualitative comparison between the numerical and experimental results. (a) The experimental and numerical stress-time curves for a strain rate range of 10 to 16 s^{-1}. (b) The experimental (dashed lines) and numerical (solid lines) stress-time curves for a strain rate range of 28 to 39 s^{-1}. (c) The experimental and numerical stress-time curves for a strain rate range of 117 to 166 s^{-1}. (d) The visualization of damage initiation and propagation in indirect tension experiments via ultra-high-speed camera images compared to those of the numerical simulation. Note that, in the numerical legend, SDV10 represents the damage parameter of the JH2-V model (see Eq. (2.8))

image in Fig. 2.6 (d) corresponding to point 2 in Fig. 2.6 (c)) and accumulation of damage at the corners. Upon reaching peak stress, the stress-bearing capacity sharply falls due to the abrupt nucleation and growth of multiple axial cracks and their later coalescing. It is observed that, the predicted curves for the ceramic materials reasonably capture the experimental results (Fig. 2.6 (a), (b), and (c)), which shows the the applicability of the current approach for modeling the alumina ceramics. Showing

in the first row of Fig. 2.6 (d) are time-resolved high-speed images of the structural failure captured experimentally by the ultra-high-speed camera, and those of the FE model corresponding to the black points on Fig. 2.6 (c) are shown in the second row of Fig. 2.6 (d)). The first figure shows that damage starts to accumulate on the left side of the specimen (i.e., the contact area with the incident bar) and a longitudinal crack parallel to the angle of the specimen created at the bottom side of the specimen. Prior to failure, more damage is accumulated in the contact area with the incident bar, and the longitudinal crack propagates parallel to the lateral edges (point 2). Upon failure, more cracks nucleate parallel to the lateral edges from both contact areas (point 3). Eventually, the interaction and coalescence of cracks together along the specimen lead to the catastrophic failure of the specimen (point 4).Overall, the rate-dependent behavior of the material (i.e., the increase in tensile and compressive strength with the increase in rate) is also numerically reflected for both FBD and compression-shear loading conditions. The model captures this effect due to the incorporation of the rate-dependent hydrostatic tensile strength of ceramics [32, 47] (see Eq. (2.6)), and accounting for the effect of inertial confinement [114] implicitly as a bulking-induced increment in pressure (Eq. (2.11)). The latter is studied in more detail in the following (see Fig. 2.10).

Lastly, the simulated stress-lateral strain and lateral strain-axial strain history of the specimen under both indirect tension and compression-shear loading (solid lines) are compared with the experimental results represented by dashed lines in Fig. 2.7. As seen in Fig. 2.7 (a), in agreement with the linear elastic response in the experiments, the numerical curves also linearly increase up to the peak stress, which confirms the correctness of the developed strain fields in the model. Fig. 2.7 (b) shows that the collapse in the experimental curves (i.e., after peak stress) follows an upward trend, which indicates the occurrence of an abrupt failure (i.e., outward expansion) caused by unstable structural failure under a tensile-dominated stress state [32, 99]. The numerically predicted lateral strain versus axial strain responses are consistent with

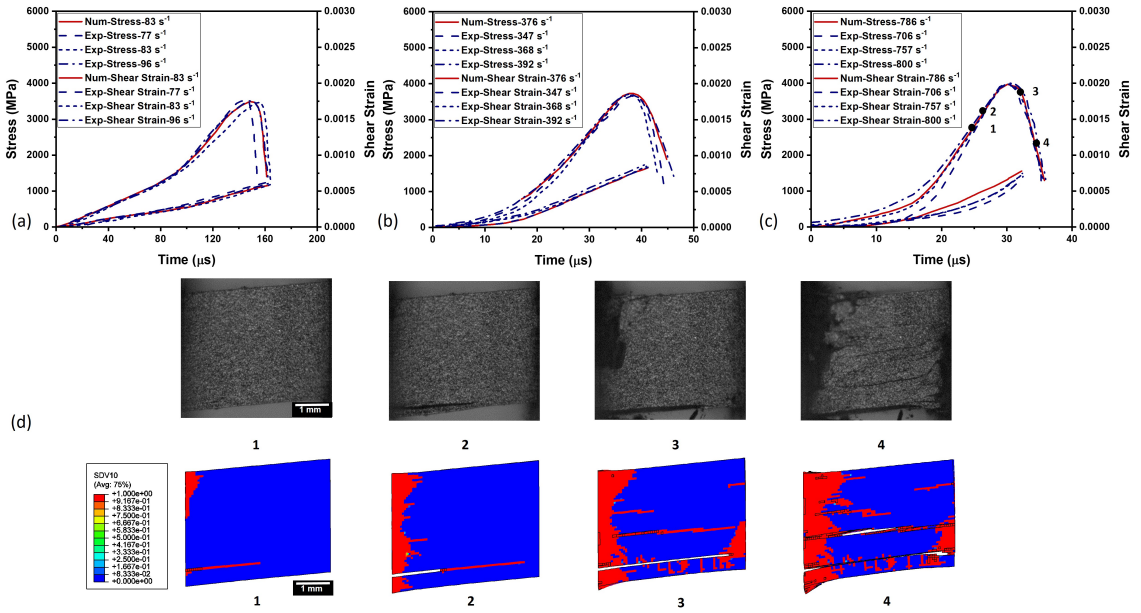

Fig. 2.6: The numerical (Num) and experimental (Exp) stress-time history of ceramic specimens under a compression-shear stress state with corresponding time-resolved images of crack propagation in the specimen captured using the ultra-high-speed camera. The marked points (numbered black points) on the stress-time plot are selected to make qualitative comparisons between the numerical and experimental results. (a) The experimental and numerical stress-time curves for a strain rate range of 77 to 98 s^{-1}. (b) The experimental (dashed lines) and numerical (solid lines) stress-time curves for a strain rate range of 347 to 392 s^{-1}. (c) The experimental and numerical stress-time curves for a strain rate range of 706 to 800 s^{-1}. (d) The visualization of damage initiation and propagation in compression-shear experiments via ultra-high-speed camera images compared to those of the numerical simulation. Note that, in the numerical legend, SDV10 represents the damage parameter of the JH2-V model (see Eq. (2.8))

the measurements in terms of the Poisson's ratio and the upward trend upon failure. In addition, Fig. 2.7 (c) shows the experimentally measured stress-axial strain (blue dashed lines) compared with simulation results (a solid red line) under compression-shear loading. It is observed that the stress-axial strain curves are nearly-straight lines and immediately decrease when the curves reach the peak due to catastrophic failure of the specimens, which is also reflected in simulation results. Shown in Fig. 2.7 (d) is the experimental data (blue dashed lines) of lateral strain-axial strain responses with comparison to numerical results (a solid red line), and the good agreement indicates that the FE model can well predict the material behavior under combined loading.

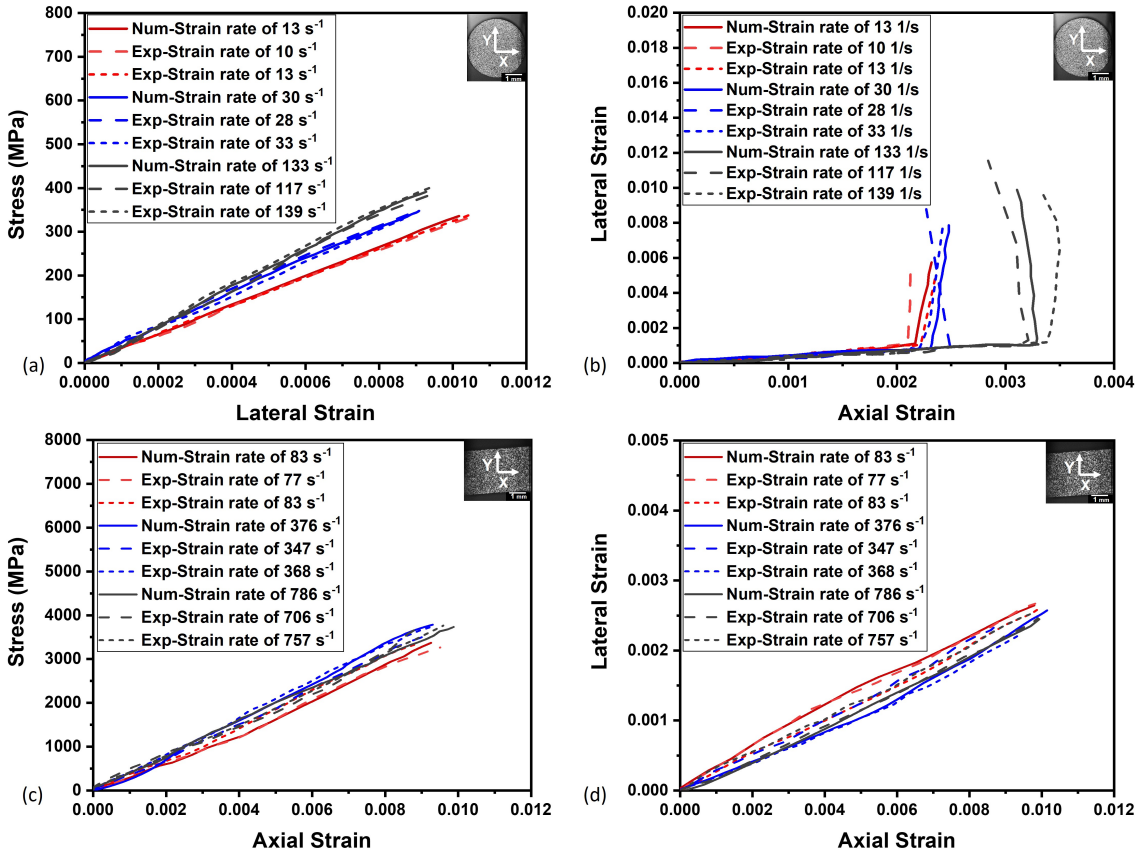

Fig. 2.7: The mechanical response of alumina under indirect tension and compression-shear stress states. (a) Representative numerical (Num) and experimental (Exp) stress-lateral strain responses of the material under indirect tension loading. (b) The numerically predicted lateral strain (Y direction)-axial strain (X direction) history compared to the experimental results measured through DIC analysis. (c) Representative numerical (Num) and experimental (Exp) stress-axial strain responses of the material under compression-shear loading. (d) The numerically predicted lateral strain (Y direction)-axial strain (X direction) history compared to the experimental results measured through DIC analysis.

The presented simulations for FBD and compression-shear loading conditions were also conducted by using the JH2 material model to provide more insights on the improvements in predicted results by the JH2-V model. The reader is referred to 2.9 for more details on comparing the JH2 and JH2-V model.

Overall, the reasonable agreement between the numerical and experimental findings, both quantitatively (e.g., stress-strain and axial strain-lateral strain curves) and qualitatively (e.g., images describing the failure process), demonstrates the appli-

cability of the current modeling approach to computationally explore the dynamic behavior of alumina ceramics.

2.5.2 Studying the effect of the JH2-V model regularization parameters on mechanical behavior of Al_2O_3 ceramics under dynamic indirect tension and compression-shear loading

In the JH2-V model, the appropriate selection of the regularization parameters, including η and $\dot{\lambda}_t$, plays an important role on the objectivity of the predicted results in terms of the damage propagation in the material. Fig. 2.8 shows how the predicted stress and damage propagation evolve in the specimen with the variation of the regularization parameters (i.e., η and $\dot{\lambda}_t$). The final calibrated values for regularization parameters in this study are chosen as η=0.025 MPa·s and $\dot{\lambda}_t$=10000 s^{-1}. First, Fig. 2.8 (a) and (b) show the predicted stress histories under indirect tension loading by considering a fixed value of $\dot{\lambda}_t$=10000 s^{-1} with different η parameters (Fig. 2.8 (a)), and a fixed value of η=0.025 MPa·s with different values for $\dot{\lambda}_t$ (Fig. 2.8 (b)). Corresponding damage profiles are shown in Fig. 2.8 (c), (d) and (e) at numbered strain levels on Fig. 2.8 (a) and (b). As seen in Fig. 2.8 (a), with the increase in the viscous parameter, the load-bearing capacity converges to the response which correlates with the measured one. It is found that when η=0 (i.e., the regularization is suppressed), the predicted peak stress is underestimated and damage accumulates at the corner of the specimen and does not propagate across the specimen (see Fig. 2.8 (c)), which is not in agreement with the experimental observations (Fig. 2.5). In Fig. 2.8 (b), low values of $\dot{\lambda}_t$ results in an underestimation of the material strength as the strain-rate-dependent spall strength of the material is not properly accounted for. Additionally, by choosing higher values for $\dot{\lambda}_t$ (higher values than calibrated data), the predicted stress-time curves converge together, and the corresponding damage profile is shown in Fig. 2.8 (d). While damage propagates at the central area of the disk, the formation of secondary circumferential cracks is not well predicted when

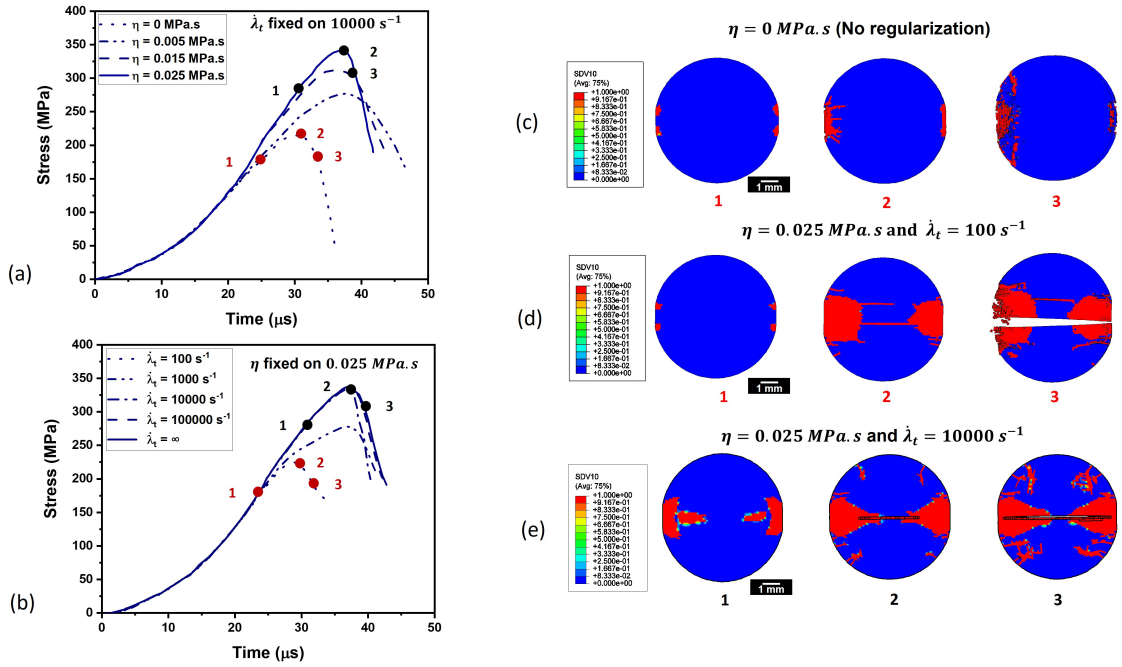

Fig. 2.8: The effect of the JH2-V model regularization parameters: the viscosity parameter (η) and the equivalent plastic strain transition parameter ($\dot{\lambda}_t$), on the predicted indirect tension response. (a) The effect of the η parameter on the predicted stress-time history for indirect tension simulations at a strain rate of 30 s^{-1}. (b) The effect of the $\dot{\lambda}_t$ parameter on the predicted history of stress for indirect tension loading at a strain rate of 30 s^{-1}. As $\dot{\lambda}_t$ exceeds 10000 s^{-1}, the predicted response remains unchanged. (c) Predicted damage pattern when η=0 MPa·s and $\dot{\lambda}_t$=10000 s^{-1} with time corresponding to the red numbered points on the subfigure (a). (d) Predicted damage pattern when η=0.025 MPa·s and $\dot{\lambda}_t$=100 s^{-1} with time corresponding to the red numbered points on the subfigure (b). (e) Predicted damage pattern in indirect tension simulation with time-resolved numbered points on the stress-time responses based on the calibrated constants (black points on the subfigures (a), and (b)). Note that, in the numerical legend, SDV10 represents the damage parameter of the JH2-V model (see Eq. (2.8))

compared to the one predicted by the calibrated $\dot{\lambda}_t$ (see Fig. 2.8 (e)).

Next, Fig. 2.9 shows the predicted history of stress and damage propagation pattern in the angled specimen under different variation of regularization parameters. Fig. 2.9 (a) and (b) show the predicted history of stress under compression-shear loading by considering a fixed value of $\dot{\lambda}_t$=10000 s^{-1} with different η parameters (Fig. 2.9 (a)), and a fixed value of η=0.025 MPa·s with different values for $\dot{\lambda}_t$. The corresponding damage profiles are shown in Fig. 2.9 (c), (d) and (e) at numbered strain levels on

Fig. 2.9 (a) and (b). It is found that when η=0 MPa·s where the regularization is suppressed, the predicted peak stress is lower than the measured one and damage accumulates at the center of the specimen (see Fig. 2.9 (c)). As shown in Fig. 2.9 (b), the model underestimates the material strength when choosing low values of $\dot{\lambda}_t$, and for higher values of $\dot{\lambda}_t$ the predicted curves converge together. From Fig. 2.9 (d), it is observed that as damage propagates in the specimen, the formation of the cracks is less accurately predicted in comparison with the predicted one by using the calibrated $\dot{\lambda}_t = 10000\ \mathrm{s}^{-1}$ (Fig. 2.9 (e)).

2.5.3 Studying the effect of bulking on mechanical behavior of Al_2O_3 ceramics under dynamic indirect tension and compression-shear loading

In brittle materials, the failure process is dominated by the initiation and growth of cracks, which leads to an incremental increase in the porosity volume of the material [115, 116]. This increase in porosity volume is known as bulking, and bulking plays an important role in the failure response of ceramics [115], rocks [117], and concretes [118]. In a study by Simons et al. [46], the effect of bulking is considered through the calculation of a volumetric plastic strain component based on the Drucker-Prager plastic potential function. In our developed model in ABAQUS, similar to the original JH2 model [43], we considered the bulking effect as the induction of an increment in pressure when damage evolution is triggered under compression (as detailed in Section 2.4). Fig. 2.10 (a) and (c) shows how bulking may affect the predicted peak stress in both indirect tension and compression-shear stress states. Bulking occurs in ceramic materials to accommodate the formation of cracks [115, 116]. As such, when bulking is not considered, the predicted peak stress is slightly underestimated, and this is observed in Fig. 2.10 (a) and (c). Fig. 2.10 (b) and (d) draw a comparison between the predicted damage propagation pattern corresponding to the specified numbered points on Fig. 2.10 (a) and (c) with the bulking effect and the one predicted when

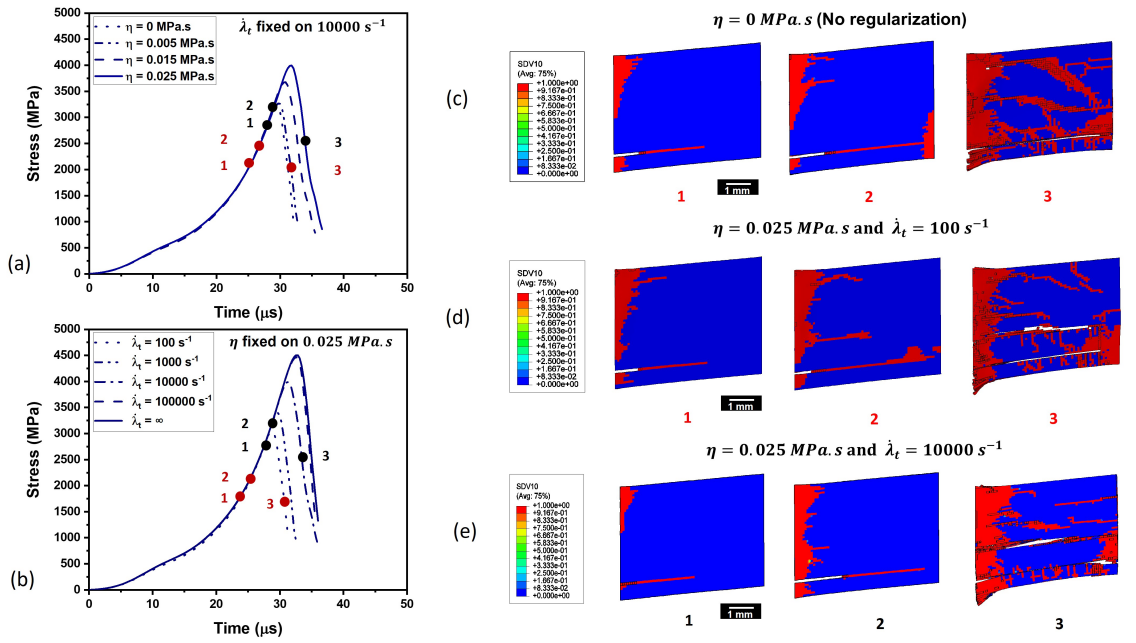

Fig. 2.9: The effect of the JH2-V model regularization parameters: the viscosity parameter (η) and the equivalent plastic strain transition parameter ($\dot{\lambda}_t$) on the predicted compression-shear response.(a) The effect of the η parameter on the predicted stress-time history for compression-shear simulation at a strain rate of 786 s^{-1}. (b) The effect of the $\dot{\lambda}_t$ parameter on the predicted history of stress for the compression-shear response at a strain rate of 786 s^{-1}. As $\dot{\lambda}_t$ exceeds 100000 s^{-1}, the predicted response remains unchanged. (c) Predicted damage pattern with η=0 and $\dot{\lambda}_t$=10000 s^{-1} with time corresponding to the red numbered points on subfigure (a). (d) Predicted damage pattern when η=0.025 MPa·s and $\dot{\lambda}_t$=100 s^{-1} with time corresponding to the red numbered points on the subfigure (b). (e) Predicted damage pattern in compression-shear simulation with time corresponding to the numbered points on the stress-time responses based on the calibrated constants (black points on the subfigures (a), and (b)). Note that, in the numerical legend, SDV10 represents the damage parameter of the JH2-V model (see Eq. (2.8))

the bulking effect is not considered. As shown, the FE model predicts no significant difference in the material response with respect to the bulking effect for the studied conditions. The same result has been also reported for alumina ceramics subject to sphere impact testing [46].

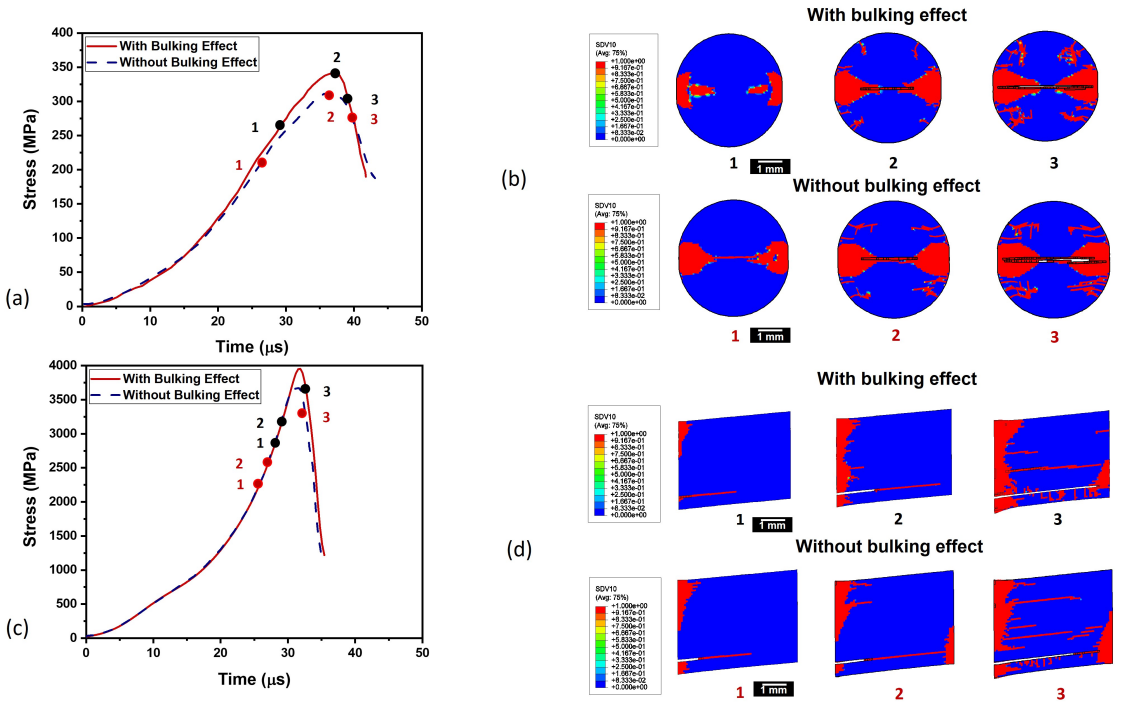

Fig. 2.10: The effect of incorporating bulking in the JH2-V model on the predicted results for the dynamic indirect tension (top b) and compression-shear loadings (bottom d). (a) The effect of bulking on the predicted history of stress-time for the indirect tension test at a strain rate of 30 s^{-1}. (b) The figures show the qualitative history of damage propagation in the material under indirect tension when the bulking effect is and is not considered. The comparison is made at the corresponding numbered points in subfigure (a). The consideration of bulking in the JH2-V model results in the prediction of secondary cracks initiating from the disk circumference. (c) The effect of incorporating bulking on the predicted results for the compression-shear test at a strain rate of 700 s^{-1}. (d) The figures show the qualitative history of damage propagation in the material under compression-shear loading when the bulking effect is and is not considered. The comparison is made at the corresponding numbered points in subfigure (c). Note that, in the numerical legend, SDV10 represents the damage parameter of the JH2-V model (see Eq. (2.8))

2.5.4 Application of the model to study the effect of shear: compression-shear specimen with different angles

The presence of shear strain plays an important role during the failure initiation and propagation in brittle materials [29, 119]. Fig. 2.11 shows the application of the current model for studying the effect of shear strain on the material response and damage growth. The implemented modeling framework has been leveraged to

quantitatively analyze the damage initiation and growth in the material to provide insight on the role of shear on the mechanical response. Shown in Fig. 2.11 (a) are the predicted stress-time curves and the corresponding shear strain-time histories for different angled compression-shear specimens at a fixed strain rate of 780 s^{-1}. It is observed that, by increasing the angle of the specimens, the induced shear strain increases while the peak stress follows a descending trend. To quantify the history of failure initiation and propagation in the material, the damage parameter of the JH2-V model is volumetrically averaged at each increment of the loading history using Python scripting. The average volumetric damage is computed as [120]:

$$D_{avg} = \frac{\sum_i^N D_i V_i}{\sum_i^N V_i} \tag{2.14}$$

where D_i and V_i are the JH2-V damage parameter and the volume of each integration point of the elements (i.e., the denominator of the Eq. (2.14) is the total volume of the simulated specimen at each increment of loading), respectively. Fig. 2.11 (b) shows the predicted stress-time histories and the volumetric average damage-time curves. As seen with the increase in shear strain (i.e., increasing in tilting angles) the damage initiates earlier in the material, and this contributes to a decrease in the peak stress. In addition, the maximum magnitude of damage reduces as a function of peak shear strain. Fig. 2.11 (c), (d), and (e) show a comparison between the numerically predicted damage propagation patterns in the alumina ceramics with $\theta = 0^{\circ}$, $\theta = 5^{\circ}$ and $\theta = 10^{\circ}$ (for the sake of brevity, the angles of $\theta = 3^{\circ}$ and $\theta = 7^{\circ}$ are not shown) at the strain levels corresponding to the numbered points in black, red, and orange, respectively, in Fig. 2.11 (a). As shown, by increasing the angle of the specimen and increasing the effect of shear deformation, damage tends to localize at the corners, and less damage propagation, and branching are observed.

Fig. 2.12 (a) shows the pattern of shear strain in the compression-shear model with different angles to provide a better understanding of how the shear strain is spatially affected. As seen, with the increase in the angle of the compression-shear model, the

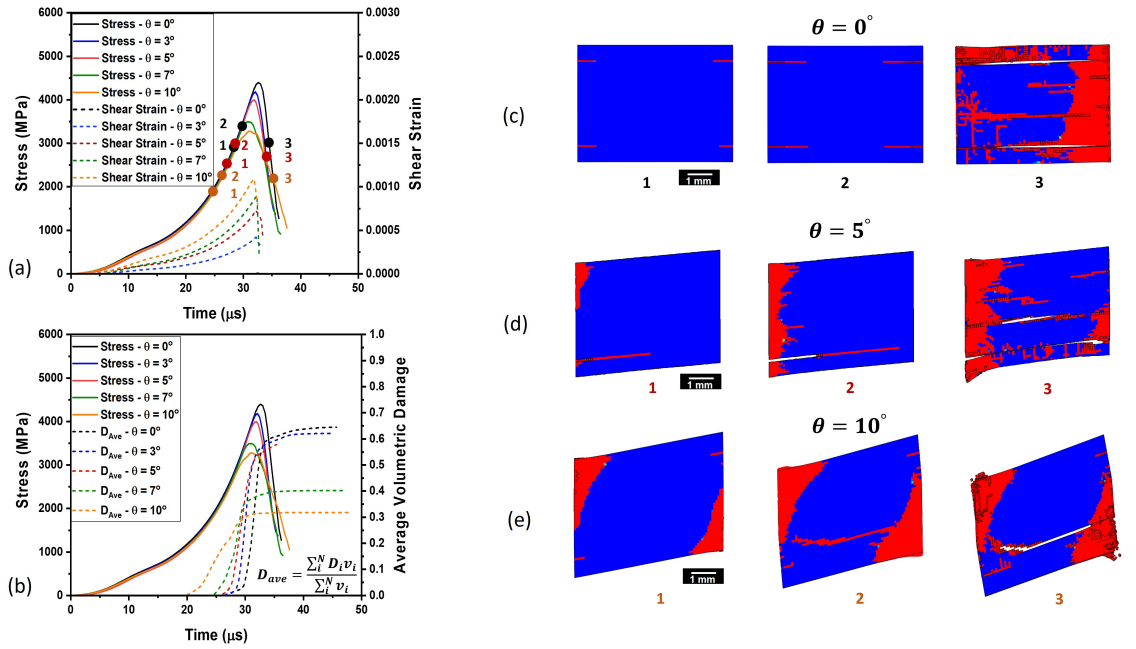

Fig. 2.11: A numerical investigation of the effect of shear on the material behavior by considering different angles ($\theta = 0^{\circ}$, 3°, 5°, 7° and 10°) in compression-shear testing. (a) Comparing the history of stress and shear strain that shows the shear strain increases with the increase in angle, and this leads to a decrease in the peak stress. (b) Comparing the stress-time history and volumetric average damage growth. With the increase in angle, the damage is initiated earlier in the material. (c), (d), and (e) shows the accumulation of damage in the material at different strains marked on subfigure (a) under different angles of $\theta = 0^{\circ}$ (black point), $\theta = 5^{\circ}$ (blue point) and $\theta = 10^{\circ}$ (red point), respectively. As seen, in all cases, damage accumulates at the corners and then propagates parallel to the specimen angle.

shear strain mainly increases in the central area and the shear strain at the corners is less affected. Note that Fig. 2.12 (a) corresponds to the time of 20 μs in Fig. 2.11 (a), when no damage is developed in the models to affect the strain distribution pattern. To confirm this observation, a p-q diagram is plotted at different locations (labeled as P1, P2, P3, P4, P5, P6, and P7 in Fig. 2.12 (a)) up to failure on the compression-shear model with different angles. The slope of the p-q curve reflects the inverse of the stress triaxiality parameter; the more the stress triaxiality, the less the effect of shear [121]. Accordingly, the p-q curve with a higher slope represents the presence of more shear. As seen in Fig. 2.12 (b), with the increase in the angle of the model, the level of shear increases minimally at the corners represented by P1 and P2 points on

Fig. 2.12 (a), while the maximum increase occurs at the center represented by P5 (i.e., the highest increase in the slope of the p-q curve). This implies that higher-angled specimens induce more shear deformation in the material locally with a predominant increase in the central area.

2.5.5 Application of the model for guidance in higher scale modeling

In real applications such as protection systems against ballistic impact, ceramics experience mixed-mode stress states that evolve spatially and temporally [122]. For the efficient use of FE modeling of ceramics at structural scales, minimizing the run-time by selecting appropriate element sizes is of great importance [108]. In this section, the current modeling framework is used to provide some guidance on the element size selection based on the stress-state-dependent mesh sensitivity of the stress-time results. Fig. 2.13 shows the predicted time history of stress in the material subject to dynamic compression-shear loading with different angles, namely $\theta = 0^{\circ}$, $\theta = 5^{\circ}$, and $\theta = 10^{\circ}$, as well as the FBD specimen under indirect tension loading when different element sizes are selected. As seen in Fig. 2.13 (a), (b), and (c), the stress state varies from uniaxial compression to shear-dominated with an increase in angle from $\theta = 0^{\circ}$ to $\theta = 10^{\circ}$. It is observed that, for all the stress states, with the decrease in the element size from 0.14 mm (7000 elements) to 0.03 mm (800000 elements), the slope of the curve remains constant while the peak stress follows a descending trend towards convergence. In addition, Fig. 2.13 (a), (b), and (c) shows that the mesh sensitivity is affected by the stress states. Specifically, the maximum sensitivity is observed under uniaxial compression with a variation of 27% in the peak stress when going from an element size of 0.03 mm to 0.14 mm, and the minimum sensitivity is obtained at the angle of $\theta = 10^{\circ}$ as the shear-dominated stress state with a variation of 14.5% in the peak stress across the same range of element sizes. Also note that the variation follows a negative correlation with increasing angles (i.e., increasing in

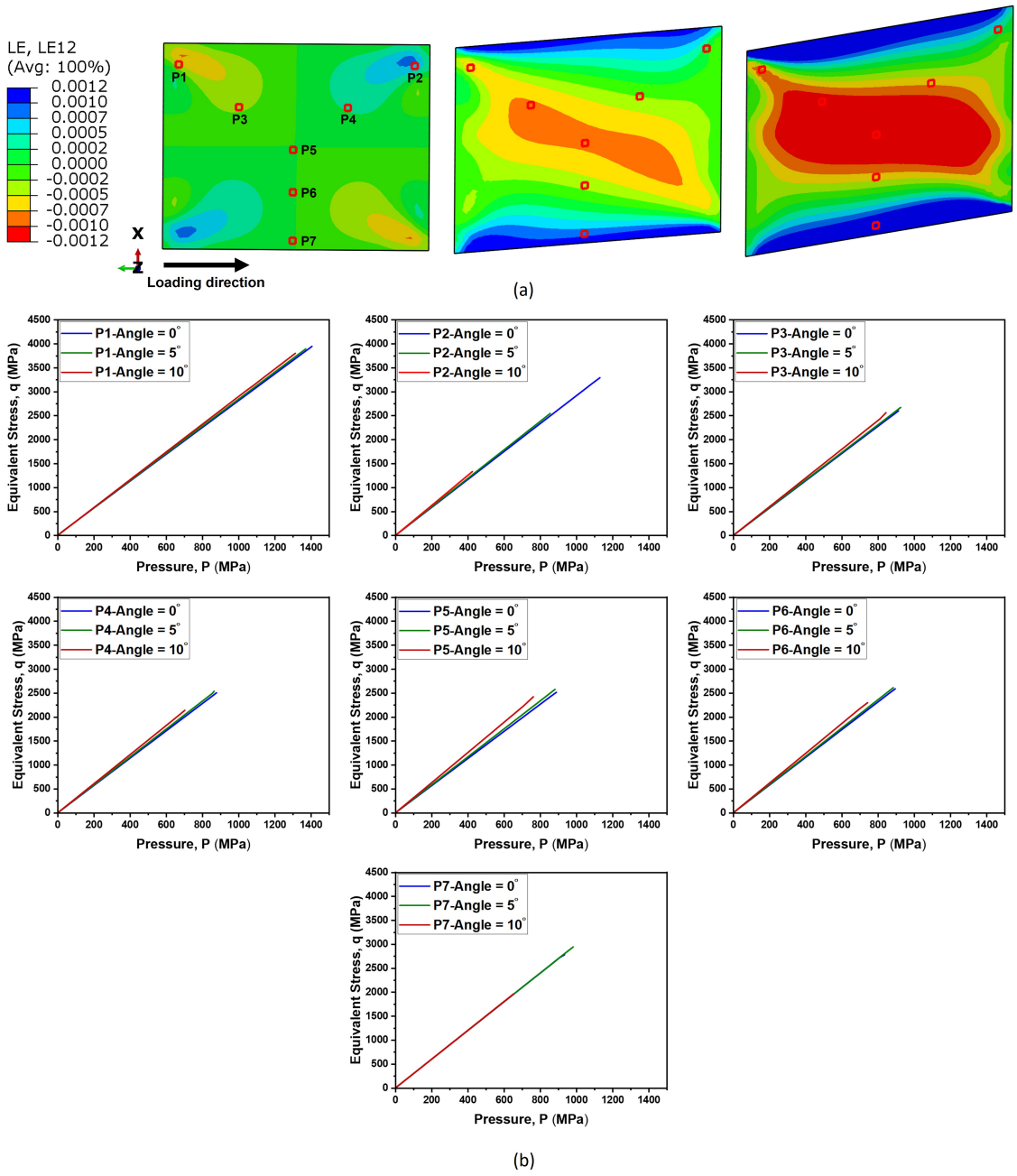

Fig. 2.12: A numerical investigation of the effect of the angle of the compression-shear specimen on the spatial distribution pattern of shear strain and its quantity. (a) The contour of shear strain distribution in the compression-shear model with different angles ($\theta = 0^{\circ}$, 5°, and 10°) at a time of 20 μs (see Fig. 2.11 (a)). (b) The p-q diagram plotted at the labeled locations on the sub-figure (a) up to failure for the compression-shear model with different angles. Note that, in the numerical legend, LE represents the shear strain in the X-Y plane.

shear dominance leads to a decrease in mesh sensitivity). Fig. 2.13 (d) shows that the predicted results are least affected by the element size for a tension-dominated stress state. As a result, the model predicts the failure response is insensitive to element size under tensile loading, and the greatest mesh dependency is introduced into the predicted failure response when a compression-dominated stress state is induced in the material. This pattern of mesh sensitivity is attributable to how the regularization method is applied in the JH2-V model, which is also related to why mesh sensitivity is mitigated in this model when compared to the JH2 model (see 2.9). The tensile strength of the material is increased the most (i.e., maximal regularization) by the proposed rate dependency model – which is also involved in the viscosity regularization approach (see Eq. (2.6)) – in the JH2-V model, while the minimal increase (i.e., minimal regularization) is applied on the strength under high pressure. As such, under tensile-dominated stress states, the regularization method is the most influenced, and with the increase in the presence of compression, the effect of regularization decreases. Accordingly, the minimum mesh sensitivity ($\sim$ 1%) is observed for FBD simulation results, and the maximum mesh sensitivity (27%) is observed for uniaxial compression simulation results (i.e., compression-shear sample with an angle of 0°).

Table 2.3 summarizes different element sizes and the corresponding run-time used for the simulation of compression-shear specimen with an angle of $\theta = 5^{\circ}$ and the FBD specimen. For the compression specimen, the peak stress varies 27% from the coarse mesh to the fine mesh which is notably lower than previous studies with the JH2 model [108, 123, 124]: this is attributable to the mesh sensitivity mitigation in the JH2-V model. As the mesh size decreases to 0.05 mm and below, the peak stress remains almost unaltered while the run-time increases by $\sim$ 125% from 24 to 54 hours. For the FBD specimen, the peak stress remains almost the same with a variation of $\sim$ 1% from coarse mesh to fine mesh, representing less mesh sensitivity when compared to compression-shear loading. From Table 2.3, as the mesh size

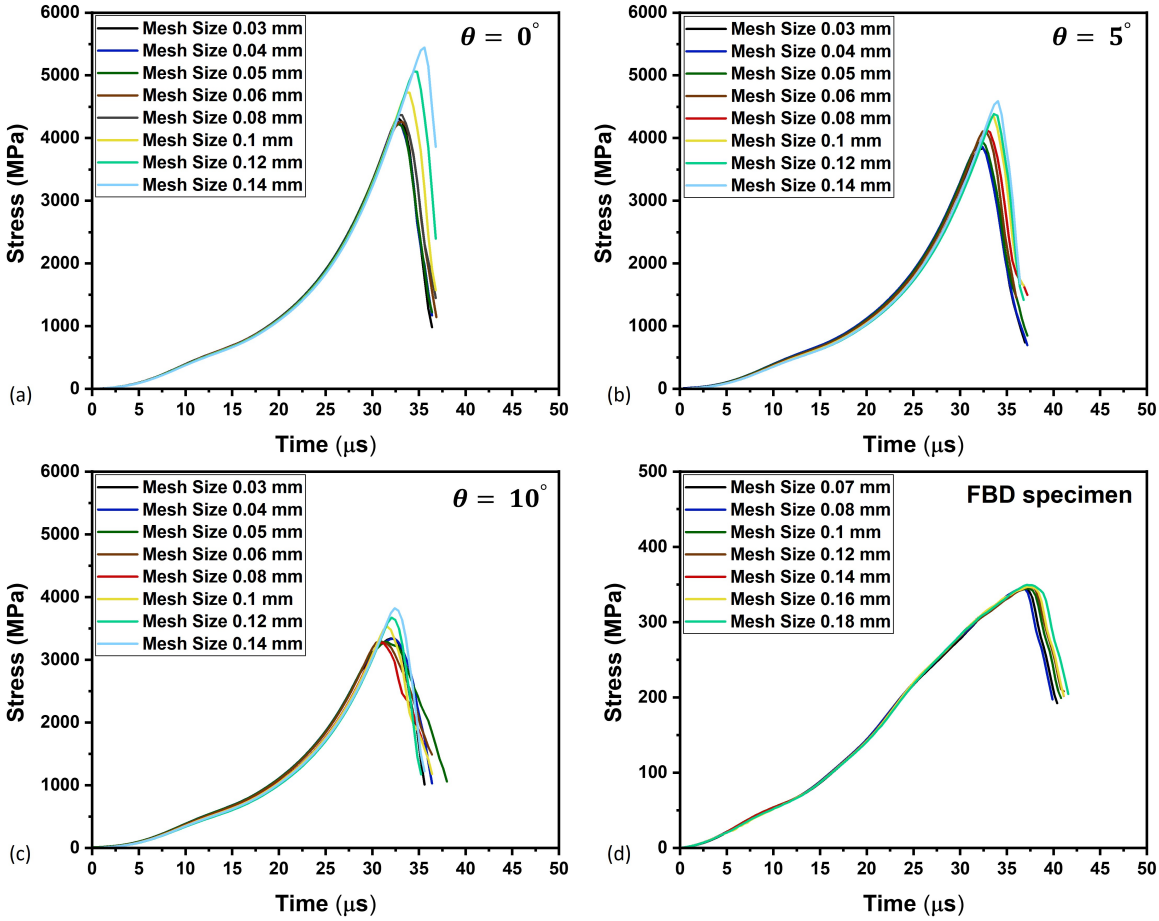

Fig. 2.13: The effect of element size on the predicted stress-time history for compression-shear specimens with different angles ($\theta = 0^{\circ}$, $\theta = 5^{\circ}$, and $\theta = 10^{\circ}$) and FBD specimen. (a) The predicted history of stress-time for an angle of $\theta = 0^{\circ}$. (b) The predicted stress-time curves for an angle of $\theta = 5^{\circ}$. (c) The stress-time response for an angle of $\theta = 10^{\circ}$. (d) The stress-time response for the FBD specimen.

decreases to 0.12 mm and below the run-time increases by $\sim$ 476% from 1.3 to 7.5 hours.

As such, to balance between the computational cost and accuracy, an element size of 0.05 mm and 0.12 mm has been chosen for further simulations of compression-shear and tension loading in this study, respectively. Based on this outcome, for the application of the JH2-V model for ceramics at higher scale modellings, a fine mesh size ($\sim$ 0.05 mm) is recommended for compression-dominated areas while a coarser mesh size may be applied to shear and tension-dominated areas to balance the computational cost and accuracy. This outcome helps avoiding the unnecessary

Table 2.3: Mesh sensitivity analysis for the compression-shear specimen with an angle of 5° and FBD specimen: A summary of different mesh sizes, the associated run-time, and the simulated peak stress.

Compression-shear specimen

Mesh size	Number of elements	Run-time (hours)	Peak stress (MPa)
0.03	810810	54	3835
0.04	341088	36	3867
0.05	173880	24	3940
0.06	100890	16	4107
0.08	43384	11	4130
0.1	21735	8	4348
0.12	12673	6	4386
0.14	7600	4.5	4588

Indirect tension (FBD) specimen

Mesh size	Number of elements	Run-time (hours)	Peak stress (MPa)
0.07	687420	7.5	347
0.08	470000	4.5	348
0.1	239360	2.5	348
0.12	141636	1.3	348
0.14	90016	0.86	349
0.16	57500	0.75	350
0.18	39248	0.68	352

use of fine mesh at the relevant parts of the model to be identified based on the dominant stress state to obtain converged results.

So far, limited efforts have been made to address the effect of the shear strain under compressive loading in ceramics, where the previous studies were mainly focused on rocks [85, 87, 88] and glasses [125, 126] subjected to a combined compression-shear loading by using experimental testing. Additionally, this study provided a foundation to quantitatively analyze the damage accumulation in ceramic materials through

numerical modeling, which has been mostly studied qualitatively by presenting time-resolved experimental images [29, 99] or numerical contours [4, 14] in the literature. Finally, the implemented JH2-V model in this study could be improved to better account for the stress-state-dependent failure of ceramics by incorporating Lode angle and stress triaxiality parameters [127, 128], and the asymmetry of damage growth under tension and compression by defining separate corresponding damage evolution laws [127, 128]. This facilitates the efficient design of high-performing ceramics that have tailored mechanical properties [129–132].

2.6 Conclusion

This study explored the behavior of CeramTec ALOTEC 98% alumina (Al_2O_3) ceramic under dynamic indirect tension and compression-shear loading via FE modeling with experimental validation. Experimentally, angled specimens were used to generate a compression-shear stress state in the material, and a tension-dominated stress state was induced through the FBD specimens. Numerically, the JH2-V model was implemented in ABAQUS software by using a VUMAT subroutine. The FE model was validated both quantitatively (i.e., stress-strain and axial strain-lateral strain responses) and qualitatively (i.e., the manifestation of damage initiation and accumulation), and a reasonable agreement was observed with the experiments. Overall, the results generated in this study will provide insights on:

1. For both indirect tension and compression-shear loading, the model showed that the peak stress is slightly underestimated when the effect of bulking is not considered, and the damage patterns remained almost independent of the bulking effect. This provides a better understanding of how the dominant stress state affects the volume increase of the material due to the accumulation of damage.

2. The pattern of damage propagation under the indirect tension is highly affected

by the regularization parameters of the JH2-V model when compared to that of the compression-shear stress state. Quantitatively, for both stress states, the predicted stress-time curves converged with increasing the regularization parameters.

3. A new quantified damage analysis was proposed to provided a better understanding of the relationships between damage accumulation and shear deformation in ceramics, which has been qualitatively addressed in previous studies by presenting time-resolved experimental images. It was found that when more shear strain (i.e., compression-shear specimen with higher angles) is induced in the material the damage accumulation triggered earlier which led to a decrease in the peak stress. In addition, the magnitude of damage decreased with the increase in shear.

4. The effect of element size was studied under different stress states, including uniaxial compression, compression-shear, and tension-dominated stress state. Accordingly, to balance the computational cost and accuracy, for compression-dominated areas a fine mesh size (~ 0.05 mm) is recommended, while a coarser mesh size may be applied to shear and tension-dominated areas of the model when applied to higher-scale applications of ceramics such as impact.

Altogether, the outcome of this study provided a better understanding of the effect of stress state and rate of loading on the failure response of alumina ceramics and the applicability of the current modeling approach to computationally explore the material behavior.

2.7 Acknowledgment

This work is supported by Defense Research and Development Canada (DRDC), General Dynamics Land Systems – Canada, and NP Aerospace through NSERC Alliance project ALLRP 560447-2020. The views and conclusions contained in this

document are those of the authors and should not be interpreted as representing the official policies, either expressed or implied, of General Dynamics, NP Aerospace, DRDC or the Government of Canada. The Government of Canada is authorized to reproduce and distribute reprints for Government purposes notwithstanding any copyright notation herein. Additionally, this research was enabled in part by support provided by Compute Ontario (www.computeontario.ca/) and Compute Canada (www.computecanada.ca) via the Graham cluster.

2.8 Appendix A: The implementation of the JH2-V model

In the following, the procedure for the implementation of the JH2-V model by using a VUMAT subroutine is summarized. Fig. 2.14 shows the flowchart for the implementation of the material model.

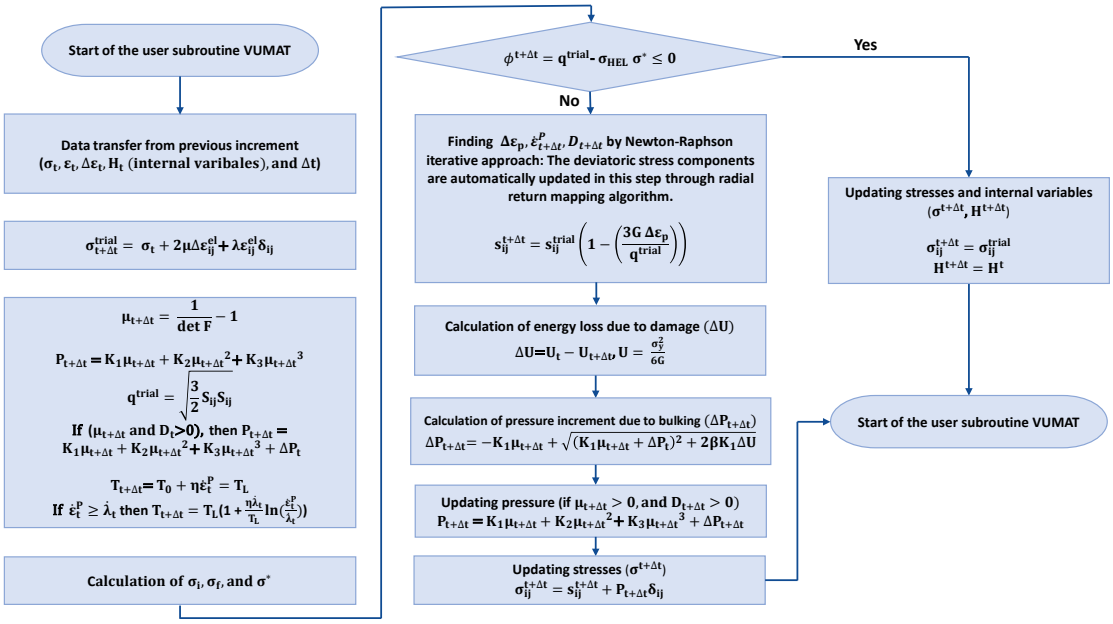

Fig. 2.14: Flowchart for the implementation of the JH2-V material model via VUMAT subroutine in ABAQUS FE solver.

Upon failure (i.e., $\phi^{t+\Delta t} > 0$), to update the stress components and internal variables (e.g., equivalent plastic strain (ϵ_p), damage parameter (D), and the increment of pressure due to bulking ΔP) ,the admissible equivalent plastic strain ($\Delta\epsilon_p$) is calculated based on an Euler backward formulation [90] through an iterative Newton-Raphson scheme. First, the following variables ($\Delta{\epsilon_p}^{(0)}$, and $\dot{\epsilon}^{(0)}_{p,t+\Delta t}$) are calculated by setting the initial guess (i.e., i = 0) for $\Delta\epsilon_p$ to zero:

$$\Delta{\epsilon_p}^{(0)} = 0 \tag{2.15}$$

$$\dot{\epsilon}^{(0)}_{p,t+\Delta t} = \frac{\Delta\epsilon_p^{(0)}}{\Delta t} \tag{2.16}$$

$$\phi^0 = \phi(\sigma^{(0)}_{t+\Delta t}, \epsilon_{p,t} + \Delta {\epsilon_p}^{(0)}, \dot{\epsilon}^{(0)}_{p,t+\Delta t}) \tag{2.17}$$

Next, the iterative Newton-Raphson method is implemented to find $\Delta\epsilon_p$ based on the following loop until convergence is reached (i.e., $|\phi^{(i+1)}| \leq \delta$, and δ is a threshold value is set to 10^{-8} in this study):

1. $H^i = [{D_e}^{-1} + \Delta {\epsilon_p}^{(i)} \frac{\partial^2 \phi}{\partial \sigma^2}]^{-1}$
2. $\beta = (\frac{\partial \phi}{\partial \sigma})^T H[\frac{\partial \phi}{\partial \sigma} + \Delta {\epsilon_p}^i \frac{\partial^2 \phi}{\partial \sigma \partial \epsilon_p} + \frac{\Delta {\epsilon_p}^{(i)}}{\Delta t} \frac{\partial^2 \phi}{\partial \sigma \partial \dot{\epsilon} p}] - \frac{\partial \phi}{\partial \epsilon_p} - \frac{1}{\Delta t} \frac{\partial \phi}{\partial \dot{\epsilon}_p}$
3. $\Delta \epsilon_p^{(i+1)} = \Delta \epsilon_p^{(i)} + \frac{\phi^{(i)}}{\beta}$
4. $\sigma^{(i+1)}_{t+\Delta t} = \sigma_t + D_e[\Delta \epsilon - \Delta \epsilon_p^{(i+1)} \frac{\partial \phi}{\partial \sigma}]$
5. $\phi^{(i+1)} = \phi(\sigma^{(i+1)}_{t+\Delta t}, \epsilon_{p,t} + \Delta \epsilon_p^{(i+1)}, \dot{\epsilon}^{(i+1)}_{p,t+\Delta t})$
6. if $|\phi^{(i+1)}| > \delta$ goto 1

   else leave the loop and go to the calculation of ΔU (see Fig. 2.14)

where D_e is the elastic stiffness tensor. Note that the equations in steps 1 to 6 are taken from Wang et al. [90]. In this study, $(\frac{\partial \phi}{\partial \sigma}^T) H (\frac{\partial \phi}{\partial \sigma})$, $\frac{\partial \phi}{\partial \sigma \partial \epsilon_p}$, $\frac{\partial^2 \phi}{\partial \sigma \partial \dot{\epsilon}_p}$, $\frac{\partial \phi}{\partial \epsilon_p}$, and $\frac{\partial \phi}{\partial \dot{\epsilon}_p}$ are derived as Eq. (2.18), Eq. (2.19), Eq. (2.20), Eq. (2.21), and Eq. (2.26), respectively.

$$(\frac{\partial \phi}{\partial \sigma}^T) H (\frac{\partial \phi}{\partial \sigma}) = G \tag{2.18}$$

$$\frac{\partial^2 \phi}{\partial \sigma \partial \epsilon_p} = 0 \tag{2.19}$$

$$\frac{\partial^2 \phi}{\partial \sigma \partial \dot{\epsilon}_p} = 0 \tag{2.20}$$

$$\frac{\partial \phi}{\partial \epsilon_p} = \frac{(\sigma_i - \sigma_f)\sigma_{HEL}}{\epsilon_p^f} \tag{2.21}$$

$$\sigma_i = A(\frac{T(\dot{\epsilon}_p)}{P_{HEL}} + \frac{P}{P_{HEL}})^n = AQ^n \tag{2.22}$$

Note that the logarithmic formulation for the hydrostatic tensile strength (Eq. (2.6)) must be used when $\dot{\epsilon}_p \geq \dot{\lambda}_t$.

$$Q = \begin{cases} \frac{T_0+\eta\dot{\epsilon}_p+P}{P_{HEL}}, & \text{for } \dot{\epsilon}_p < \dot{\lambda}_t \\ \frac{T_t(1+\frac{\eta\dot{\lambda}_t}{T_t}(\ln \dot{\epsilon}_p/\dot{\lambda}_t))+P}{P_{HEL}}, & else \end{cases} \tag{2.23}$$

$$\frac{\partial Q}{\partial \dot{\epsilon}_p} = \begin{cases} \frac{\eta}{P_{HEl}}, & \text{for } \dot{\epsilon}_p < \dot{\lambda}_t \\ \frac{\eta\dot{\lambda}_t}{P_{HEL}\dot{\epsilon}_p}, & else \end{cases} \tag{2.24}$$

$$\sigma_f = B(\frac{P}{P_{HEL}})^m = B(P^*)^m \tag{2.25}$$

$$\frac{\partial \phi}{\partial \dot{\epsilon}_p} = -\sigma_{HEL} A Q^{n-1} \frac{\partial Q}{\partial \dot{\epsilon}_p}[1-D] \tag{2.26}$$

$$D = \sum \frac{\Delta\epsilon_p^{eff}}{\epsilon_p^f} \tag{2.27}$$

$$\epsilon_p^f = \begin{cases} \epsilon_p^{min}, & p < p_t \\ \frac{p(\sigma)-p(t)}{p(c)-p(t)}(\epsilon_p^{max} - \epsilon_p^{min}) + \epsilon_p^{min}, & p_t < p < p_c, \ and \\ \epsilon_p^{max}, & p_c < p \end{cases} \tag{2.28}$$

2.9 Appendix B: Comparison between the JH2 model and the JH2-V model

In this study, the simulations for both the FBD and compression-shear conditions represented in Fig. 2.5 and Fig. 2.6, respectively, were conducted with the JH2 model available in ABAQUS software as a built-in material model. The constants used for the JH2 model are exactly the same as the ones used for the JH2-V model represented in Table 2.2. The JH2 model constants for fracture strain, including d_1, and d_2 were taken from the literature [14] for alumina ceramics. Fig. 2.15 compares the predicted results from the JH2 and JH2-V models in terms of stress-time histories and damage patterns for a coarse to a fine mesh size (see Table 2.3 for more details). As seen in Fig. 2.15 (a), for the FBD loading condition where the stress state is tensile dominated, the predicted curves by the JH2 model represent dependency on the element size, while the ones by the JH2-V model are mesh insensitive. Particularly, under a tensile-dominated stress state, the damage pattern is significantly affected by the mesh size in the JH2 model when compared to the JH2-V model. As shown in Fig. 2.15 (c), for coarse mesh size, the JH2 model damage pattern is localized in the contact regions and no propagation is caught in the central area, while that of the JH2-V model reasonably captures the experimentally observed damage propagation pattern, and this is attributable to the viscosity regularization method incorporated into the JH2-V model. As shown in Fig. 2.15 (b), the JH2 model predicts more mesh-sensitive stress-time responses under compression-shear stress states when compared to the JH2-V model; The peak stress varies by 41% and 27% predicted by the JH2 and JH2-V model, respectively, from the coarse to the fine mesh size. Similar to the FBD loading conditions, when a coarse mesh is applied to the model, the JH2 model fails to capture the major features of the damage pattern (e.g., the growth of primary axial cracks) in compression-shear stress state (see Fig. 2.15 (d)), while the predicted damage pattern by the JH2-V model is in a better agreement with the experiments.

Likewise, when the model is discretized by a fine mesh, the JH2 damage pattern and deletion of elements tend to localize at the corners when compared to that of the JH2-V model where the damage growth pattern is more consistent with the experiments (e.g., the growth of an axial crack at the bottom side of the sample). Overall, the JH2-V model improves on the JH2 model in terms of the dependency of qualitative and quantitative results on the mesh and stress-state-dependent damage growth due to the viscosity regularization that leads to a rate-dependent yield surface.

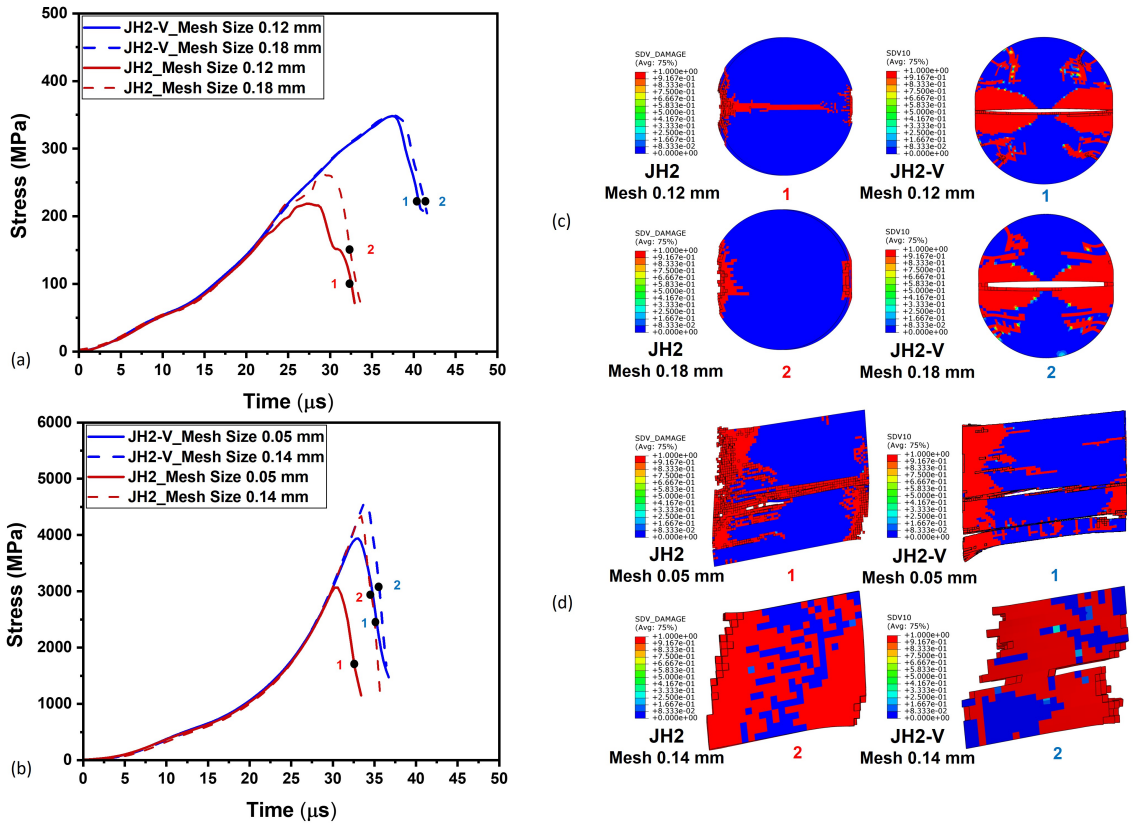

Fig. 2.15: Comparison of the JH2 and JH2-V models for predicting the response of the alumina ceramics under FBD and compression-shear loading conditions. (a) The predicted stress-time histories of the simulated FBD sample discretized with coarse (0.18 mm) and fine (0.12 mm) mesh size subjected to a strain rate of 30 s^{-1}. (b) Comparing the predicted pattern of damage growth by the JH2 and JH2-V models in the FBD sample. (c) The predicted stress-time histories of the simulated compression-shear sample discretized with coarse (0.14 mm) and fine (0.05 mm) mesh size subjected to a strain rate of 786 s^{-1}. (d) Comparing the predicted pattern of damage growth by the JH2 and JH2-V models in the compression-shear sample. Note that, in the numerical legend, SDV_ DAMAGE and SDV10 represent the damage parameter of the JH2 and JH2-V models, respectively.

Chapter 3

Strain-rate-dependent behavior of additively manufactured alumina ceramics: Characterization and mechanical testing

Published as **Zahra Zaiemyekeh**, Haoyang Li, Dan L. Romanyk, James D. Hogan. "Strain-rate-dependent behavior of additively manufactured alumina ceramics: Characterization and mechanical testing ", *Journal of Materials Research and Technology*, 2023, 49, 13878–13895.

3.1 abstract

This study experimentally investigates the mechanical behavior of additively manufactured (AM) alumina ceramics by stereolithography technique. The AM alumina specimens with two different printing orientations (POs) are tested under quasi-static and dynamic loading rates. The material shows a quasi-static (i.e., a strain rate of 10^{-3} s^{-1}) compressive strength of 1640.54 ± 99.33 MPa and 1494.25 ± 260.08 MPa for the PO1 and PO2, respectively, and a dynamic (i.e., a strain rate of 640-730 s^{-1}) compressive strength of 3077.25 ± 174.07 MPa and 3107.33 ± 97.03 MPa for the PO1 and PO2, respectively, which are among the highest reported values for AM alumina due to the higher density and finer grain size. The strain-rate-dependent

compressive strength of the material is slightly affected by the PO which is alleviated with the increase in strain rate from quasi-static to dynamic loading conditions. In contrast, the PO noticeably affects the macro-scale failure pattern. The fractography analysis shows the dominant contribution of the intergranular failure mechanism and a combination of intergranular and transgranular mechanisms under quasi-static and dynamic loading, respectively. The crack speed propagation is found to be 785 $\pm$ 174 m/s on average which is $\sim$ 68% less than that of conventional ones in the literature. The current AM alumina shows a hardness of 24.45 $\pm$ 0.88 GPa which is higher than that of the majority of other AM alumina. Overall, this study discusses the potentiality of using AM ceramics in engineering fields replacing the conventionally-made counterparts, and provides implications for designing better-performing AM ceramics.

3.2 Introduction

High hardness, high strength-to-weight ratio, and good thermal and chemical stability have made alumina ceramics attractive for use in different industrial sectors (e.g., defense [11], health [133], and aerospace [134]) [16, 34]. Conventional manufacturing processes of alumina ceramics (e.g., injection molding [17]) are complex, time-consuming, and need post-processing (i.e., machining) [18]. As such, additive manufacturing (AM) methods are gaining high popularity and progress for the fabrication of ceramic structures with flexibility in the design of end-user customized geometries [19, 20, 135]. AM methods are based on using material deposition to fabricate 3D parts, typically through a layer-by-layer process governed by a computer-based model [136]. Different AM technologies have been developed for ceramics, including stereolithography (SLA) [23], digital light processing (DLP) [137], binder jetting (3DP) [21], selective laser melting (SLM) [22], fused deposition modeling (FDM) [138] and selective laser sintering (SLS) [23], and these methods are categorized into powder-based (e.g., 3DP, and SLS), slurry-based (e.g., SLA, and DLP), and bulk solid-based (e.g., FDM) techniques based on pre-processed feedstock prior to printing (defined

by ASTM F42 [139] on AM methods) [22, 23, 140]. Powder-based methods (i.e., SLS, and SLM) rely on melting processes that induce residual stresses generated by thermal gradients under fast laser heating and cooling rates, and these are major factors contributing to the formation of defects (e.g., microvoids) [22, 140]. Contrarily, slurry-based photopolymerization techniques (i.e., SLA, and DLP) have shown more promise for the fabrication of ceramic structures due to the achievement of controllable feature resolution and surface finish [24]. Particularly, SLA has gained increasing popularity due to its high forming accuracy, high resolution, and high-quality surface finish [24, 25]. As such, this study focused on the mechanical behavior of AM alumina ceramics fabricated by SLA method. This method is based on the deposition of consecutive layers of a photoreactive material, and, in consequence, the orientation of the printed layer may influence the mechanical behavior of the printed structure [22, 135].

The wide application of ceramics in extreme conditions (e.g., impact [32, 34, 101, 141], and ballistic protection systems [14, 26, 29]) has motivated many studies on the stress-state- and strain-rate-dependent mechanical behavior of ceramic materials [26, 32, 34, 55, 67]. Here, previous studies have primarily focused on conventionally-made ceramics [14, 26, 27, 29, 32, 34, 55, 67], while very limited efforts have been made toward investigating the strain-rate-dependent mechanical properties and failure response of 3D-printed ceramics [31, 142–144]. The purpose and innovation of the current work are to study the strain-rate-dependent failure behavior of AM alumina ceramics as future materials that are scarcely addressed in the literature. In one study, DeVries et al. [31] studied the effect of microstructure on the mechanical properties of 3D-printed alumina manufactured by pressurized spray deposition (PSD). It is found that the 3D-printed material showed lower quasi-static and dynamic compressive strength compared with sintered ceramics, while negligible differences are observed in the Vickers hardness. Typically, the strength of AM materials has been frequently reported to be lower than those made by conventional approaches due to

the AM processing-induced microstructural defects and weak grain boundaries [21, 31, 145], and this requires further research on AM ceramics to better understand the failure behavior and mechanisms of the material to expand their applications [137, 146, 147], and this will be done in the current study.

While AM ceramics enable the design of multifunctional and complex-shaped structures, further studies are needed to improve their properties compared to their conventionally-made counterparts. Accordingly, building on the previous studies on AM alumina ceramics [31, 143], the current study experimentally investigates the micro-indentation and strain-rate-dependent failure behavior of AM alumina ceramics by SLA under uniaxial compression. The material microstructure is characterized by using Electron Backscatter Diffraction (EBSD), Scanning Electron Microscopy (SEM), energy dispersion spectroscopy (EDS), and transmission electron microscopy (TEM) with EDS. Next, the Vickers hardness is measured and compared with that of conventionally-made and AM alumina ceramics from previous studies. Additionally, the AM ceramics with two different printing orientations (POs) are tested under quasi-static and dynamic loading conditions by using an MTS 810 machine and split-Hopkinson Pressure Bar (SHPB) apparatus, where the failure process and full-field strains are captured by ultra-high-speed imaging and digital image correlation (DIC). The fracture surfaces are characterized by SEM to reveal the contributing failure mechanisms. Lastly, the crack propagation speed in the AM alumina ceramics is measured and compared with that of the conventional ones in the literature. Altogether, the outcomes of this study provide new insights into the mechanical properties and failure behavior of AM alumina, and these have implications for the design of better-performing AM ceramics as promising future materials.

3.3 Experimental methods

3.3.1 Material and characterization

Cuboidal α-Al_2O_3 ceramic green bodies with nominal dimensions of 3.5 × 2.3 × 2.7 mm^3 (Fig. 3.1(a)) are printed through an SLA method in two different directions, namely PO1 and PO2 by Lithoz, America. In the SLA process, the laser energy and exposure time of each layer is set to be 30 mW/cm^2, and 10 s, respectively. The printed layer height is 25 μm with a pixel size (DLP XY) of 40 μm. The specimens are printed 1.235 times larger in the X-Y plane and 1.275 times larger in Z to account for sintering shrinkage at room temperature, and all green bodies are sintered at 1650°C for 2 hours after debinding. The above-mentioned size and shape are selected for the AM specimens to provide sufficient time for the material to reach stress equilibrium, as detailed in previous studies [26, 55, 99, 148] and to provide flat surfaces for applying DIC analysis to measure strain components and observe failure sequences on specimen surfaces. In this study, SEM (Zeiss Sigma FESEM, 20 kV) equipped with EDS (AZtec software from Oxford Instrument) is performed to determine the microstructure characterization and obtain the chemical composition of the polished surface (i.e., 0.25 μm surface finish) of the as-received AM alumina specimens. Fig. 3.1(b) shows an SEM micrograph of the material, where the hollow spots indicate the surface pores likely to be caused by the polishing process. The SEM-EDS analysis demonstrates the material is comprised of aluminum (atomic 40.51%, wt.% 53.43) and oxygen (atomic 59.38%, wt.% 46.44) mixed with a trace of Mg (atomic 0.11%, wt.% 0.13) in low quantity. In addition, EBSD analysis (Oxford INCA, Bruker Quantax, 20 KV) is used to determine grain size distribution and crystallographic orientation of the grains at the surface of the specimens. In the EBSD inverse pole figure (IPF) for both POs obtained on the X-Y plane in Fig. 3.1(c) and (d), the darker areas represent surface damage or pores. In addition, the corresponding reduced IPF triangle indicates no preferred crystal orientation. For both POs in

the X-Y plane, the grain size follows a log-normal distribution as shown in Fig. 3.1(c) and (d). The average grain size is computed as 2.94 ± 1.94 μm for PO1, and 2.92 ± 1.91 μm for PO2, and these are smaller than the grain sizes reported in the literature on other AM alumina (e.g., $\sim$ 12 μm [31], and $\sim$ 25 μm [149]). In the current work, the difference between the averaged grain size for the specimens with PO1 and PO2 is less than $\sim$ 0.68% and this negligible difference might be considered as a variability induced by the SLA manufacturing method. Additionally, the grain size distribution was obtained from EBSD analysis, and this was conducted on an area of 100 μm × 100 μm on the specimens. As such, by changing the size and position of this area or increasing the number of repetitions in measurements, the average grain size may insignificantly differ from each other for the specimens with different printing orientations (POs).

To further understand the grain structure and grain boundary morphology, high-resolution (HR)-TEM (FEI Tecnai TF-20 FEG/TEM, 200kV) is shown in Fig. 3.2(a) and TEM-EDS is shown in Fig. 3.2(b) are conducted. The TEM specimens taken from the X-Y plane for both POs are capped with sputtered Ir and e-Pt/I-Pt prior to milling, and the final lamella thickness is $\sim$ 100 nm. Fig. 3.2(a) reveals that the grain boundary (i.e., blue lines) is $\sim$ 0.79 ± 0.12 nm for PO1 and $\sim$ 0.78 ± 0.14 for PO2 in width, and these values vary slightly along the boundary due to deviations from edge-on-orientation caused by grain boundary curvature. Additionally, the grains of the specimen are tightly bonded, and the grain boundaries are clean and straight. No evident pores or impurities that may cause scattering of incident light are observed [150]. From Fig. 3.2(a), well-defined lattices indicate the clear crystalline structure of the current AM alumina, with the fringe size of the grain (i.e., red lines) measured to be 0.288 ± 0.021 nm and 0.291 ± 0.025 nm for PO1 and PO2, respectively, and these values are in agreement with the previous measurements [151, 152]. No grain boundary amorphous phase is detected between the grains. The composition analysis of grain boundaries is shown in Fig. 3.2(b), indicating that it is rich in Al and O, and

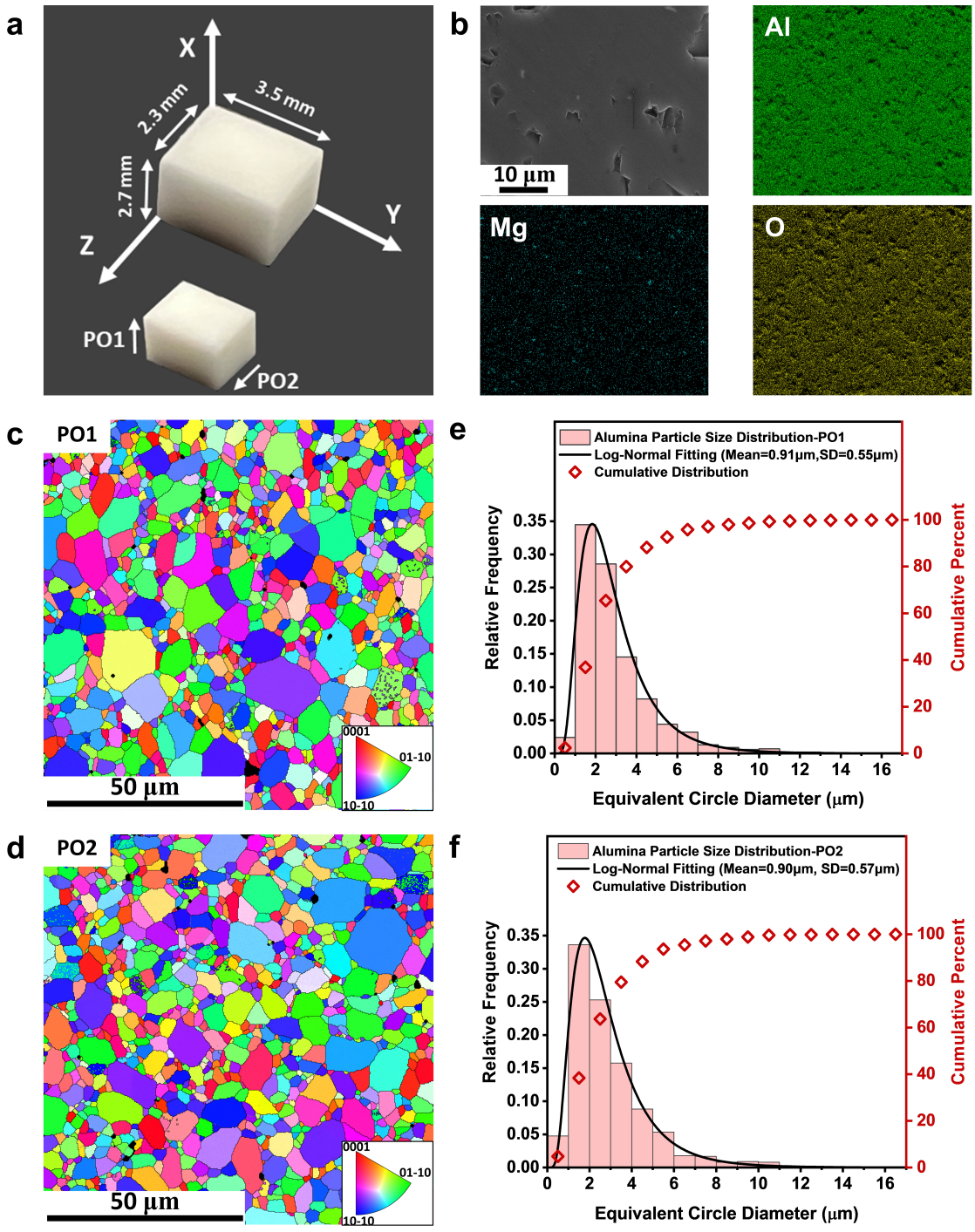

Fig. 3.1: Characterization of the AM alumina ceramic: (a) The geometry of the printed specimens with two different POs. (b) Microstructural characterization through SEM imaging and EDS analysis. (c,d) EBSD IPF representation of the PO1 and PO2 polycrystalline structure, obtained on the X-Y plane. (e,f) The grain size distribution of the material (following a log-normal curve with fit parameters indicated in legend) is based on the equivalent circle diameter for PO1 and PO2 specimens, respectively.

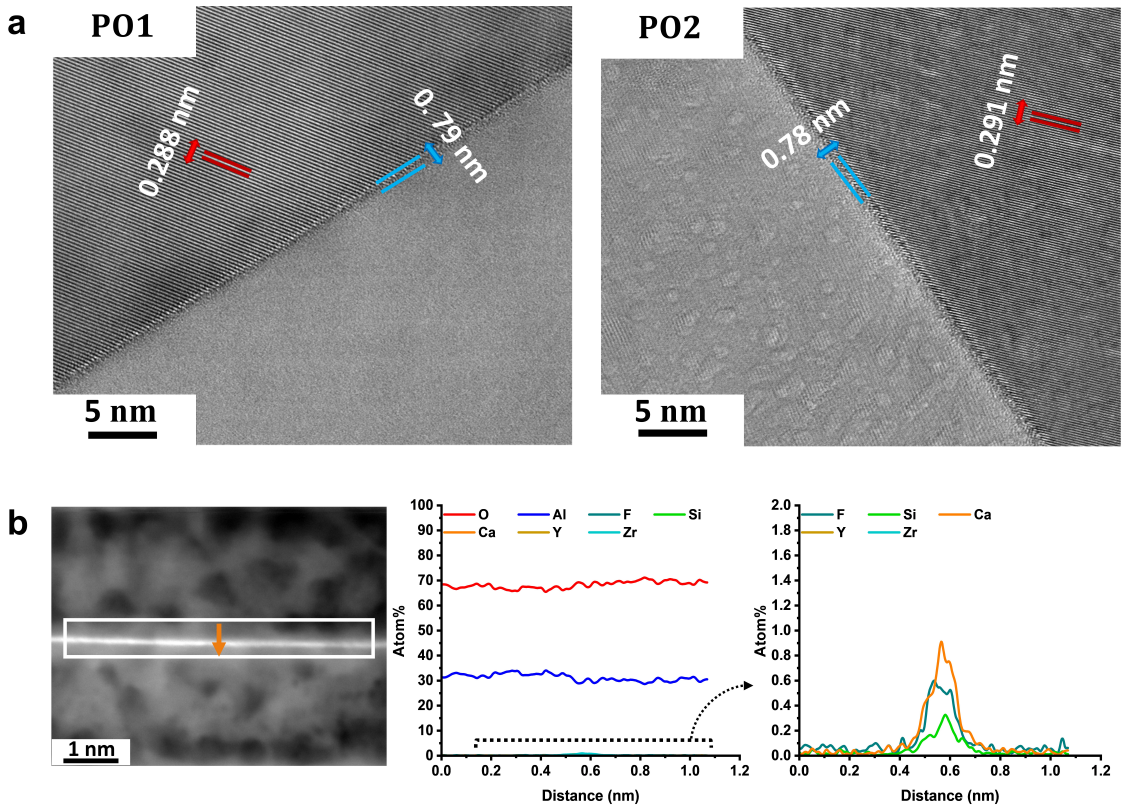

Fig. 3.2: Representative HR-TEM, and TEM-EDS analysis of the grain interface of AM alumina crystalline structures on the X-Z plane: (a) Typical HR-TEM micrographs for PO1 and PO2, respectively. (b) TEM-EDS analysis of the grain boundary inside the white box shown in the TEM image.

secondary elements including F, Si, Ca, Y, and Zr shown in the magnified diagram.

3.3.2 Mechanical testing set up

Next, the AM alumina ceramics are tested under 10^{-4} s^{-1} to 10^{2} s^{-1} strain rates. The quasi-static uniaxial compression experiments are performed on a standard servohydraulic MTS 810 machine. Various nominal strain rates of 10^{-4} s^{-1}, 10^{-3} s^{-1}, and 10^{-2} s^{-1} are achieved by using displacement control setting along the long dimension (3.5mm). To visualize and record the surface deformation process on the specimen, a high-speed AOS PROMON U750 camera at 3 to 300 frames per second (FPS, its value is adjusted based on the loading rate) with a full resolution of 1280 $\times$ 1024 pixels is used. To capture the strain fields by the DIC technique, random speckle pat-

terns are sprayed on the surface of the specimens using a fine-tipped airbrush with a 0.15 mm diameter nozzle. A non-repetitive, isotropic, and highly contrasted speckle pattern is important in DIC analysis [153]. To protect MTS machine platens from being indented by AM alumina specimens during the loading process, two polished tungsten carbides (WC) are placed between the loading platens and the specimen. Additionally, high-pressure grease is used between protection platens and AM specimens to eliminate the friction effect and free lateral motion. The experimental testing setup is detailed in our previous studies [32, 34, 55]. The dynamic tests are conducted under 10 s^{-1} to 10^2 s^{-1} strain rates using a modified SHPB setup adapted for testing brittle materials [154, 155]. The incident bar and transmission bar with a diameter of 12.7 mm and a length of 1016 mm and 914 mm, respectively, are made of the same hardened maraging steel (Service Steel America C-350) with density, elastic modulus, yield strength, and Poisson's ratio of 8080 kg/m^3, 200 GPa, 2.68 GPa, and 0.29, respectively. Different types of pulse shaping configurations are attached in front of the incident bar to generate a ramped signal under dynamic loading, which allows the ceramic specimens to achieve the required stress equilibrium and constant strain rates [101]. In the current experiments, tin, high-density polyethylene (HDPE), and paper pulse shapers are used to induce a strain rate of 80 to 100 s^{-1}, 260 to 310 s^{-1}, and 640 to 730 s^{-1} in the specimen, respectively. Two impedance-matched Ti-6Al-4V titanium alloy jacketed tungsten carbides are placed between the SHPB bars and specimen interfaces to protect the end of the bars from being indented by the hard AM ceramics and reduce stress concentration during the testing process. High-pressure grease is applied between the protection platens and specimen to reduce frictional effects and minimize lateral force when the specimen experiences deformation. In the current SHPB device, two strain gauges (Micro 184 Measurements CEA-13–250UN-350) attached to the bars are used to collect the incident and transmission strain signal data, where the transmission strain signal (i.e., $\epsilon_t(t)$) is used to measure the stress-time response $\sigma(t)$ [101]:

$$\sigma(t) = \frac{A_0}{A_s} E_0 \epsilon_t(t), \tag{3.1}$$

where, A_0 (m^2) and A_s (m^2) are the cross-sectional areas of the bar, and specimen, respectively, and E_0 (N/m^2) is the elastic modulus of the bar material. Additionally, an ultra-high-speed camera (Shimadzu HPV-X2) is used to record the dynamic tests at 0.5 million to 2 million FPS, and these images are used to capture the full-field strain maps with the DIC technique. Details on the SHPB apparatus used in this study are documented in previously published papers by the authors [32, 55, 99].

3.3.3 Digital image correlation analysis

In the current study, experimental testing is combined with the DIC technique coupled with ultra-high-speed imaging to observe the localized deformation mechanisms activated during loading and allow for measurement of the spatial and temporal histories of strain components (e.g., axial, lateral, and shear strains). In this study, VIC-2D V6 software from Correlated Solution Inc. (USA) is used for the DIC analysis, where the first image of each test captured by the cameras is chosen as the reference image. For quasi-static uniaxial compression tests, the surface of the AM specimen is discretized with a subset size of 51 $\times$ 51 pixels, with a step size of 7 pixels. For analyzing experiments under dynamic loading, the subset size is chosen as 31 $\times$ 31 pixels, with a step size of 5 pixels adjusted based on the camera resolution, speckle size, and the eventual smoothness of the strain profiles. The zero normalized sum of squared differences (ZNSSD) criterion with the optimized 8-tap interpolation scheme is utilized in the analysis. In this research, the engineering strain is computed by DIC analysis, and the slope of the linear portions of the strain-time curves is taken as the strain rate. The DIC analysis setups are detailed in our previous works [32, 34]. Fig. 3.3 shows the representative stress and strain histories of a full-surface global average and six local areas of interest (AOIs) on the specimen surface to verify the stress equilibrium condition in dynamic experiments. The overlapping of strain histories across various AOIs on the specimen surface and the corresponding stress

history indicate developing uniform deformation and reaching good equilibrium in the specimen [100].

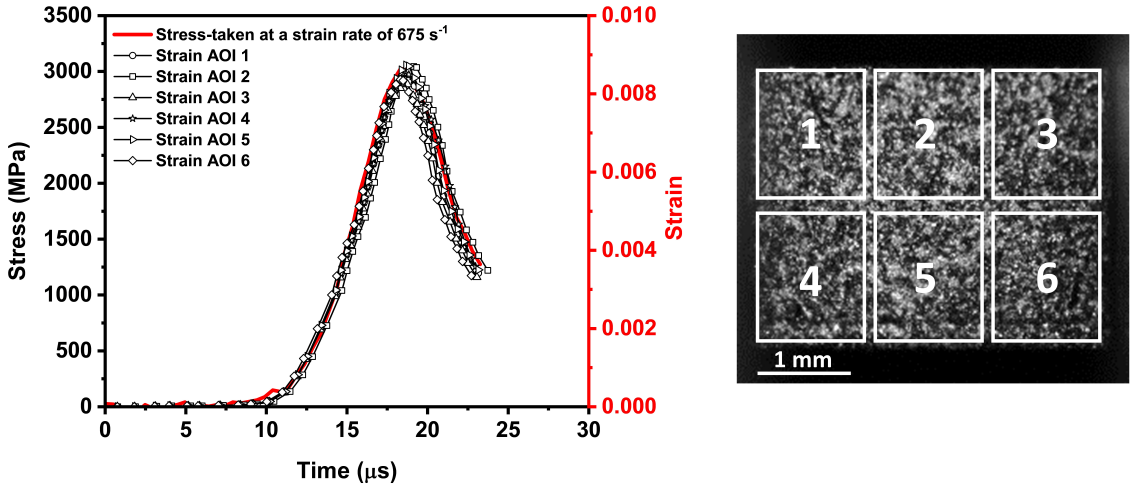

Fig. 3.3: Combined compressive stress and strain curves as a function of time for AM alumina on the right, and the specimen showing the various DIC areas of interest (AOI) on the left. The average strain-time response and the stress-time response overlap with each other, showing that the specimen is experiencing good equilibrium and uniform deformation. The slope of the strain-time curves is reasonably linear, indicating a constant strain rate of 675 s^{-1}.

3.3.4 Vickers hardness testing

The Vickers hardness is carried out using a Vickers hardness testing machine (VH1202, Buehler Wilson, Lake Bluff, Illinois, USA) following the ASTM C1327 standard [156] by applying a load of 9.81 N (1 kg = HV1) with a dwell time of 10 s on a polished surface of the specimen. In total, twelve points are measured on each plane of the specimen (i.e., Y-Z plane, X-Y plane, and X-Z plane showing at Fig. 3.1 (a)) at locations from one edge to the center. Vickers hardness measurements (in HV) are converted to GPa for better comparison with previous studies [157–175].

3.4 Results and discussion

In this section, the results on the micro-indentation and strain-rate-dependent behavior of AM alumina ceramics under uniaxial compression loading are outlined.

Section 3.4.1 highlights the hardness of the AM alumina ceramics which is measured by micro-indentation Vickers test and the strain-rate-dependent uniaxial compressive strength of the material in comparison with other AM and that of conventionally-made counterparts in the literature. Following this section, the time history of stress and strain, and the time-resolved failure evolution of the material under uniaxial compression experiments are detailed for both quasi-static and dynamic loading in Section 3.4.2. In Section 3.4.3, for both quasi-static and dynamic loading, SEM images of the fracture surface of the specimens are presented to better understand the contribution of intergranular and transgranular failure mechanisms. Lastly, crack speed measurements are presented in Section 3.4.4 to provide insights into the differences in crack propagation in the AM alumina ceramics and conventionally-made ones in previous studies under dynamic uniaxial compression.

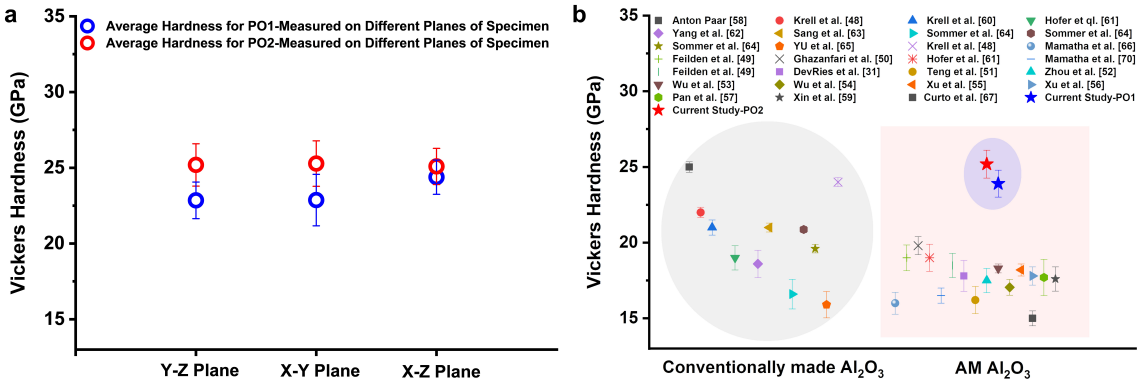

Fig. 3.4: The Vickers hardness measurements of the studied AM alumina ceramics. (a) The hardness of the current AM alumina materials measured on the different planes of the specimen (i.e., Y-Z plane, X-Y plane, and X-Z plane shown in Fig. 4.1 (a)) for both POs. (b) Comparison of the hardness of the current AM alumina ceramics shown in red and blue stars with those of the conventionally-made and other AM alumina counterparts in the literature.

3.4.1 Vickers hardness measurements and strain-rate-dependent compressive strength of AM alumina ceramics

The hardness of the current AM alumina ceramics is measured using the micro-indentation Vickers test and compared with those of the conventionally-made and other AM alumina counterparts in the literature. For both POs, Fig. 3.4 (a) shows the hardness of the current AM ceramics measured on the different planes of the specimen (i.e., Y-Z plane, X-Y plane, and X-Z plane shown in Fig. 3.4 (a)). The measured hardness is slightly higher for the specimen with the PO2, and this minor change in hardness from the PO of the material is consistent with previous studies [31, 168]. In addition, for both POs, the value of hardness remains almost unaltered for different planes. The average measured value of hardness for PO1 and PO2 are 23.8 $\pm$ 0.9 GPa and 25.1 $\pm$ 0.87 GPa, respectively.

To further analyze the hardness of the current AM alumina ceramics, Fig. 3.4 (b) summarizes the hardness of other alumina ceramics from previous studies, where the gray area and pink area show those of the conventionally-made [157–164] and additively manufactured [31, 157, 160, 165, 166, 168–176] materials, respectively, in comparison with the AM ceramics used in this study represented by the red and blue stars. With regard to the average values, the AM alumina ceramics seem to represent slightly lower quantities of hardness when compared to the conventionally-made ones, and this is attributable to the higher porosity, lower density, and structural defects in the AM specimens [31, 160, 176–178]. The current AM alumina materials show higher hardness than the AM alumina ceramics in the literature. Based on previous studies [176, 177], the hardness of ceramic materials mainly depends on the crystalline structure/microstructure of the material, pores, and grain size.

Accordingly, the higher hardness of the current AM alumina ceramic could be attributed to finer grain size (i.e., 2.92 μm in our work compared to 11.42 μm in [176], 9.67 μm in [179], and 7.61 μm in [160]), and higher relative density (i.e., $\sim$ 98% in our work compared to 85% in [181], 88% in [182], and 85% in [183]) with smaller

Table 3.1: Summary of AM Al_2O_3 characteristics previously studied in the literature shown in Fig. 3.4(b). Note that all the studies are not included due to the lack of the reported data.

Manufacturing method	Grain size (μm)	Relative density (%)	Porosity size (μm)	Hardness (GPa)	Source
SLA	9.68	97	8	16.5	[179]
PSD	12	94	35	19.2	[31]
SLA	9.6	82	4	11	[176]
SLA	4	97	45	16	[180]
SLA	3.2	95	3	20	[176]
SLA	2	97	5	16	[174]
CODE	0.34	96	2	19.6	[167]
Robocasting	1.4	97	2.5	18.6	[166]
DLP	1.71	83	4	14	[172]
DLP	2.19	92	1	14.5	[172]
SLA	2.94	98	1.3	23.8	Current study-PO1
SLA	2.92	98	1.3	25.1	Current study-PO2

Note: CODE is the abbreviation for Ceramic On-Demand Extrusion.

average pore size (i.e., 1.3 μm in our work compared to 6 μm in [160], 10 μm in [184], and 45 μm in [180]). In Table 3.1 the available characteristics of the AM alumina in the literature are summarized which are shown in Fig. 3.4 (b).

In Fig. 3.5(a) the relationship between the compressive strength and strain rate for the AM alumina is shown. Here, the compressive strength corresponds to the peak point of the measured stress-time curves where the stress-bearing capacity of the material starts decreasing rapidly due to the coalescence of multiple axial cracks resulting in the loss of material integrity. To better analyze the role of PO on the strain-rate-dependent compressive strength of the material, Table 3.2 and Table 3.3 summarize and compare the average compressive strength (ACS) of both POs under quasi-static and dynamic rates, respectively, and it shows that the ACS becomes more independent of the PO with the increase of strain rate from quasi-static to dynamic loading condition (see the ratio $\frac{PO2_{ACS}-PO1_{ACS}}{PO1_{ACS}} \times 100$ in Table 3.2 and Table 3.3). With a maximum difference of 10% (i.e., the strain rate of 10^{-4} s^{-1}) in ACS under quasi-static rates, the strain-rate-dependent compressive strength of the AM alumina seems to present a minor dependency on the PO. Additionally, one may observe no apparent trend of dependency of the compressive strength on the POs across strain rates since the ratio presented in Table 3.2 and Table 3.3 shows both positive and negative values. The fitted curves in Fig. 3.5(a) (i.e., the solid black and red lines) also show that no specific POs produce higher strength across all strain rates, and this is likely due to adequate sintering.

Next, Fig. 3.5(b) summarizes the compressive strength of alumina ceramics made by AM (i.e., the present study and study by DeVries et al. [31]) and conventional approaches (i.e., AD98 [32], AD98 [27], AD-995 [31], and AD-995 [26], with the number indicating weight percentage of alumina) across different strain rates. It is observed that the quasi-static and dynamic compressive strength of current AM alumina is among the highest ones reported for AM alumina in the literature [31], but is lower by $\sim$ 40% and $\sim$ 25% under quasi-static and dynamic rates, respectively,

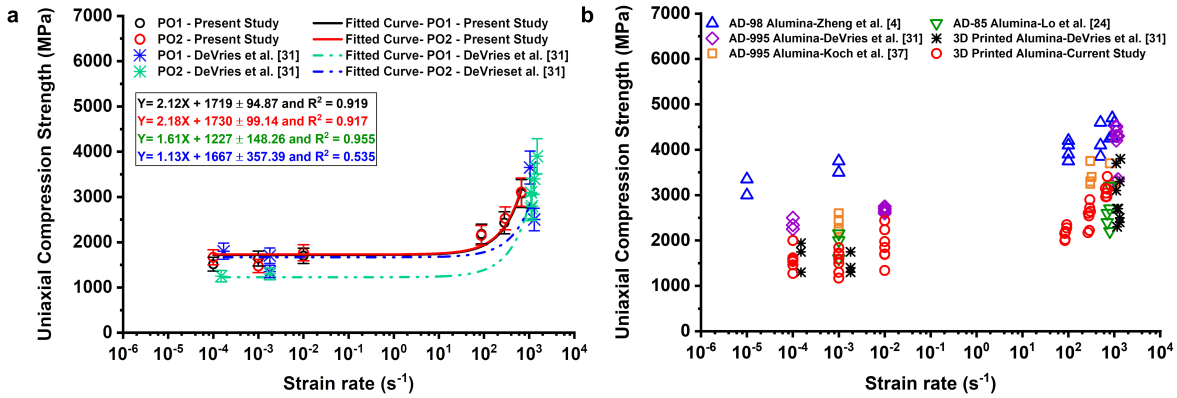

Fig. 3.5: Material testing under uniaxial quasi-static and dynamic compression. (a) The compressive strength-strain rate of the AM alumina ceramics in this study and compared to the data in the literature on AM alumina [31]. Linear curve fitting (Y=aX+b and R^2 shows the goodness of fitted curves) is carried out to better show the trends. (b) A comparison of the rate-dependent compressive strength of AM and conventionally-made alumina ceramics.

when compared to the conventional counterparts, and this result is consistent with the study by DeVries et al. [31]. The lower strength of the current AM ceramics compared to conventional ones is linked with the microstructural defects that cause local failure (see the time-resolved images in Fig. 3.6 and Fig. 3.7), resulting in the loss of structural integrity of the specimens [185].

Table 3.2: Average compressive strength (ACS) of AM Al_2O_3 under quasi-static loading for both POs shown in Fig. 3.5(a).

Strain rate (s^{-1})	10^{-4}	10^{-3}	10^{-2}
PO1-ACS (MPa)	1514.25 ± 139.98	1640.54 ± 99.33	1700.31 ± 112.72
PO2-ACS (MPa)	1666.66 ± 237.73	1494.25 ± 260.08	1766.75 ± 235.66
$\frac{PO2_{ACS}-PO1_{ACS}}{PO1_{ACS}} \times 100$	10%	-8.8%	3.9%

While the current AM alumina ceramics show a lower compressive strength compared to the conventional counterparts (see Fig. 3.5), their measured hardness is comparable with the highest reported quantities for the conventional ones. This behavior is likely to be explained by the way that the randomly distributed pores and microstructural defects contribute to the compressive strength and hardness behavior

Table 3.3: Average compressive strength (ACS) of AM Al_2O_3 under dynamic loading for both POs shown in Fig. 3.5(a).

Strain rate (s^{-1})	80-100	260-310	640-730
PO1-ACS (MPa)	2181.66 ± 221.18	2430.68 ± 205.43	3077.25 ± 174.07
PO2-ACS (MPa)	2151.67 ± 56.51	2526.52 ± 73.86	3107.33 ± 97.03
$\frac{PO2_{ACS}-PO1_{ACS}}{PO1_{ACS}} \times 100$	-1.4%	3.9%	0.97%

of the material. Under uniaxial compression loading, the material is loaded to fail under a global state of deformation, where the weak interface boundaries in addition to the pores are the sites for the tension-dominated stress concentration and the initiation/coalescence of failure that governs the strength of the material [159, 160, 163]. In contrast, under the micro-indentation as a non-destructive characterization method to measure the resistance of the material against deformation, a small surface area of the specimen with a size of a few microns is locally deformed under the Vickers indenter, where the microscale failure mechanisms are less likely to be activated [31, 159, 160, 163].

3.4.2 Time-resolved stress, strain, and failure evolution under quasi-static and dynamic uniaxial compression experiments

Fig. 3.6 and Fig. 3.7 show the stress and strain histories coupled with the time-resolved images of failure and DIC strain contours for quasi-static (Fig. 3.6(a) and (b)) and dynamic (Fig. 3.7(a) and (b)) rates to better demonstrate the axial (ϵ_{xx}) and lateral (ϵ_{yy}) strain evolution associated with the onset of fracture. The image frame numbers (1-4) correspond to those labeled on the stress-time curve. Upon reaching equilibrium in the specimen, the stress and strain histories almost linearly increase up to the peak and then sharply decrease due to the catastrophic failure, and the strain is not measured since the DIC pattern is lost. As shown in Fig. 3.6 and Fig. 3.7, shear strain holds almost zero which confirms the induction of uniaxial

compression and no in-plane rotation during the loading process. The still images on the right side of Fig. 3.6 and Fig. 3.7 show the distribution of axial (ϵ_{xx}) and lateral (ϵ_{yy}) strains correlated to the numbered points on the curves. Note that the DIC pattern is lost at the early stages of quasi-static loading due to localized failure (see Fig. 3.6(a) at point 2), and this impedes the measurement of a Poisson's ratio. Under dynamic rates, the Poisson's ratio is measured to be 0.24 $\pm$ 0.03. In Fig. 3.6 and Fig. 3.7, the accumulation of strain and failure pattern of the material is noticeably influenced by the PO, while the quantitative data in terms of stress and strain histories are not highly affected. For the quasi-static rates (Fig. 3.6(a) and (b)), before any local failure, the localization of lateral strain as an indicator of tensile failure progression is observed for both POs, with PO2 being more prominent. Also, a more diffusive accumulation of axial strain is observed in PO2. Both PO1 and PO2 specimens first undergo local failure (see frame 2 and frame 3 of Fig. 3.6(a) and (b), respectively) under quasi-static loading likely to be caused by manufacturing-related microstructural defects (e.g., pores and weak grain boundaries) causing the loss of DIC correlation. The red areas in the contour of the frame (2)) show a strain localization zone, which indicates the site for fracture nucleation. After point 3 for both POs, stress-bearing capacity keeps rising until point 4 at which a global catastrophic failure occurs from a few dominant cracks propagating through the specimen. As seen in Fig. 3.6(a), under quasi-static loading, the history of lateral strain (ϵ_{xx}) represents quantities that are close to those of the axial strain (ϵ_{yy}), by which the ratio of $\frac{\epsilon_{xx}}{\epsilon_{yy}}$ may not replicate a typical Poisson's ratio of 0.22 for alumina ceramics. This is attributable to the local failure of the current AM alumina from the early stages of loading due to process-induced microstructural defects manifesting as axial cracks at the macroscale (see the status of the specimen in the time-resolved image for Point 2 in Fig. 3.6(a)). These axial cracks, in consequence, lead to the lateral expansion of the specimen, thereby increasing the measured lateral strain by the DIC analysis under quasi-static loading. As such, to avoid any misinterpretation of the measured

data, the ratio of $\frac{\epsilon_{xx}}{\epsilon_{yy}}$ under quasi-static loading was not reported as Poisson's ratio in this study.

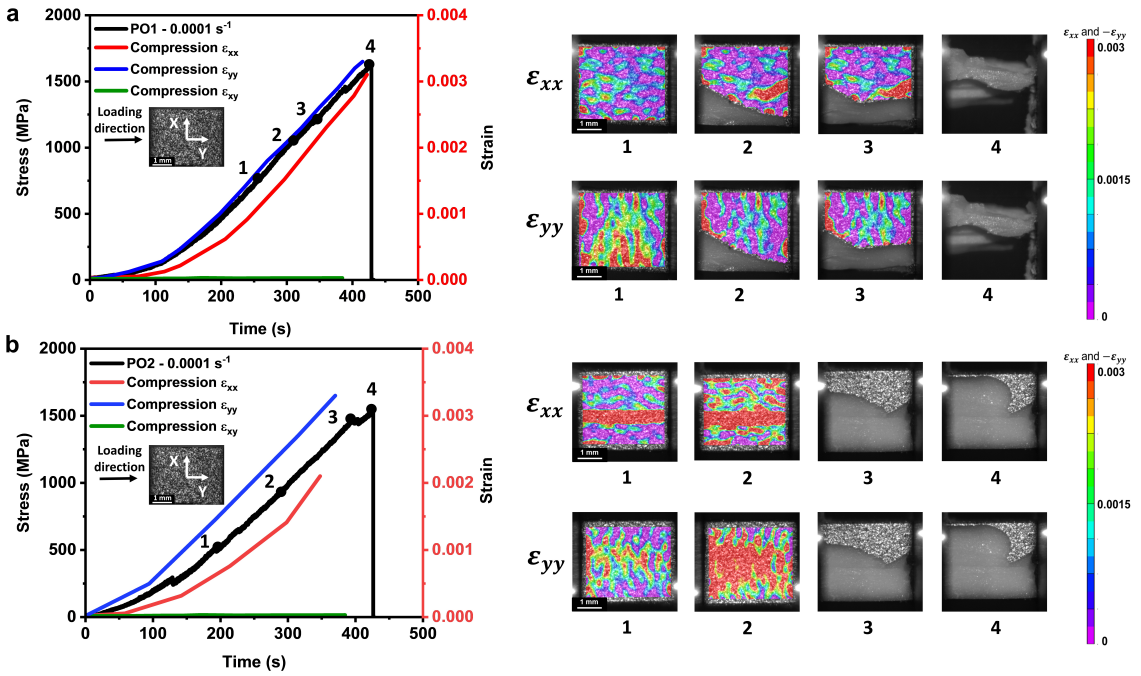

Fig. 3.6: The quantitative and qualitative history of stress-time and strain-time developed under uniaxial compression. (a,b) The AM alumina ceramic under quasi-static loading at a rate of 0.0001 s^{-1} for the PO1 and PO2, respectively. The time-resolved DIC contours show the evolution of axial strain (first row) and lateral strain (second row) components that correspond to the specified numbered point on the stress-time curves.

From Fig. 3.7(a) and (b), the PO-dependent failure pattern of the material becomes more noticeable when compared to quasi-static loading. In the PO1 specimen, primary axial cracks at the top and bottom of the specimen are initiated, and this causes softening in the stress-time curve prior to peak stress (see point 2 on Fig. 3.7(a)). Subsequently, the propagation of the axial primary cracks and damage at the corners lead to a sharp decrease in the stress (points 3 and 4 in Fig. 3.7(a)). In PO2 specimens shown in Fig. 3.7(b), both axial and lateral strains concentrate at the top corners (specifically the top left corner, see frames 2 and 3), and failure is initiated in these areas. Next, after peak stress, a primary axial crack nucleates in the middle where the lateral strain is accumulated and then the formation of multiple axial cracks causes

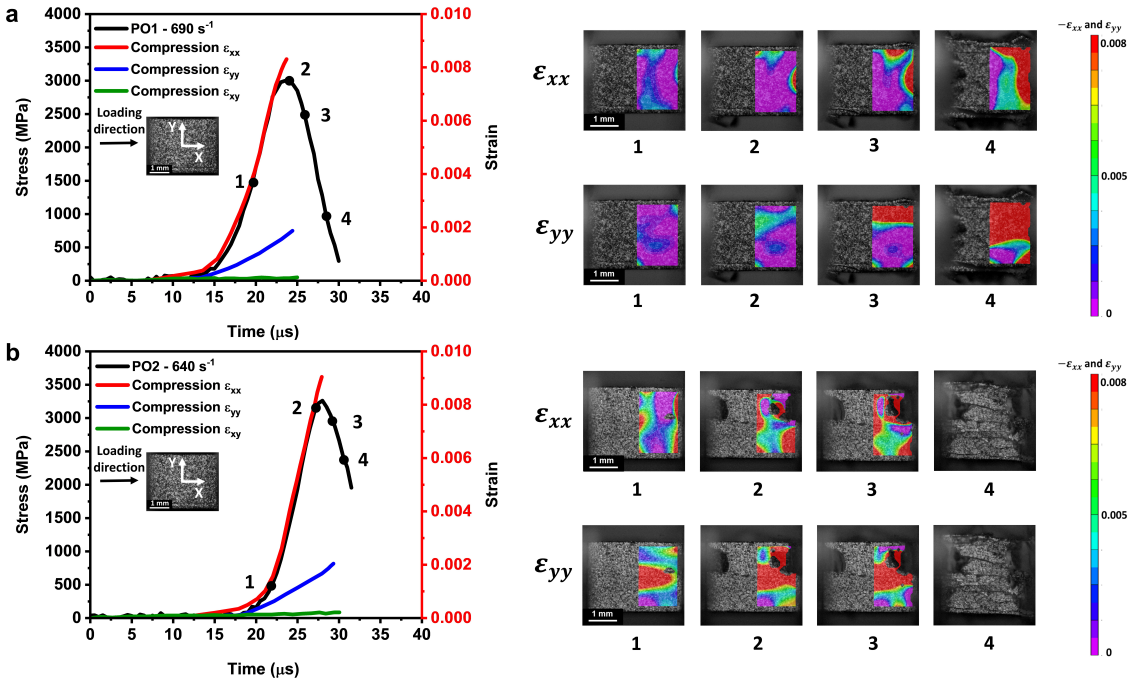

Fig. 3.7: The quantitative and qualitative history of stress-time and strain-time developed under uniaxial compression. (a,b) The AM alumina ceramic under dynamic loading at a rate of 690 s^{-1} for the PO1 and PO2, respectively. The time-resolved DIC contours show the evolution of axial strain (first row) and lateral strain (second row) components that correspond to the specified numbered point on the stress-time curves.

the catastrophic failure of the specimen. Overall, the PO notably affects the failure pattern of the AM alumina likely caused by the layer-by-layer printing process, while minimally affecting the stress and strain time histories. This minor difference in the quantity of mechanical properties (i.e., compressive strength) of both POs could be attributed to the layer-by-layer printing process and the resulting orientation of layers relative to the loading direction, where its effect is manifested in the macroscale failure pattern shown in Fig. 3.7 and Fig. 3.7. From previous research [186, 187], it is known that the strength of the layers is higher within the layer than the interfaces between the layers. In the current work, for the PO1, the layers are along the loading direction (x direction in Fig. 3.6(a) and Fig. 3.7(a)) but perpendicular to the lateral tensile strain (see the DIC patterns in Fig. 3.6(a) and Fig. 3.7(a)) that may result in a lower compressive strength when compared to the specimen with PO2.

3.4.3 Post-mortem fractographic studies

In this sub-section, the failure behaviors (i.e., intergranular fracture, transgranular fracture, and cleavage) on surfaces of fragments retrieved from both quasi-static and dynamic uniaxial compression experiments are compared to determine the failure competition mechanisms. Fig. 3.8(a) and (b) show a magnified view of the fracture surface of specimens with PO1 and PO2, respectively, under quasi-static loading, and Fig. 3.8(c) and (d) represent the same for PO1 and PO2, respectively, under dynamic loading. In Fig. 3.8(a) under quasi-static loading, rough fracture planes with sharp edges appeared on the fragments, and there are more intergranular cracks propagated in the PO1 specimen compared to PO2, and this may be related to the weaker interfacial bonding at the grain boundaries [14, 32].

In Fig. 3.8(b) evidence of transgranular fracture through cleavage in the PO2 specimen is shown. The magnified fracture surfaces indicate that intergranular fracture is the dominant mechanism for both POs under quasi-static loading. As shown in Fig. 3.8(c) and (d) for dynamic rates, both intergranular and transgranular cracks,

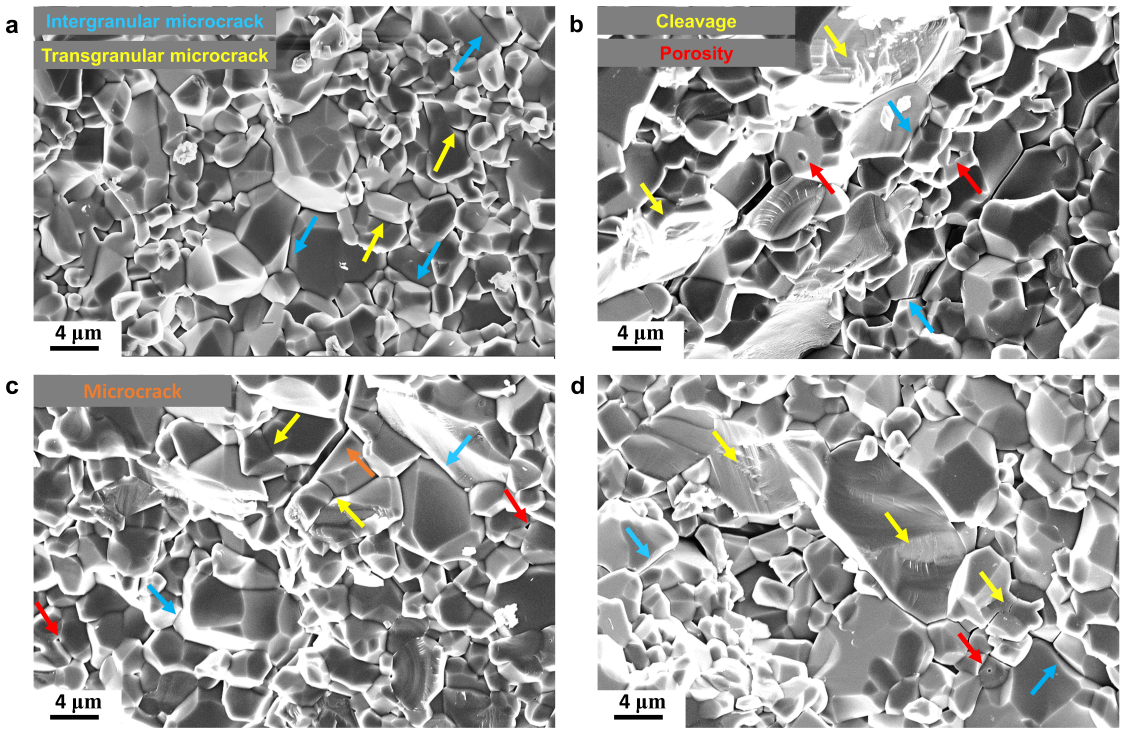

Fig. 3.8: SEM micrograph showing the fractography of the AM alumina. (a,b) SEM images showing the fractography of the material under quasi-static loading for PO1 and PO2, respectively. (c,d) SEM images showing the fractography of the material under dynamic loading for PO1 and PO2, respectively.

and micro-crack branching are observable on the fracture surface, and this may act as another underlying reason for a higher strength when the material is subjected to dynamic rates [32]. Overall, it is observed that the intergranular failure mechanism contributes predominantly under quasi-static conditions (Fig. 3.8(a) and (b)), while a combination of intergranular and transgranular failure mechanisms governs the failure process of the material under dynamic loading (Fig. 3.8(c) and (d)). This observation is consistent with the previous studies [14, 32, 188] on alumina across quasi-static and dynamic loading conditions. Under high strain rates, the material deforms in a short span of time, thereby inducing a significantly higher level of kinetic energy in the material [14]. This condition suppresses the strain localization –which mainly occurs under quasi-static loading– and this allows more nucleation and coalescence of micro-cracks within the grain boundaries (i.e., transgranular failure mechanism) under high strain rates [14, 32].

3.4.4 Crack speed measurements

In Fig. 3.9 the measured crack speed propagation in the current AM ceramics compared to those of conventionally-made alumina across different strain rates is demonstrated. Here, the image on the plots is captured by an ultra-high-speed camera that indicates the primary cracks by red arrows for which the crack speed is measured. No quasi-static experiments are considered since the camera is not fast enough to record the fracture process. The length of the cracks and the selection of the frames are identified manually, and this may cause uncertainty in crack speed measurement. To reduce error, ultra-high-speed imaging is conducted with 0.5 to 2 million fps and different sets of points along the crack tip are measured to obtain the average speed value for each crack. From Fig. 3.9 (a), the average crack speed of the AM ceramics increases from 150 $\pm$ 104 to 1190 $\pm$ 245 m/s for PO1 and 110 $\pm$ 116 to 1280 $\pm$ 254 m/s for PO2 when the strain rate increases from 80 to 730 s^{-1}. In a study by Ji et al. [32], an average value of 2.5 $\pm$ 1.4 km/s for strain rates between 71 and 1064

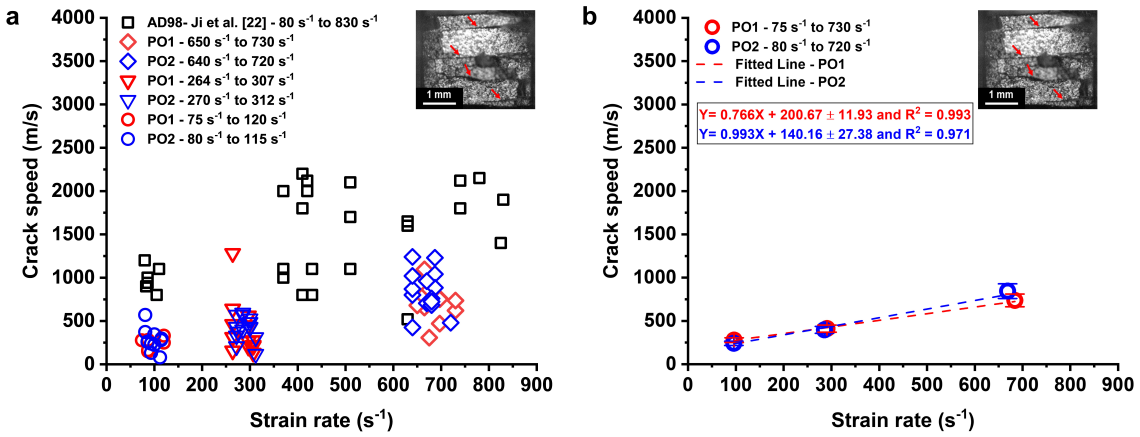

Fig. 3.9: Plot of strain-rate-dependent average crack speed in AM alumina ceramics under uniaxial compression experiments. The inset image indicates the primary cracks for which the crack speed is measured. (a) The crack propagation speed in the specimen is compared with conventionally-made AD98. (b) Comparison of crack propagation speed in the specimens printed with different orientations. A linear fit (Y=aX+b and R^2 show the goodness of fitted curves) is provided to better compare the dependency of crack speed on the printing direction.

s^{-1} is reported for AD98 which is 218% higher than the current AM alumina. The crack speed in the AM alumina is consistently lower than that of the conventional alumina across different strain rates, and this is attributed to the larger average pore size in the AM alumina ($\sim$ 1.3 μm) when compared to the conventional ones (much less than 1 μm [32, 34]), where the crack speed is related to initial defect size by $v = 0.38c_0\left(1 - \frac{a_0}{a}\right)$ [189], where c_0 is the speed of sound wave propagation, a is the current crack length, and a_0 is the initial crack size which is the pore size in our study. In Fig. 3.9(b), a linear fit is applied on the average crack speed for PO1 and PO2, which shows that the crack speed propagation in the PO2 specimen is slightly more sensitive to the strain rate. Altogether, the current data sets allow the development and validation of computational models for AM ceramics to account for the rate sensitivity of mechanical properties and damage growth [55, 190].

3.5 Conclusions

In this study, AM alumina ceramics by stereolithography are characterized and subjected to micro-indentation and compressive loading across quasi-static and dynamic loading rates (i.e., 10^{-4} s^{-1} to 10^{2} s^{-1}). The micro-indentation Vickers hardness experiments show that the hardness of the AM alumina is nearly independent of the POs, and it also remains almost unaltered when measured on different planes of the specimen (i.e., Fig. 3.4). The current AM alumina shows a higher hardness compared to the other AM alumina ceramics and this is attributable to a higher relative density, smaller pore size, and a finer grain size. The material shows quasi-static and dynamic strength that is among the highest ones reported for AM alumina in the literature, but it is $\sim 40\%$ and $\sim 25\%$ lower than that of the conventionally-made alumina in the literature under quasi-static and dynamic rates, respectively (i.e., Fig. 3.5). This may be attributable to manufacturing-induced microstructural defects (i.e., weak grain boundaries and porosity) that cause local failure resulting in loss of structural integrity of the specimens. The PO is found to slightly affect the strain-rate-dependent compressive strength (i.e., 10% and 3.9% as the maximum under quasi-static and dynamic loading regimes, respectively) of the material while remarkably influencing the failure pattern at the macroscale likely caused by the layer-by-layer printing process (i.e., Fig. 3.6, and Fig. 3.7). For both the POs, the fractography shows that the intergranular failure is the dominant mechanism under quasi-static rates, while both the intergranular and transgranular mechanisms in combination govern the failure of the material under dynamic loading (i.e., Fig. 3.8). This transition in the contribution of failure mechanisms might be attributable to a significantly higher level of kinetic energy in the material under dynamic loading that suppresses the localization of strain, thus allowing more nucleation and coalescence of micro-cracks within the grain boundaries (i.e., transgranular failure mechanism) under high strain rates. The crack speed propagation in the AM alumina is found to be less than that of conven-

tional counterparts (i.e., Fig. 3.9) possibly due to a smaller pore size in the current AM ceramics. Altogether, this study provides a better understanding of the behavior of AM alumina ceramics that pave the way for the design of AM ceramics with mechanical properties comparable to conventionally-made counterparts. Additionally, this research generates valuable data sets that are applicable to the development and validation of computational models for AM ceramics [55, 190] to accelerate the process of material design and optimization [29, 190].

3.6 Acknowledgments

This work is supported by the Natural Sciences and Engineering Research Council of Canada (Grant # 2016-04685).

Chapter 4

Understanding the effect of microstructure on the failure behavior of additively manufactured Al_2O_3 ceramics: 3D micromechanical modeling

Published as **Zahra Zaiemyekeh**, Saman Sayahlatifi, Dan L. Romanyk, James D. Hogan. "Understanding the Effect of Microstructure on the Failure Behavior of Additively Manufactured Al_2O_3 Ceramics: 3D Micromechanical Modeling", *Materials and Design*, 2024.

4.1 Abstract

Additively manufactured (AM) ceramics are gaining popularity due to improved flexibility in the design of customized structures. Microstructure-based finite element (FE) models were developed to study the strain-rate-dependent failure behavior of AM Al_2O_3 ceramics under uniaxial compression. Upon validation with experimental data, the model was leveraged to quantify the history of intergranular and transgranular failure mechanisms across microstructures. It was revealed that the intergranular mechanism plays a key role in the material strength across strain rates. Crystallographic orientations were found to remarkably decrease the material strength due

to the earlier initiation and faster growth of the intergranular mechanism. The increase in porosity was found to amplify the transgranular mechanism resulting from a higher number of pores acting as crack nucleation sites, decreasing the material strength regardless of strain rate. The model reflected the existence of a threshold for grain boundary strength, beyond which further enhancements yield marginal improvements in material strength. Additionally, the effect of grain size on the initiation and evolution of failure mechanisms was studied and the corresponding limitations of the model were discussed. The current work correlates the microstructure of the material to its macroscale response through micromechanical models, informing the design of better-performing AM Al_2O_3 ceramics.

4.2 Introduction

Additively manufactured (AM) Al_2O_3 ceramics have gained popularity in various industries (e.g., defense [11], biomedical [191], and aerospace [134]) as they offer flexibility in design and manufacturing of complex shape end-use components with satisfactory mechanical properties (e.g., high strength [101], hardness [192], and wear resistance [67]). Different AM methods, including binder jetting [193], stereolithography (SLA) [194], and selective laser sintering (SLS) [22] technologies have been developed, where the SLA technique offers high surface accuracy and relatively fast construction speed to fabricate ceramic components [30]. The development and design of better-performing AM ceramic materials with tailored properties (e.g., strength), and microstructures (e.g., porosity) requires a foundational understanding of the interplay between microstructural failure mechanisms that govern the behavior of the material at the structural scale [195–197]. To date, limited efforts [55, 198] have been made to explore the microstructure-property-performance relationships of AM ceramics and address the evolution/competition of failure mechanisms toward advancing the design of optimized ceramic-based structures. Accordingly, this study focuses on developing experimentally validated micromechanical models to provide insights into

the correlation between the microstructure and mechanical behavior of AM alumina ceramics fabricated by the SLA method.

Previous studies have primarily sought to experimentally explore the mechanical response and failure behavior related to the microstructure (e.g., grain size [199, 200], pores [201, 202], and impurity distributions [203, 204]) of conventionally made ceramics under different loading rates [14, 32, 34], while very limited efforts have been focused on AM ceramics. For example, Koch et al. [99] found that the greater strain rate sensitivity and higher crack speed of AD-995 alumina compared with AD-85 are related to the smaller grain size, larger pore sizes, and higher impurities of AD-85. In another study by Ji et al. [32], it was reported that the smaller average grain size of AD-98 alumina is potentially a factor contributing to the relatively higher strength in comparison with other alumina ceramics (e.g., AD-85 [99], and AD-995 [205]). The effect of grain and porosity size on the ballistic performance of ceramic materials [206, 207] and the strength of brittle polycrystallines [208, 209] has also been investigated previously, where it was determined that the finer the grain/porosity size, the higher the strength of ceramic materials [30, 32, 210]. In addition to the microstructural characteristics, the microscale failure mechanisms, namely intergranular and transgranular failure mechanisms, were studied by post-mortem scanning electron microscopy (SEM) imaging analysis. For conventionally made AD-98 alumina, the work by Ji et al. [32] revealed that intergranular fracture was more likely to appear under quasi-static loading and transgranular fracture under dynamic loading. The same observation was also reported by Zaiemyekeh et al. [30] and Wang et al. [14]. Among the limited studies on AM ceramics [30, 31, 143, 211], in the work by Zaiemyekeh et al. [30] on AM alumina fabricated by the SLA method, the material showed higher hardness in comparison with other AM counterparts [31, 160, 169, 176] due to smaller grain and porosity sizes, and a higher relative density. In addition, the dominant contribution of the intergranular failure mechanism and a combination of intergranular and transgranular mechanisms under quasi-static and

dynamic loading, respectively, were reported, and this is in agreement with the study by DeVries et al.[31]. While previous experimental efforts [30, 176, 177] provided insights into the role of microstructural features on the mechanical properties of AM ceramics, there is still a gap in our knowledge of microstructure-dependent initiation, interaction, and evolution of failure mechanisms and their correlation with macroscale mechanical performance of these emerging AM ceramic materials.

Microstructure-based FE approaches implemented by the concept of RVE modeling have shown a great potential for unraveling the role of microstructural characteristics on the failure behavior of materials; these include particulate reinforced composites [212], fiber-reinforced polymeric composites [213], cementitious composites/concretes [214], and polycrystalline metals [215], to name a few. While the failure behavior of ceramics at a structural scale is extensively studied in the literature [14, 36, 55], RVE-based FE models are scarcely leveraged to explore the initiation and growth of failure in the material at the microstructural level [216–218]. For example, Falco et al. [216] developed Representative volume elements (RVEs) accounting for the polycrystalline microstructure of conventionally made alumina ceramics to numerically study the effect of microstructural variability on the mechanical properties of the material. Additionally, in the work by Falco et al. [216], the failure behavior of the material as a function of microstructural defects in the form of voids was explored. To the best of our knowledge, no effort has been made to study the microscale failure behavior of AM alumina ceramics incorporating the experimentally informed porous polycrystalline microstructure of the material under both quasi-static and dynamic loading while accounting for both intergranular and transgranular mechanisms; this is the focus of the current paper.

Building on the previous studies [216, 217], the current work developed an experimentally validated microstructure-based computational model in which RVEs of the AM alumina ceramics are generated in the Neper software informed by the microstructural characteristics, including grain size distribution and grain orientations from the

electron backscattered diffraction (EBSD) analysis, and porosity features determined by X-Ray Microscopy (XRM) examination to unravel the strain-rate-dependent evolution/competition of failure mechanisms when different microstructural variables are considered. The alumina grains are constitutively modeled by a viscosity-regularized form of the Johnson–Holmquist-II (JH2) material model (i.e., JH2-V [55]) implemented via a VUMAT subroutine in Abaqus/Explicit FE solver and the interfaces between the grains are modeled by a bi-linear cohesive law implemented through a surface-based CZM approach [219]. First, the developed model was validated by experimental results for both quasi-static (10^{-3} s^{-1}) and dynamic (690 s^{-1}) rates. Once validated, the model is exercised to quantify the growth of the transgranular and intergranular mechanisms in terms of the fraction of fully damaged elements and fully debonded interfacial nodes, respectively. Next, the model was leveraged to identify the relationship between microstructural features (e.g., grain Eulerian orientation, porosity, and interfacial properties) and the macroscale response of the materials.

Overall, the current microstructure-based FE models provide better insight into discovering the links between the microstructure, microscale failure mechanisms, and macroscale behavior (e.g., strength) of AM ceramics under different strain rates which inform on the accelerated design and development of next-generation AM ceramics with higher performance for dynamic applications [30, 56]. Design-wise, the developed model could be leveraged to tailor the microstructure of the material to optimally withstand loading conditions specific to a desired application. In addition, aided by the prediction of the growth history of failure mechanisms, the current model informs on the critical microstructural features across strain rates, which could guide the design process of AM ceramic components by controlling or manipulating them to achieve enhanced mechanical performance. Lastly, as a dataset generator, the developed micromechanical framework lays the foundation for establishing cross-scale constitutive models by machine learning approaches [220] that guide the design of advanced AM ceramic components with tailored micro- and macro-structures.

4.3 Methodology

The experimental methods including AM alumina specimen fabrication and microstructural characterization needed to inform the model are briefly discussed in Section 4.3.1. The reader is referred to previously published work by the authors [30] for more details on the experimental approaches. Next, in Section 4.3.2, the generation process of RVEs by Neper informed by microstructural features (e.g., grain size distribution, grain Eulerian angles, and porosity characteristics) is first outlined, and then the FE model including boundary and loading conditions is described. Lastly, the theoretical framework, including the JH2-V constitutive material model, and the bi-linear CZM model with the corresponding constants used in this study are given.

4.3.1 Experimental methods: Material and characterization

In the current study, α-Al_2O_3 ceramics were additively manufactured through the SLA method by Lithoz, America. The samples were printed into cuboids with dimensions of 2.3 mm $\times$ 2.7 mm $\times$ 3.5 mm, as shown in Fig. 4.1(a). The dimensions described above were chosen for the specimens to provide enough time for the material to achieve stress equilibrium under testing, as outlined in previous investigations [30, 34, 99]. In the SLA method, the laser energy and exposure duration for each layer were established at 30 mW/cm^2 and 10 s, respectively. The layer thickness during printing was 25 µm, with a pixel size (DLP XY) of 40 µm. Following debinding, all green bodies underwent a sintering process at 1650°C for 2 hours.

The AM Al_2O_3 ceramics were tested under quasi-static (10^{-3} s^{-1}) and dynamic (690 s^{-1}) strain rates. Quasi-static uniaxial compression tests were conducted using a conventional servohydraulic MTS 810 machine, applying displacement control settings along the longer dimension (i.e., 3.5 mm as shown in Fig. 1(a)). A high-speed AOS PROMON U750 camera was employed to observe the surface deformation of the specimen. The camera operated at 50 frames per second (FPS), concerning the

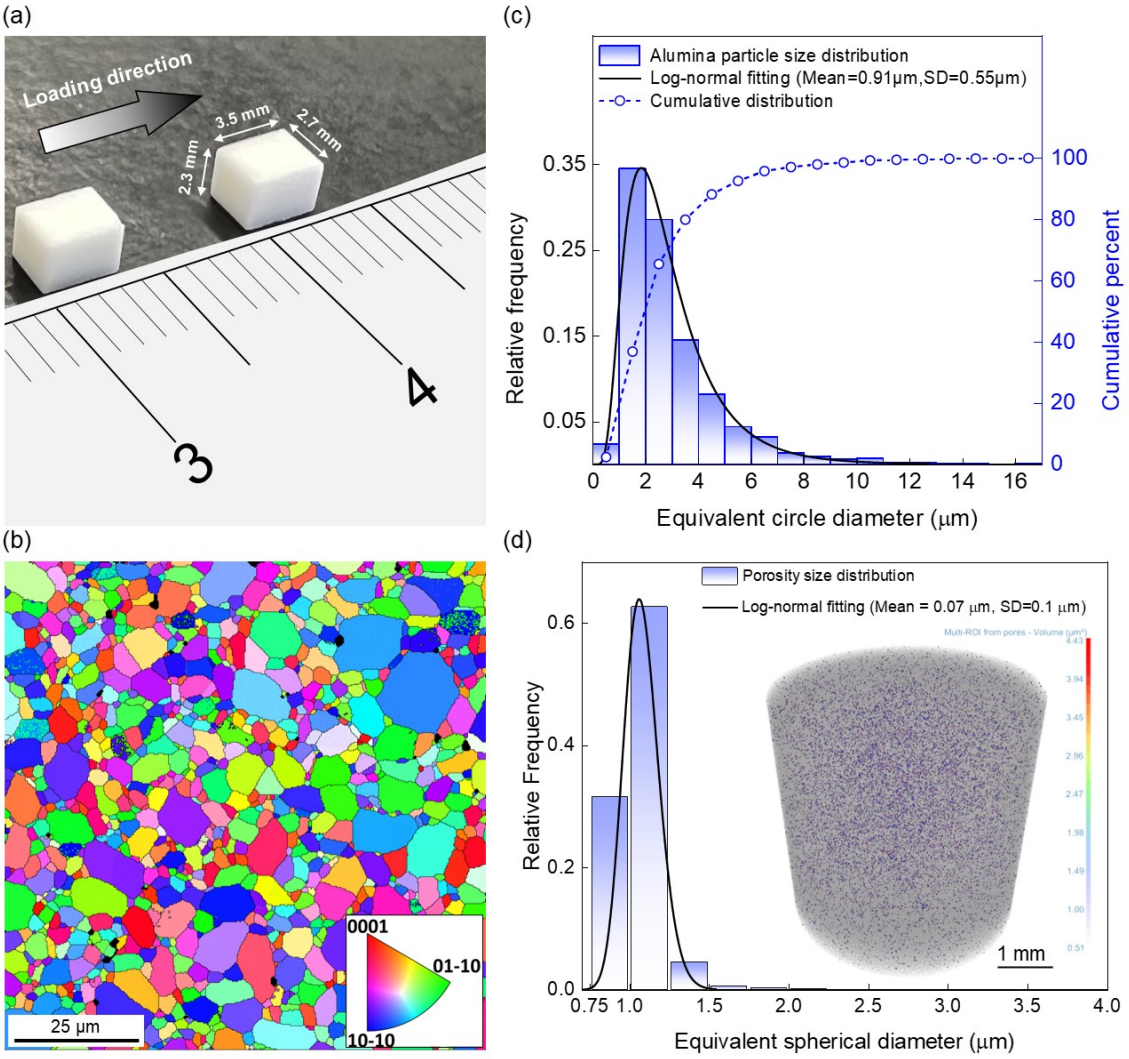

Fig. 4.1: Fabrication and characterization of the AM alumina ceramic: (a) AM alumina samples studied in the current work. (b) EBSD map of the AM alumina, showing the grain size scatter and crystallographic orientations. (c) The histogram distribution of the equivalent circle diameter of the grains in the AM alumina. The particle size distribution follows a log-normal curve with mean and standard deviation values of 0.91 μm and 0.55 μm, respectively, that was used to generate the microstructure-informed RVEs by Neper software. (d) The histogram distribution of the relative frequency of pores acquired using XRM. The inserted figure is a 3D render of the reconstructed XRM scanned volume with pores color-coded.

loading rate. To protect the MTS machine platens from indentation caused by the AM Al_2O_3 specimens, two polished tungsten carbide (WC) plates were interposed between the loading platens and the specimen. Additionally, high-pressure grease was applied between the protective plates and the AM Al_2O_3 specimens to mitigate

friction and allow unrestricted lateral movement. The dynamic tests were conducted using a modified SHPB setup adapted for testing brittle materials [154, 155] with an incident bar and a transmission bar with a diameter of 12.7 mm and a length of 1016 mm and 914 mm, respectively, which are made of the same hardened maraging steel (Service Steel America C-350) with density, elastic modulus, yield strength, and Poisson's ratio of 8080 kg/m^3, 200 GPa, 2.68 GPa, and 0.29. To protect the end of the bars from being indented by the hard AM Al_2O_3 ceramics and to minimize stress concentration during testing, two impedance-matched Ti-6Al-4V titanium alloy jacketed tungsten carbides were placed between the interfaces of the SHPB bars and specimens. High-pressure grease was employed between the protective platens and the specimen to mitigate frictional effects and decrease lateral force during specimen deformation. The SHBP testing setup was equipped with an ultra-high-speed camera (Shimadzu HPV-X2) to record the dynamic tests at a rate of 2 million FPS. In this SHPB apparatus, two strain gauges (Micro 184 Measurements CEA-13–250UN-350) are attached to the bars to gather incident and transmission strain signal data. The transmission strain signal ($\epsilon_t(t)$) was employed to determine the stress-time response of the material [101]:

$$\sigma(t) = \frac{A_0}{A_s} E_0 \epsilon_t(t), \tag{4.1}$$

where, A_0 (m^2) and A_s (m^2) represent the cross-sectional areas of the bar and specimen, respectively, and E_0 (N/m^2) denotes the elastic modulus of the bar material [32, 55, 99]. The experimentally captured stress-time histories were used to quantitatively validate the micromechanical model. The experimental testing setups are more detailed in our previously published research work [30, 34, 99]. As shown in Fig. 4.1(b), the grain size distribution and crystallographic orientations were characterized by the EBSD analysis (Oxford INCA, Bruker Quantax, 20 KV) to be fed into the micromechanical model. Accordingly, from Fig. 4.1(c), the grain size follows a log-normal distribution with a mean value of 0.91 µm and a standard deviation of

0.55 µm – the average grain size was computed as 2.94 µm. Additionally, to estimate the pores in the as-received AM alumina, XRM analysis was conducted, where scans were performed using a ZEISS Xradia Versa 620 machine with an X-ray voltage of 100 kV at 14.02 W for a total of 1601 projections, with a resolution of 0.5275 µm per voxel. After scanning, image processing software (Dragonfly Pro 2.0) was used for the 3D reconstruction of the AM alumina. Fig. 4.1(d) represents the histogram of the relative frequency of the volume of pores in the material from the XRM examination. It is observed that the pores are evenly distributed throughout the AM ceramic with a log-normal size distribution with an average of 0.07 µm and a standard deviation of 0.1 µm – the average pore size was computed as 1.3 µm. The data was used to incorporate porosity in the RVE model which will be further discussed in the Section 4.3.3.

4.3.2 Numerical methods: RVE generation and loading conditions

The polycrystalline microstructure of the AM alumina was reproduced by Neper software using the Voronoi tessellation algorithm [221] where the log-normal grain size distribution by the EBSD analysis (see Fig. 4.1(c)) was used as the input. Here, the effect of printing orientation [30] was not considered in the micromechanical models since no reflection of such effect (i.e., microscale phenomena/features in direct association with the layer-by-layer printing process) was observed in the EBSD maps and SEM images of the material, particularly concerning the 25 µm length size of the RVE models. As shown in Fig. 4.2(a), the polycrystalline-based geometry was imported into the Abaqus/CAE environment to incorporate the porosity and grain orientations measured by the XRM and EBSD analysis, respectively. Regarding the shape of the voids in the EBSD maps (see Fig. 4.1(b)) and the XRM reconstruction (see Fig. 4.1(d)), the voids were simplified as spheres in the RVE model. Note that the shape and orientation of pores are likely to influence the initiation and propagation of

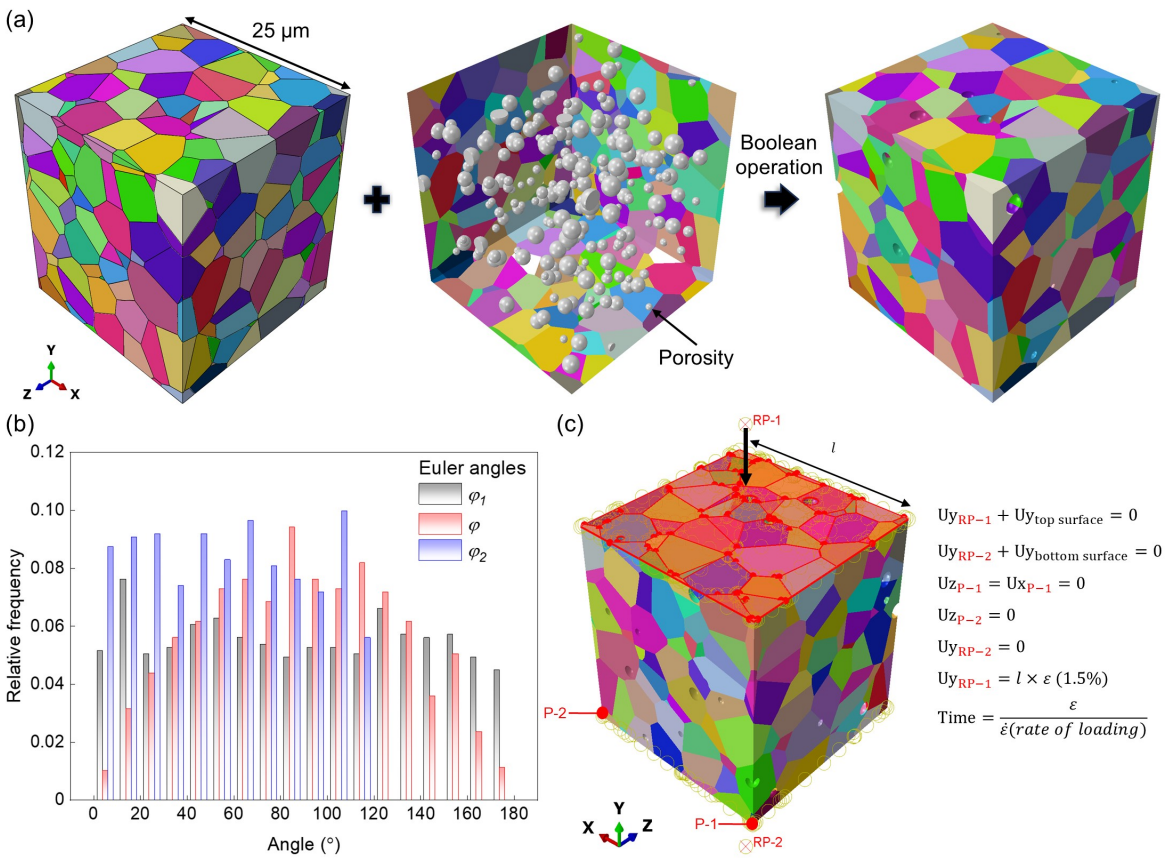

Fig. 4.2: RVE model reconstruction: (a) The polycrystalline model of the material is first generated based on the grain size distribution in Neper software. Next, spherical-shaped pores with a log-normal size distribution with an average of 0.07 µm and a standard deviation of 0.1 µm are generated to reach a volume fraction of 2.5%. The porous polycrystalline RVE is then produced by the Boolean operation in Abaqus/-CAE. (b) The histogram of the Euler angles obtained from the EBSD analysis used as inputs for assigning grain orientations in Abaqus/CAE. (c) The mixed-kinematic boundary condition is applied to the RVE by defining equations between the reference points and the surfaces.

damage in the material [222] due to the variation in local stress concentrations around the pores and the interaction between adjacent pores [223]. Since the current work is focused on the overall strain rate-dependent failure behavior of the material, the role of different pore morphologies is not investigated in this study. A Python script was developed, by which randomly distributed spheres with a randomly assigned equivalent diameter based on the pore size distribution in Fig. 4.1(d) were generated (see the white spheres in Fig. 4.2(a)) to reach a void volume fraction (VVF) of $\sim 2.5\%$ in

accordance with the XRM analysis. Next, the porous polycrystalline RVE of the AM alumina was produced through a Boolean operation by which the spheres were cut from the original geometries by Neper software, as shown in Fig. 4.2(a). The pores were allowed to cross the grain boundaries as the same phenomenon is observed in the EBSD maps (see black spots in Fig. 4.1(b)). Here, an RVE size of 25 µm was selected as was found to meet the convergence condition of stress-time response, and this is later discussed in Section 4.4. Fig. 4.2(b) shows the distribution of the measured Euler angles (ϕ_1,ϕ,ϕ_2) that were incorporated into the RVE model. To assign the grain orientations, the three Eulerian angles (ϕ_1,ϕ,ϕ_2) captured from the EBSD analysis (see Fig. 4.2(b)) are defined as a $n \times 3$ matrix, where n is the number of sets of Eulerian angles. Next, by having n sets of the three Eulerian angles, n number of local coordinate systems is defined that are oriented with respect to the global coordinate system (XYZ), as shown in Fig. 4.2(c). Subsequently, each grain ($\sim$ 300 grains) is randomly attributed to one of the n local coordinate systems, based on which the elastic stiffness tensor (D_{ijkl}, see Eq. (4.3)) of the grain is defined. The process of incorporating crystallographic orientations in the RVE models was automated by a Python script, as detailed in the Algorithm (i.e., Fig. 4.3).

The RVEs were loaded under uniaxial compression using an Abaqus/Explicit FE solver and a mixed static-kinematic boundary condition [217]. As shown in Fig. 4.2(c), the lateral boundary surfaces were free to deform while the top and bottom surfaces were coupled to the reference points, namely RP-1 and RP-2, respectively, for the Y-direction degree of freedom (DOF). X-direction and Z-direction DOFs of these two surfaces remained free to allow lateral expansion. Here, the RP-1 was used to apply the compressive load on the RVE in the form of a displacement inducing a nominal axial strain of 1.5% considering the fracture strain of the material, while the RP-2 was restricted in the Y direction. To prevent rigid body motion, two corners of the bottom face denoted by P-1 and P-2 were restricted as shown by the equations noted in Fig. 4.2(c). Here, to induce the experimentally measured strain rate, the loading

```
import numpy as np
import math
from part import *
from material import *
from section import *
from assembly import *
from step import *
from interaction import *
from load import *
from mesh import *
from optimization import *
from job import *
from sketch import *
from visualization import *
from connectorBehavior import *
# Definition of the Eulerian angles as a matrix of n × 3
AM = np.array([[φ1_1,Φ_1,φ2_1],[φ1_2,Φ_2,φ2_2], # Repeat for each row])
# Automating the assignment of the grain orientations
for 0 ≤i ≤Number of grains do
    # Definition of local coordinate system
    (1): MatrixRy_Phi1 = [[math.cos(AM[i][0]),0,math.sin(AM[i][0])],[0,1,0],[-
      math.sin(AM[i][0]),0,math.cos(AM[i][0])]];
    (2): MatrixRy_PHI = [[math.cos(AM[i][1]),-
      math.sin(AM[i][1]),0],[math.sin(AM[i][1]),math.cos(AM[i][1]),0],[0,0,1]];
    (3): MatrixRy_Phi2 = [[math.cos(AM[i][2]),0,math.sin(AM[i][2])],[0,1,0],[-
      math.sin(AM[i][2]),0,math.cos(AM[i][2])]];
    (4): P_a = [[1],[0],[0]];
    P_b = [[0],[1],[0]];
    (5): Phi1_PHI = np.dot(MatrixRy_Phi1,MatrixRy_PHI);
    RotM = np.dot(Phi1_PHI,MatrixRy_Phi2);
    (6): P_a_t = np.dot(RotM,P_a);
    P_b_t = np.dot(RotM,P_b);
    (7): mdb.models['Your Model
      Name'].parts['Grains-'+str(i+1)+"].DatumCsysByThreePoints(
      coordSysType=CARTESIAN, name='Datum csys-Gr-'+str(i+1)+", origin=(0.0, 0.0, 0.0),
      point1=(P_a_t[0][0], P_a_t[1][0], P_a_t[2][0]), point2=(P_b_t[0][0], P_b_t[1][0],
      P_b_t[2][0])) ;
    (8): CSYS_ID = mdb.models['Your Model
      Name'].parts['Grains-'+str(i+1)+"].features['Datum csys-Gr-'+str(i+1)+"].id ;
    # Attributing the local coordinate system to a grain
    (9): mdb.models['Your Model Name'].parts['Grains-'+str(i+1)+"].MaterialOrientation(
      additionalRotationField=", additionalRotationType=ROTATION_NONE, angle=0.0 ,
      axis=AXIS_3, fieldName=", localCsys= mdb.models['Your Model
      Name'].parts['Grains-'+str(i+1)+"].datums[CSYS_ID], orientationType=SYSTEM,
      region=mdb.models['Your Model
      Name'].parts['Grains-'+str(i+1)+"].sets['Set-Grains_'+str(i+1)+"],
      stackDirection=STACK_3)
end
```

Fig. 4.3: Incorporation of the grain orientations into the RVE model.

time was defined as (Time = $\frac{\epsilon}{\dot{\epsilon}(rate\ of\ loading)}$) while considering a strain of 1.5%. To reduce the computational cost for all the simulated strain rates, a fixed mass-scaling parameter was applied to the RVE model to increase the stable time increment to be in the order of 10^{-8} s to avoid artificial effects as a strain-rate-dependent constitutive model (i.e., the JH2-V model) was used here [55, 217]. For the quasi-static loading with the Abaqus/Explicit FE solver, the ratio of the kinetic energy to the internal energy of the model is typically recommended to be less than 10% in the literature [224–226]. In our simulations, this ratio of the RVE model was monitored to be below 5% throughout the course of quasi-static loading up to the failure point with the applied mass scaling parameter. Note that this ratio increases upon failure due to the brittle fracture and rapid propagation of damage in the model. Regarding the complex modeled microstructure with porosity, the RVE was discretized by tetrahedron-shaped C3D4 elements with a mesh size of 0.35 µm following a mesh convergence study (see Fig. 4.5(c) and (d) and Fig. 4.13). The Digital Research Alliance of Canada clusters were used to run the micromechanical models by parallel computing using 64 cores that led to a runtime of $\sim$ 24 hours and $\sim$ 8 hours for quasi-static and dynamic loading, respectively, for the models with the converged element size of 0.35 µm.

4.3.3 Theoretical framework

In this section, the theoretical framework of the constitutive models to account for the transgranular and intergranular failure mechanisms in the micromechanical model by the JH2-V model and the CZM approach, respectively, is outlined. The JH2-V model was implemented by a VUMAT subroutine in Abaqus/Explicit FE solver.

The JH2-V material model

The JH2-V model was originally proposed by Simons et al. [40, 47] as a modified version of the widely used softening plasticity JH2 model that is commonly used

for ceramic materials [42]. In the JH2-V model, the spall strength of the material ($\mathrm{T}(\dot{\epsilon_P})$) is linked to the rate of the equivalent plastic strain ($\dot{\epsilon_P}$) through a viscosity parameter (η) and this leads to a strain rate-dependent yield function that allows mesh regularization in addition to capturing the strain rate-dependent behavior of the ceramic material. Additionally, the original formulation of the fracture strain in the JH-2 model is revised in the JH2-V model to be a function of the hydrostatic pressure ($\mathrm{P}(\sigma)$) to better account for the asymmetry in damage growth rate in ceramic materials under tension and compression. In the current work, the original JH2-V model was modified to account for the EBSD-based Eulerian angles (ϕ_1,ϕ,ϕ_2) that are geometrically assigned to the grains in the model. To do so, the elastic stress components are calculated by the generalized Hooke's law for linear elastic anisotropic materials:

$$\sigma_{ij} = D_{ijkl}\epsilon_{kl}, \tag{4.2}$$

$$D_{ijkl} = \begin{bmatrix} 497 & & & & & \\ 163 & 497 & & & & \\ 116 & 116 & 501 & & sym & \\ 22 & -22 & 0 & 147 & & \\ 0 & 0 & 0 & 0 & 147 & \\ 0 & 0 & 0 & 0 & 22 & 167 \end{bmatrix} \tag{4.3}$$

where σ_{ij}, ϵ_{kl}, and D_{ijkl} denotes the elastic stress tensor, elastic strain tensor, and elastic stiffness matrix of each grain, respectively. Here, the elastic stress components in Eq. (4.2) are calculated in the local coordinate system of the grain by which the elastic stiffness tensor (D_{ijkl}) is spatially oriented, hence accounting for the crystallographic texture of the material. The components of D_{ijkl} for Al_2O_3 are taken from the work by Falco et al. [216] – the unit is in GPa. In the JH2-V model, the normalized strength of the brittle material is defined as an analytical function of the hydrostatic pressure, spall strength, and an accumulative scalar damage parameter as:

$$\sigma^* = \sigma_i^* - D\left(\sigma_i^* - \sigma_f^*\right), \tag{4.4}$$

$$\sigma_i^* = A\left(p^* + T^*(\dot{\bar{\epsilon}}_p)\right)^N, \text{ and} \tag{4.5}$$

$$\sigma_f^* = B\left(p^*\right)^M, \tag{4.6}$$

where σ_i^*, σ_f^*, and D represent the normalized intact strength, the normalized fractured strength, and the accumulated damage, respectively. $\sigma^* = \frac{\sigma}{\sigma_{HEL}}$ and σ_{HEL} is the equivalent stress at the Hugoniot elastic limit; $p^* = \frac{p}{p_{HEL}}$ and $T^* = \frac{T}{p_{HEL}}$ is the normalized pressure and tensile hydrostatic strength (i.e., the spall strength), respectively, and p_{HEL} is the pressure at the HEL. A, B, M, and N are empirical constants to be calibrated for the material. The spall strength of the material ($\mathrm{T}(\dot{\epsilon_P})$) is regularized as a function of the equivalent plastic strain rate ($\dot{\bar{\epsilon}}_p$) and this results in a rate dependent yield surface in the JH2-V model (see Eq. (4.8)). In the JH2-V model, T is correlated to $\dot{\bar{\epsilon}}_p$ as:

$$T(\dot{\epsilon}_p) = T(\dot{\lambda}) = \begin{cases} T_0 + \eta\dot{\lambda}, & \text{for } \dot{\lambda} < \dot{\lambda}_t \\ T_t(1 + \frac{\eta\dot{\lambda}_t}{T_t}(\ln\dot{\lambda}/\dot{\lambda}_t)), & \text{for } else \end{cases} \tag{4.7}$$

where T_0, η, and $\dot{\bar{\epsilon}}_p^T$ represent the reference spall strength; the viscosity parameters, and the transitional equivalent plastic strain rate, respectively. The $\dot{\bar{\epsilon}}_p^T$ is leveraged to automatically adjust the size of the failure zone at higher strain rates. When the yield surface of the JH2-V model ($\Phi\left(\sigma, D, \dot{\bar{\epsilon}}_p\right)$) is met, D begins to grow from 0 to 1 as a function of the equivalent plastic strain ($\bar{\epsilon}_p$) as:

$$\Phi\left(\sigma, D, \dot{\bar{\epsilon}}_p\right) = \sigma_q - \sigma_{HEL}\sigma^*, \tag{4.8}$$

$$\sigma_q = \sqrt{\frac{3}{2}(\sigma_{ij} - \sigma_{kk}\delta_{ij})(\sigma_{ij} - \sigma_{kk}\delta_{ij})}, \tag{4.9}$$

$$\dot{D} = \frac{\dot{\bar{\epsilon}}_p}{\bar{\epsilon}_p^f\left(p\right)}, \text{ and} \tag{4.10}$$

$$\bar{\epsilon}_p^f(p) = \begin{cases} \bar{\epsilon}_p^{min} & \text{if } p(\sigma) < p_t \\ \frac{p(\sigma)-p_t}{p_c-p_t}\left(\bar{\epsilon}_p^{max} - \bar{\epsilon}_p^{min}\right) + \bar{\epsilon}_p^{min}, & p_t < p(\sigma) < p_c \\ \bar{\epsilon}_p^{max} & p(\sigma) > p_c \end{cases}, \tag{4.11}$$

where σ_q is the von Mises stress calculated based on the orientation-dependent elastic stress tensor of the grain (see Eq. (4.2)), $\bar{\epsilon}_p^f$ is the equivalent plastic strain at failure; $\bar{\epsilon}_p^{min}$, $\bar{\epsilon}_p^{max}$, p_t, and p_c are the constants to define the transitional behavior of the ceramic material from a brittle to a ductile mode with the increase in hydrostatic pressure [47] – these parameters are experimentally determined, involving spall [15] and plate impact [227] tests. In this study, these constants are taken from the literature on Al_2O_3 ceramics. When failure is triggered in the material (i.e., $\Phi\left(\sigma, D, \dot{\bar{\epsilon}}_p\right) > 0$, see Eq. (4.8)), an iterative Newton-Raphson algorithm [55] is used to update σ_q, and internal variables (i.e., $\dot{\bar{\epsilon}}_p$, D, and ΔP) via an Euler-backward integration scheme [90]. A summary of the iterative algorithm for updating the stress components and internal variables upon the initiation of failure is given in the Algorithm (i.e., Fig. 4.4).

Input: Trial anisotropic elastic stresses $(\sigma_{ij}^{t+\Delta t})$, $\bar{\epsilon}_p^t$, D^t, Δt

Output: $\Phi\left(\sigma_q^{t+\Delta t}, D^{t+\Delta t}, \dot{\bar{\epsilon}}_p^{t+\Delta t}\right) \leq 0$, $\sigma^{t+\Delta t}$, $\Delta\bar{\epsilon}_P^{t+\Delta t}$, $D^{t+\Delta t}$

Initialization $\Delta\bar{\epsilon}_P^{(i)} = 0$, $\dot{\bar{\epsilon}}_p^{(i)} = \frac{\Delta\bar{\epsilon}_P^{(i)}}{\Delta t} = 0$, $k = 1000$, $i = 0$, $\delta = 10^{-8}$;

while $i \leq k$ **do**

  (1): $H^{(i)} = [D_{ijkl}^{-1} + \Delta\bar{\epsilon}_P^{(i)}\frac{\partial^2\phi}{\partial\sigma^2}]^{-1}$, where D_{ijkl} is the elastics stiffness tensor (see Eq. (3));

  (2): $\beta^{(i)} = (\frac{\partial\phi}{\partial\sigma})^T H^{(i)}[\frac{\partial\phi}{\partial\sigma} + \Delta\bar{\epsilon}_P^{(i)}\frac{\partial^2\phi}{\partial\sigma\partial\bar{\epsilon}_p} + \frac{\Delta\bar{\epsilon}_P^{(i)}}{\Delta t}\frac{\partial^2\phi}{\partial\sigma\partial\dot{\bar{\epsilon}}_p}] - \frac{\partial\phi}{\partial\bar{\epsilon}_p} - \frac{1}{\Delta t}\frac{\partial\phi}{\partial\dot{\bar{\epsilon}}_p}$;

  (3): $\Delta\bar{\epsilon}_P^{(i+1)} = \Delta\bar{\epsilon}_P^{(i)} + \frac{\phi^{(i)}}{\beta}$;

  (4): $D^{t+\Delta t} = \frac{\bar{\epsilon}_p^t + \Delta\bar{\epsilon}_P^{(i+1)}}{\bar{\epsilon}_p^f}$;

  (5): $\sigma_{t+\Delta t}^{(i+1)} = \sigma_t + D_{ijkl}[\Delta\epsilon - \Delta\bar{\epsilon}_P^{(i+1)}\frac{\partial\phi}{\partial\sigma}]$;

  (6): $\phi^{(i+1)} = \phi\left(\sigma_{t+\Delta t}^{(i+1)}, \bar{\epsilon}_p^t + \Delta\bar{\epsilon}_P^{(i+1)}, \dot{\bar{\epsilon}}_p^{t+\Delta t}\right)$;

  (7): $i = i + 1$;

  if $|\phi^{(i+1)}| < \delta$ **then**

    leave the loop;

  end

end

Fig. 4.4: The Newton-Raphson iterative algorithm used for the JH2-V model.

To account for the bulking effect [43] after damage initiation, the hydrostatic pres-

sure in the material is related to the volumetric strain (μ) via a polynomial equation of state as:

$$p = \begin{cases} K_1\mu + K_2\mu^2 + K_3\mu^3 + \Delta p, & \text{if } \mu > 0 \ , \\ K_1\mu & \text{if } \mu \leq 0 \end{cases} \tag{4.12}$$

$$\Delta p_{t+\Delta t} = -K_1\mu_{t+\Delta t} + \sqrt{\left(K_1\mu_{t+\Delta t} + \Delta P_t\right)^2 + 2\beta K_1 \Delta U}, \tag{4.13}$$

$$\Delta U = U_t - U_{t+\Delta t}, \text{ and} \tag{4.14}$$

$$U = \frac{\sigma_y^2}{6G}, \tag{4.15}$$

where K_1, K_2, and K_3 are the bulk modulus, and the material constants, respectively. U, σ_y, and G denote the internal energy, the flow stress, and the shear modulus, respectively. Δp represents the bulking-induced increment of pressure when damage progression is triggered (i.e., $D > 0$) that is calculated based on the conversion of elastic energy to potential hydrostatic energy (see Eq. (4.13)), where β determines the fraction of conversion. Table 4.1 summarizes the constants of the JH2-V model assigned to the grains of the AM Al_2O_3 micromechanical model in this study. These quantities are selected from the literature on Al_2O_3 ceramics. Note that the parameters accounting for the strain rate-dependent behavior, including η, and $\dot{\bar{\epsilon}}_p^T$ are required to be tuned as material constants. Here, the corresponding values are selected from the previous studies on Al_2O_3 ceramics [40, 55]. More details on the effect of these parameters on the failure behavior of ceramics are available in previous studies by Zaiemyekeh et al. [55] and Simons et al. [40]. To capture the transgranular failure mechanism, an equivalent plastic strain ($\bar{\epsilon}_p$) $\geq 20\%$ at the integration points of elements [55, 217, 225] was considered as the criterion for the deletion of fully damaged elements (i.e., an element with $D = 1$ at the integration points).

Cohesive zone model (CZM)

In this study, the surface-based CZM approach with a bi-linear traction-separation law was employed to model the grain boundaries and capture the intergranular failure

Table 4.1: The JH2-V model constants used for the AM Al_2O_3 ceramic in this study. Note that the value of density (i.e., ρ) is measured in the current study.

Parameter	Value	Unit	Source
A	0.93	-	[109]
B	0.31	-	[109]
N	0.6	-	[109]
M	0.6	-	[109]
K_1	226	GPa	[55]
K_2	0	GPa	[109]
K_3	0	GPa	[109]
ρ	3800	kg/m^3	—
T_0	0.2	GPa	[40]
HEL	6.25	GPa	[40]
P_{HEL}	7.5	GPa	[40]
β	1	-	[40]
η	25×10^{-6}	GPa·s	[55]
$\dot{\lambda}_t$	10000	s^{-1}	[55]
ϵ_p^{max}	0.496	-	[40]
ϵ_p^{min}	1.5×10^{-4}	-	[40]
p_c	3.02	GPa	[40]
p_t	-0.17	GPa	[40]

mechanism; the surface-based method was selected due to a lower computational cost when compared to the element-based CZM approach. Here, the interfacial failure is triggered when a quadratic function of the tractions acting on the grain interfaces is met as [228]:

$$\left(\frac{\langle t_n \rangle}{t_n^0}\right)^2 + \left(\frac{t_s}{t_s^0}\right)^2 + \left(\frac{t_t}{t_t^0}\right)^2 = 1, \tag{4.16}$$

where t_n, t_s, and t_t represent the normal and in-plane components of the traction vector on the interfaces, respectively. The corresponding interfacial strength is denoted by t_n^0, t_s^0, and t_t^0, respectively. Upon the satisfaction of the failure criterion (see

Eq. (4.16)) at interfacial nodes, the traction components begin to linearly deteriorate based on a scalar damage parameter (D):

$$t_i = (1 - D)\, t_i^*, \quad i \in [\, n, s, t\,], \tag{4.17}$$

$$D = \begin{cases} 0 & \text{if } \delta_m^{max} \leq \delta_m^0 \\ \frac{\delta_m^f \left(\delta_m^{max} - \delta_m^0\right)}{\delta_m^{max} \left(\delta_m^f - \delta_m^0\right)} & \text{if } \delta_m^0 < \delta_m^{max} < \delta_f^{max} \\ 1 & \text{if } \delta_m^{max} \geq \delta_f^{max} \end{cases}, \text{ and} \tag{4.18}$$

$$\delta_m^{max} = \sqrt{\langle \delta_n^2 \rangle + \delta_s^2 + \delta_t^2}, \tag{4.19}$$

where t_i^* represent the undamaged traction components, which are calculated based on the elastic traction-separation law. The effective separation at the onset of debonding and complete failure is denoted by δ_m^0 and δ_m^f, respectively. δ_m^{max} is the effective separation at the interfacial nodal points that are calculated based on the Euclidean norm of the relative separation components (see Eq. (4.19)). Note that to simplify the model and avoid adding additional numerical constants to be calibrated, the CZM in the current work does not explicitly account for strain rate-sensitive behavior of grain boundaries that is likely to be caused by grain boundary sliding mechanisms [229], dislocation motions [230], and amorphous/glassy phases at the interfaces [231]. Additionally, a strain rate-dependent CZM [232] may require experimental data on the rate-sensitive response of the grain boundaries which is not available in the literature on AM Al_2O_3 ceramics, to the best of the author's knowledge. Table 4.2 summarizes the CZM constants used for modeling the grain boundaries of the AM Al_2O_3 in the current work. Here, the CZM constants are calibrated based on a trial-and-error process to achieve the best match with the experimental stress-time histories under both quasi-static and dynamic loading while considering the experimental measurements on the grain boundary properties of Al_2O_3 ceramics in the literature [216, 233]. The effect of the grain boundary properties by the CZM approach are also discussed in detail in Section 4.4.5 in the following. It is worth noting that a frictionless CZM approach is taken in the current work, which is also employed in previous studies on

Table 4.2: The CZM constants used for the AM Al_2O_3 ceramic in this study. Note that these values are calibrated in the current study.

Parameter	Value	Unit
K_{nn}, K_{ss}, K_{tt}	2E5	GPa mm^{-1}
t_n^0, t_s^0, t_t^0	2	GPa
δ_m^f	45×10^{-6}	mm

polycrystalline modeling of Al_2O_3 ceramics [216]. The effect of friction between the grains on the failure behavior of polycrystalline ceramics is numerically well-studied in the literature [234, 235].

4.4 Results and discussion

In this section, first, the effect of the geometric parameters, including the RVE length size, element size, and randomness of RVE generation on the predicted stress-time history was investigated under both quasi-static and dynamic strain rates in Section 4.4.1. In Section 4.4.2, the developed micromechanical model was validated with the experimental results in terms of stress-time histories (i.e., quantitative validation) and microscale failure mechanisms observed in post-mortem SEM images (i.e., qualitative validation). Here, for the first time in the literature, the intergranular and transgranular failure mechanisms were quantified by using the model to inform on the initiation and evolution of failure in the AM material. Upon validation, the micromechanical model was exercised to study the effect of grain crystallographic orientations on the material failure behavior, and this is described in Section 4.4.3. Next, the model was further extended to inform on the effect of porosity (i.e., VVF) and grain boundary properties on the strain-rate-dependent failure progression in the material in Section 4.4.4 and Section 4.4.5, respectively. Lastly, in Section 4.4.6, the model was employed to investigate the correlation between the grain size and the failure behavior of the AM Al_2O_3.

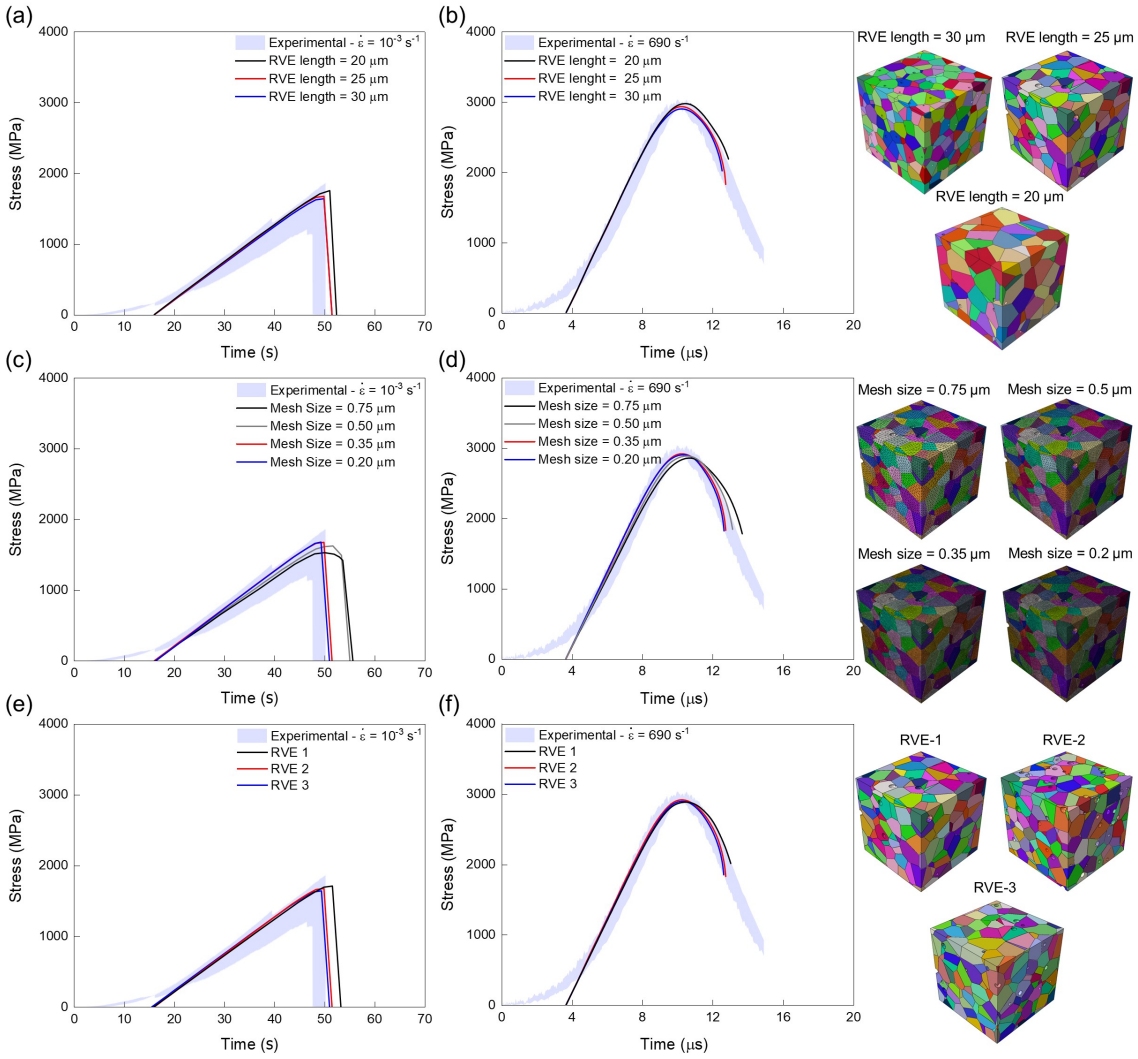

Fig. 4.5: The effect of the RVE size and element size on the predicted stress–time response of the AM alumina under quasi-static and dynamic uniaxial compression. (a, b) The effect of the RVE length size on the predicted response under quasi-static and dynamic loading, respectively. An RVE size of 25 µm was selected for further studies. (c, d) The effect of the element size on the predicted stress-time response under quasi-static and dynamic loading, respectively, with the RVE size of 25 µm. (e, f) The effect of RVE realizations on the predicted stress-time response under quasi-static and dynamic loading, respectively, with the RVE size of 25 µm. Note that repeated experimental results (five specimens for each loading rate) are shown as the shaded areas on the sub-figures.

4.4.1 The effect of the geometric parameters on the model predictions

The variation in the model prediction of the strain-rate-dependent stress–time history of AM Al_2O_3 was explored based on the RVE length size, mesh size, and random RVE realizations. Fig. 4.5(a) and (b) show the predicted stress-time curves using an RVE size of 20 µm, 25 µm, and 30 µm under quasi-static and dynamic compression, respectively. Note that the data from the repeated experiments are presented by the shadow areas. With the increase in RVE length size, the peak stress and softening rate of the stress-time history are mainly affected likely due to a slower growth rate of the failure mechanisms in RVEs with a smaller length size. As the RVE size increased from 25 µm to 30 µm, the predicted stress-time responses merged under both quasi-static and dynamic loading. Accordingly, we selected the RVE size of 25 µm due to a lower computational cost compared to 30 µm-long RVE for further studies. This selected size results in a ratio of RVE length to the average grain size of more than 5, which demonstrates an acceptable statistical representation of the material microstructure [236, 237]. Shown in Fig. 4.5(c) and (d) is the variation in the predicted stress-time curves with the change in mesh size from 0.75 µm to 0.2 µm under quasi-static and dynamic loading, respectively. Concerning the converging pattern of stress-time curves and the corresponding runtime presented in the Appendix. A, a mesh size of 0.35 µm was selected to make a balance between the computational cost and model results (i.e., predicting an element size-independent stress-time history). The effect of micromechanical model variability on the prediction of stress-time response is shown in Fig. 4.5(e) and (f) under quasi-static and dynamic compression, respectively. Here, three random realizations, namely RVE-1, RVE-2, and RVE-3 are generated with the same grain size/porosity size distributions, VVF, and length size; the major difference is associated with the spatial distribution of grains and their crystallographic orientations that are randomly assigned. As seen, the stress-time histories of the random RVEs negligibly differ in terms of the peak stress (i.e., quasi-

static loading (see Fig. 4.5(e))) and post-peak softening regime (i.e., dynamic loading (see Fig. 4.5(f))), and this demonstrates the reliability of the current micromechanical model for further studies on the correlations between the microstructural features and macroscale response of the AM Al_2O_3.

4.4.2 Experimental validation and quantification of the failure mechanisms

The micromechanical model was validated by the experimental data on the material under quasi-static (i.e., $\dot{\epsilon} = 10^{-3}$ s^{-1}) and dynamic (i.e., $\dot{\epsilon} = 690$ s^{-1}) uniaxial compression. Fig. 4.7 (a) and (b) compare the numerical stress-time history with that of the experiments (i.e., the shaded areas representing the outcomes from repeated tests five times) under quasi-static and dynamic loading, respectively. At the early stages of loading, the macroscale experimental stress-time curves increase non-linearly due to either the closure of pre-existing defects/microcracks [238] or the establishment of equilibrium conditions for specimen deformation. Subsequently, (i.e., after $\sim$ 15 s and $\sim$ 5 µs under quasi-static and dynamic loading, respectively), the experimental curves start following a linear trend, as expected from Al_2O_3 as a linear elastic material. As such, an effect is absent in the microscale simulations, the numerical curves increase linearly from the beginning. Accordingly, the numerical stress-time histories are shifted from the origin along the time axis to provide a more realistic comparison with the experiments. The micromechanical model reproduces a stress rate (i.e., the slope of the stress-time history upon equilibrium) that agrees with that of the experiments across strain rates. Additionally, the predicted peak stress and softening behavior are consistent with those experimentally captured under different strain rates.

Next, the validated RVE model was leveraged for the quantification of the growth history of failure mechanisms in the AM Al_2O_3. The transgranular mechanism (TGM) is quantified based on the fraction of fully damaged elements (i.e., $D = 1$ (see

Eq. (4.10)) and $\bar{\epsilon}_p \geq 0.2$ [55, 225] at the integration points), and the intergranular mechanisms (IGM) is quantified based on the fraction of fully debonded nodes (i.e., $D = 1$ (see Eq. (4.18))) at the grain boundaries as:

$$TGM = \frac{\sum_{k=1}^{V_d} V_k}{\sum_{k=1}^{V_t} V_k}, \text{ and} \tag{4.20}$$

$$IGM = \frac{\sum_{k=1}^{N_d} N_k}{\sum_{k=1}^{N_t} N_k}, \tag{4.21}$$

where V_d and V_t are the number of fully damaged elements and the total number of elements, respectively; N_d and N_t are the number of fully debonded nodes and the total number of interfacial nodes, respectively. A Python script was developed to calculate the above-mentioned fractions for the TGM and IGM over the course of loading (e.g., see the curves in red and blue in Fig. 4.7 (a) and (b)). The developed script is detailed in the Algorithm (i.e., Fig. 4.6).

From Fig. 4.7 (a) and (b), regardless of the strain rate, the quantification framework shows that the intergranular mechanism grows exponentially and at a higher rate compared to the transgranular mechanism, playing a key role in the strength of the material. Under dynamic loading, as shown in Fig. 4.7 (b), the transgranular mechanism grows at a slower rate compared to the quasi-static condition (e.g., comparing the magnitude of transgranular mechanism at a stress level of $\sim$ 1800 MPa that corresponds to the quasi-static peak stress) and this results in a higher strength in comparison with the quasi-static condition (see Fig. 4.7 (a)). The model captures such an effect due to the incorporation of the strain-rate-dependent spall strength of the material using the viscosity parameter (see Eq. (4.7)). Additionally, the intergranular mechanism is saturated under dynamic loading upon reaching the peak point, which is attributable to the increasing growth of damage within the grains by the transgranular mechanism, relaxing the load being transferred through the boundaries. Fig. 4.7(c) shows the time-resolved images of the evolution of failure mechanisms by the micromechanical model corresponding to the lettered points in

```
from visualization import *
# Reading the output file
odb = openOdb(path='Your ODB File.odb');
myAssembly = odb.rootAssembly;
frameRepository = odb.steps['Step-1'].frames;
# Creating lists for storing data
list_Interface_NEle = [];list_ParCrack_NEle = [];list_Ave_Dam = [];list_Node_Number = [];
# Creating output text files
output_file_Interface_NEle = open('File Name.dat','w');
output_file_ParCrack_NEle = open('File Name.dat','w');
output_file_Ave_Dam = open('File Name.dat','w');
output_file_Nodes = open('File Name.dat','w');
# Defining region of interest of the model
myregion=myAssembly.elementSets['Element Set of Whole RVE']
# Quantification process
for 0 ≤i ≤Number of frames do
    (1): frameStat1 = frameRepository[i].fieldOutputs['CSQUADSCRT
      General_Contact_Domain'].getSubset(position=NODAL).values ;
    (2): frameStat2 = frameRepository[i].fieldOutputs['STATUS'].getSubset(region=myregion).values ;
    (3): frameSDV10 = frameRepository[i].fieldOutputs['SDV10'].getSubset(region=myregion,
      position=CENTROID).values ;
    (4): frameIVOL = frameRepository[i].fieldOutputs['EVOL'].values ;
    (5): Tot_Vol = 0.; Tot_Stat1 = 0.; COUNTER=0;CSQUADSCRTValue=0.; Tot_SDV10 = 0.;
      Avg_SDV10 = 0.; Nnodes = 0;
    (6): for v in frameStat1 do
        CSQUADSCRTValue = v.data;
        if CSQUADSCRTValue ≥ 0.999 then
            COUNTER=COUNTER+1;
        end
    end
    (7): for v in frameStat2 do
        Tot_Stat1+=v.data;
    end
    (8): for 0 ≤i ≤len(frameIVOL) do
        Tot_Vol+=frameIVOL[i].data;
    end
    (9): for 0 ≤i ≤len(frameSDV10) do
        Tot_SDV10+=frameSDV10[i].data * frameIVOL[i].data;
    end
    (10): Avg_SDV10 = Tot_SDV10/Tot_Vol ;
    Nnodes = len(frameStat1) ;
    (11): list_Interface_NEle.append(COUNTER)  list_ParCrack_NEle.append(Tot_Stat1)
      list_Ave_Dam.append(Avg_SDV10)  list_Node_Number.append(Nnodes)
end
# Writing the output text files
for 0 ≤i ≤len(list_Interface_NEle) do
    (1): output_file_Interface_NEle.write('%16.8E '% (list_Interface_NEle[i]));
    (2): output_file_ParCrack_NEle.write('%16.8E '% (list_ParCrack_NEle[i]));
    (3): output_file_Ave_Dam_NEle.write('%16.8E '% (list_Ave_Dam_NEle[i]));
    (4): output_file_Nodes.write('%16.8E '% (list_Node_Number.[i]));
end
output_file_Interface_NEle.close(); output_file_ParCrack_NEle.close(); output_file_Ave_Dam.close();
output_file_Nodes.close()
```

Fig. 4.6: Quantification of the growth history of failure mechanisms by the model.

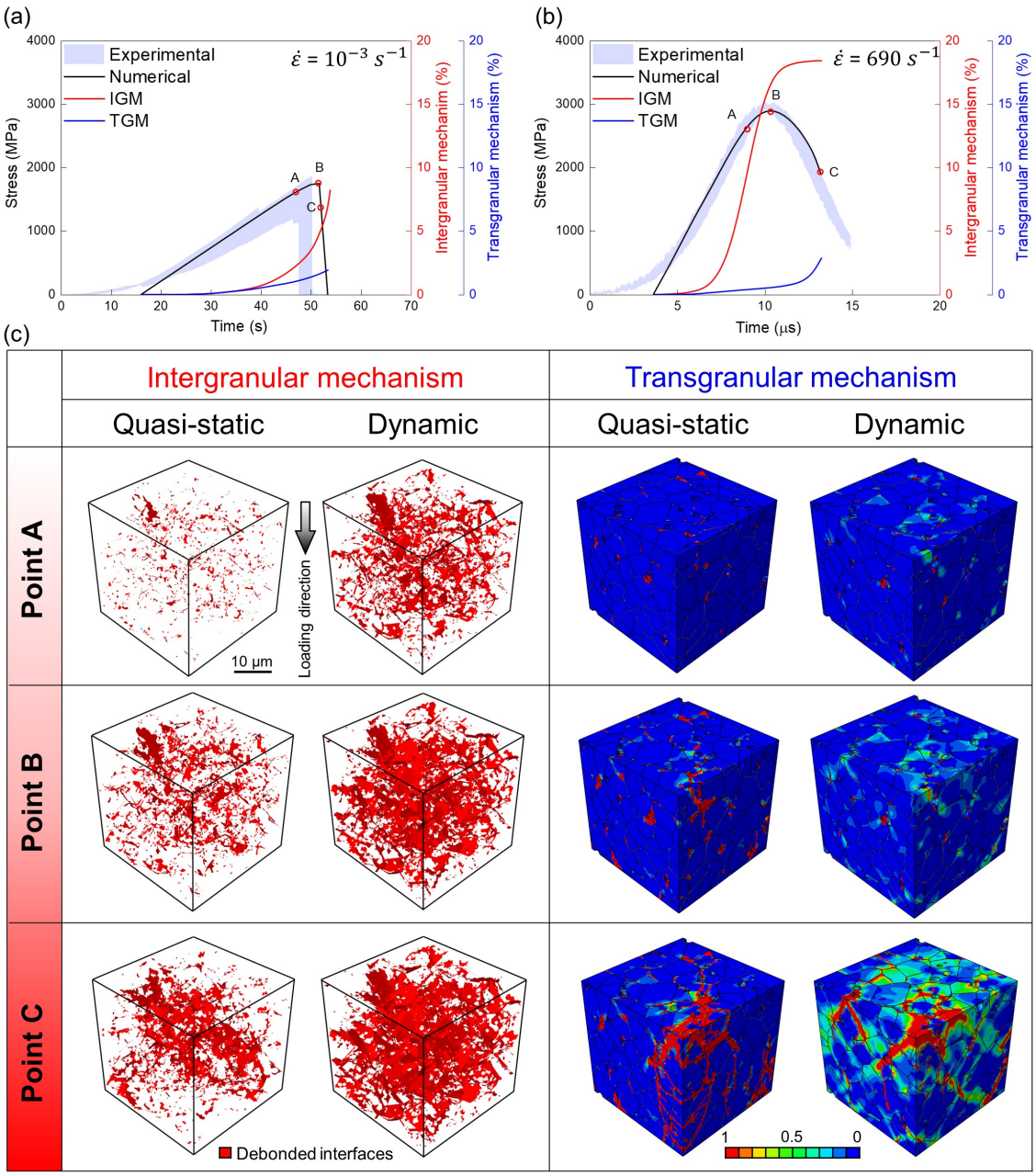

Fig. 4.7: Quantitative validation of the micromechanical model with the experimental stress-time histories and quantification of the failure mechanisms by the validated model: (a) Quasi-static loading at a strain rate of $10^{-3}s^{-1}$, (b) Dynamic loading at a strain rate of 690 s^{-1}. (c) Time-resolved images of the evolution of failure mechanisms in the material by the model corresponding to the lettered points on the stress-time curves. IGM and TGM refer to the intergranular and transgranular mechanisms, respectively.

Fig. 4.7(a) and (b). At point A before the peak stress, the intergranular mechanism is nucleated dispersedly under both quasi-static and dynamic loading. With the in-

crease in load, it coalesces into a localized $\sim 45^{\circ}$ plane under quasi-static loading (see the last row in Fig. 4.7(c) at point C) while it grows with a distributed pattern under dynamic loading. This is likely attributable to the reverberation of stress waves under dynamic loading that induce tension-dominated stress states at the grain boundaries [217], thereby decreasing the localization of the failure pattern. In addition, the micromechanical model shows that the transgranular mechanism is activated either at the grain boundaries or primarily around the pores (see the areas in red Fig. 4.7(c) under the transgranular mechanism column) due to the stress concentration.

As the load increases (i.e., at Point B and Point C), preceded by the intergranular mechanism, the transgranular mechanism propagates in the material, which accelerates the loss of stress-bearing capacity. Similar to the intergranular mechanism, the transgranular mechanism emerges with a localized pattern under quasi-static loading when compared to the diffusive pattern under dynamic loading, and this localization of failure contributes to the sharp fall of stress-bearing capacity under quasi-static compression.

According to the post-mortem fractography analysis shown in Fig. 4.8, the size of fragments is smaller under quasi-static loading when compared to those of the dynamic loading which represents the localization effect under quasi-static loading, and this is consistent with the numerical visualization of failure mechanisms (see Fig. 4.7(c)). The high-magnification SEM images demonstrate the presence of both intergranular (i.e., non-smooth areas showing the grain interfaces) and transgranular (i.e., the flat areas showing the cleavage facets and river-like patterns) mechanisms across strain rates, where the former is noticeable under high strain rate loading which agrees with that of the micromechanical model predictions shown in Fig. 4.7(b) and (c). Additionally, regardless of the strain rate, pores annotated by the yellow arrows are frequently observed on the fracture surfaces. Correspondingly, as shown in the time-resolved images in Fig. 4.7(c), the model also confirms that pores act as the sites for the nucleation of damage and crack propagation in the AM Al_2O_3 ceramic.

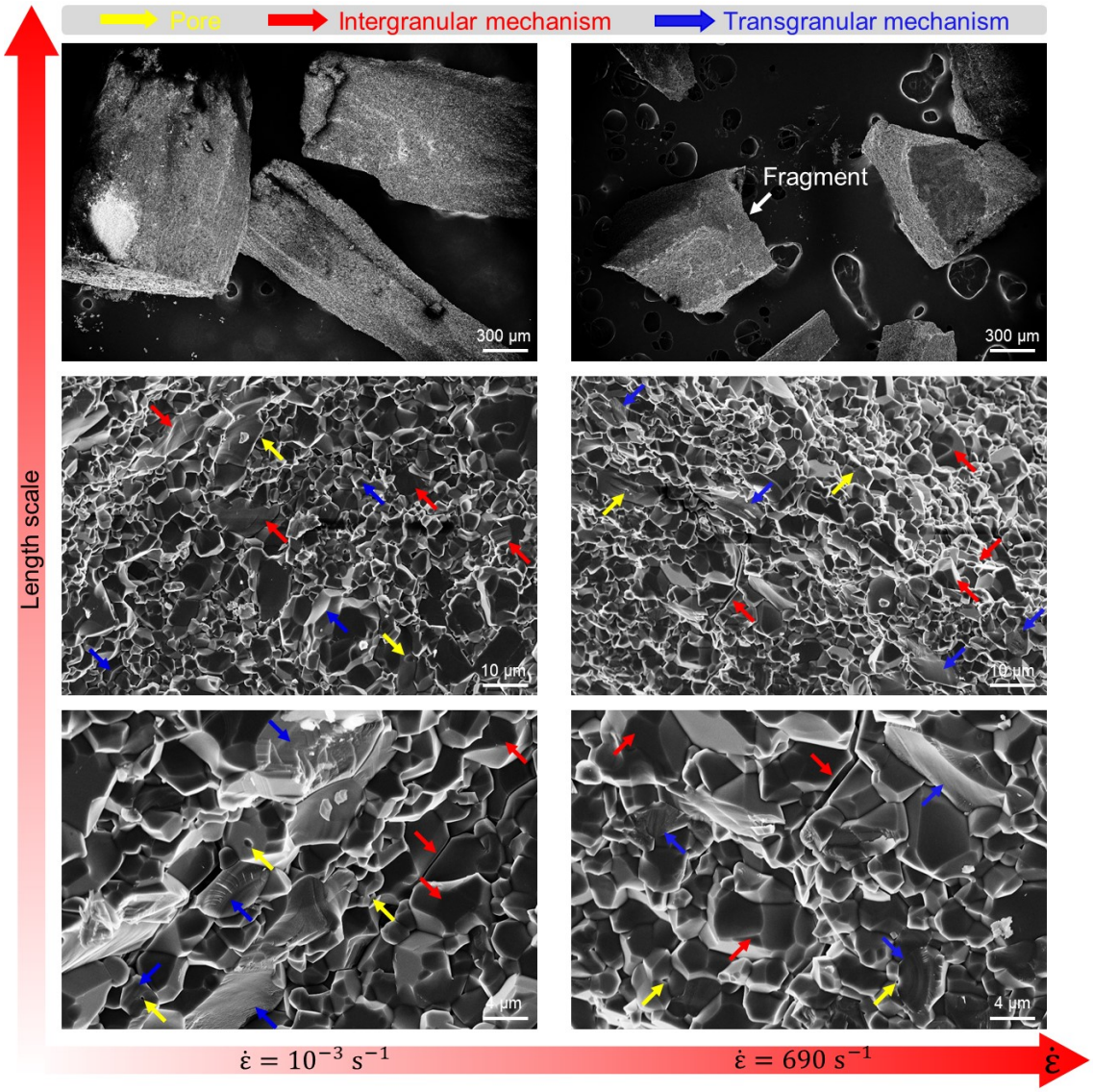

Fig. 4.8: Low- and high-magnification SEM imaging of the AM Al_2O_3 after being tested under strain-rate-dependent uniaxial compression showing the presence of failure mechanisms and pores on the fracture surfaces.

4.4.3 The effect of crystallographic orientations on the failure behavior

The validated micromechanical model was leveraged to inform on the role of grain crystallographic orientations on the failure behavior of the material across strain rates. Fig. 4.9 (a) and (b) compares the stress-time history and the quantified evolution of failure mechanisms of the material involving the crystallographic orientations

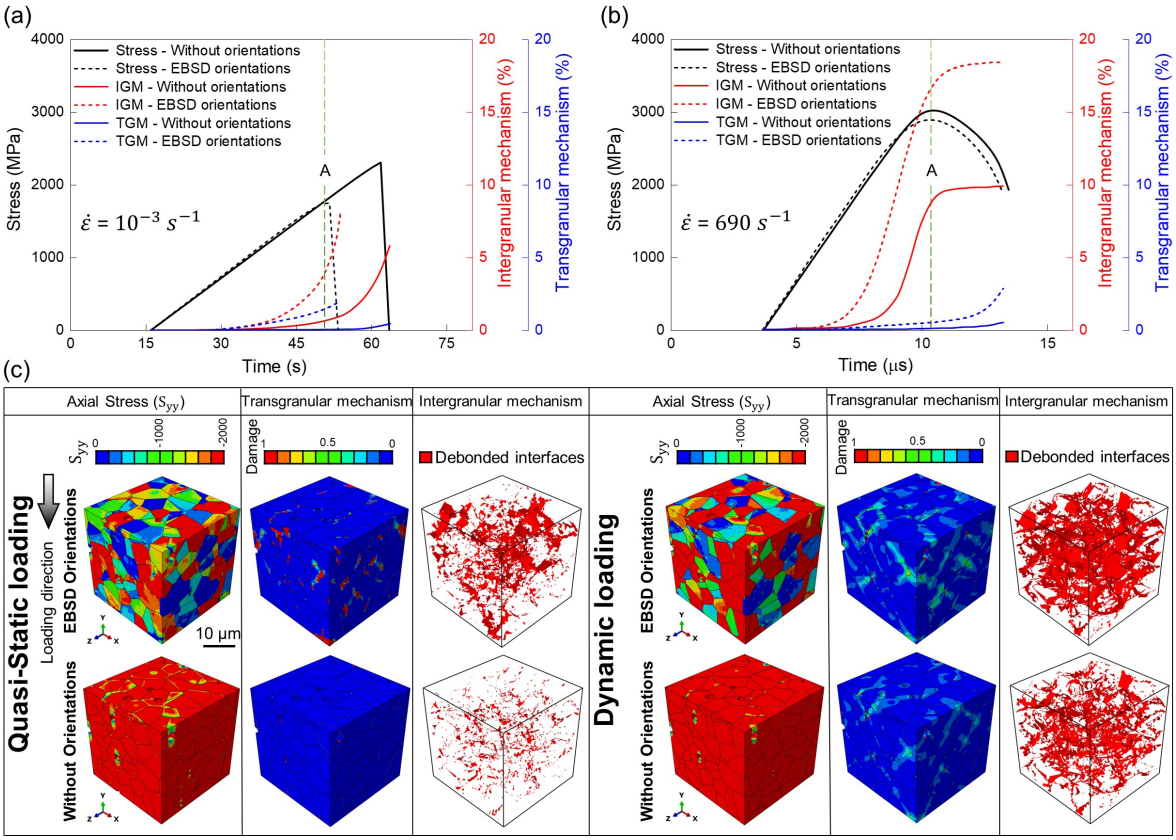

Fig. 4.9: The effect of grain crystallographic orientations on the failure behavior of the material in terms of the stress-time histories and the quantified evolution of failure mechanisms under (a) quasi-static loading, and (b) dynamic loading. (c) The effect of grain orientations on the spatial contour of axial stress and distribution of failure mechanisms corresponding to the time point specified by letter A on the stress-time curves. IGM and TGM refer to the intergranular and transgranular mechanisms, respectively.

obtained from the EBSD analysis and those of the isotropic condition (i.e, no random orientations are assigned and the anisotropic elastic stiffness tensor in Eq. (4.3) downgrades to an isotropic elastic stiffness tensor). Here, the EBSD-captured Eulerian orientations were initially assigned to the RVE model by different random assignments (see Algorithm (**??**)), which resulted in no apparent differences in the predicted stress-time and failure mechanisms histories. Accordingly, only one set of the stress-time histories and profiles of IGM and TGM is reported for the model with the EBSD orientations in Fig. 4.9 (a) and (b). The existence of grain orientations increases the growth rate of the intergranular mechanism under both quasi-static and

dynamic loading which accelerates the loss of material integrity, and this promotes an earlier initiation and faster growth of the transgranular mechanism. Consequently, the earlier activation and the higher evolution rate of the failure mechanisms induced by the crystallographic orientations result in lower strength of the AM Al_2O_3, as shown in Fig. 4.9 (a) and (b) under quasi-static and dynamic loading, respectively. The quasi-static strength of the material seems to be more noticeably affected by the grain orientations when compared to that of the dynamic loading, and this is likely caused by a higher increase in the magnitude of failure mechanisms under quasi-static loading owing to the localization effect. Fig. 4.9(c) shows the effect of grain orientations on the axial (i.e., parallel to the loading direction) stress contour, and the spatial distribution of failure mechanisms at the time point lettered by A. In the model with the grain orientations from the EBSD analysis, the axial stress distribution pattern becomes highly heterogeneous, inducing a mismatch between the stress state of grains at the boundaries, which results in the earlier activation of the intergranular mechanism as quantitatively represented in Fig. 4.9(a) and (b). This numerical outcome is in agreement with previous studies [239] on the effect of grain boundary misorientation angles, lowering the grain boundary strength due to the mismatch between the atoms on either side of the boundaries. In our study, however, the grain boundary strength values (i.e., t_n^0, t_s^0, and t_t^0) are constant and not explicitly a function of the misorientation angles. Here, the effect of grain boundary misorientations are captured through the incorporation of the Eulerian angles of grains that manifest themselves as stress state mismatches at the interfaces (see Fig. 4.9(c) and Supplementary Video S1) which are reflected into the calculation of traction components t_n, t_s, and t_t (see Eq. (4.16)) and relative displacements δ_n, δ_s, δ_t (see Eq. (4.19)) in the CZM approach. Supplementary Video S1 shows the failure progression in the material under quasi-static compression in terms of the consideration of the grain crystallographic orientations.

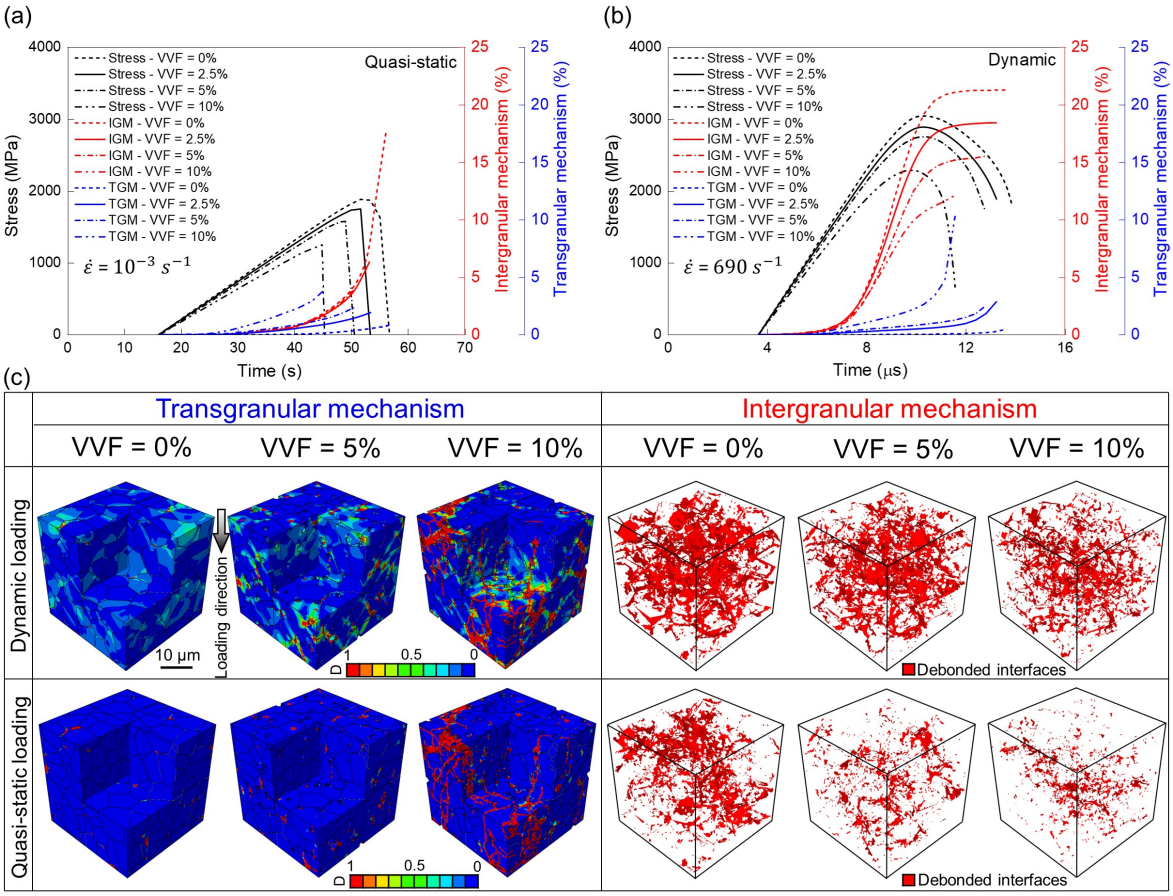

Fig. 4.10: The effect of VVF on the stress-time response and the evolution of failure mechanisms of the AM Al_2O_3 material under (a) quasi-static loading, and (b) dynamic loading by the micromechanical model. (c) Time-resolved images of the evolution of intergranular and transgranular failure mechanisms of the material with different VVFs corresponding to the peak stress shown in Fig. 4.10(a) and (b). IGM and TGM refer to the intergranular and transgranular mechanisms, respectively.

4.4.4 The effect of porosity on the failure behavior

The validated micromechanical model was leveraged to study the role of porosity (i.e., VVF) in the failure behavior of the AM Al_2O_3 ceramic. Fig. 4.10(a) and (b) show the effect of porosity on the stress-time response and history of failure mechanisms under quasi-static and dynamic loading, respectively, by varying the VVF from 0% (i.e., a pore-free microstructure) to 10%. The maximum bound of 10% was selected based on the frequently reported values on VVF in AM Al_2O_3 ceramics [30, 181, 182]. The slope of the stress-time response decreases with the increase in VVF and this is related

to the increase in the compliance of the material with a higher porosity. Under quasi-static compression, the increase in VVF affects the transgranular mechanism through an earlier activation and a higher growth rate, as shown in Fig. 4.10(a), leading to a lower strength of the material. The growth profile of the intergranular mechanism, however, is marginally altered with the variation in VVF under quasi-static loading. As shown in Fig. 4.10(c), a higher VVF corresponds to a higher number of pores in the microstructure that act as the nucleation sites for the transgranular mechanism (e.g., comparing the transgranular damage spatial distribution in the microstructure with 0% VVF with that of the 10% VVF), thereby a more noticeable shift in the history of transgranular mechanism in comparison with that of the intergranular mechanism with the rise in porosity. This porosity-induced bias in affecting the growth history of the failure mechanisms more pronounced under quasi-static loading when compared with dynamic loading, which is likely due to the localization effect and the absence of the strain rate-strengthening effect (see Eq. (4.7)) – e.g., the transgranular mechanism precedes the intergranular mechanism under quasi-static loading when VVF increases to 10% (see Fig. 4.10(a)). Under dynamic loading, with the rise in VVF, the transgranular mechanism growth rate is amplified while that of the intergranular mechanism decreases. The latter is attributable to the VVF-induced accelerated growth rate of the transgranular mechanism that correspondingly dampens the growth of failure at the grain interfaces (i.e., the intergranular mechanism) due to the deterioration of microstructural integrity as a result of damage propagation within the grain boundaries (see Fig. 4.10(c)). The Supplementary Video S2 draws a comparison between the evolution of failure in the material with 10% VVF with that of the one with 0% VVF. Similar to the quasi-static loading, the higher growth rate of the transgranular mechanism promotes a lower dynamic compressive strength in the AM Al_2O_3 with higher porosity in addition to increasing the post-peak softening rate, as shown in Fig. 4.10(b).

4.4.5 The effect of grain boundary properties on the failure behavior

In this section, the validated micromechanical model was employed to explore the effect of grain boundary properties – represented by the concept of the CZM – on the history of failure mechanisms and the stress-time response of the material. To do so, as shown in Fig. 4.11(a), the interfacial properties were varied in terms of the strength of the grain boundaries (i.e., t_i^0 in Eq. (4.16)) annotated by Case 1, and the effective separation at complete failure (i.e., δ_m^f in Eq. (4.19)) of the interface annotated by Case 2. As shown in Fig. 4.11(b) for Case 1, under quasi-static loading, with the increase in strength of grain boundaries from 1 GPa to 2 GPa, the intergranular mechanism is initiated later and grows slower, which consequently delays the initiation and growth of the transgranular mechanism, leading to the increase in the material strength.

As the strength of grain boundaries rises from 2 GPa to 3 GPa, however, the material strength is slightly enhanced. This suggests the existence of a threshold for the grain boundary strength, beyond which the material strength is marginally improved due to the propagation of damage within the grains by the transgranular mechanism. Note that these current values of the strength of grain boundaries are realistic considering the experimental measurements on conventionally made Al_2O_3 ceramics [216, 233].

The same trend of behavior with the increase in interfacial strength is also predicted by the micromechanical model when the strain rate increases to the dynamic regime, as shown in Fig. 4.11(c) for Case 1. Concerning Case 2, with the increase in effective separation at complete failure from 10 nm (i.e., an elastic-brittle response) to 22 nm, the material strength increases under both quasi-static and dynamic loading as shown in Fig. 4.11(b) and (c), respectively, due to the deaccelerated growth of the intergranular failure mechanism that subsequently dampens that of the transgranular mechanism. However, with the further increase in effective separation at

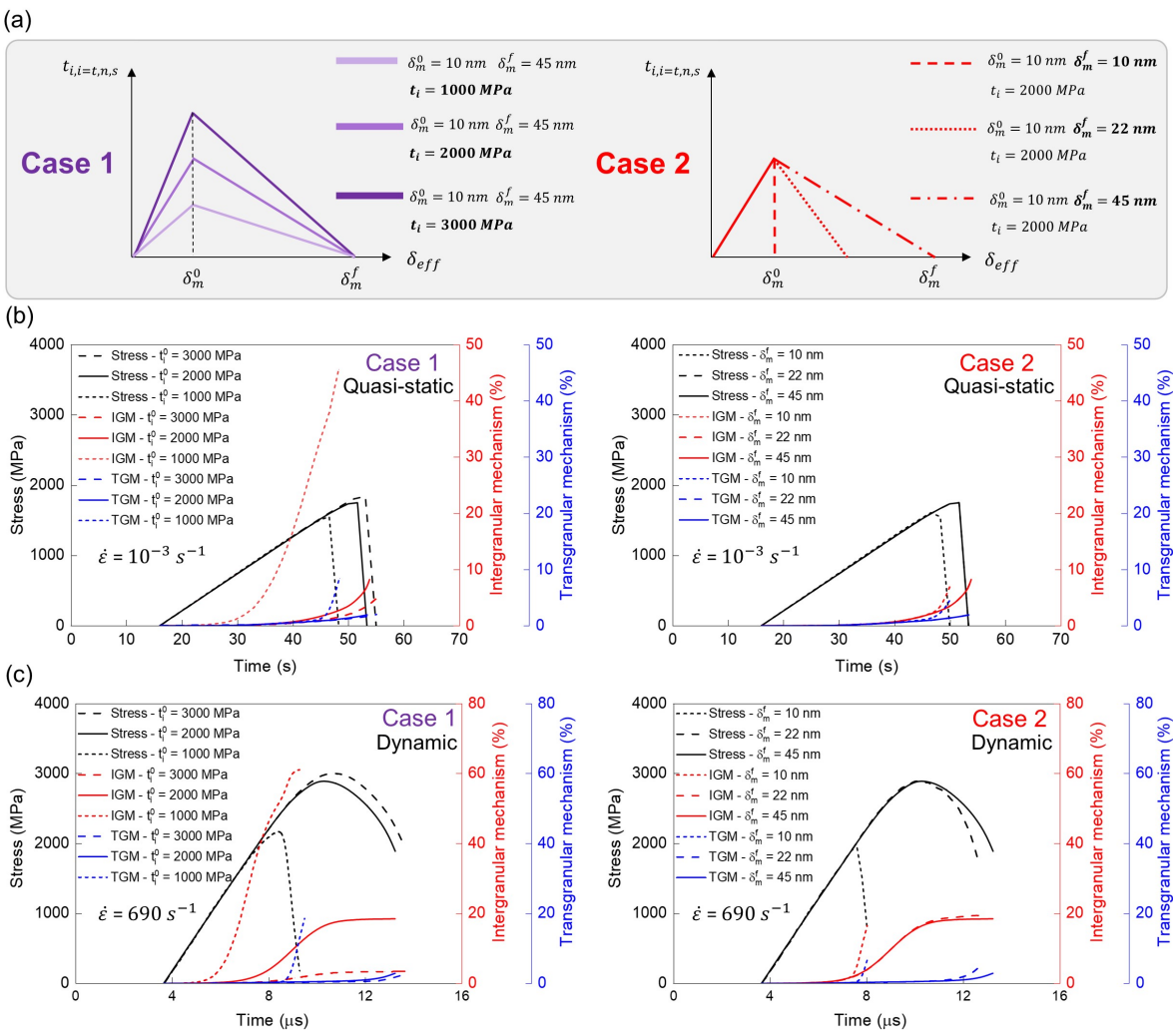

Fig. 4.11: The effect of interfacial properties on the stress-time response and the evolution of failure mechanisms of the AM Al_2O_3 material. (a) The variations considered in the interfacial properties in terms of the grain boundary strength (i.e., Case 1) and the effective separation at the complete failure of the interface (i.e., Case 2). (b) Quasi-static loading, and (c) Dynamic loading. IGM and TGM refer to the intergranular and transgranular mechanisms, respectively.

complete failure (i.e., from 22 nm to 45 nm), the strength of the material remains unaltered across strain rates, while only the softening rate of the dynamic stress-time response decreases due to the growth of the transgranular mechanism with a lower rate (see Case 2 in Fig. 4.11(c)). Such an effect is not manifested in the quasi-static stress-time response (see Case 2 in Fig. 4.11(b)), where the corresponding curves are overlapped) likely due to the absence of the strain rate-strengthening effect. Similar

to the grain boundary strength represented by Case 1, the model shows the existence of a threshold for the fracture toughness of grain boundaries – which was represented by the effective separation at complete failure – beyond which the material failure behavior is slightly affected. Eventually, comparing the strain-rate-dependent stress-time histories from Case 1 with those of Case 2, the model shows that the strength of grain boundaries plays a more important role than the fracture toughness of grain boundaries in improving the mechanical behavior (e.g., strength) of the AM Al_2O_3 ceramics.

4.4.6 The effect of grain size on the failure behavior

The micromechanical model is further extended to study the effect of grain size on the mechanical behavior of the material under uniaxial compression within this section. To do so, polycrystalline RVEs with an average grain size of 6 µm and 10 µm were reconstructed, incorporating a VVF of 2.5% similar to the RVE of the AM Al_2O_3 that is fabricated and tested in the current study. To be consistent with the outcomes of the original 25 µm-long RVE with an average grain size of $\sim$ 3 µm (see Fig. 4.1 (b) and (c)), the new RVEs with the average grain size of 6 µm and 10 µm were generated with a length size of 80 µm, leading to a minimum RVE length size to average grain size of 8, as discussed in Section 4.4.1. These average grain sizes were selected based on the reported values in previous studies on AM Al_2O_3 ceramics [30, 176, 179].

Note that the grain size distribution in the new 80 µm-long RVEs follows the experimentally obtained log-normal pattern (see Fig. 4.1(c)).

As shown in Fig. 4.12(a) and (b) for quasi-static and dynamic loading, respectively, the model predicts the reduction in the slope of the stress-time response from the early stages of loading with the decrease in average grain size. This is likely caused by the higher number of interfaces in the RVE with a smaller grain size that induces more deformability/compliance in the model. Regardless of the strain rate, a smaller average grain size is predicted to amplify the intergranular mechanism while

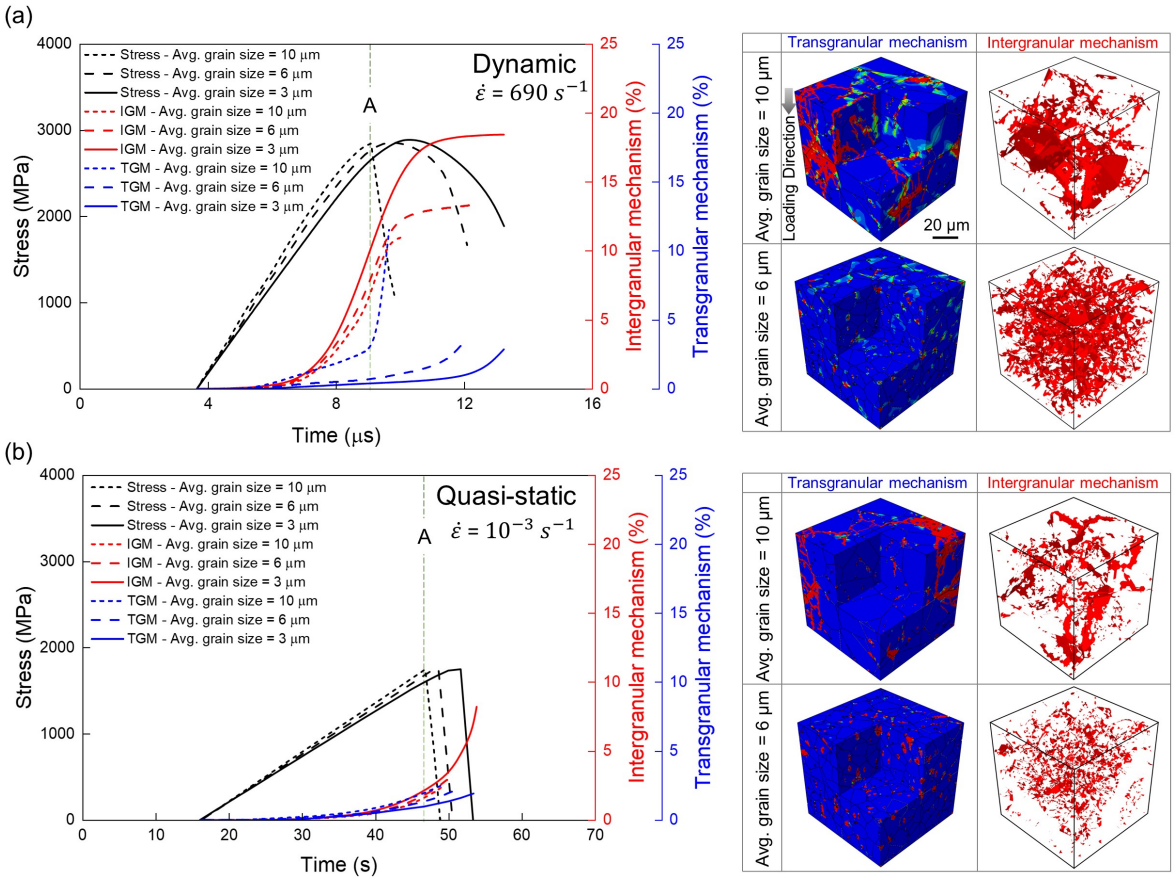

Fig. 4.12: The micromechanical model prediction of the effect of grain size on the stress-time response and growth history of the failure mechanisms of the AM Al_2O_3 ceramic under (a) Quasi-static uniaxial compression, and (b) Dynamic uniaxial compression. IGM and TGM refer to the intergranular and transgranular mechanisms, respectively.

delaying the initiation and dampening the growth rate of the transgranular mechanism; such effects are more pronounced under dynamic loading. The former (i.e., the amplification of the intergranular mechanism) is attributable to the increase in the propensity of interfacial failure in the polycrystalline microstructure with a finer grain size due to the higher number of interfaces while keeping the grain boundary properties unaltered in the model. Regarding the latter (i.e., dampening the transgranular mechanism), a polycrystalline microstructure model with a finer grain size is comprised of a higher number of grains, and correspondingly a higher number of grain boundaries, which increases the damage tolerance of the material by hindering

the coalescence and propagation of transgranular cracks across a higher number of grains and grain boundaries. Accordingly, the growth of transgranular mechanism with a higher rate within the microstructural model with a coarser grain size results in a sharper (i.e., under dynamic loading)/sooner (i.e., under quasi-static loading) fall of stress-bearing capacity after the peak stress when compared to that of the model with a finer grain size, as shown in Fig. 4.12(a) and (b). Additionally, the qualitative images draw a comparison between the spatial distribution of failure mechanisms in the RVEs with the average grain size of 6 µm and 10 µm at the time point lettered by A corresponding to the peak stress of the model with coarser average grain size. As seen, at the same time point, the transgranular mechanism is propagated across the microstructure with an average grain size of 10 µm while it is localized around the pores/interfaces in the RVE with an average grain size of 6 µm under both quasi-static and dynamic loading.

The experimentally measured strength of ceramic materials is shown to typically increase with the decrease in grain size in previous studies [208, 240] – which is analytically expressed by the Hall-Petch relationship [241] for polycrystalline ceramics and metals. The current micromechanical model, however, shows limitations by not replicating such a relationship; the model shows no dependency of compressive strength on the average grain size as shown in Fig. 4.12(a) and (b). This limitation of the model may stem from the following origins: (a) Manufacturing-wise, the grain size and void/defect volume fraction in microstructure are intertwined parameters [30], meaning that VVF is likely to be changed with the variation in grain size, and this effect is neglected in the current model by considering a constant VVF of 2.5% owing to the lack of data. (b) A polycrystalline microstructure with a finer grain size may result in grain boundaries with a higher strength due to decreasing the length size of the grain boundaries as the primary crack initiation sites (i.e., the Griffith law that relates the fracture energy to the square root of flaw size [242]), while size-dependent interfacial properties are not incorporated into the model. This observation suggests

the incorporation of size-dependent mechanical properties [243] or length-scale regularization parameters [244] to enhance the predictability of micromechanical models in future studies.

4.5 Conclusions

The current study developed a 3D microstructure-based model for investigating the failure behavior of AM Al_2O_3 ceramics under quasi-static and dynamic uniaxial compression. Polycrystalline RVEs of the material were generated where the grain size distribution, porosity, and crystallographic orientations obtained from the SEM and EBSD analysis were used as the inputs. A strain-rate-dependent constitutive model was implemented by using a VUMAT subroutine in the Abaqus/FE solver to account for the transgranular mechanism, and the grain boundaries were modeled by a bi-linear CZM approach to capture the intergranular mechanism. The micromechanical model was validated by the experimental stress-time histories and failure mechanisms observed in post-mortem fractography analysis. The key findings of the current study are outlined as:

- The quantification of the growth history of failure mechanisms revealed that the intergranular mechanism plays a key role in determining the material strength across different strain rates.
- The model showed that the growth of the transgranular mechanism at a lower rate under high strain rates leads to the higher strength of the material under dynamic loading conditions.
- The grain crystallographic orientations promote an earlier initiation and faster growth of the intergranular mechanism that subsequently amplifies the growth of the transgranular mechanism, causing a decrease in the material strength.
- The increase in VVF was found to markedly amplify the transgranular mech-

anism due to a higher number of pores acting as the crack nucleation sites, decreasing the material strength under both quasi-static and dynamic loading.

- The model informed on the thresholds for grain boundary strength and fracture toughness, beyond which the material strength experienced marginal enhancements due to the growth of the transgranular mechanism.

- The model showed limitations in capturing the experimentally observed increase in strength with finer grain size, suggesting the incorporation of size-dependent mechanical properties or length-scale regularization parameters to advance the model for future studies.

Overall, the current work provides a better understanding of the relationships between the microstructure (i.e., microstructural features, including grain orientations, VVF, and interfacial properties) and the macroscale mechanical behavior (i.e., material strength and failure progression) of the material that paves the way for the design of AM Al_2O_3 ceramics with higher mechanical performance tailored to specific applications.

4.6 Acknowledgments

This work is supported by the Natural Sciences and Engineering Research Council of Canada (NSERC)(Grant # 2023-04457).

4.7 Appendix: Mesh convergence study

Fig. 4.13 summarizes the mesh convergence analysis in terms of the number of elements associated with each mesh size, and the corresponding computational cost in hours. All the simulations were run on the Graham cluster of the Digital Research Alliance of Canada using 64 cores (2 x Intel E5-2683 v4 Broadwell @ 2.1GHz). As seen, when the mesh size exceeds 0.35 µm, the runtime significantly increases for both

quasi-static and dynamic loading, while the predicted stress-time response remains almost unaltered, as shown in Fig. 4.5(c) and (d). Accordingly, an element size of 0.35 µm was selected for further investigations in the current study.

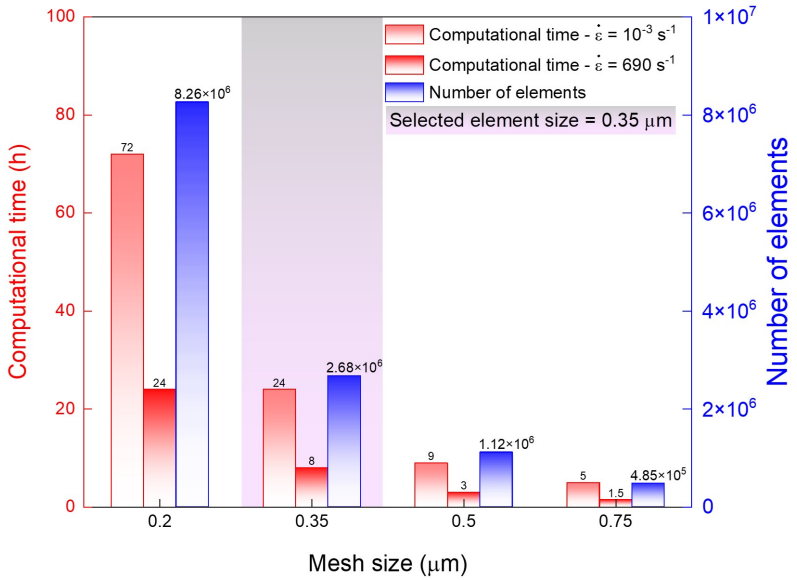

Fig. 4.13: A summary of the mesh convergence study that involves the element size, the number of elements, and the corresponding computational runtime under quasi-static and dynamic loading. The corresponding predicted stress-time responses are presented in Fig. 5.3(c) and (d).

Chapter 5

On the role of stress state in the failure behavior of alumina ceramics via stereolithography: Quasi-static and dynamic loading

Submitted as **Zahra Zaiemyekeh**, Mohammad Rezasefat, Yogesh Kumar, Saman Sayahlatifi, Jie Zheng, Haoyang Li, Dan L. Romanyk, James D. Hogan. "On the role of stress state in the failure behavior of alumina ceramics via stereolithography: Quasi-static and dynamic loading", *Submitted for peer review publication in Ceramics International*, 2024.

5.1 Abstract

This study investigates strain-rate- and stress-state-dependent failure behavior of additively manufactured (AM) alumina (Al_2O_3) ceramics fabricated by the stereolithography (SLA) technique printed in three different orientations. Mechanical testing was carried out under a combined shear-compression and indirect tension stress state using angled specimens and flattened Brazilian Disk (FBD) specimens, respectively, across quasi-static and dynamic strain rates. Ultra-high-speed imaging combined with digital image correlation (DIC) was employed to observe the time-evolving strain field and failure sequence of AM alumina ceramic throughout experiments. It was found

that when the printing orientation (PO) is perpendicular to the loading direction the material shows a higher strength under both stress states, likely due to the layer-by-layer printing process and how the corresponding processing-induced microstructural defects contribute to the damage propagation. Additionally, the results revealed that with the increase in shear strain, the peak stress decreases due to the earlier damage initiation. The fractography analysis showed a higher presence of the intergranular mechanism under quasi-static loading, while a combination of intergranular and transgranular mechanisms was noted under dynamic loading. This study comprehensively informs on the mechanical performance of AM Al_2O_3 ceramics across different stress states and strain rates, which is rarely investigated in the literature, providing implications for model development and design of AM ceramic structures with a tailored mechanical performance.

5.2 Introduction

Given their favorable mechanical properties (e.g., the high strength-to-weight ratio [245], and high hardness [67]), advanced ceramics are widely used in different industrial sectors (e.g., defense [246], aerospace [134], and health applications [133]), where the material is subjected to complex loading conditions, such as extreme pressure (e.g., shock [7]), high strain rate loading [8], and high temperatures [9]. The conventional manufacturing processes of ceramics (e.g., hot pressing [247], and casting [164]) are time-consuming and may require post-sintering processes such as machining [18]. Recently, additive manufacturing (AM) methods such as stereolithography (SLA) [146], selective laser sintering (SLS) [22], fused deposition ceramics (FDC) [138] and binder jet 3D printing (BJ3DP) [248] have emerged as popular manufacturing methods due to their ability to fabricate ceramic structures with high resolution, and high dimensional accuracy with a relatively fine surface finish [249], as well as reduction of raw material usage [24]. Among different AM methods, the SLA technique is widely used due to the advantages of flexibility in the design of customized geometries, and ac-

curacy [18]. This technique is based on the process of photopolymerization, in which a liquid resin is converted into a solid polymer under light irradiation [250]. The solidification process is repeated in a layer-by-layer pattern to produce a 3D geometry, and this (i.e., orientation of the printed layer) may influence the macro-scale failure pattern and the quantitative response (e.g., rate-dependent strength) of the material [30, 31, 186]. The focus of the current study is on investigating the strain-rate- and stress-state-dependent mechanical behavior and failure response of AM alumina (Al_2O_3) ceramics manufactured via SLA methods printed in three different printing orientations (POs).

The mechanical properties of ceramic materials, including hardness and strength increase with the increase in strain rate, making ceramics an ideal material for incorporating into different structures under a wide variety of stress states [26, 201]. As such, the use of ceramics in application requires a thorough understanding of the strain-rate- and stress-state-dependent behavior of the materials [55, 146, 147], particularly for ceramics manufactured by AM methods as emerging materials used for complex geometries [146]. To date, the strain-rate-dependent behavior of conventionally made alumina ceramics has been widely investigated under uniaxial compression and indirect tension stress states [26, 27, 29, 32, 34], while limited efforts have been made toward exploring the rate-dependent mechanical behavior of AM ceramics under compression [30, 31]. For instance, DeVries et al. [31] explored the quasi-static and dynamic mechanical properties of AM alumina manufactured through a pressurized spray deposition process and compared them with those of traditionally manufactured alumina (i.e., AD-995). The AM alumina exhibited a lower quasi-static and dynamic compressive strength due to stress-concentrating porosity that weakened the AM structure, and negligible differences in Vickers hardness when compared to conventionally made alumina ceramics. The same results on Vickers hardness by DeVries et al. [31] were also reported in a separate study by Mariani et al. [144]. In another study by Zaiemyekeh et al. [30] on AM alumina, the PO was found to

minimally affect the strength-strain rate behavior while influencing the macroscale failure pattern. To the best of our knowledge, no studies have sought to investigate the mechanical response and evolution of failure mechanisms of AM ceramics under different stress states (i.e., indirect tension, and a combined shear-compression) across different loading rates, which is the main focus of this paper.

In previous studies on brittle materials, different methods have been proposed to investigate their tensile and combined loading behaviors [32, 34, 59, 84]. The Brazilian disk (BD) [59, 77] and Flatted Brazilian disk (FBD) [32, 79] geometries are commonly employed as indirect tension tests to explore the tensile strength of such materials. In Ji et al. [32], the tensile behavior of CeramTec Alotec 98% alumina was assessed by testing FBD specimens at various strain rates, showing that the peak strength of the material in indirect tension is at least 10 times lower than in compression, and this is attributable to the fundamental physics of the initiation and competition of cracks. In the literature, hydraulic confinement techniques [83, 84] and angled specimen methods [85, 87] have been mainly employed to study the shear-compression behavior of brittle solids. Recently, in a study by Zheng et al. [34], the mechanical response of conventionally made CeramTec ALOTEC 98% alumina under a combined shear-compression stress state was studied using angled specimens (cuboidal specimen with tilting angles between parallel ends of 5°). The strength of the material was found to be lower under the combined shear-compression than compression alone, which is consistent with a published work by Karanjgaokar et al. [251]. In a separate study by Zaiemyekeh et al. [55], it was numerically shown that the presence of shear deformation in angled specimens leads to the earlier activation of damage accumulation, resulting in a lower strength compared to that of uniaxial compression.

Motivated by the limited previous experimental efforts on AM ceramics [30, 31, 143], which primarily focus on the compressive response of the material, this study aims to probe the microstructural characteristics and mechanical behavior of AM alu-

mina ceramics under a wide range of strain rates (i.e., 10^{-4} s^{-1} to 10^{2} s^{-1}) and stress states (i.e., indirect tension and shear-compression). The micromechanical features of the material (e.g., material composition, grain size distribution, and porosity) were characterized through scanning electron microscopy (SEM) equipped with energy dispersion spectroscopy (EDS), electron backscattered diffraction (EBSD), and X-Ray Microscopy (XRM). Following material characterization, the stress-state-dependent behavior of the material was investigated by designing FBD (indirect tension) specimens, and angled specimens for indirect tension, and combined shear-compression stress states, respectively. The specimens are loaded across quasi-static and dynamic rates where ultra-high-speed imaging combined with digital image correlation (DIC) analysis is employed to capture the in-situ failure process and full-field strain measurements. The outcomes of this study for AM alumina are mainly compared with those of the conventionally made AD-98 from the literature [32, 34, 55, 251] in terms of mechanical properties. For the first time in the literature, the outcomes of this study provide insights into the strain-rate- and stress-state-dependent mechanical response and failure behavior of AM alumina ceramics, which has implications for the design and improvement of this novel AM material. Additionally, the datasets provided in this study are foundational for developing and validating microstructure-informed numerical models [190, 217, 252] to be used for establishing microstructure-property-performance relationships applicable to material optimization.

5.3 Experimental methodology

The material used in this study was α-Al_2O_3 ceramic from Lithoz, America, printed via an SLA technique in three different directions (i.e., PO1, PO2, and PO3) as shown in Fig. 5.1. During the SLA process, the laser energy and exposure time for each layer were set to 30 mW/cm^2 and 10 s, respectively. Each printed layer has a height of 25 μm, with a pixel size (DLP XY) of 40 μm. To accommodate sintering shrinkage at room temperature, the specimens were printed 1.235 times larger in the

X–Y plane and 1.275 times larger in the Z direction. Following debinding, all green bodies undergo sintering at 1650°C for 2 hours. To induce a shear-compression stress state in the material, cuboidal specimens with nominal dimensions of 3.5 × 2.7 × 2.3 mm^3, and tilting angles of 12° and 25° were designed (see Fig. 5.1(a), and (b)). The selection of these sizes aims to provide the material with sufficient time to reach stress equilibrium, as discussed in the literature [26, 32, 34, 55]. The choice of a cuboidal shape facilitates DIC analysis on the surface of the specimen during testing to measure strain components and observe the deformation mechanisms activated during loading, which provide insights into the transitional behavior between intact, damaged, and fragmented states of the material. To promote a tension-dominated stress state in the material, the FBD specimens with a diameter of 8 mm and thickness of 4 mm were fabricated following geometries from the literature [32, 94, 98]. Fig. 5.1(c) shows the dimensions and geometry of the FBD (indirect tension) specimen. In the FBD specimens, two parallel flat ends were incorporated at the disk edge to minimize stress concentrations [94, 103], and a thickness-to-diameter ratio of 0.5 was selected to facilitate the formation of a central crack [32, 94]. Additionally, a loading angle of 20° was chosen in accordance with Griffith's strength theory [98], facilitating crack initiation at the center of the disk. This loading angle has also been employed in previously published papers [94, 95].

5.3.1 Material characterization

Material characterization was conducted using SEM (Zeiss Sigma FESEM, 20 kV) equipped with EDS (AZtec software from Oxford Instrument) and EBSD (Oxford INCA, Bruker Quantax, 20 KV) to characterize the microstructure, obtain chemical composition, as well as determine grain size distribution and crystallographic orientation of the grain, respectively, on the polished surface (i.e., 0.25 μm surface finish) of the as-received AM alumina specimens. Shown in Fig. 5.2(a) is an SEM micrograph of the surface of the specimen with hollow spots indicating surface pores likely result-

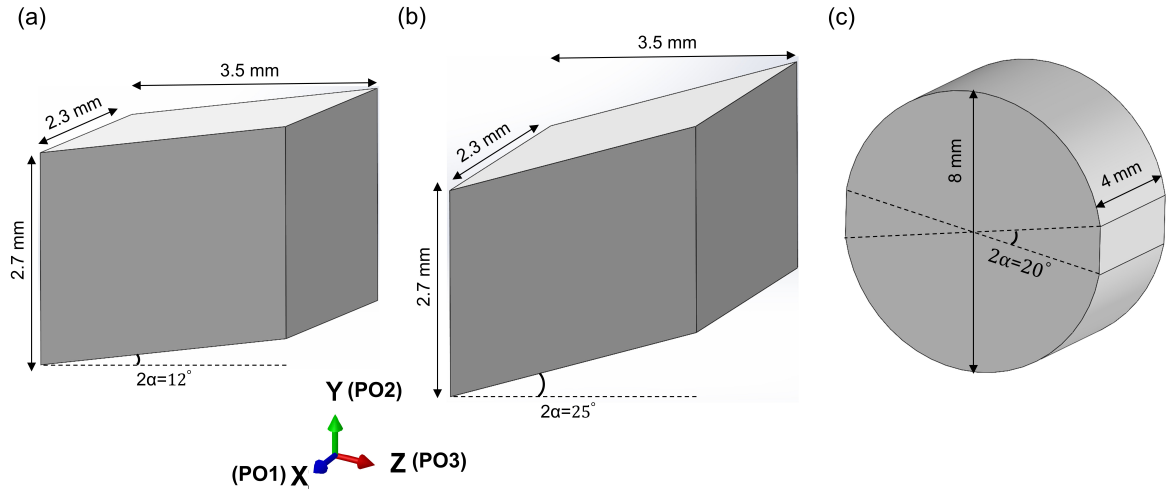

Fig. 5.1: Geometry of AM alumina specimens designed and fabricated for testing the material under different stress states. (a) shear-compression specimen with an angle of 12° for the combined effect of shear and compression. (b) Shear-compression specimen with an angle of 25° for the combined effect of shear and compression. (c) Flattened Brazilian disk (FBD) for inducing tension-dominated failure. Note that the printing orientations (POs) are shown on the coordinate system.

ing from the polishing process. Additionally, in Fig. 5.2(a) the SEM-EDS analysis demonstrates that the material is primarily composed of aluminum (wt.% 53.43) and oxygen (wt.% 46.44) mixed with a trace of Mg (wt.% 0.13). To further analyze the microstructure of the material and characterize the defects (e.g., pores and impurities) in the AM alumina specimens, XRM analysis was applied. XRM scans were conducted using a ZEISS Xradia Versa 620 machine, utilizing an X-ray voltage of 100 kV, power of 14.02 W, and a resolution of $0.5275 \times 0.5275 \times 0.5275$ μm^3 per voxel. Subsequently, image processing software (Dragonfly Pro 2.0) was employed for the 3D reconstruction of the AM alumina. Fig. 5.2(b) represents the histogram of the relative frequency of the pore volume in the material, as observed through XRM examination. The analysis reveals that the pores are uniformly distributed throughout the AM ceramic with a log-normal size distribution with an average of 0.07 μm and a standard deviation of 0.1 μm – the average pore size was computed as 1.3 μm. Next, in Fig. 5.2(c), (d), and (e), the EBSD inverse pole figure (IPF) for all POs obtained

on the X–Y plane was shown. The darker areas within the IPF demonstrate surface damage or pores. The reduced IPF triangle corresponding to these areas indicates the absence of any preferred crystal orientation. As shown in Fig. 5.2(c), (d), and (e), the grain size distribution for all POs follows a log-normal distribution. The average grain size was calculated as 2.94 $\pm$1.94 μm for PO1, 2.92 $\pm$1.91 μm for PO2, and 2.9 $\pm$1.9 μm for PO3. These values are smaller than the grain sizes reported in the previously published paper on other AM alumina (e.g., $\sim$9.68 μm [179], $\sim$12 μm [31], and $\sim$25 μm [149]).

5.3.2 Mechanical testing setup

To explore the effect of strain rate and stress state on mechanical behavior and failure response of AM alumina ceramic, specimens were tested under a variety of strain rates (10^{-4} s^{-1} to 10^{2} s^{-1}) and stress states (i.e., shear-compression, and tensile) using a material testing system (MTS) 810 machine and split-Hopkinson Pressure Bar (SHPB) apparatus coupled with high-speed imaging and DIC to monitor the strain maps and failure sequence of the specimen during the experiments. The description of these setups is detailed in previously published papers by the authors [30, 32, 34, 55]. Before testing, random speckle patterns were sprayed on the surface of the specimens using an airbrush with a 0.15 mm diameter nozzle to facilitate DIC analysis. The reader may refer to [26, 30, 34] for further details on the DIC setup. Experiments at each strain rate were conducted at least five times to show repeatability.

Quasi-static experiments

Quasi-static experiments were performed using a standard servohydraulic MTS 810 machine, with the force history being recorded by a 100 kN load cell. Two nominal strain rates of $\sim 10^{-4}$ s^{-1} and $\sim 10^{-3}$ s^{-1} were obtained using the displacement control setting. A high-speed AOS PROMON U750 camera monitored the macroscopic deformation process on the specimen with a full resolution of 1280 $\times$ 1024 pixels,

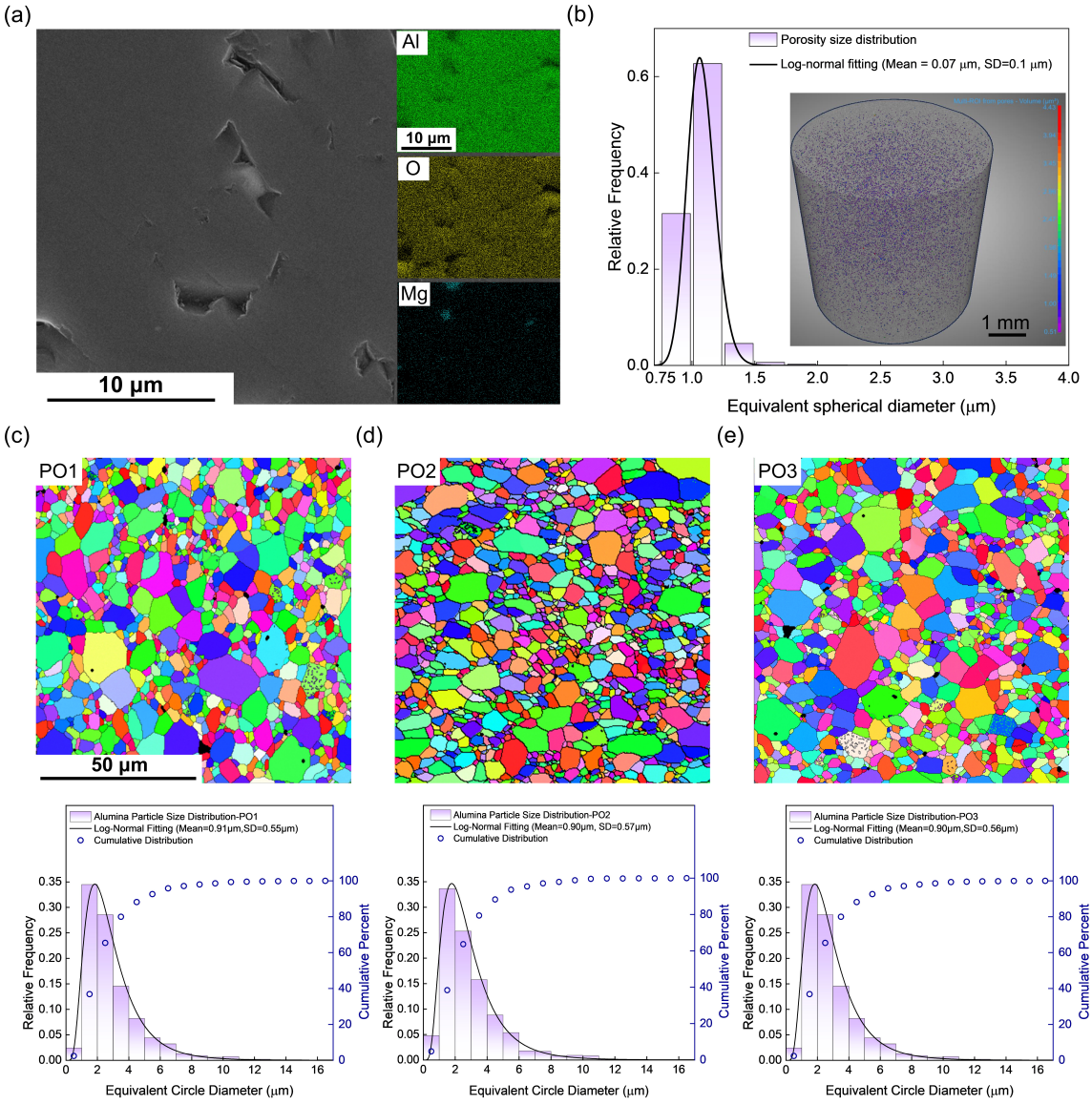

Fig. 5.2: Microstructural characterization of the AM alumina with different printing orientations (POs). (a) SEM image of the material showing the micro-structural features of the AM alumina and EDS images showing the chemical composition of the printed material. (b) Histogram distribution showing the relative frequency of pores and impurities acquired using X-ray microscopy. The inserted figure is a 3D render of the reconstructed X-ray microscopy scanned volume with pores and impurities color-coded. (c-e) EBSD analysis is represented by inverse pole figures (IPFs) for the material with PO1, PO2, and PO3, respectively, along the corresponding grain size distribution on the bottom row.

recording at 5 to 50 frames per second (FPS, its value is adjusted based on the loading rate). During quasi-static loading, to prevent the MTS machine platens from

indentation caused by AM alumina specimens and fragments during the loading process, polished tungsten carbide (WC) platens were placed between the specimen and the loading platens. For FBD specimens, high-pressure grease was used between the specimen and surfaces of the WC platen to mitigate the frictional effect and enable lateral motion [32, 55]. Conversely, for the shear-compression specimens, no grease was applied to induce tangential force via friction, ensuring that no surface sliding occurred between the specimen and platens [34, 85].

Dynamic experiments

Dynamic indirect tension and compression–shear experiments were carried out on an SHPB system comprising a projectile, an incident bar, a transmitted bar, and a data acquisition system (HBM Gen 3i at 20 MHz). The incident and transmission bars had a diameter of 12.7 mm and lengths of 1016 mm and 914 mm, respectively. Made from hardened maraging steel (Service Steel America C-350), the bars possessed a density, elastic modulus, yield strength, and Poisson's ratio of 8080 kg/m^3, 200 GPa, 2.68 GPa, and 0.29, respectively. At the interfaces between the bars and the specimens, two impedance-matched platens manufactured from Ti–6Al–4V titanium alloy jacketed tungsten carbide with diameters the same as the bars were attached, aiming to protect the ends of the bars from indentation and minimize stress concentration during the loading procedure. Note that, in the indirect tension experiments, a thicker specimen may make secondary contact with the loading platens upon fracture, which may cause a secondary peak to appear in the recorded stress history [32, 55]. As such, no protective platens were employed in the indirect tension tests. Similar to the quasi-static tests, no grease was used for shear-compression specimens to induce adequate friction for shearing [55]. However, in the indirect tension experiments, the specimen was placed between the bars lubricated with high-pressure grease to minimize the frictional effect [34]. For dynamic experiments, an ultra-high-speed camera (Shimadzu HPV-X2) was used to record the dynamic tests at 0.5 million to 1 mil-

lion FPS, and these images are used to capture the full-field strain maps with the DIC technique. Additionally, an ultra-bright LED ring light was employed to ensure sufficient lighting, enhancing imaging quality and facilitating DIC analysis. Different pulse shaping configurations are attached in front of the incident bar to produce near triangular pulses under dynamic loading. This setup enables the ceramic specimens to achieve the necessary stress equilibrium and minimize stress pulse oscillation resulting from dispersion effects [26, 100, 104]. To achieve dynamic strain rates spanning from $\sim$ 80 to 100 s^{-1}, $\sim$ 250 to 300 s^{-1}, and $\sim$ 640 to 730 $^{-1}$ in shear-compression experiments, tin, high-density polyethylene (HDPE), and paper pulse shapers were used, respectively. In indirect tension tests, strain rates between $\sim$ 25 to 40 s^{-1} were obtained by using tin pulse shapers, strain rates between $\sim$ 87 to 110 s^{-1} were achieved with HDPE pulse shapers, and strain rates between $\sim$ 150 to 202 s^{-1} were reached using paper pulse shapers. These pulse shapers have been used in previous studies by the authors [26, 34, 55]. In the current SHPB setup, two strain gauges (Micro 184 Measurements CEA- 13-250UN-350) attached to the bars were used to collect the incident and transmission strain signal data. The transmission strain signal (i.e., $\epsilon_t(t)$) was used to measure the stress-time response $\sigma(t)$ [101]:

$$\sigma(t) = \frac{A_0}{A_s} E_0 \epsilon_t(t) \tag{5.1}$$

where, A_0 (m^2) and A_s (m^2) denote the cross-sectional areas of the bar, and specimen, respectively, and E_0 (N/m^2) represents the elastic modulus of the bar material. To compare the uniaxial compression results (investigated in the previously published work by the author [30], and [34]) and the compression–shear results (obtained in the current study and the study by Karanjgaokar et al. [251]) across the range of strain rates, the equivalent stress and equivalent strain rate, which are expressed as Eq. (5.2), and Eq. (5.3), respectively, are used:

$$\sigma_e = \sqrt{\frac{1}{2}[(\sigma_x - \sigma_y)^2 + (\sigma_y - \sigma_z)^2 + (\sigma_z - \sigma_x)^2 + 6(\tau_{xy}^2 + \tau_{xz}^2 + \tau_{yz}^2)]} \tag{5.2}$$

$$\dot{\epsilon}_e = \sqrt{\frac{1}{2(1+\nu)^2}[(\dot{\epsilon}_x - \dot{\epsilon}_y)^2 + (\dot{\epsilon}_y - \dot{\epsilon}_z)^2 + (\dot{\epsilon}_z - \dot{\epsilon}_x)^2 + 6(\dot{\epsilon}_{xy}^2 + \dot{\epsilon}_{xz}^2 + \dot{\epsilon}_{yz}^2)]} \tag{5.3}$$

For the indirect tension experiments, the tensile stress is calculated using the elasticity theory [102]:

$$\sigma_\theta = K\frac{2P}{\pi Dt} \tag{5.4}$$

where P, D, and t are the loading force applied to the specimen, diameter, and thickness of the disk, respectively. Here, K is a dimension coefficient as a function of the loading angle (i.e., 2α) of the flattened disk [103]. If $2\alpha = 0^\circ$ (i.e., coventional Brazilian disk), K is equal to 1, and if $2\alpha = 20^\circ$, K is approximated to 0.95 [102, 103].

5.3.3 Digital image correlation analysis

The methodology for DIC analysis utilized in this research aligns with previous studies [30, 32, 34]. The study employed VIC-2D V6 software from Correlated Solutions Inc. (USA) for the DIC analysis, selecting the first captured image by the cameras as the reference image. For quasi-static tests, the AM specimen surface was divided into subsets of 51 × 51 pixels with a step size of 7 pixels. Dynamic rate experiments used subsets of 27 × 27 pixels with a step size of 5 pixels, adjusted based on camera resolution, speckle size, and desired smoothness of strain profiles. The DIC analysis applied the zero-normalized sum of squared differences (ZNSSD) criterion with an optimized 8-tap interpolation scheme. Engineering strain was calculated through DIC analysis, where the slope of linear sections in strain-time curves determined the strain rate. Fig. 5.3(a) shows the stress and strain histories across a full-surface global average and six local areas of interest (AOIs) on the shear-compression specimen, confirming stress equilibrium during dynamic experiments. The overlapping strain histories from different AOIs, along with the corresponding stress curve, indicated uniform deformation and good equilibrium within the specimen [100]. To verify the reliability of the

indirect tension experiments, Fig. 5.3(b) illustrates the typical displacement curves for both the upper and lower halves of the FBD specimen overtime during an SHPB experiment. Additionally, the figure shows full-field displacement contours obtained through DIC analysis at six specific time points, corresponding to the labeled points 1-6 on the displacement curves. Initially, the displacement curves for both halves of the specimen gradually increase over time, followed by a sharp rise near point 4. This point corresponds to the rapid propagation of an axial surface crack at the center of the specimen, creating two distinct semicircular regions separated by a boundary line along the diametrical loading direction. The displacement field displays a symmetric pattern, resulting in an average displacement of approximately 0 along the central line of the specimen, indicating the occurrence of a near-symmetric tensile mode failure and good equilibrium—both of which are desirable in indirect tension experiments [32, 78].

5.4 Results and discussion

The behavior of AM alumina ceramics under varying strain rates (i.e., 10^{-4} s^{-1} to 10^{2} s^{-1}) and stress states (i.e., shear-compression and indirect tension), in comparison to other AM alumina and traditionally manufactured alumina ceramics, is discussed in Section 5.4.1 and Section 5.4.2. Additionally, the time-resolved images of the specimens covered by the DIC contour during both shear-compression and indirect tension tests are presented to show the initial crack evolution, fracture process, and the evolution of full-field strains. Lastly, in Section 5.4.3, SEM images of the fracture surfaces from the shear-compression and indirect tension experiments were shown under both quasi-static and dynamic loading, to inform on the contribution of intergranular and transgranular failure mechanisms.

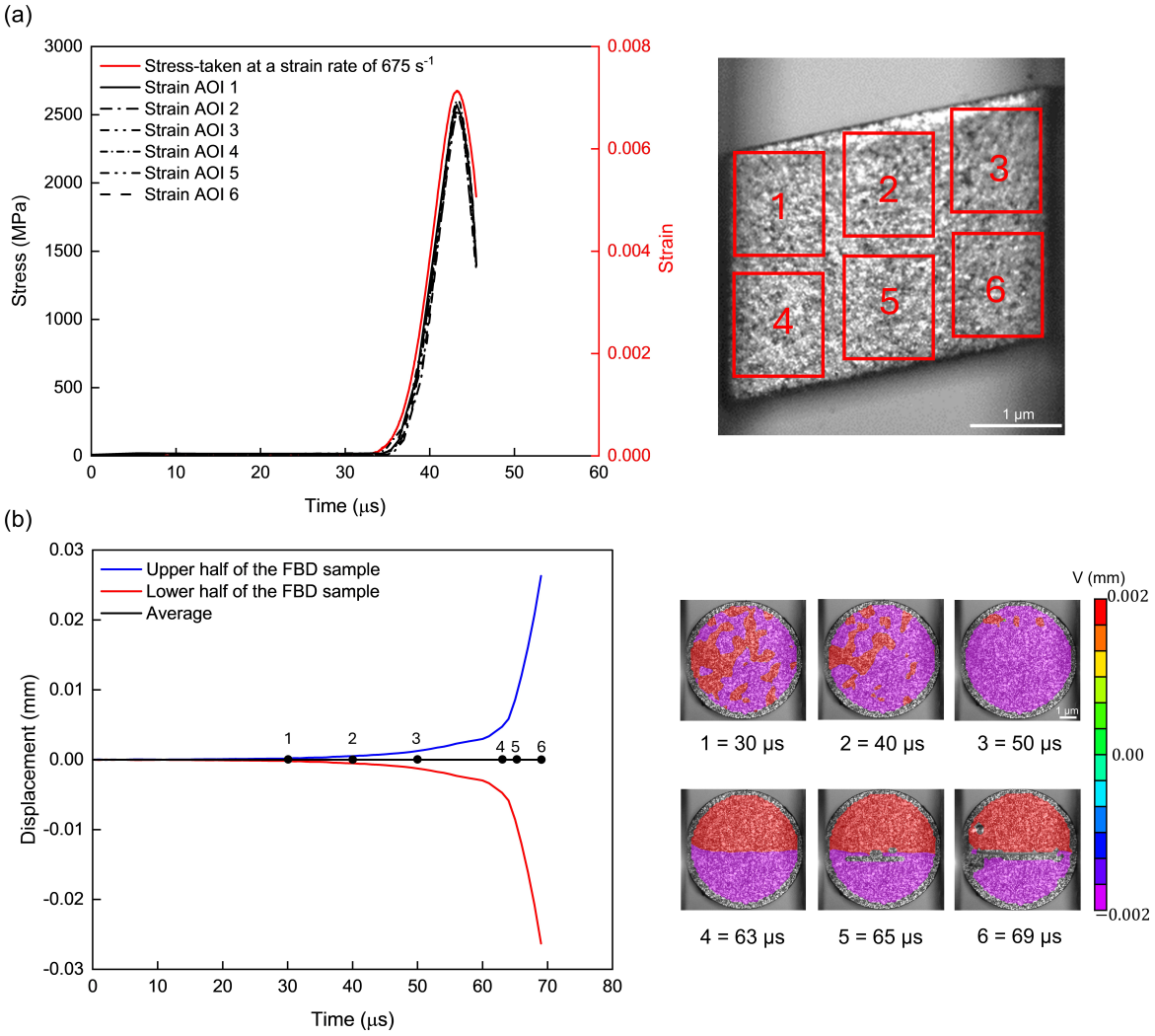

Fig. 5.3: Demonstrating the reliability of the shear-compression and indirect tension experiments. (a) Combined stress and strain curves as a function of time for AM alumina on the right, and shear-compression specimen showing the various DIC areas of interest (AOI) on the left. The average strain-time and stress-time responses overlap, showing that the specimen is experiencing good equilibrium and uniform deformation. The slope of the strain-time curves is reasonably linear, indicating a constant strain rate of 675 s^{-1}. (b) A plot of displacement of the upper and lower half of AM alumina FBD specimen as a function of time during a dynamic experiment at a strain rate of 60 s^{-1}. The symmetric displacement curves and DIC contour indicate good stress equilibrium and failure during the loading process.

5.4.1 Strain-rate dependent shear-compression experiments

In Fig. 5.4 the equivalent strength of AM alumina specimens with tilting angles of 12°, and 25 °across equivalent strain rates was summarized, respectively, in comparison with other AM alumina [34, 251] and those of conventionally made counterparts in the literature [30, 31]. Here, for simplifying the comparison, each subfigure primarily focuses on one specific angle (the first one is for 12°and the second one is for 25°), represented by a solid data point, while transparent data points represent the data related to the second angle. It was found that the equivalent strength of alumina ceramic increases with strain rate, with a significant rise in strength at higher strain rates, which is also observable in the study by DeVries et al. [31] and Zaiemyekeh et al. [30].

At higher strain rates, the AM alumina materials demonstrated comparable strength to conventional alumina, particularly those with PO3, which is likely due to the printing layer direction being perpendicular to the loading direction. The increase in the angle induces a larger shear strain in the material which results in the earlier initiation of damage [34, 55, 251], thereby lowering the peak strength. The PO affects the strength of AM alumina across different strain rates: I- PO3 provides the highest strength, especially at 12°, and high strain rates, making it the most effective orientation. II- PO2 offers moderate to high strength, with better performance than PO1 at both 12° and 25° angles. III- PO1 results in the lowest strength values, indicating it is the least favorable orientation for applications requiring high strength. To better analyze the role of PO on the strain-rate-dependent equivalent strength of the material, Table 5.1 and Table 5.2 summarize the average equivalent strength (AES) of all POs under quasi-static and dynamic rates for the shear angles of 12° and 25°, respectively. As seen in Fig. 5.4, the quasi-static and dynamic compressive strength of current AM alumina is lower compared with those of DeVries et al. [31] and Zaiemyekeh et al. [30], where cuboidal AM alumina specimens (i.e., a specimen

with a tilting angle of 0°) were used to induce uniaxial compression stress state in the material. This outcome is attributable to inducing a combined shear-compression stress state in the current AM alumina ceramic angled specimens, resulting in the earlier initiation of shear failure in the material [34, 55]. AM alumina ceramics have lower strength when compared to their conventional counterparts, and this result is

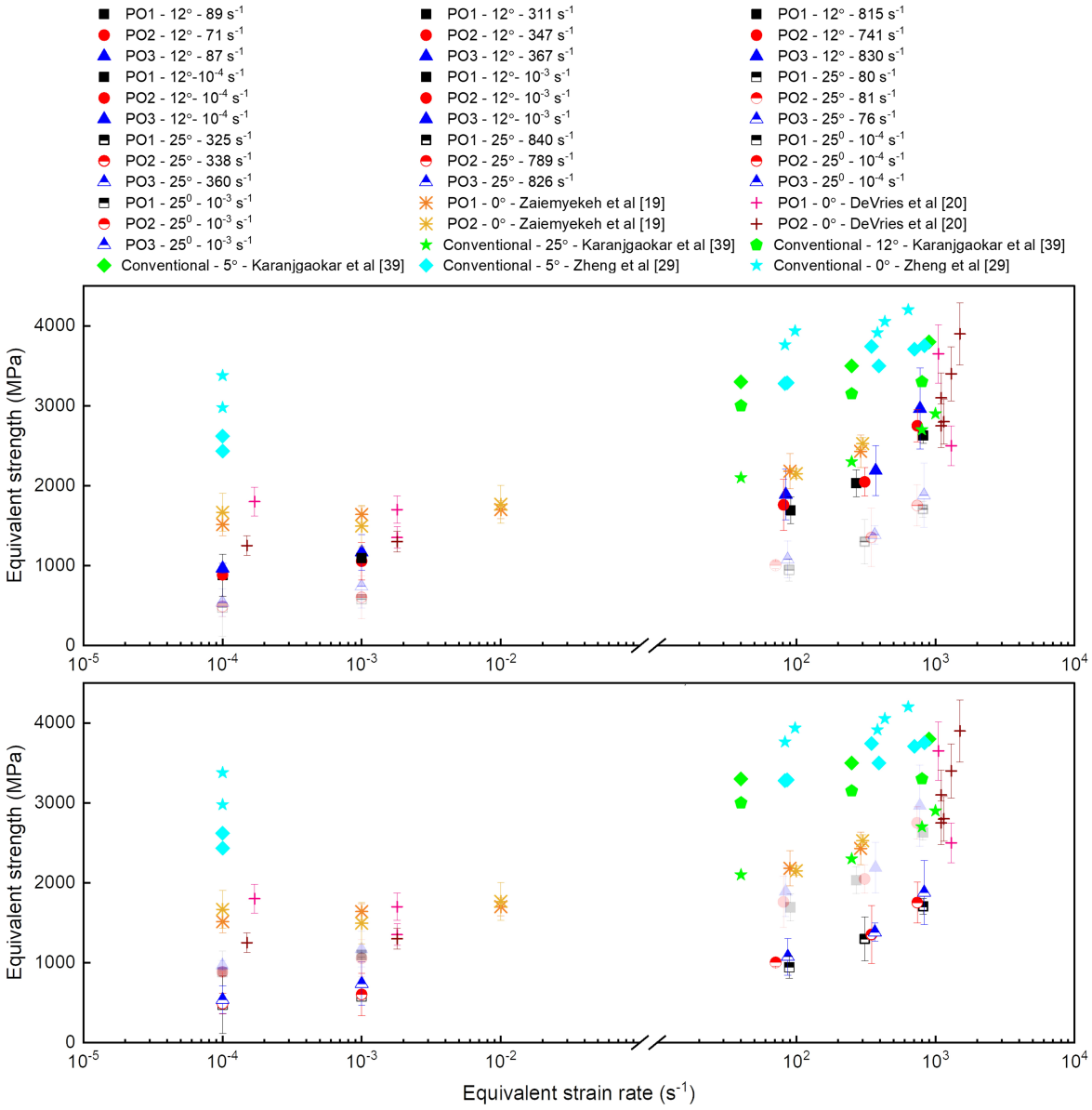

Fig. 5.4: Comparing the strain rate-dependent equivalent strength of the AM alumina with different POs with other AM alumina ceramics and those of the conventionally made counterparts in the previous studies under compression and shear-compression loading.

consistent with the study by DeVries et al. [31] and Zaiemyekeh et al. [30]. The lower strength of the current AM ceramics compared to conventional ones is likely to be caused by the printing-induced microstructural defects that lead to local failure, as evidenced by the time-resolved images in Fig. 5.5, Fig. 5.6, Fig. 5.8, and Fig. 5.9, resulting in the loss of structural integrity of the specimens in the earlier stages of loading [185].

Table 5.1: Average equivalent strength (AES) of AM Al_2O_3 specimen with shear angle of 12° under quasi-static and dynamic loading for all POs shown in Fig. 5.4.

Quasi-static loading			
Strain rate (s^{-1})	10^{-4}	10^{-3}	
PO1-AES (MPa)	879 ± 366.4	1094 ± 140.4	
PO2-AES (MPa)	884 ± 126.4	1055 ± 266.3	
PO3-AES (MPa)	966 ± 173.2	1167 ± 235.7	
Dynamic loading			
Strain rate (s^{-1})	70-100	250-360	700-815
PO1-AES (MPa)	1692 ± 139.2	2031 ± 276.5	2469 ± 43.6
PO2-AES (MPa)	1760 ± 45.9	2047 ± 363.7	2510 ± 254.5
PO3-AES (MPa)	1890 ± 230	2189 ± 114.3	2721 ± 401.3

Shown in Fig. 5.5, and Fig. 5.6 are the AM alumina response under quasi-static (i.e., 10^{-4} s^{-1}) and dynamic (10^2 s^{-1}) shear-compression loading, respectively, with the tilting angle of 25°. The figure includes the temporal stress and strain responses and ultra-high-speed camera images covered by DIC contours to better demonstrate the strain evolution. The image frame numbers (1-4) corresponded to the numbered points on the stress-time curve. As shown in Fig. 5.5, and Fig. 5.6(a), (b), and (c), upon reaching equilibrium in the specimen, the stress and strain histories increased linearly, and upon reaching the peak point, the stress-time curve sharply decreased due to the catastrophic failure which is governed by the and growth and coalescence

Table 5.2: Average equivalent strength (AES) of AM Al_2O_3 specimen with shear angle of 25° under quasi-static and dynamic loading for all POs shown in Fig. 5.4.

Quasi-static loading			
Strain rate (s^{-1})	10^{-4}	10^{-3}	
PO1-AES (MPa)	473 ± 263.1	576 ± 24.3	
PO2-AES (MPa)	488 ± 24	603 ± 233.9	
PO3-AES (MPa)	537 ± 136.2	738 ± 223.7	
Dynamic loading			
Strain rate (s^{-1})	70-100	250-360	700-815
PO1-AES (MPa)	944 ± 167.8	1298 ± 166.5	1705 ± 97.6
PO2-AES (MPa)	1004 ± 318.8	1352 ± 178.4	1752 ± 202.2
PO3-AES (MPa)	1075 ± 315.7	1382 ± 314.6	1879 ± 507.4

of multiple axial cracks. Note that the DIC pattern was lost at the early stages of quasi-static and dynamic loading due to localized failure. From the DIC patterns, one may observe that the accumulation of strain and failure pattern of the material was noticeably influenced by the PO, while the quantitative data in terms of stress and strain histories were not highly affected for PO1 and PO2. As shown in Fig. 5.5(a), (b), and (c), PO1 and PO2 exhibited similar stress responses but with slight variations in peak stress and timing. The PO3 showed the highest strength, likely attributable to the direction of layering deposition perpendicular to the loading direction and the resultant microstructural flaws contributing to the failure initiation and growth. In addition, from previous research [186, 187, 253], it is known that the strength is higher within the material as compared to the interface between print layers. Fig. 5.5(d) shows the qualitative evolution of the lateral (ϵ_{xx}) and shear (ϵ_{xy}) strains for PO1, PO2, and PO3, respectively. From the early stages of loading, lateral tensile strain (i.e., the red areas on the contour) primarily developed in the specimen for all the POs, particularly with PO2 and PO3, which contributed to the earlier failure of the

material. In addition, a more diffusive accumulation of shear strain (purple areas) was observed in PO2 and PO3. All specimens first underwent local failure (see frame 1 and frame 2 of Fig. 5.5(d), respectively) under quasi-static loading likely to be caused by manufacturing-related microstructural defects (e.g., pores and weak grain boundaries) causing the loss of DIC correlation. Upon point 2, for all the POs, stress-bearing capacity kept rising until point 3, when a global catastrophic failure occurred caused by a few dominant cracks propagating through the specimen. As seen in Fig. 5.5(a), (b), and (c), under quasi-static loading, the ratio of $\frac{\epsilon_x}{\epsilon_y}$ may not reflect the typical Poisson's ratio of ~ 0.22 for alumina ceramic materials. This is likely to be caused by the local failure of the current AM alumina from the early stages of loading, manifesting as axial cracks at the macroscale, which consequently lead to the lateral expansion of the specimen, thereby increasing the lateral strain under quasi-static loading. To avoid any misinterpretation of the measured data, the ratio of $\frac{\epsilon_x}{\epsilon_y}$ under quasi-static was not reported as Poisson's ratio in this study. Overall, the comparison revealed that the PO3 shows a higher strength and a different failure pattern at the macro scale (see the point 3 status in Fig. 5.5(d)) under quasi-static loading when compared to the PO1 and PO2, indicating the effect of printing direction under low strain rates.

Under dynamic loading, as shown in Fig. 5.6(a), (b), and (c), the stress-bearing capacity increased linearly almost up to the peak point where damage is initiated at the corners and center of the specimens and axial cracks emerge. From Fig. 5.6(d), the PO-dependent failure pattern of the material is more noticeable under quasi-static loading when compared to dynamic loading. In the specimen with PO1, primary axial cracks at the center of the specimen were initiated, and this caused softening in the stress-time curve prior to peak stress (see point 2 on Fig. 5.6(d)). Subsequently, the propagation of the axial primary cracks and damage at the center led to a sharp decrease in the stress (points 3 and 4 in Fig. 5.6(d)). In the specimen with PO2, shown in Fig. 5.6(d), the lateral and shear strains were concentrated at the center

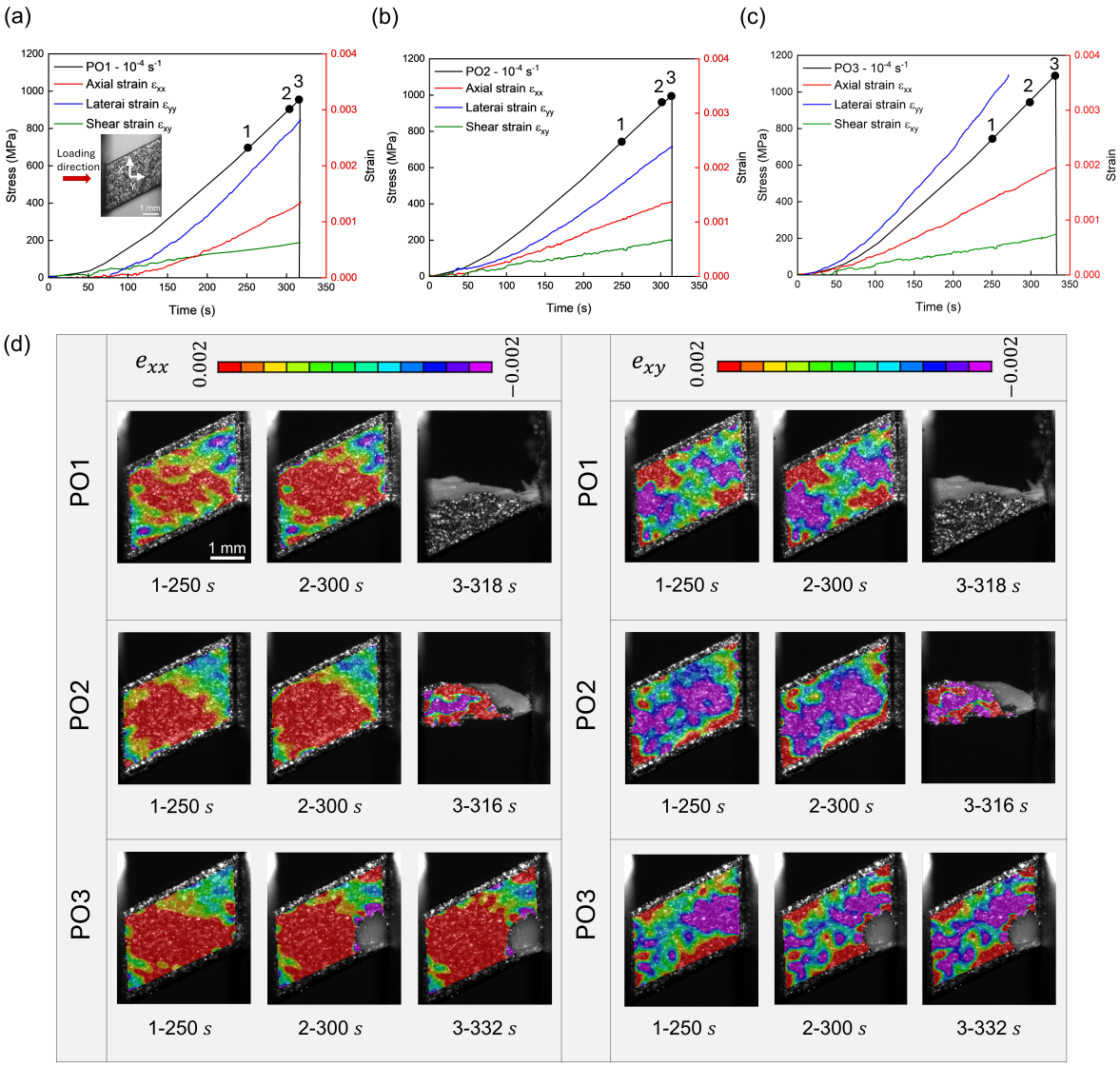

Fig. 5.5: Stress-time history of the shear-compression specimen with the angle of 25° under quasi-static loading (i.e., 10^{-4} s^{-1}) along with time-resolved images of failure progression in the material. (a) AM alumina with PO1. (b) AM alumina with PO2. (c) AM alumina with PO3. (d) The time-resolved DIC contours show the evolution of axial strain (first column) and shear strain (second column) components that correspond to the specified numbered point on the stress-time curves.

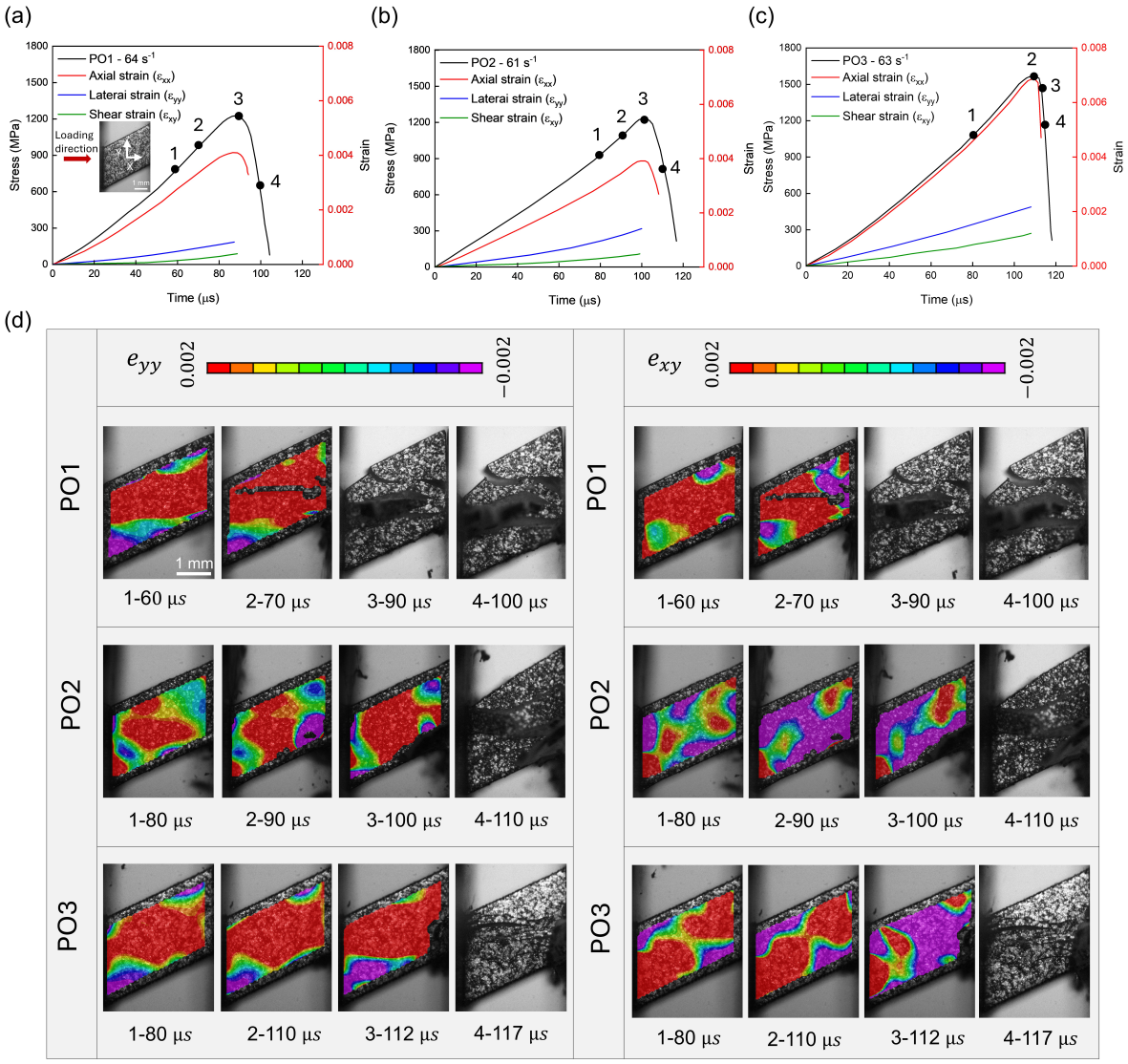

Fig. 5.6: Stress-time history of the shear-compression specimen with the angle of 25° under dynamic loading (i.e., 10^2 s^{-1}) along with time-resolved images of failure progression in the material. (a) AM alumina with PO1. (b) AM alumina with PO2. (c) AM alumina with PO3. (d) The time-resolved DIC contours show the evolution of axial strain (first column) and shear strain (second column) components that correspond to the specified numbered point on the stress-time curves.

and top corner, where failure was initiated. Next, the primary axial crack nucleated in the lower corner after peak stress, and damage accumulated at the top left corner where the shear strain accumulated. Subsequently, the formation of multiple axial cracks caused the catastrophic failure of the specimen. As seen for the specimen with PO3, lateral strain and shear strain were diffused at the top corner and center of the specimen, resulting in crack nucleation and propagation in these areas of the specimen. Overall, the PO was found to affect the mechanical response of the AM alumina in terms of the strength and failure pattern, particularly the failure pattern under quasi-static loading due to a more pronounced effect of microstructural defect-induced localization of failure under low-rate loading. This is likely due to the layer-by-layer printing process, which may induce defects across length scales contributing differently to the failure behavior of the material with respect to the global loading direction. For brevity, the corresponding outcomes of the shear-compression specimens with 12° were not presented here as similar trends as those of 25° specimen were captured.

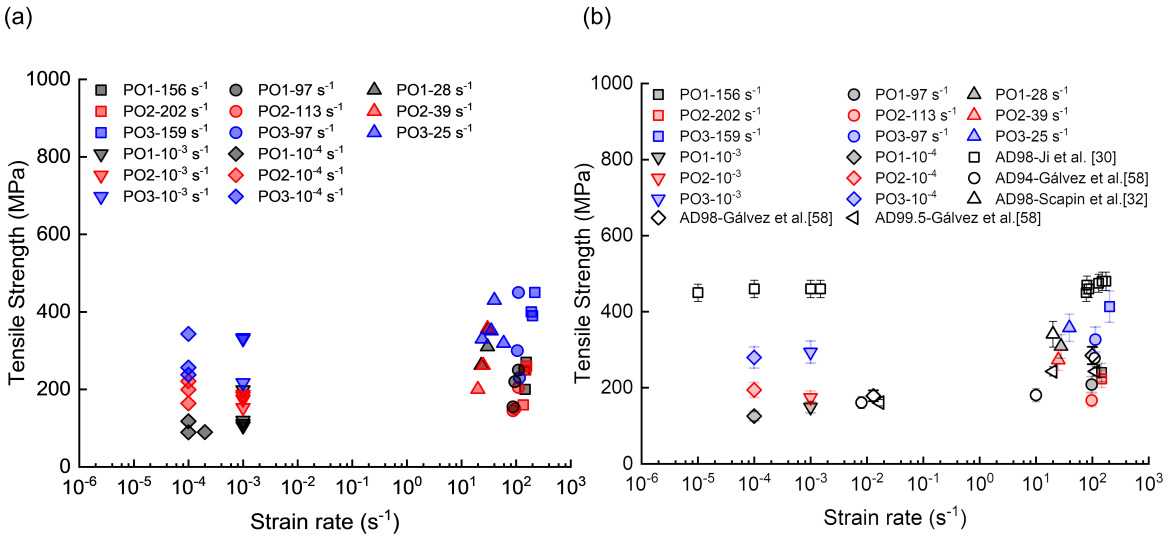

Fig. 5.7: Tensile strength of the material across strain rates and comparison with conventionally made counterparts. (a) Scatter plot of the strain rate-dependent tensile strength of the AM alumina with different printing orientations by the FBD specimen. (b) Comparing the average tensile strength of the AM alumina with those of the conventionally made alumina materials in the literature across strain rates.

Table 5.3: Average tensile strength (ATS) of AM Al_2O_3 specimen under quasi-static and dynamic loading for all POs shown in Fig. 5.7.

Quasi-static loading			
Strain rate (s^{-1})	10^{-4}	10^{-3}	
PO1-ATS (MPa)	125 ± 16	148 ± 43	
PO2-ATS (MPa)	170 ± 28	174 ± 15	
PO3-ATS (MPa)	279 ± 56	293 ± 66	
Dynamic loading			
Strain rate (s^{-1})	25-40	87-110	150-202
PO1-ATS (MPa)	308 ± 46	209 ± 48	240 ± 36
PO2-ATS (MPa)	273 ± 79	166 ± 33	223± 55
PO3-ATS (MPa)	357 ± 50	326 ± 68	413 ± 32

5.4.2 Strain-rate dependent indirect tension experiments

The tensile strength of the current AM alumina ceramics with different POs is shown in Fig. 5.7(a), which was calculated by using Eq. (5.4). It was found that the PO also affects the tensile strength of the AM alumina material, with PO3 being the most favorable orientation for achieving higher tensile strength, especially at higher strain rates, and PO1 as the weakest and with the largest variability, particularly at lower strain rates. The layer-by-layer printing process of the AM method and the corresponding orientation of the layer defects relative to the loading direction likely caused these PO-dependent outcomes, as evidenced by the macroscale failure patterns observed in Fig. 5.8 and Fig. 5.9. To further investigate the tensile strength of AM alumina ceramics, Fig. 5.7(b) presents a summary of the tensile strength of conventionally manufactured alumina ceramics from previous studies [32, 59, 254], compared with the AM ceramics in this research. From Fig. 5.7(b), the AM alumina materials show tensile strengths that are comparable to conventionally made ceramics at high strain rates, and this is likely to be caused by the high strain rate strengthen

effect by which microstructural defects (e.g., voids and micro-cracks) are hindered to grow and coalesce due to the short duration of the loading process [201, 255]. This outcome suggests that AM alumina can be a viable alternative for high-strain-rate applications. For clarity, Table 5.3 lists the average tensile strength (ATS) of the material.

Fig. 5.8 and Fig. 5.9 show the indirect tension stress and strain histories coupled with the ultra-high-speed camera images analyzed by the DIC analysis used to inform on the time-evolved failure of the material in a tensile stress state under quasi-static and dynamic loading, respectively. The image frame numbers (1–3) correspond to the numbered points on the stress-time curve. The lateral strain contours are overlaid on the time-resolved images on the Fig. 5.8(d) and Fig. 5.9(d) in order to show the initial crack evolution and fracture process in the material due to tension. As shown in Fig. 5.8 and Fig. 5.9(a), (b), and (c), the shear strain (ϵ_{xy}) is near zero for all the POs, confirming negligible in-plane rotation in the specimen during loading and a reasonable accuracy for measuring tensile strength.

For the specimen with PO1 under quasi-static loading (see Fig. 5.8(d)), the first frame showed the specimen surface before the appearance of the first axial crack, with a near-uniform lateral strain distribution across the specimen surface. In the next frame, the tensile lateral strain was localized at the center of the specimen (indicated by the red area), identifying the location of crack initiation. As the load increased further to point 3, an axial crack propagated in this strain concentration region at the center of the specimen. Upon exceeding point 3, the central axial crack propagated, eventually causing catastrophic failure. Such failure pattern is frequently observed in previous studies on conventional alumina ceramics [32, 55]. Regarding the specimen with PO2 under quasi-static loading (see Fig. 5.8(d)), the lateral tensile strain accumulated adjacent to the loading platen on the left rather than the center, which eventually led to a different failure pattern compared to the PO1. In the specimen with PO3, the lateral tensile strain evolution followed a pattern similar to

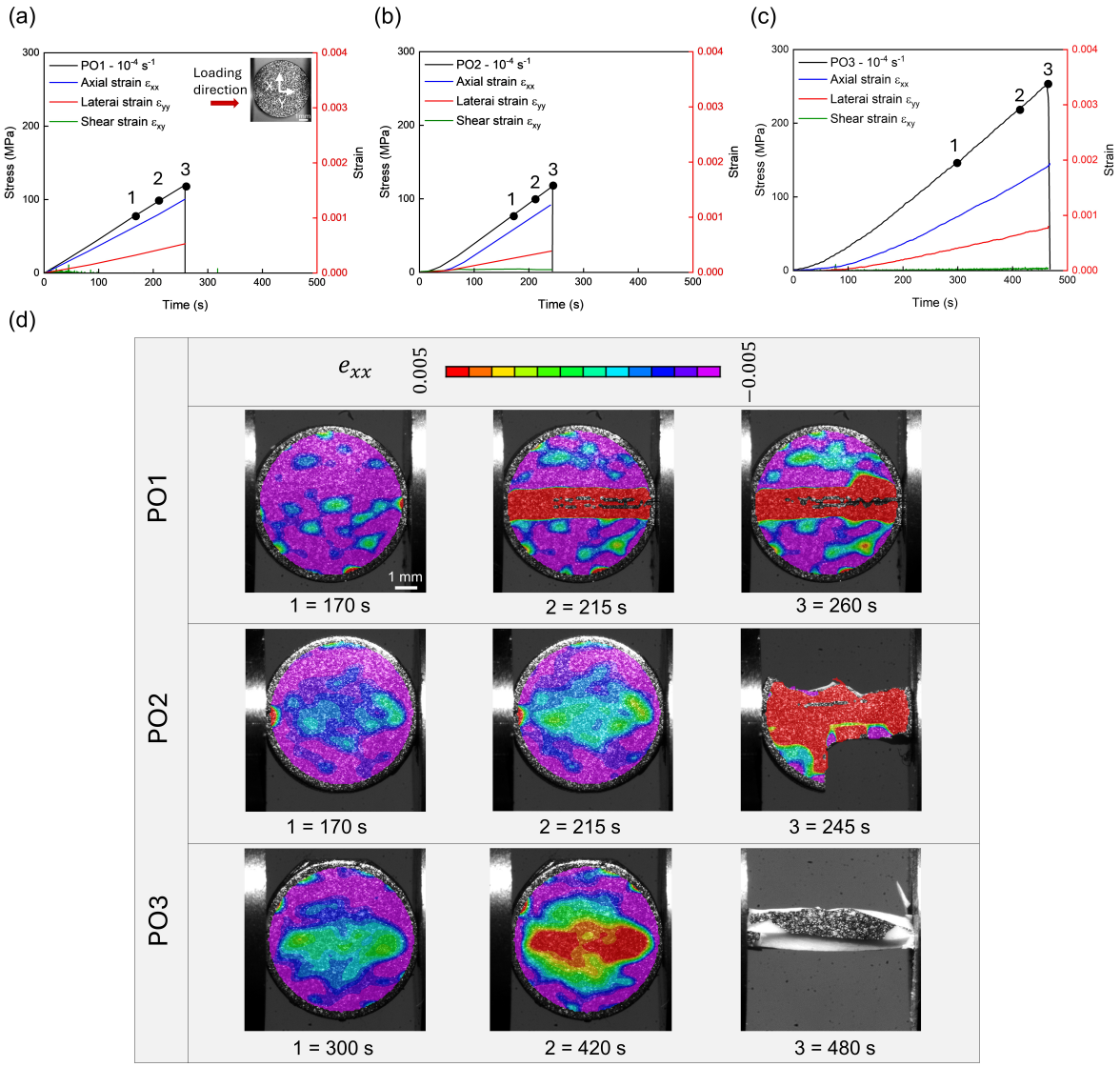

Fig. 5.8: Stress-time history of the FBD specimen under quasi-static loading (i.e., 10^{-4} s^{-1}) along with time-resolved images of failure progression in the material that corresponds to the specified numbered point on the stress-time curves. (a) AM alumina with PO1. (b) AM alumina with PO2. (c) AM alumina with PO3. (d) The time-resolved DIC contours show the evolution of lateral strain (i.e., ϵ_{xx}) component that corresponds to the specified numbered point on the stress-time curves.

the PO1, while leading to multiple axial cracks in the central region resulting in the abrupt decrease in the stress-bearing capacity of the material after point 3.

Under dynamic indirect tension testing represented in Fig. 5.9, the stress history almost linearly grew upon equilibrium (i.e., after $\sim$ 40 µs) up to the peak point, and then sharply decreased due to the brittle failure governed by tension. For all the POs, it was observed that damage accumulates at the central region of the specimen, indicating less variation in the pattern of failure when compared to that of the quasi-static loading (see Fig. 5.8(d)). At the onset of the peak stress (point 2), an axial primary crack appeared at the center of the specimen, where the lateral tensile strain is expected to be at its maximum, followed by the emergence of secondary cracks near the primary cracks when reaching point 3. In the softening regime (point 3 and point 4), multiple primary cracks were observed along the center of the specimen, and secondary circumferential cracks formed at the edge of the specimen.

5.4.3 Post-mortem fractographic studies

Post-mortem fractography analysis on shear-compression specimen

Fig. 5.10 shows the SEM images of fracture surfaces of the AM alumina under quasi-static and dynamic loading with shear-compression specimens with an angle of 25° with different POs. Comparing the outcomes in Fig. 5.10 across the strain rates, for all the POs, it was observed that intergranular fracture reflected by the uneven surfaces and sharp edges (see red arrows) is the governing failure mechanism under quasi-static loading with a combined shear-compression stress state. The key role of intergranular mechanism in the compressive failure behavior of alumina ceramics under quasi-static rates is also reported in literature [14, 30–32]. Note that the occurrence of intergranular fracture is likely related to the relatively weak interfacial strength at the grain boundaries [14, 30, 31]. Fig. 5.10(b), (d), and (f) show the fracture surfaces under dynamic shear-compression conditions, based on which a combination of intergranular and transgranular fractures was observed to govern the

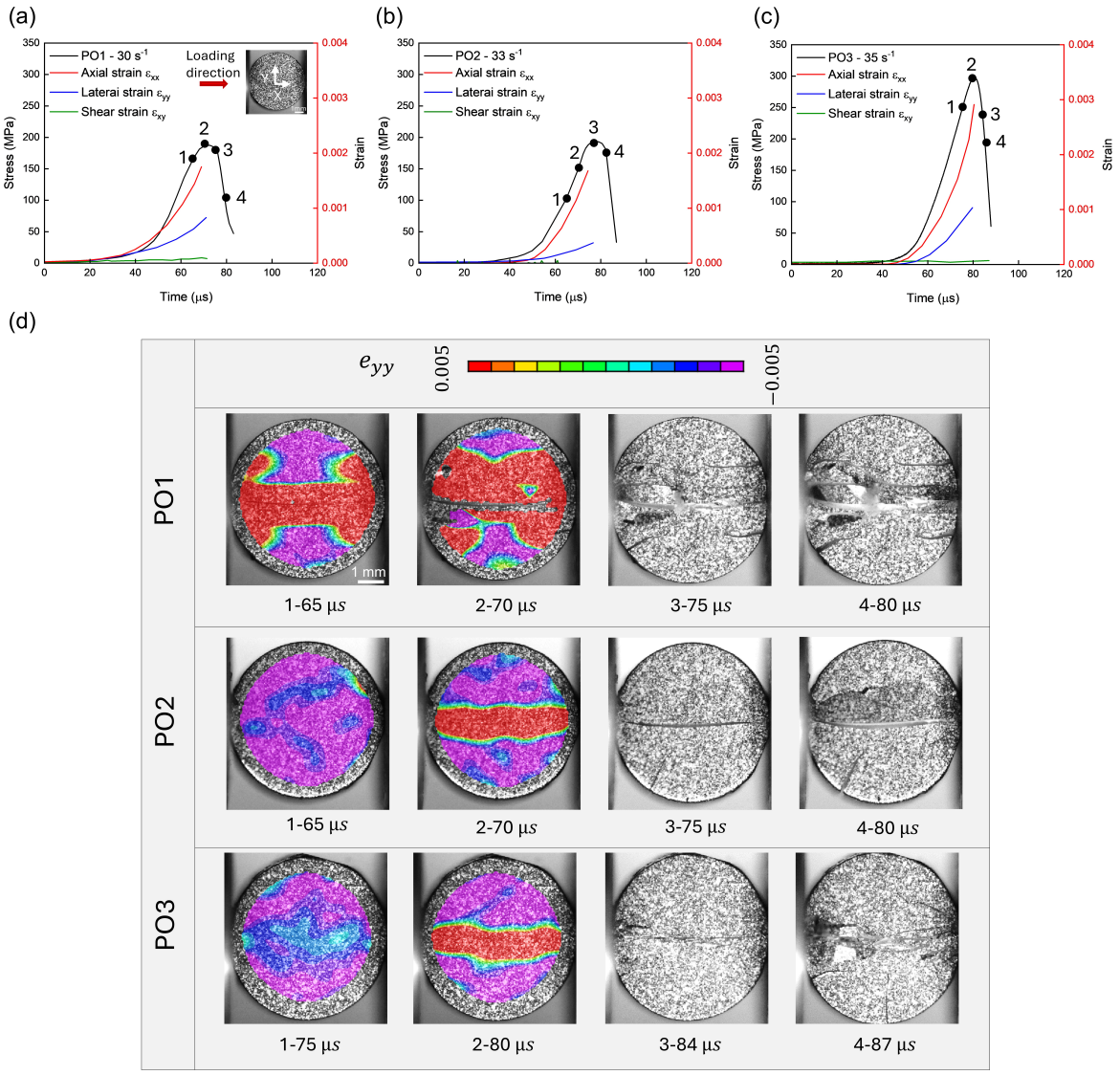

Fig. 5.9: Stress-time history of the FBD specimen under dynamic loading (i.e., 10^2 s^{-1}) along with time-resolved images of failure progression in the material that corresponds to the specified numbered point on the stress-time curves. (a) AM alumina with PO1. (b) AM alumina with PO2. (c) AM alumina with PO3. (d) The time-resolved DIC contours show the evolution of lateral strain (i.e., ϵ_{yy}) component that corresponds to the specified numbered point on the stress-time curves.

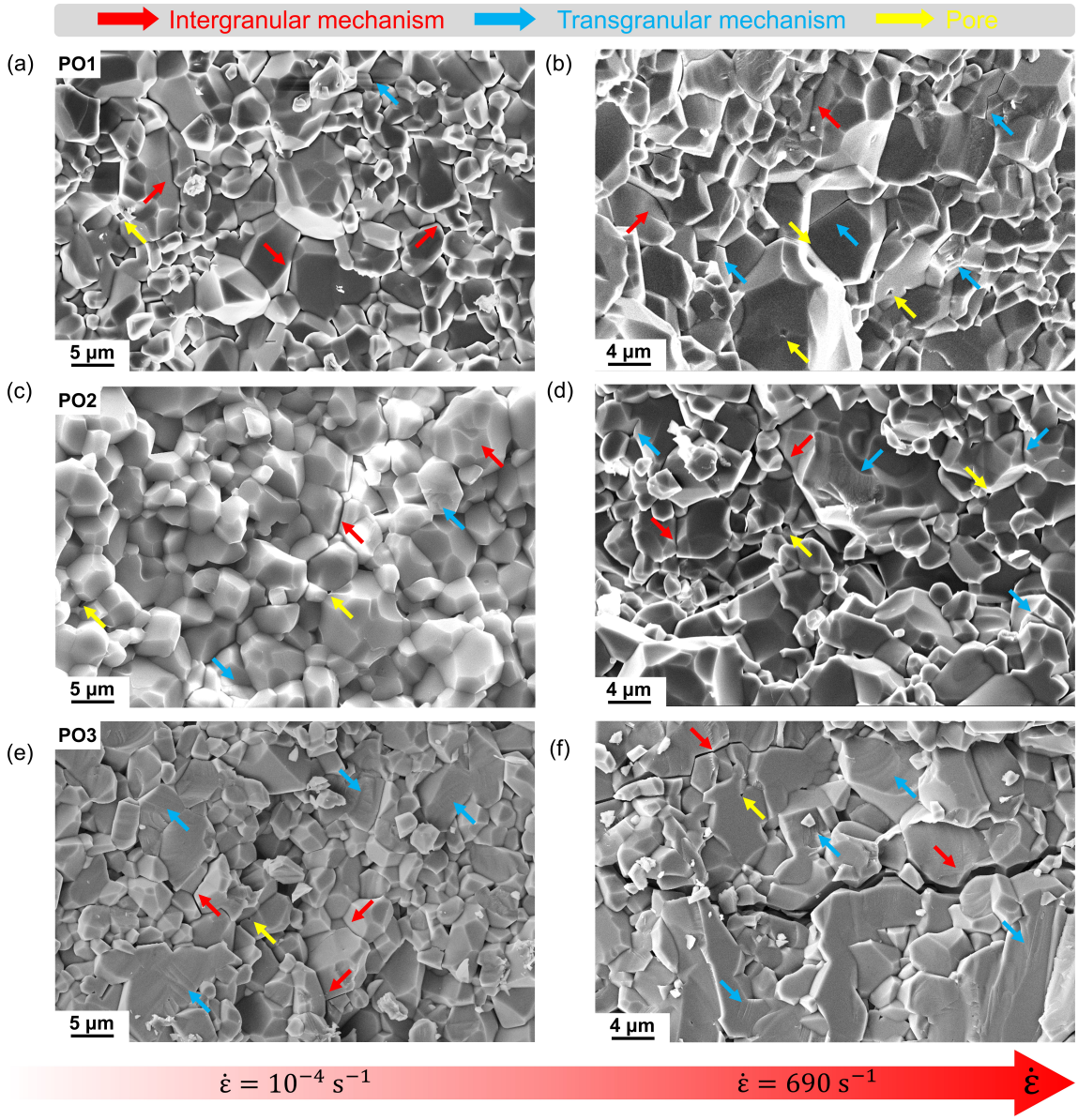

Fig. 5.10: SEM micrograph showing the fractography of the AM alumina under shear-compression loading. (a, c, e) SEM images showing the fractography of the material under quasi-static loading for PO1, PO2, and PO3, respectively. (b, d, f) SEM images showing the fractography of the material under dynamic loading for PO1, PO2, and PO3, respectively.

failure of the material, and this is associated with higher energy absorption and a higher level of kinetic energy in the material under dynamic loading that suppresses the localization of strain, thus allowing more nucleation and coalescence of microcracks within the grain boundaries (i.e., transgranular failure mechanism) under high strain rates [14, 30]. Here, the transgranular mechanism was identified by the cleavage facets shown by the blue arrows. Accordingly, one may observe a higher presence of the transgranular fracture in the PO3 specimen across strain rates, which is likely to be one of the contributors to the higher strength of the material with PO3 compared to the other POs. Overall, the relative roughness of the captured fracture surfaces suggested that the intergranular fracture was likely the dominant failure mechanism under quasi-static shear-compression loading, while a combination of intergranular and transgranular failure mechanisms governs the failure process of the material under dynamic loading.

Post-mortem fractographic analysis on FBD (indirect tension) specimen

Fig. 5.11 presents fracture surfaces captured from the fragments from the quasi-static and dynamic indirect tension experiments. Similar to compression-shear loading, under quasi-static loading, the intergranular fracture was observed to be the dominant failure mechanism under indirect tension across all the POs. Note that transgranular fracture was observed with a higher presence on the fracture surfaces of the PO3 under quasi-static loading, and this is consistent with the higher tensile strength of the material with this PO (see Fig. 5.7(a)). With the increase in strain rate to dynamic regimes (see Fig. 5.11(b,d,f,)) the transgranular mechanism is more frequently observed on the fracture surface when compared to those of the quasi-static loading. Additionally, a greater number of microcracks was observed on the fracture surface of the dynamically loaded specimens, particularly with PO3. This is likely in association with less localization of damage in the specimen with PO3, which in consequence contributes to a higher strength compared to the other POs (see Fig. 5.7(a)) under

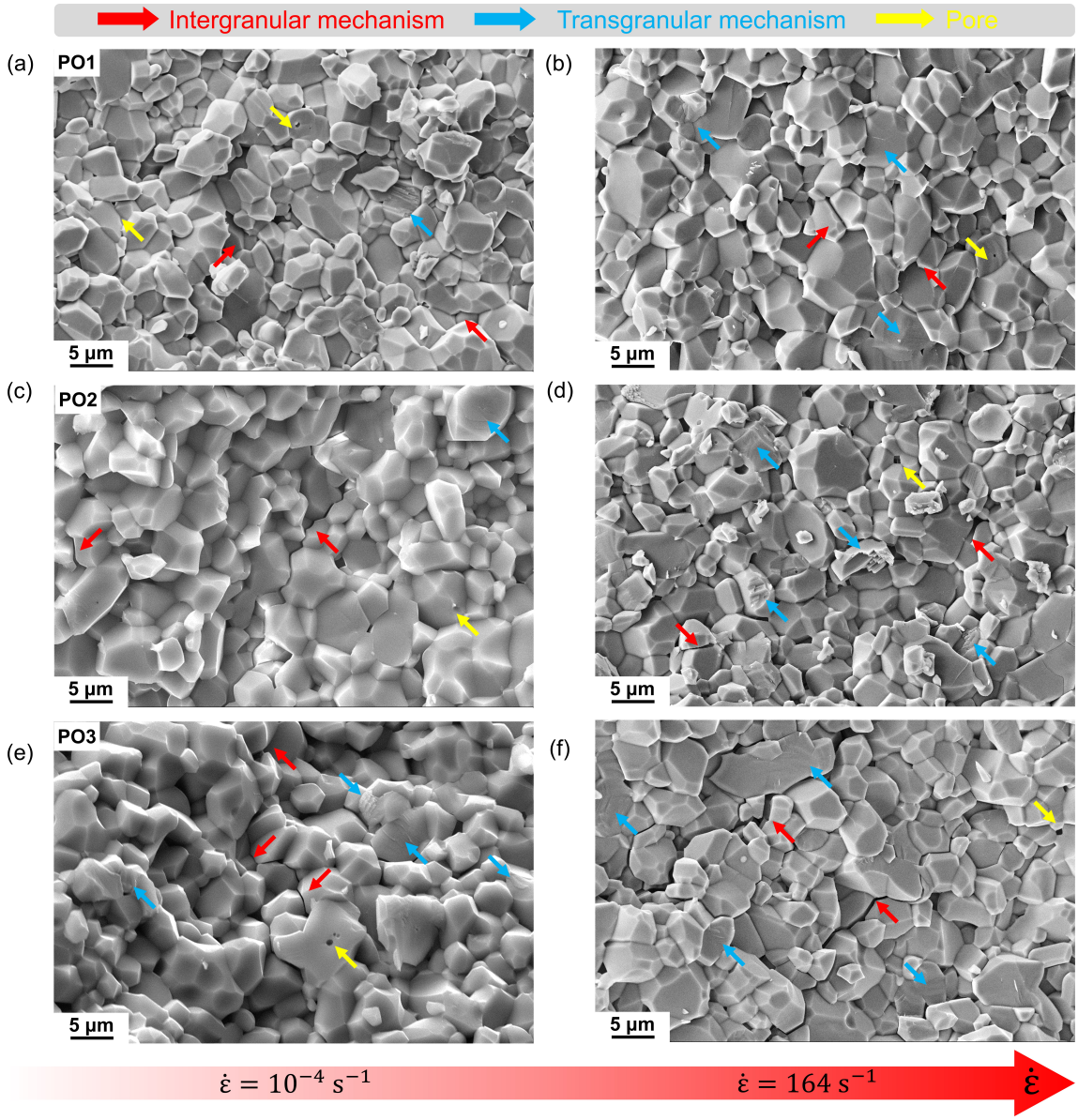

Fig. 5.11: SEM micrograph showing the fractography of the AM alumina under indirect tension loading. (a, c, e) SEM images showing the fractography of the material under quasi-static loading for PO1, PO2, and PO3, respectively. (b, d, f) SEM images showing the fractography of the material under dynamic loading for PO1, PO2, and PO3, respectively.

high strain rate loading.

5.5 Conclusion

This study explored the effect of strain rate (i.e., 10^{-4} s^{-1} to 10^{2} s^{-1}) and stress state (i.e., shear-compression and indirect tension) on the failure behavior of AM alumina ceramics manufactured by the SLA method with three different PO. To induce shear-compression and indirect tension stress states in the material, angled specimens (i.e. cuboidal specimens with tilting angles between parallel ends of 12° and 25°) and FBD specimens were designed, respectively. The PO was found to affect the strain-rate-dependent strength and the failure pattern of the material at the macroscale, which was likely to be caused by the layer-by-layer printing process and the resultant defects across length scales contributing differently to failure initiation and propagation in the material. For both stress states, the macroscale failure pattern showed higher dependency on PO under quasi-static loading likely due to the higher effect of localization of failure under low-strain-rate loading. The AM alumina ceramics with PO3 (i.e., PO perpendicular to the loading direction) demonstrated comparable strength to conventional alumina under dynamic loading, underscoring the importance of optimizing print orientation to enhance the performance of AM ceramics structures for high strain-rate applications. The equivalent strength of AM alumina materials decreased with the increase in shear angle from 12° to 25°, which is attributable to the increase in shear, resulting in the earlier initiation and growth of damage in the material. Regardless of the stress state, the fractography analysis showed the dominant contribution of the intergranular mechanism to the failure of the AM ceramic under quasi-static loading. Under dynamic loading, a combination of intergranular and transgranular mechanisms were observed on the post-mortem SEM images. In addition, under both stress states, the transgranular mechanism was more frequently observed on the fracture surfaces of the specimens with PO3, underlying the higher strength of the material with PO3 compared to other POs. Overall, for

the first time, this study provides a comprehensive understanding of how strain rate and stress state affect the failure behavior of AM alumina ceramics. The findings have implications for designing high-performing AM ceramic structures required for environments including high strain-rate loading, such as aerospace (e.g., engine components [53]) and defense (e.g., protection systems [54]) industries. Additionally, this research generates valuable data sets applicable to the development and validation of computational models for AM ceramics [55, 190, 219] to accelerate the process of material design and optimization [55, 190].

5.6 Acknowledgments

This work is supported by the Natural Sciences and Engineering Research Council of Canada (Grant 2023-04457).

Chapter 6

Conclusions & Future Work

6.1 Conclusions

This thesis comprehensively investigated the mechanical properties and failure behavior of CM and AM alumina ceramics across different stress states and strain rates by combining experimental testing and multiscale simulations. The microstructure of the materials was experimentally characterized using EBSD, SEM, TEM, and XRM to capture the grain size distribution, grain crystallographic orientations, and porosity. Next, the CM and AM alumina ceramics were tested under different stress states (i.e., compression, shear-compression, and tension) and strain rates (i.e., 10^{-4} s^{-1} to 10^{2} s^{-1}), where ultra-high-speed imaging was combined with the DIC analysis to capture the failure progression process and time-evolving full-field strains. The experimental quantitative measurements (i.e., stress versus strain histories, and lateral strain versus axial strain histograms) and qualitative observations (i.e., the initiation and propagation of cracks captured by the ultra-high-speed imaging and post-mortem fractography analysis) were used to validate the FE models. Computationally, a rate-dependent viscosity regularized version of the phenomenological JH-2 material model (i.e., JH2-V) was implemented by using a VUMAT subroutine in ABAQUS software, to better account for the strain-rate- and stress-state-dependent behavior of the material compared to the well-known JH2 model. Upon validation, the developed FE models at the macroscale were leveraged for investigating the effect of

bulking, regularization parameters of the JH2-V model, quantitative analysis of the damage initiation and growth in the material, and stress-state-dependent mesh sensitivity analysis for guiding higher scale modeling (e.g., impact events [91, 92]). Next, informed by the microstructural characterization outcome (e.g., grain size distribution by the EBSD and porosity by XRM analysis), polycrystalline-based RVEs were generated by Neper software and then imported into Abaqus FE solver, where the grain crystallographic orientations by the EBSD analysis were incorporated into the model. To account for the transgranular failure mechanisms, the JH2-V model was further enhanced to include the crystallographic orientations and assigned to grains. The intergranular failure mechanism was accounted for by implementing the CZM approach at the grain boundaries. Upon validation with the experimental data, the developed micromechanical model was leveraged to provide insights into the evolution/competition of failure mechanisms and unravel the effect of microstructure (e.g., grain size and interfacial properties) on the macroscale behavior of the material (e.g., strength).

Building on the limited previous studies [30, 31], this thesis combines experimental testing and multiscale simulations to inform on the dependency of the failure behavior/mechanical properties of advanced alumina ceramics on stress state and strain rates. This thesis achieves its objectives in the form of three peer-reviewed papers (Chapter 2, Chapter 3, Chapter 4) and one submitted for peer review (Chapter 5). The key outcomes from this thesis are summarized below for further emphasis:

- The AM ceramic materials show compressive quasi-static and dynamic strength that is among the highest ones reported for AM alumina in the literature, but it is $\sim 40\%$ and $\sim 25\%$ lower than that of the conventionally-made alumina on average in the literature under quasi-static and dynamic rates, respectively. This may be attributable to manufacturing-induced microstructural defects (i.e., weak grain boundaries and porosity) that cause local failure resulting in loss

of structural integrity of the specimens.

- It was found that when the PO of AM specimens was perpendicular to the loading direction the material showed a higher strain-rate-dependent strength under shear-compression, and tension stress states, likely due to the layer-by-layer printing effect and how the corresponding processing-induced microstructural defects across length scales contributed to the damage propagation. Additionally, the PO was found to influence the failure pattern at the macroscale.

- Regardless of the stress state, the fractography analysis showed the dominant contribution of the intergranular mechanism to the failure of the AM ceramic under quasi-static loading. Under dynamic loading, a combination of intergranular and transgranular mechanisms was observed in the post-mortem SEM images. In addition, under all the investigated stress states, the transgranular mechanism was more frequently observed on the fracture surfaces of the specimens with PO3, underlying the higher strength of the material with PO3 compared to other POs.

- The crack speed propagation in the AM alumina is found to be less than that of conventional counterparts possibly due to a smaller pore size in the current AM ceramics. The micro-indentation Vickers hardness experiments show that the hardness of the AM alumina is independent of the POs, and it also remains almost unaltered when measured on different planes of the specimen. The current AM alumina shows a higher hardness compared to the other AM alumina ceramics in the literature and this is attributable to a higher relative density, smaller pore size, and a finer grain size.

- The proposed quantification analysis provided a better understanding of the relationship between damage accumulation and shear deformation in ceramics at the macroscale, which is challenging to access through experimental mechan-

ics due to the brittle failure. The quantified framework showed that damage initiates earlier in the material with the increase in shear, and this contributes to a decrease in the strength. Additionally, by increasing the angle of the compression-shear specimen and increasing the effect of shear deformation, the maximum magnitude of damage reduces, indicating less damage tolerance in the material when shear dominates.

- To reduce the computational cost of simulations of ceramics at the structural scale with the JH2-V model, we conducted a stress-state-dependent mesh sensitivity analysis. As such, the maximum mesh sensitivity is observed under the uniaxial compression with a variation of $\sim 27\%$ in the predicted strength from fine to coarse mesh size. The lowest sensitivity is observed at a shear-dominated (variation of $\sim 14\%$) and tensile-dominated (variation of $\sim 1\%$) stress state, respectively. Accordingly, to balance the computational cost and accuracy, for compression-dominated areas, a fine mesh size is recommended, while a coarser mesh size may be applied to shear and tension-dominated areas of the model when applied to higher-scale applications of ceramics such as impact events. These outcomes reflect new guidelines that could be applied to the modeling of ceramics in higher-scale applications.

- The developed 3D microstructure-informed finite element (FE) model based on the grain size distribution, porosity, and crystallographic orientations was leveraged to quantify the history of failure mechanisms to uncover the initiation and growth of the intergranular and transgranular mechanisms in AM alumina, implying the key role of the intergranular mechanism in the strength of the material across strain rates. The model showed that the higher strength of the material under dynamic loading is facilitated by the growth of transgranular mechanisms at a lower rate under high-strain-rate loading.

- The micromechanical model showed that the grain crystallographic orientations

promote an earlier initiation and faster growth of the intergranular mechanism due to the stress mismatch at the grain boundaries, and this subsequently amplifies the growth of transgranular mechanisms, causing a decrease in the material strength. With the increase in porosity, the transgranular mechanism was found to be markedly amplified due to the presence of a higher number of pores in the microstructure acting as the crack nucleation sites, decreasing the material strength across strain rates. The model also suggests the existence of a threshold for both the grain boundary strength and fracture toughness, beyond which the strength of the material is marginally enhanced due to the growth of the transgranular mechanism.

6.2 Future Work

While this study has provided a better understanding of the failure behavior of advanced alumina ceramics across stress states and strain rates, there remain several research thrusts to be built on the current work, which will eventually expand the practical applications of alumina ceramic structures fabricated by advanced additive manufacturing. Accordingly, based on this thesis, the following research directions are recommended:

- Investigating the process-microstructure-property-performance relationships of AM alumina ceramics by designing different SLA processing parameters (e.g., variables of the sintering process, printing layer thickness, etc) proceeded with experimental characterization and testing. The outcomes of such experimental research could be further leveraged for developing ML models that understand the process-microstructure-property-performance links of the material to accelerate the design process of AM ceramic structures.

- Designing novel specimen geometries enabling the understanding of the AM alumina ceramic mechanical properties and failure behavior under stress states

that are not explored yet, including pure shear and biaxial tension/compression. The outcomes will allow us to feed further and validate the micromechanical models and enable the development of constitutive models that more accurately capture the mechanical behavior of AM ceramic materials.

- Developing 2D polycrystalline-based models from the current 3D FE modeling framework is essential for generating datasets encompassing various stress states and strain rates. Reducing the current micromechanical model from 3D to 2D is necessary due to the high computational cost associated with the 3D RVE model and also being compatible with the experimental input data in terms of the EBSD maps. These generated datasets will be crucial for training and validating neural networks, such as conventional neural networks [256], which will be utilized as surrogate models for establishing microstructure-property-performance relationships. The significance of such ML-based surrogate models lies in their ability to serve as non-destructive testing tools, enabling real-time prediction of material mechanical performance (i.e., strength) based on microstructural characterization outcomes from EBSD images, including grain size distribution and porosity.

Bibliography

[1] Z. He, J Ma, H. Wang, G. Tan, D. Shu, and J. Zheng, "Dynamic fracture behavior of layered alumina ceramics characterized by a split hopkinson bar," *Materials Letters*, vol. 59, no. 8-9, pp. 901–904, 2005.

[2] J. Delage, E. Saiz, and N. Al Nasiri, "Fracture behaviour of sic/sic ceramic matrix composite at room temperature," *Journal of the European Ceramic Society*, 2022.

[3] J. Pittari III, G. Subhash, J. Zheng, V. Halls, and P. Jannotti, "The rate-dependent fracture toughness of silicon carbide-and boron carbide-based ceramics," *Journal of the European Ceramic Society*, vol. 35, no. 16, pp. 4411–4422, 2015.

[4] J Venkatesan, M. A. Iqbal, and V Madhu, "Experimental and numerical study of the dynamic response of B_4C ceramic under uniaxial compression," *Thin-Walled Structures*, vol. 154, p. 106 785, 2020.

[5] M. R. I. Islam, J. Zheng, and R. C. Batra, "Ballistic performance of ceramic and ceramic-metal composite plates with JH1, JH2 and JHB material models," *International Journal of Impact Engineering*, vol. 137, p. 103 469, 2020.

[6] A. B. Dresch, J. Venturini, and C. P. Bergmann, "Improving the flexural-strength-to-density ratio in alumina ceramics with the addition of silicon nitride," *Ceramics International*, vol. 47, no. 3, pp. 3964–3971, 2021.

[7] S. V. Krishnan, M. M. Ambalam, R. Venkatesan, J. Mayandi, and V. Venkatachalapathy, "Technical review: Improvement of mechanical properties and suitability towards armor applications–alumina composites," *Ceramics International*, 2021.

[8] C.-Y. Huang and Y.-L. Chen, "Effect of mechanical properties on the ballistic resistance capability of Al2O3-ZrO2 functionally graded materials," *Ceramics International*, vol. 42, no. 11, pp. 12 946–12 955, 2016.

[9] R. Savino, L. Criscuolo, G. D. Di Martino, and S. Mungiguerra, "Aero-thermochemical characterization of ultra-high-temperature ceramics for aerospace applications," *Journal of the European Ceramic Society*, vol. 38, no. 8, pp. 2937–2953, 2018.

[10] Z. Wang, R. Li, and W. Song, "Dynamic failure and inelastic deformation behavior of sic ceramic under uniaxial compression," *Ceramics International*, vol. 46, no. 1, pp. 612–617, 2020.

[11] Y. Gao, Y. Ge, P. Xu, W. Zhang, X. Cai, and J. Zhang, "Dynamic fracture mechanism and fragmentation analysis of fine grained Al2O3/SiC composite," *Materials Science and Engineering: A*, p. 141 976, 2021.

[12] A. Krell and E. Strassburger, "Order of influences on the ballistic resistance of armor ceramics and single crystals," *Materials Science and Engineering: A*, vol. 597, pp. 422–430, 2014.

[13] A. Bhattacharjee, A. Bhaduri, R. C. Hurley, and L. Graham-Brady, "Failure modeling and sensitivity analysis of ceramics under impact," *Journal of Applied Mechanics*, vol. 88, no. 5, p. 051 007, 2021.

[14] Z. Wang and P. Li, "Dynamic failure and fracture mechanism in alumina ceramics: Experimental observations and finite element modelling," *Ceramics International*, vol. 41, no. 10, pp. 12 763–12 772, 2015.

[15] J. Zinszner, B Erzar, P. Forquin, and E Buzaud, "Dynamic fragmentation of an alumina ceramic subjected to shockless spalling: An experimental and numerical study," *Journal of the Mechanics and Physics of Solids*, vol. 85, pp. 112–127, 2015.

[16] X. Zhang *et al.*, "3d-printed bioinspired al2o3/polyurea dual-phase architecture with high robustness, energy absorption, and cyclic life," *Chemical Engineering Journal*, vol. 463, p. 142 378, 2023.

[17] C. Billotte, E. R. Fotsing, E. Ruiz, *et al.*, "Optimization of alumina slurry for oxide-oxide ceramic composites manufactured by injection molding," *Advances in Materials Science and Engineering*, vol. 2017, 2017.

[18] Y Lakhdar, C Tuck, J Binner, A Terry, and R Goodridge, "Additive manufacturing of advanced ceramic materials," *Progress in Materials Science*, vol. 116, p. 100 736, 2021.

[19] S. Li *et al.*, "Mechanical properties of al2o3 and al2o3/al interpenetrated functional gradient structures by 3d printing and melt infiltration," *Journal of Alloys and Compounds*, vol. 950, p. 169 948, 2023.

[20] J. Lee, S. Park, B. K. Ryu, and C.-J. Bae, "Facilitation mechanisms of ceramic additive manufacturing: Acceleration and phase transition," *Journal of the European Ceramic Society*, vol. 42, no. 6, pp. 3044–3048, 2022.

[21] J. Deckers, J. Vleugels, and J.-P. Kruth, "Additive manufacturing of ceramics: A review," *Journal of Ceramic Science and Technology*, vol. 5, no. 4, pp. 245–260, 2014.

[22] F. Zhang, Z. Li, M. Xu, S. Wang, N. Li, and J. Yang, "A review of 3D printed porous ceramics," *Journal of the European Ceramic Society*, 2022.

[23] Z. Chen *et al.*, "Dense ceramics with complex shape fabricated by 3D printing: A review," *Journal of Advanced Ceramics*, vol. 10, pp. 195–218, 2021.

[24] J. Hostaša *et al.*, "Transparent laser ceramics by stereolithography," *Scripta Materialia*, vol. 187, pp. 194–196, 2020.

[25] N. Furong *et al.*, "Fused deposition modeling of Si3N4 ceramics: A cost-effective 3D-printing route for dense and high performance non-oxide ceramic materials," *Journal of the European Ceramic Society*, vol. 42, no. 15, pp. 7369–7376, 2022.

[26] B. M. Koch, C Lo, H Li, T Sano, J Ligda, and J. D. Hogan, "Dynamic mechanical response of damaged alumina AD995," *Journal of the European Ceramic Society*, vol. 41, no. 3, pp. 2034–2048, 2021.

[27] C. Lo, T. Sano, and J. D. Hogan, "Microstructural and mechanical characterization of variability in porous advanced ceramics using x-ray computed tomography and digital image correlation," *Materials Characterization*, vol. 158, p. 109 929, 2019.

[28] C Lo, T Sano, and J. D. Hogan, "Deformation mechanisms and evolution of mechanical properties in damaged advanced ceramics," *Journal of the European Ceramic Society*, vol. 40, no. 8, pp. 3129–3139, 2020.

[29] B. M. Koch, C. Lo, H. Li, T. Sano, J. Ligda, and J. D. Hogan, "Two-dimensional dynamic damage accumulation in engineered brittle materials," *Engineering Fracture Mechanics*, vol. 244, p. 107 539, 2021.

[30] Z. Zaiemyekeh, H. Li, D. L. Romanyk, and J. D. Hogan, "Strain-rate-dependent behavior of additively manufactured alumina ceramics: Characterization and mechanical testing," *Journal of Materials Research and Technology*, vol. 28, pp. 3794–3804, 2024.

[31] M. Devries *et al.*, "Quasi-static and dynamic response of 3D-printed alumina," *Journal of the European Ceramic Society*, vol. 38, no. 9, pp. 3305–3316, 2018, ISSN: 0955-2219.

[32] M. Ji, H. Li, J. Zheng, S. Yang, Z. Zaiemyekeh, and J. D. Hogan, "An experimental study on the strain-rate-dependent compressive and tensile response of an alumina ceramic," *Ceramics International*, 2022.

[33] P. H. Lin, L. Tsai, and N. Liou, "Dynamic response of alumina ceramics under brazilian disc test conditions," in *Dynamic Behavior of Materials, Volume 1*, Springer, 2018, pp. 31–38.

[34] J. Zheng, M. Ji, Z. Zaiemyekeh, H. Li, and J. D. Hogan, "Strain-rate-dependent compressive and compression-shear response of an alumina ceramic," *Journal of the European Ceramic Society*, vol. 42, no. 16, pp. 7516–7527, 2022.

[35] T. J. Holmquist, D. W. Templeton, and K. D. Bishnoi, "Constitutive modeling of aluminum nitride for large strain, high-strain rate, and high-pressure applications," *International Journal of Impact Engineering*, vol. 25, no. 3, pp. 211–231, 2001.

[36] S. K. Lahiri, A. Shaw, and L. Ramachandra, "On performance of different material models in predicting response of ceramics under high velocity impact," *International Journal of Solids and Structures*, vol. 176-177, pp. 96–107, 2019.

[37] J. Wade, S. Robertson, Y. Zhu, and H. Wu, "Plastic deformation of polycrystalline alumina introduced by scaled-down drop-weight impacts," *Materials Letters*, vol. 175, pp. 143–147, 2016.

[38] I Girlitsky, E Zaretsky, S Kalabukhov, M. Dariel, and N Frage, "Dynamic compressive and tensile strengths of spark plasma sintered alumina," *Journal of Applied Physics*, vol. 115, no. 24, p. 243 505, 2014.

[39] R. Scazzosi, M. Giglio, and A. Manes, "Fe coupled to sph numerical model for the simulation of high-velocity impact on ceramic based ballistic shields," *Ceramics International*, vol. 46, no. 15, pp. 23 760–23 772, 2020.

[40] E. Simons, J Weerheijm, and L. J. Sluys, "Simulating brittle and ductile response of alumina ceramics under dynamic loading," *Engineering Fracture Mechanics*, vol. 216, p. 106 481, 2019.

[41] D Fernández-Fdz, R Zaera, and J Fernández-Sáez, "A constitutive equation for ceramic materials used in lightweight armors," *Computers & structures*, vol. 89, no. 23-24, pp. 2316–2324, 2011.

[42] G. Johnson and T. Holmquist, "A computational constitutive model for brittle materials subjected to large strains, high strain rates and high pressures," *Shock wave and high-strain-rate phenomena in materials*, pp. 1075–1081, 1992.

[43] G. R. Johnson and T. J. Holmquist, "An improved computational constitutive model for brittle materials," in *AIP conference proceedings*, American Institute of Physics, vol. 309, 1994, pp. 981–984.

[44] G. R. Johnson, T. J. Holmquist, and S. R. Beissel, "Response of aluminum nitride (including a phase change) to large strains, high strain rates, and high pressures," *Journal of Applied Physics*, vol. 94, no. 3, pp. 1639–1646, 2003.

[45] C. H. M. Simha, S. Bless, and A Bedford, "Computational modeling of the penetration response of a high-purity ceramic," *International journal of impact engineering*, vol. 27, no. 1, pp. 65–86, 2002.

[46] E. Simons, J Weerheijm, G Toussaint, and L. Sluys, "An experimental and numerical investigation of sphere impact on alumina ceramic," *International Journal of Impact Engineering*, vol. 145, p. 103 670, 2020.

[47] E. Simons, J Weerheijm, and L. J. Sluys, "A viscosity regularized plasticity model for ceramics," *European Journal of Mechanics-A/Solids*, vol. 72, pp. 310–328, 2018.

[48] A. Rajendran, "Modeling the impact behavior of AD85 ceramic under multiaxial loading," *International Journal of Impact Engineering*, vol. 15, no. 6, pp. 749–768, 1994.

[49] A. Rajendran and D. Grove, "Modeling the shock response of silicon carbide, boron carbide and titanium diboride," *International Journal of Impact Engineering*, vol. 18, no. 6, pp. 611–631, 1996.

[50] V. Deshpande and A. Evans, "Inelastic deformation and energy dissipation in ceramics: A mechanism-based constitutive model," *Journal of the Mechanics and Physics of Solids*, vol. 56, no. 10, pp. 3077–3100, 2008.

[51] V. S. Deshpande, E. N. Gamble, B. G. Compton, R. M. McMeeking, A. G. Evans, and F. W. Zok, "A constitutive description of the inelastic response of ceramics," *Journal of the American Ceramic Society*, vol. 94, s204–s214, 2011.

[52] B Paliwal, K. Ramesh, and J. McCauley, "Direct observation of the dynamic compressive failure of a transparent polycrystalline ceramic (alon)," *Journal of the American Ceramic Society*, vol. 89, no. 7, pp. 2128–2133, 2006.

[53] H. Ohnabe, S. Masaki, M. Onozuka, K. Miyahara, and T. Sasa, "Potential application of ceramic matrix composites to aero-engine components," *Composites Part A: Applied Science and Manufacturing*, vol. 30, no. 4, pp. 489–496, 1999.

[54] S. Siengchin, "A review on lightweight materials for defence applications: Present and future developments," *Defence Technology*, vol. 24, pp. 1–17, 2023.

[55] Z. Zaiemyekeh *et al.*, "Computational finite element modeling of stress-state- and strain-rate-dependent failure behavior of ceramics with experimental validation," *Ceramics International*, vol. 49, no. 9, pp. 13 878–13 895, 2023.

[56] A. E. Medvedev, T. Maconachie, M. Leary, M. Qian, and M. Brandt, "Perspectives on additive manufacturing for dynamic impact applications," *Materials & Design*, vol. 221, p. 110 963, 2022.

[57] X. Zhang, K. Zhang, B. Zhang, Y. Li, and R. He, "Additive manufacturing, quasi-static and dynamic compressive behaviours of ceramic lattice structures," *Journal of the European Ceramic Society*, vol. 42, no. 15, pp. 7102–7112, 2022.

[58] N Kawai, T Kotani, Y Kakimoto, and E Sato, "Fracture behavior of silicon nitride ceramics under combined compression–torsion stresses analyzed by multiaxial fracture statistics," *Journal of the European Ceramic Society*, vol. 31, no. 9, pp. 1827–1833, 2011.

[59] M. Scapin, L. Peroni, and M. Avalle, "Dynamic brazilian test for mechanical characterization of ceramic ballistic protection," *Shock and Vibration*, vol. 2017, 2017.

[60] C. Wu, B. Wan, A. Entezari, J. Fang, Y. Xu, and Q. Li, "Machine learning-based design for additive manufacturing in biomedical engineering," *International Journal of Mechanical Sciences*, vol. 266, p. 108 828, 2024.

[61] M. H. Hamza and A Chattopadhyay, "Multi deep learning-based stochastic microstructure reconstruction and high-fidelity micromechanics simulation of time-dependent ceramic matrix composite response," *Composite Structures*, p. 118 360, 2024.

[62] Y. Zhu, B. Yan, M. Deng, H. Deng, and D. Cai, "Surrogate model for energy release rate and structure optimization of double-ceramic-layers thermal barrier coatings system," *Surface and Coatings Technology*, vol. 430, p. 127 989, 2022.

[63] Z. Zaiemyekeh, S. Sayahlatifi, D. L. Romanyk, and J. D. Hogan, "Understanding the effect of microstructure on the failure behavior of additively manufactured Al2O3 ceramics: 3D micromechanical modeling," *Materials Design*, p. 113 167, 2024.

[64] M. R. I. Islam, J. Zheng, and R. C. Batra, "Ballistic performance of ceramic and ceramic-metal composite plates with JH1, JH2 and JHB material models," *International Journal of Impact Engineering*, vol. 137, p. 103 469, 2020, ISSN: 0734-743X.

[65] E. Medvedovski, "Ballistic performance of armour ceramics: Influence of design and structure. part 1," *Ceramics International*, vol. 36, no. 7, pp. 2103–2115, 2010.

[66] N. P. Padture, "Advanced structural ceramics in aerospace propulsion," *Nature materials*, vol. 15, no. 8, pp. 804–809, 2016.

[67] Z. Zaiemyekeh, G. Liaghat, and M. K. Khan, "Effect of Al2O3 nanoparticles on the mechanical behaviour of aluminium-based metal matrix composite synthesized via powder metallurgy," *Proceedings of the Institution of Mechanical Engineers, Part L: Journal of Materials: Design and Applications*, vol. 235, no. 10, pp. 2340–2355, 2021.

[68] S. Yang, S. Yang, Y. Zhu, L. Fan, and M. Zhang, "Flash sintering of dense alumina ceramic discs with high hardness," *Journal of the European Ceramic Society*, vol. 42, no. 1, pp. 202–206, 2022.

[69] E Strassburger, "Visualization of impact damage in ceramics using the edge-on impact technique," *International Journal of Applied Ceramic Technology*, vol. 1, no. 3, pp. 235–242, 2004.

[70] R. Zhang, B. Han, and T. J. Lu, "Confinement effects on compressive and ballistic performance of ceramics: A review," *International Materials Reviews*, vol. 66, no. 5, pp. 287–312, 2021.

[71] T Sathish, S Arunkumar, R Saravanan, and V Dhinakaran, "Experimental investigation on material characterization of zirconia reinforced alumina ceramic composites via powder forming process," in *AIP Conference Proceedings*, AIP Publishing LLC, vol. 2283, 2020, p. 020 124.

[72] J. Gong, B. Deng, and D. Jiang, "The efficiency of normal distribution in statistical characterization of the experimentally measured strength for ceramics," *Journal of Materials Engineering and Performance*, vol. 30, no. 1, pp. 42–55, 2021.

[73] G. Subhash, A. Awasthi, and D. Ghosh, *Dynamic Response of Advanced Ceramics*. John Wiley & Sons, 2021.

[74] M. Fejdyś, K. Kośla, A. Kucharska-Jastrzabek, and M. Łandwijt, "Influence of ceramic properties on the ballistic performance of the hybrid ceramic–multilayered UHMWPE composite armour," *Journal of the Australian Ceramic Society*, vol. 57, no. 1, pp. 149–161, 2021.

[75] H. Mei, Y. Tan, W. Huang, P. Chang, Y. Fan, and L. Cheng, "Structure design influencing the mechanical performance of 3D printing porous ceramics," *Ceramics International*, vol. 47, no. 6, pp. 8389–8397, 2021.

[76] T. Sano *et al.*, "Correlation of microstructure to mechanical properties in two grades of alumina," in *TMS Annual Meeting & Exhibition*, Springer, 2018, pp. 75–81.

[77] S. Nohut, A Usbeck, H. Özcoban, D. Krause, and G. A. Schneider, "Determination of the multiaxial failure criteria for alumina ceramics under tension–torsion test," *Journal of the European Ceramic Society*, vol. 30, no. 16, pp. 3339–3349, 2010.

[78] J. Chen, B. Guo, H. Liu, H Liu, and P. Chen, "Dynamic brazilian test of brittle materials using the split hopkinson pressure bar and digital image correlation," *Strain*, vol. 50, no. 6, pp. 563–570, 2014.

[79] A Elghazel, R Taktak, and J Bouaziz, "Determination of elastic modulus, tensile strength and fracture toughness of bioceramics using the flattened brazilian disc specimen: Analytical and numerical results," *Ceramics International*, vol. 41, no. 9, pp. 12 340–12 348, 2015.

[80] N. Erarslan and D. J. Williams, "Experimental, numerical and analytical studies on tensile strength of rocks," *International Journal of Rock Mechanics and Mining Sciences*, vol. 49, pp. 21–30, 2012.

[81] S. Xu, J. Huang, P. Wang, C. Zhang, L. Zhou, and S. Hu, "Investigation of rock material under combined compression and shear dynamic loading: An experimental technique," *International Journal of Impact Engineering*, vol. 86, pp. 206–222, 2015.

[82] H.-b. Du, F. Dai, Y. Liu, Y. Xu, and M.-d. Wei, "Dynamic response and failure mechanism of hydrostatically pressurized rocks subjected to high loading rate impacting," *Soil Dynamics and Earthquake Engineering*, vol. 129, p. 105 927, 2020.

[83] C. E. Anderson, P. E. O'Donoghue, J. Lankford, and J. D. Walker, "Numerical simulations of shpb experiments for the dynamic compressive strength and failure of ceramics," *International journal of fracture*, vol. 55, no. 3, pp. 193–208, 1992.

[84] M. Shafiq and G. Subhash, "An extended mohr–coulomb model for fracture strength of intact brittle materials under ultrahigh pressures," *Journal of the American Ceramic Society*, vol. 99, no. 2, pp. 627–630, 2016.

[85] Y. Xu and F. Dai, "Dynamic response and failure mechanism of brittle rocks under combined compression-shear loading experiments," *Rock Mechanics and Rock Engineering*, vol. 51, no. 3, pp. 747–764, 2018.

[86] Y. Xu, A. Pellegrino, F. Dai, and H. Du, "Experimental and numerical investigation on the dynamic failure envelope and cracking mechanism of precompressed rock under compression-shear loads," *International Journal of Geomechanics*, vol. 21, no. 11, p. 04 021 208, 2021.

[87] Q. Zhang, F. Dai, and Y. Liu, "Experimental assessment on the dynamic mechanical response of rocks under cyclic coupled compression-shear loading," *International Journal of Mechanical Sciences*, vol. 216, p. 106 970, 2022.

[88] H.-b. Du, F. Dai, Y. Xu, Z. Yan, and M.-d. Wei, "Mechanical responses and failure mechanism of hydrostatically pressurized rocks under combined compression-shear impacting," *International Journal of Mechanical Sciences*, vol. 165, p. 105 219, 2020.

[89] S. Sayahlatifi, C. Shao, A. McDonald, and J. D. Hogan, "3D microstructure-based fe simulation of cold-sprayed Al-Al2O3 composite coatings under indentation and quasi-static compression," in *ITSC2021*, ASM International, 2021, pp. 386–395.

[90] W. Wang, L. Sluys, and R De Borst, "Viscoplasticity for instabilities due to strain softening and strain-rate softening," *International Journal for Numerical Methods in Engineering*, vol. 40, no. 20, pp. 3839–3864, 1997.

[91] M. Khan and M. Iqbal, "Failure and fragmentation of ceramic target with varying geometric configuration under ballistic impact," *Ceramics International*, 2022.

[92] Y. F. Gao, J. Wang, Q. Y. Li, and Y. H. Ding, "Dynamic response behaviours of Al2O3 ceramics with different grain sizes under SHPB compression loading," in *Key Engineering Materials*, Trans Tech Publ, vol. 922, 2022, pp. 45–51.

[93] W. G. Fahrenholtz, E. J. Wuchina, W. E. Lee, and Y. Zhou, *Ultra-high temperature ceramics: materials for extreme environment applications*. John Wiley & Sons, 2014.

[94] Q.-Z. Wang and L. Xing, "Determination of fracture toughness kic by using the flattened brazilian disk specimen for rocks," *Engineering fracture mechanics*, vol. 64, no. 2, pp. 193–201, 1999.

[95] J. J. Swab, C. S. Meredith, D. T. Casem, and W. R. Gamble, "Static and dynamic compression strength of hot-pressed boron carbide using a dumbbell-shaped specimen," *Journal of Materials Science*, vol. 52, no. 17, pp. 10 073–10 084, 2017.

[96] J. J. Swab, J. Yu, R. Gamble, and S. Kilczewski, "Analysis of the diametral compression method for determining the tensile strength of transparent magnesium aluminate spinel," *International journal of fracture*, vol. 172, no. 2, pp. 187–192, 2011.

[97] H. Lin, W. Xiong, and Q. Yan, "Modified formula for the tensile strength as obtained by the flattened brazilian disk test," *Rock Mechanics and Rock Engineering*, vol. 49, no. 4, pp. 1579–1586, 2016.

[98] A. Griffith, "Proceedings of the first international congress on applied mechanics," *Delft. J. Waltman Jr, Delft*, pp. 55–63, 1924.

[99] B. M. Koch, P. Jannotti, D. Mallick, B. Schuster, T. Sano, and J. D. Hogan, "Influence of microstructure on the impact failure of alumina," *Materials Science and Engineering: A*, vol. 770, p. 138 549, 2020.

[100] C. Lo, H. Li, G. Toussaint, and J. D. Hogan, "On the evaluation of mechanical properties and ballistic performance of two variants of boron carbide," *International Journal of Impact Engineering*, vol. 152, p. 103 846, 2021.

[101] Z Zaiemyekeh, G. Liaghat, H Ahmadi, M. Khan, and O. Razmkhah, "Effect of strain rate on deformation behavior of aluminum matrix composites with Al2O3 nanoparticles," *Materials Science and Engineering: A*, vol. 753, pp. 276–284, 2019.

[102] Q. Wang, W Li, and H. Xie, "Dynamic split tensile test of flattened brazilian disc of rock with shpb setup," *Mechanics of Materials*, vol. 41, no. 3, pp. 252–260, 2009.

[103] Q. Wang, X. Jia, S. Kou, Z. Zhang, and P.-A. Lindqvist, "The flattened brazilian disc specimen used for testing elastic modulus, tensile strength and fracture toughness of brittle rocks: Analytical and numerical results," *International Journal of Rock Mechanics and Mining Sciences*, vol. 41, no. 2, pp. 245–253, 2004.

[104] D. J. Frew, M. J. Forrestal, and W Chen, "Pulse shaping techniques for testing brittle materials with a split Hopkinson pressure bar," *Experimental mechanics*, vol. 42, no. 1, pp. 93–106, 2002.

[105] Z Rosenberg, N. Brar, and S. Bless, "Dynamic high-pressure properties of aln ceramic as determined by flyer plate impact," *Journal of applied physics*, vol. 70, no. 1, pp. 167–171, 1991.

[106] M. Kipp and D. Grady, "Shock phase transformation and release properties of aluminum nitride," *Le Journal de Physique IV*, vol. 4, no. C8, pp. C8–249, 1994.

[107] M. Chen, J. McCauley, D. Dandekar, and N. Bourne, "Dynamic plasticity and failure of high-purity alumina under shock loading," *Nature materials*, vol. 5, no. 8, pp. 614–618, 2006.

[108] P. Baranowski *et al.*, "Fracture and fragmentation of dolomite rock using the JH2 constitutive model: Parameter determination, experiments and simulations," *International Journal of Impact Engineering*, vol. 140, p. 103 543, 2020.

[109] Y. Zhu, G. Liu, Y. Wen, C. Xu, W. Niu, and G. Wang, "Back-spalling process of an Al2O3 ceramic plate subjected to an impact of steel ball," *International Journal of Impact Engineering*, vol. 122, pp. 451–471, 2018.

[110] G. Subhash, S. Maiti, P. H. Geubelle, and D. Ghosh, "Recent advances in dynamic indentation fracture, impact damage and fragmentation of ceramics," *Journal of the American Ceramic Society*, vol. 91, no. 9, pp. 2777–2791, 2008.

[111] C. Y. Rena, G. Ruiz, and A. Pandolfi, "Numerical investigation on the dynamic behavior of advanced ceramics," *Engineering Fracture Mechanics*, vol. 71, no. 4-6, pp. 897–911, 2004.

[112] M. Z. Sheikh *et al.*, "Static and dynamic brazilian disk tests for mechanical characterization of annealed and chemically strengthened glass," *Ceramics International*, vol. 45, no. 6, pp. 7931–7944, 2019.

[113] ABAQUS, "Simulia. abaqus/cae version 6.14-2 (2014). dassault systèmes simulia corp," *Provid. RI, USA*, 2014.

[114] Q. Li and H Meng, "About the dynamic strength enhancement of concrete-like materials in a split hopkinson pressure bar test," *International Journal of solids and structures*, vol. 40, no. 2, pp. 343–360, 2003.

[115] S Nemat-Nasser and M Obata, "A microcrack model of dilatancy in brittle materials," 1988.

[116] B. M. Koch, C. Lo, T. Sano, and J. D. Hogan, "Bulking as a mechanism in the failure of advanced ceramics," in *Hypervelocity Impact Symposium*, American Society of Mechanical Engineers, vol. 883556, 2019, V001T05A001.

[117] K. J. Stone and D. M. Wood, "Effects of dilatancy and particle size observed in model tests on sand," *Soils and Foundations*, vol. 32, no. 4, pp. 43–57, 1992.

[118] M. Poliotti and J.-M. Bairán, "A new concrete plastic-damage model with an evolutive dilatancy parameter," *Engineering structures*, vol. 189, pp. 541–549, 2019.

[119] D. Warner and J. Molinari, "Micromechanical finite element modeling of compressive fracture in confined alumina ceramic," *Acta Materialia*, vol. 54, no. 19, pp. 5135–5145, 2006.

[120] J. Zhou, A. M. Gokhale, A. Gurumurthy, and S. P. Bhat, "Realistic microstructural rve-based simulations of stress–strain behavior of a dual-phase steel having high martensite volume fraction," *Materials Science and Engineering: A*, vol. 630, pp. 107–115, 2015.

[121] L Malcher, F. A. Pires, and J. C. De Sá, "An extended gtn model for ductile fracture under high and low stress triaxiality," *International Journal of Plasticity*, vol. 54, pp. 193–228, 2014.

[122] S. Bavdekar and G. Subhash, "Failure mechanisms of ceramics under quasi-static and dynamic loads: Overview," *Handbook of damage mechanics*, pp. 579–607, 2022.

[123] Z. Wang, T. Ren, T. Suo, and A. Manes, "Quasi-static and low-velocity impact biaxial flexural fracture of aluminosilicate glass—an experimental and numerical study," *Thin-Walled Structures*, vol. 165, p. 107 939, 2021.

[124] K Krishnan, S Sockalingam, S Bansal, and S. Rajan, "Numerical simulation of ceramic composite armor subjected to ballistic impact," *Composites Part B: Engineering*, vol. 41, no. 8, pp. 583–593, 2010.

[125] L. Zhang, "Influence of shear stress state on dynamic fracture of a glass ceramic macor," *Ceramics International*, 2022.

[126] S. Tan, X. Yao, S. Long, X. Zhang, and S. Zang, "Static and dynamic strength of soda-lime glass under combined compression-shear loading," *Journal of Non-Crystalline Solids*, vol. 516, pp. 14–25, 2019.

[127] L. Yang, G. Wang, G.-F. Zhao, and L. Shen, "A rate-and pressure-dependent damage-plasticity constitutive model for rock," *International Journal of Rock Mechanics and Mining Sciences*, vol. 133, p. 104 394, 2020.

[128] S. Tan, S. Long, X. Yao, and X. Zhang, "An improved material model for loading-path and strain-rate dependent strength of impacted soda-lime glass plate," *Journal of Materials Research and Technology*, vol. 15, pp. 1905–1919, 2021.

[129] M. D. S. Lucio, S. Kultayeva, and Y.-W. Kim, "Improved mechanical strength and thermal resistance of porous sic ceramics with gradient pore sizes," *Journal of the European Ceramic Society*, 2022.

[130] K. Zheng *et al.*, "Compositional tailoring effect on crystal structure, mechanical and thermal properties of γ-AlON transparent ceramics," *Journal of the European Ceramic Society*, vol. 42, no. 6, pp. 2983–2993, 2022.

[131] Y. Zhou, K. Hirao, Y. Yamauchi, and S. Kanzaki, "Tailoring the mechanical properties of silicon carbide ceramics by modification of the intergranular phase chemistry and microstructure," *Journal of the European Ceramic Society*, vol. 22, no. 14-15, pp. 2689–2696, 2002.

[132] M. Zhang *et al.*, "Improved fracture behavior and mechanical properties of alumina textured ceramics," *Materials Letters*, vol. 221, pp. 252–255, 2018.

[133] A. J. Ruys, *Alumina ceramics: biomedical and clinical applications*. Woodhead Publishing, 2018.

[134] X. Zhang, Y. Chen, and J. Hu, "Recent advances in the development of aerospace materials," *Progress in Aerospace Sciences*, vol. 97, pp. 22–34, 2018.

[135] Z. Liu, C. Ma, Z. Chang, P. Yan, and F. Li, "Advances in crack formation mechanism and inhibition strategy for ceramic additive manufacturing," *Journal of the European Ceramic Society*, 2023, ISSN: 0955-2219.

[136] ISO/ASTM52900-15, "Standard terminology for additive manufacturing–general principles–terminology," *International Organization for Standardization: Geneva, Switzerland*, 2015.

[137] R. Chaudhary, P. Fabbri, E. Leoni, F. Mazzanti, R. Akbari, and C. Antonini, "Additive manufacturing by digital light processing: A review," *Progress in Additive Manufacturing*, vol. 8, no. 2, pp. 331–351, 2023.

[138] L. C. Hwa, S. Rajoo, A. M. Noor, N. Ahmad, and M. Uday, "Recent advances in 3D printing of porous ceramics: A review," *Current Opinion in Solid State and Materials Science*, vol. 21, no. 6, pp. 323–347, 2017.

[139] A. International, *Astm committee F42 on additive manufacturing technologies*, 2012.

[140] Z. Li *et al.*, "Direct laser powder-bed fusion additive manufacturing of complex-shaped TiB2-B4C composite with ultra-fine eutectic microstructure and outstanding mechanical performances," *Journal of the European Ceramic Society*, vol. 43, no. 3, pp. 1230–1236, 2023.

[141] X. Zhang, K. Zhang, B. Zhang, Y. Li, and R. He, "Mechanical properties of additively-manufactured cellular ceramic structures: A comprehensive study," *Journal of Advanced Ceramics*, vol. 11, no. 12, pp. 1918–1931, 2022.

[142] B. Zhang *et al.*, "Mechanical properties of additively manufactured Al2O3 ceramic plate-lattice structures: Experiments & simulations," *Composite Structures*, vol. 311, p. 116 792, 2023.

[143] X. Zhang, K. Zhang, B. Zhang, Y. Li, and R. He, "Quasi-static and dynamic mechanical properties of additively manufactured Al2O3 ceramic lattice structures: Effects of structural configuration," *Virtual and Physical Prototyping*, vol. 17, no. 3, pp. 528–542, 2022.

[144] M. Mariani, R. Beltrami, P. Brusa, C. Galassi, R. Ardito, and N. Lecis, "3D printing of fine alumina powders by binder jetting," *Journal of the European Ceramic Society*, vol. 41, no. 10, pp. 5307–5315, 2021.

[145] L. Rueschhoff, W. Costakis, M. Michie, J. Youngblood, and R. Trice, "Additive manufacturing of dense ceramic parts via direct ink writing of aqueous alumina suspensions," *International Journal of Applied Ceramic Technology*, vol. 13, no. 5, pp. 821–830, 2016.

[146] T. Lube, M. Staudacher, A.-K. Hofer, J. Schlacher, and R. Bermejo, "Stereolithographic 3d printing of ceramics: Challenges and opportunities for structural integrity," *Advanced engineering materials*, vol. 25, no. 7, p. 2 200 520, 2023.

[147] X. Wu *et al.*, "Research progress of the defects and innovations of ceramic vat photopolymerization," *Additive Manufacturing*, p. 103 441, 2023.

[148] G. Ravichandran and G. Subhash, "Critical appraisal of limiting strain rates for compression testing of ceramics in a split hopkinson pressure bar," *Journal of the American Ceramic Society*, vol. 77, no. 1, pp. 263–267, 1994.

[149] D. Zhao *et al.*, "Heat treatment of melt-grown alumina ceramics with trace glass fabricated by laser directed energy deposition," *Materials Characterization*, vol. 196, p. 112 639, 2023.

[150] M Liu, S. Wang, D. Tang, L. Chen, and J Ma, "Fabrication and microstructures of yag transparent ceramics," *Science of Sintering*, vol. 40, no. 3, pp. 311–317, 2008.

[151] H. Li *et al.*, "Evolution of the microstructure and mechanical properties of stereolithography formed alumina cores sintered in vacuum," *Journal of the European Ceramic Society*, vol. 40, no. 14, pp. 4825–4836, 2020.

[152] X.-T. Jia *et al.*, "Investigation on mechanical properties of alon ceramics synthesized by spark plasma sintering," *Journal of the European Ceramic Society*, vol. 43, no. 3, pp. 889–899, 2023.

[153] M. Jerabek, Z. Major, and R. W. Lang, "Strain determination of polymeric materials using digital image correlation," *Polymer Testing*, vol. 29, no. 3, pp. 407–416, 2010.

[154] W. Chen and G Ravichandran, "Dynamic compressive failure of a glass ceramic under lateral confinement," *Journal of the Mechanics and Physics of Solids*, vol. 45, no. 8, pp. 1303–1328, 1997.

[155] W. W. Chen and B. Song, *Split Hopkinson (Kolsky) bar: design, testing and applications*. Springer Science & Business Media, 2010.

[156] A. Standard, "C1327; standard test method for vickers indentation hardness of advanced ceramics," *ASTM International: West Conshohocken, PA, USA*, 2015.

[157] A. Krell and P. Blank, "Grain size dependence of hardness in dense submicrometer alumina," *Journal of the American Ceramic Society*, vol. 78, no. 4, pp. 1118–1120, 1995.

[158] A. Paar, "Ultra nanoindentation tester (UNHT^3)," *www.anton-paar.com/ca-en/products/details/ultra-nanoindentation-tester-unht3/*,

[159] A Krell and S. Schädlich, "Nanoindentation hardness of submicrometer alumina ceramics," *Materials Science and Engineering: A*, vol. 307, no. 1-2, pp. 172–181, 2001.

[160] A.-K. Hofer, I. Kraleva, T. Prötsch, A. Vratanar, M. Wratschko, and R. Bermejo, "Effect of second phase addition of zirconia on the mechanical response of textured alumina ceramics," *Journal of the European Ceramic Society*, vol. 43, no. 7, pp. 2935–2942, 2023.

[161] S. Yang *et al.*, "Strengthened the dense alumina ceramics by flash treatment," *Ceramics International*, vol. 49, no. 12, pp. 21 105–21 110, 2023.

[162] G. Sang *et al.*, "Strong and tough alumina ceramic from the particle-stabilized foam," *Advanced Engineering Materials*, vol. 25, no. 2, p. 2 200 971, 2023.

[163] F Sommer, F Kern, and R Gadow, "Injection molding of ceramic cutting tools for wood-based materials," *Journal of the European Ceramic Society*, vol. 33, no. 15-16, pp. 3115–3122, 2013.

[164] M. Yu *et al.*, "Optimization of the tape casting process for development of high performance alumina ceramics," *Ceramics International*, vol. 41, no. 10, pp. 14 845–14 853, 2015.

[165] S. Mamatha, P. Biswas, P. Ramavath, D. Das, and R. Johnson, "3D printing of complex shaped alumina parts," *Ceramics International*, vol. 44, no. 16, pp. 19 278–19 281, 2018.

[166] E. Feilden, E. G.-T. Blanca, F. Giuliani, E. Saiz, and L. Vandeperre, "Robocasting of structural ceramic parts with hydrogel inks," *Journal of the European Ceramic Society*, vol. 36, no. 10, pp. 2525–2533, 2016.

[167] A. Ghazanfari, W. Li, M. Leu, J. Watts, and G. Hilmas, "Mechanical characterization of parts produced by ceramic on-demand extrusion process," *International Journal of Applied Ceramic Technology*, vol. 14, no. 3, pp. 486–494, 2017.

[168] J. Teng, X. Wu, Y. Jin, X. Ji, C. Xu, and Z. Zhang, "Effects of platelet addition and loading direction on the mechanical properties of textured alumina fabricated by ceramic mask stereolithography," *Ceramics International*, vol. 49, no. 18, pp. 30 763–30 775, 2023.

[169] M. Zhou *et al.*, "Preparation of a defect-free alumina cutting tool via additive manufacturing based on stereolithography–optimization of the drying and debinding processes," *Ceramics international*, vol. 42, no. 10, pp. 11 598–11 602, 2016.

[170] H. Wu, W. Liu, Y. Xu, L. Lin, Y. Li, and S. Wu, "Vat photopolymerization-based 3D printing of complex-shaped and high-performance Al2O3 ceramic tool with chip-breaking grooves: Cutting performance and wear mechanism," *Journal of Asian Ceramic Societies*, vol. 11, no. 1, pp. 159–169, 2023.

[171] H. Wu *et al.*, "Realization of complex-shaped and high-performance alumina ceramic cutting tools via vat photopolymerization based 3D printing: A novel surface modification strategy through coupling agents aluminic acid ester and silane coupling agent," *Journal of the European Ceramic Society*, vol. 43, no. 3, pp. 1051–1063, 2023.

[172] X. Xu, S. Zhou, J. Wu, S. Liu, S. Ma, and T. Cheng, "Study of alumina ceramic parts fabricated via DLP stereolithography using powders with different sizes and morphologies," *International Journal of Applied Ceramic Technology*, vol. 20, no. 2, pp. 1167–1193, 2023.

[173] X. Xu, S. Zhou, J. Wu, S. Liu, S. Ma, and T. Cheng, "A comprehensive study of alumina ceramic parts fabricated via digital light processing stereolithography using alumina powders with different sizes and morphologies," *Available at SSRN 4144042*,

[174] Y. Pan *et al.*, "Effect of holding time during sintering on microstructure and properties of 3d printed alumina ceramics," *Frontiers in Materials*, vol. 7, p. 54, 2020.

[175] M. Xin, Z. Liu, B. Wang, and Q. Song, "Microstructures and mechanical properties of additively manufactured alumina ceramics with digital light processing," *Archives of Civil and Mechanical Engineering*, vol. 23, no. 1, p. 52, 2022.

[176] H. Curto *et al.*, "Coupling additive manufacturing and microwave sintering: A fast processing route of alumina ceramics," *Journal of the European Ceramic Society*, vol. 40, no. 7, pp. 2548–2554, 2020.

[177] A Krell, "A new look at the influences of load, grain size and grain boundaries on the room temperature hardness of ceramics," *International Journal of refractory Metals and Hard materials*, vol. 16, no. 4-6, pp. 331–335, 1998.

[178] J. A. Wollmershauser *et al.*, "An extended hardness limit in bulk nanoceramics," *Acta Materialia*, vol. 69, pp. 9–16, 2014.

[179] S. Mamatha, P. Biswas, P. Ramavath, D. Das, and R. Johnson, "Effect of parameters on 3D printing of alumina ceramics and evaluation of properties of sintered parts," *Journal of Asian Ceramic Societies*, vol. 9, no. 3, pp. 858–864, 2021.

[180] W. Li, W. Liu, F. Qi, Y. Chen, and Z. Xing, "Determination of micro-mechanical properties of additive manufactured alumina ceramics by nanoindentation and scratching," *Ceramics International*, vol. 45, no. 8, pp. 10 612–10 618, 2019.

[181] S Maleksaeedi, H Eng, F. Wiria, T. Ha, and Z He, "Property enhancement of 3D-printed alumina ceramics using vacuum infiltration," *Journal of Materials Processing Technology*, vol. 214, no. 7, pp. 1301–1306, 2014.

[182] Z. Liu, J. J. Nolte, J. Packard, G. Hilmas, F. Dogan, and M.-C. Leu, "Selective laser sintering of high-density alumina ceramic parts," in *Proceedings of the 35th International MATADOR Conference: Formerly the International Machine Tool Design and Research Conference*, Springer, 2007, pp. 351–354.

[183] K. Zhang, R. He, G. Ding, X. Bai, and D. Fang, "Effects of fine grains and sintering additives on stereolithography additive manufactured Al2O3 ceramic," *Ceramics International*, vol. 47, no. 2, pp. 2303–2310, 2021.

[184] J. Gonzalez, J. Mireles, Y. Lin, and R. B. Wicker, "Characterization of ceramic components fabricated using binder jetting additive manufacturing technology," *Ceramics International*, vol. 42, no. 9, pp. 10 559–10 564, 2016.

[185] F. Zhou and J.-F. Molinari, "Stochastic fracture of ceramics under dynamic tensile loading," *International journal of solids and structures*, vol. 41, no. 22-23, pp. 6573–6596, 2004.

[186] K. Rane, M. A. Farid, W. Hassan, and M. Strano, "Effect of printing parameters on mechanical properties of extrusion-based additively manufactured ceramic parts," *Ceramics International*, vol. 47, no. 9, pp. 12 189–12 198, 2021.

[187] M. Vlasea, R. Pilliar, and E. Toyserkani, "Control of structural and mechanical properties in bioceramic bone substitutes via additive manufacturing layer stacking orientation," *Additive Manufacturing*, vol. 6, pp. 30–38, 2015.

[188] Y. Ma, Z. Wang, and Y. Qin, "Impact of characteristic length and loading rate upon dynamic constitutive behavior and fracture process in alumina ceramics," *Ceramics International*, vol. 49, no. 3, pp. 4775–4784, 2023.

[189] D. Roberts and A. Wells, "The velocity of brittle fracture," *Engineering*, vol. 178, no. 4639, pp. 820–821, 1954.

[190] K. Ramesh, J. D. Hogan, J. Kimberley, and A. Stickle, "A review of mechanisms and models for dynamic failure, strength, and fragmentation," *Planetary and Space Science*, vol. 107, pp. 10–23, 2015.

[191] H. Budharaju *et al.*, "Ceramic materials for 3d printing of biomimetic bone scaffolds–current state–of–the–art & future perspectives," *Materials & Design*, p. 112 064, 2023.

[192] T. Dreier *et al.*, "3D printing of aluminum oxide via composite extrusion modeling using a ceramic injection molding feedstock," *Materials & Design*, vol. 227, p. 111 806, 2023.

[193] P.-J. Chiang, K. P. Davidson, J. M. Wheeler, A. Ong, K. Erickson, and M. Seita, "Site-specific alloying through binder jet 3d printing," *Materials & Design*, vol. 235, p. 112 384, 2023.

[194] S. Zhou, G. Liu, C. Wang, Y. Zhang, C. Yan, and Y. Shi, "Thermal debinding for stereolithography additive manufacturing of advanced ceramic parts: A comprehensive review," *Materials & Design*, p. 112 632, 2024.

[195] J. A. Choren, S. M. Heinrich, and M. B. Silver-Thorn, "Young's modulus and volume porosity relationships for additive manufacturing applications," *Journal of materials science*, vol. 48, pp. 5103–5112, 2013.

[196] C. M. Laursen, S. A. DeJong, S. M. Dickens, A. N. Exil, D. F. Susan, and J. D. Carroll, "Relationship between ductility and the porosity of additively manufactured AlSi10Mg," *Materials Science and Engineering: A*, vol. 795, p. 139 922, 2020.

[197] S. Zhou *et al.*, "Additive manufacturing of Al_2O_3 with engineered interlayers and high toughness through multi-material co-extrusion," *Acta Materialia*, vol. 246, p. 118 704, 2023.

[198] A. Y. Al-Maharma, S. P. Patil, and B. Markert, "Effects of porosity on the mechanical properties of additively manufactured components: A critical review," *Materials Research Express*, vol. 7, no. 12, p. 122 001, 2020.

[199] T. El-Raghy, M. W. Barsoum, A. Zavaliangos, and S. R. Kalidindi, "Processing and mechanical properties of Ti_3SiC_2: Ii, effect of grain size and deformation temperature," *Journal of the American ceramic society*, vol. 82, no. 10, pp. 2855–2860, 1999.

[200] R Halouani, D Bernache-Assolant, E Champion, and A Ababou, "Microstructure and related mechanical properties of hot-pressed hydroxyapatite ceramics," *Journal of Materials Science: Materials in Medicine*, vol. 5, pp. 563–568, 1994.

[201] C. C. Holland and R. M. McMeeking, "The influence of mechanical and microstructural properties on the rate-dependent fracture strength of ceramics in uniaxial compression," *International Journal of Impact Engineering*, vol. 81, pp. 34–49, 2015.

[202] R. Cavuoto, P. Lenarda, A. Tampieri, D. Bigoni, and M. Paggi, "Phase-field modelling of failure in ceramics with multiscale porosity," *Materials & Design*, vol. 238, p. 112 708, 2024.

[203] G. Hu, J. Liu, L. Graham-Brady, and K. Ramesh, "A 3D mechanistic model for brittle materials containing evolving flaw distributions under dynamic multiaxial loading," *Journal of the Mechanics and Physics of Solids*, vol. 78, pp. 269–297, 2015.

[204] S. Meille, M. Lombardi, J. Chevalier, and L. Montanaro, "Mechanical properties of porous ceramics in compression: On the transition between elastic, brittle, and cellular behavior," *Journal of the European Ceramic Society*, vol. 32, no. 15, pp. 3959–3967, 2012.

[205] H. Luo and W. Chen, "Dynamic compressive response of intact and damaged AD995 alumina," *International Journal of Applied Ceramic Technology*, vol. 1, no. 3, pp. 254–260, 2004.

[206] R. Landingham and A. Casey, "Final report of the light armor materials program," California Univ., Tech. Rep., 1972.

[207] Z. Gong *et al.*, "Influence of grain boundary and grain size on the mechanical properties of polycrystalline ceramics: Grain-scale simulations," *Journal of the American Ceramic Society*, vol. 103, no. 10, pp. 5900–5913, 2020.

[208] F. Knudsen, "Dependence of mechanical strength of brittle polycrystalline specimens on porosity and grain size," *Journal of the American Ceramic Society*, vol. 42, no. 8, pp. 376–387, 1959.

[209] S. Norouzi, A. Baghbanan, and A. Khani, "Investigation of grain size effects on micro/macro-mechanical properties of intact rock using voronoi element—discrete element method approach," *Particulate Science and Technology*, vol. 31, no. 5, pp. 507–514, 2013.

[210] Y. Zhao, G. Shi, J.-T. Miao, X. Sang, and R. Liu, "Near-infrared photothermal dual crosslinking strategy for precise and efficient direct ink writing of high solids ceramic slurries," *Materials & Design*, vol. 235, p. 112 398, 2023.

[211] Y. Gao, Z. Li, Y. Ge, and L. Shi, "Experimental and theoretical investigation of failure mechanism in al2o3/sic composite under plane shock waves," *Materials & Design*, p. 112 958, 2024.

[212] S. Sayahlatifi, C. Shao, A. McDonald, and J. D. Hogan, "3D microstructure-based finite element simulation of cold-sprayed Al-Al_2O_3 composite coatings under quasi-static compression and indentation loading," *Journal of Thermal Spray Technology*, vol. 31, pp. 102–118, 2022.

[213] Z. Peng, X. Wang, L. Ding, and Z. Wu, "Integrative tensile prediction and parametric analysis of unidirectional carbon/basalt hybrid fiber reinforced polymer composites by bundle-based modeling," *Materials & Design*, vol. 218, p. 110 697, 2022.

[214] Y. Zhang *et al.*, "An improved micromechanical model for the thermal conductivity of multi-scale fiber reinforced ultra-high performance concrete under high temperatures," *Materials & Design*, vol. 236, p. 112 503, 2023.

[215] M. T. Andani, M. R. Karamooz-Ravari, R. Mirzaeifar, and J. Ni, "Micromechanics modeling of metallic alloys 3d printed by selective laser melting," *Materials & Design*, vol. 137, pp. 204–213, 2018.

[216] S Falco, N Fogell, S Kasinos, and L Iannucci, "Homogenisation of micromechanical modeling results for the evaluation of macroscopic material properties of brittle ceramics," *International Journal of Mechanical Sciences*, vol. 220, p. 107 071, 2022.

[217] S. Sayahlatifi, Z. Zaiemyekeh, C. Shao, A. McDonald, and J. D. Hogan, "Micromechanical damage analysis of Al-Al_2O_3 composites via cold-spray additive manufacturing," *International Journal of Mechanical Sciences*, vol. 259, p. 108 573, 2023.

[218] J. Zhang, T. Sui, B. Lin, B. Lv, H. Du, and N. Song, "Quantification of microdamage evolution process in ceramics through extensive analysis of multisource heterogeneous data," *Materials & Design*, vol. 237, p. 112 600, 2024.

[219] S. Sayahlatifi, Z. Zaiemyekeh, C. Shao, A. McDonald, and J. D. Hogan, "Strain rate-dependent behavior of cold-sprayed additively manufactured al–al2o3 composites: Micromechanical modeling and experimentation," *Composites Part B: Engineering*, vol. 280, p. 111 479, 2024.

[220] X. Liu, J. He, and S. Huang, "Mechanistically informed artificial neural network model for discovering anisotropic path-dependent plasticity of metals," *Materials Design*, vol. 226, p. 111 697, 2023.

[221] Q. Du, V. Faber, and M. Gunzburger, "Centroidal voronoi tessellations: Applications and algorithms," *SIAM review*, vol. 41, no. 4, pp. 637–676, 1999.

[222] N. Miyazaki and T. Hoshide, "Influence of porosity and pore distributions on strength properties of porous alumina," *Journal of Materials Engineering and Performance*, vol. 27, pp. 4345–4354, 2018.

[223] R. Rice, "Limitations of pore-stress concentrations on the mechanical properties of porous materials," *Journal of Materials Science*, vol. 32, no. 17, pp. 4731–4736, 1997.

[224] S. Sayahlatifi, G. Rahimi, and A. Bokaei, "The quasi-static behavior of hybrid corrugated composite/balsa core sandwich structures in four-point bending: Experimental study and numerical simulation," *Engineering Structures*, vol. 210, p. 110 361, 2020.

[225] S. ABAQUS, "Users' manual version 6.13 documentation," *Dassault Systemes*, 2013.

[226] C. Jiang, D. Lu, M. Zhou, B. Kou, and W. Gong, "A numerical study of the mechanical and fracture properties of ZTA (zirconia toughened alumina)p/40Cr steel spatial spherical dot matrix composite," *International Journal of Solids and Structures*, vol. 260-261, p. 112 047, 2023, ISSN: 0020-7683.

[227] Y Partom, "Calibrating a material model for AD995 alumina from plate impact visar profiles," *Le Journal de Physique IV*, vol. 4, no. C8, pp. C8–495, 1994.

[228] A. Kurşun, E. Bayraktar, and H. M. Enginsoy, "Experimental and numerical study of alumina reinforced aluminum matrix composites: Processing, microstructural aspects and properties," *Composites Part B: Engineering*, vol. 90, pp. 302–314, 2016.

[229] O. A. Ruano, J. Wadsworth, and O. D. Sherby, "Deformation of fine-grained alumina by grain boundary sliding accommodated by slip," *Acta Materialia*, vol. 51, no. 12, pp. 3617–3634, 2003.

[230] K. Padmanabhan, "Grain boundary sliding controlled flow and its relevance to superplasticity in metals, alloys, ceramics and intermetallics and strain-rate dependent flow in nanostructured materials," *Journal of materials science*, vol. 44, no. 9, pp. 2226–2238, 2009.

[231] J. Clayton and J. Knap, "Phase field modeling of directional fracture in anisotropic polycrystals," *Computational Materials Science*, vol. 98, pp. 158–169, 2015, ISSN: 0927-0256.

[232] A. Ekhtiyari and M. M. Shokrieh, "A novel rate-dependent cohesive zone model for simulation of mode I dynamic delamination in laminated composites," *Composite Structures*, vol. 281, p. 114 962, 2022, ISSN: 0263-8223.

[233] A. Norton, S Falco, N Young, J Severs, and R. Todd, "Microcantilever investigation of fracture toughness and subcritical crack growth on the scale of the microstructure in Al_2O_3," *Journal of the European Ceramic Society*, vol. 35, no. 16, pp. 4521–4533, 2015.

[234] I. Benedetti and M. Aliabadi, "A three-dimensional cohesive-frictional grain-boundary micromechanical model for intergranular degradation and failure in polycrystalline materials," *Computer Methods in Applied Mechanics and Engineering*, vol. 265, pp. 36–62, 2013, ISSN: 0045-7825.

[235] R. Kraft, J. Molinari, K. Ramesh, and D. Warner, "Computational micromechanics of dynamic compressive loading of a brittle polycrystalline material using a distribution of grain boundary properties," *Journal of the Mechanics and Physics of Solids*, vol. 56, no. 8, pp. 2618–2641, 2008, ISSN: 0022-5096.

[236] J. Zhang *et al.*, "3D microstructure-based finite element modeling of deformation and fracture of SiCp/Al composites," *Composites Science and Technology*, vol. 123, pp. 1–9, 2016.

[237] P. Peng *et al.*, "Deformation behavior and damage in B_4C_p/6061Al composites: An actual 3D microstructure-based modeling," *Materials Science and Engineering: A*, vol. 781, p. 139 169, 2020.

[238] T. Xu, T.-F. Fu, M. J. Heap, P. G. Meredith, T. M. Mitchell, and P. Baud, "Mesoscopic damage and fracturing of heterogeneous brittle rocks based on three-dimensional polycrystalline discrete element method," *Rock Mechanics and Rock Engineering*, vol. 53, pp. 5389–5409, 2020.

[239] H. Vahidi *et al.*, "A review of grain boundary and heterointerface characterization in polycrystalline oxides by (scanning) transmission electron microscopy," *Crystals*, vol. 11, no. 08, p. 878, 2021.

[240] R. Rice, "Ceramic tensile strength-grain size relations: Grain sizes, slopes, and branch intersections," *Journal of materials science*, vol. 32, no. 7, pp. 1673–1692, 1997.

[241] N. Hansen, "Hall–petch relation and boundary strengthening," *Scripta Materialia*, vol. 51, no. 8, pp. 801–806, 2004, Viewpoint set no. 35. Metals and alloys with a structural scale from the micrometer to the atomic dimensions, ISSN: 1359-6462.

[242] A. A. Griffith, "Vi. the phenomena of rupture and flow in solids," *Philosophical transactions of the royal society of london. Series A, containing papers of a mathematical or physical character*, vol. 221, no. 582-593, pp. 163–198, 1921.

[243] J. Peng, L. N. Y. Wong, and C. I. Teh, "Influence of grain size on strength of polymineralic crystalline rock: New insights from DEM grain-based modeling," *Journal of Rock Mechanics and Geotechnical Engineering*, vol. 13, no. 4, pp. 755–766, 2021, ISSN: 1674-7755.

[244] W. Li, Z. Cai, H. Li, L. Peng, X. Lai, and M. Fu, "The modified GTN-Thomason criterion for modelling of ductile fracture considering shear factor and size effect in micro-scaled plastic deformation," *International Journal of Mechanical Sciences*, vol. 204, p. 106 540, 2021, ISSN: 0020-7403.

[245] M. Weiss, P. Sälzler, N. Willenbacher, and E. Koos, "3D-printed lightweight ceramics using capillary suspensions with incorporated nanoparticles," *Journal of the European Ceramic Society*, vol. 40, no. 8, pp. 3140–3147, 2020.

[246] I. G. Crouch, G. Appleby-Thomas, and P. J. Hazell, "A study of the penetration behaviour of mild-steel-cored ammunition against boron carbide ceramic armours," *International Journal of Impact Engineering*, vol. 80, pp. 203–211, 2015.

[247] X. Zhang *et al.*, "Characterization of thermophysical and mechanical properties of hafnium carbonitride fabricated by hot pressing sintering," *Journal of Materials Research and Technology*, vol. 23, pp. 4432–4443, 2023.

[248] X. Lv, F. Ye, L. Cheng, S. Fan, and Y. Liu, "Binder jetting of ceramics: Powders, binders, printing parameters, equipment, and post-treatment," *Ceramics International*, vol. 45, no. 10, pp. 12 609–12 624, 2019.

[249] Q. Li, J. Liang, Y. Zhang, J. Li, Y. Zhou, and X. Sun, "Fused silica ceramic core based on network-structured zircon design via 3d printing," *Scripta Materialia*, vol. 208, p. 114 342, 2022.

[250] L. Yang and H. Miyanaji, "Ceramic additive manufacturing: A review of current status and challenges," 2017.

[251] A. Karanjgaokar, H. Li, and J. D. Hogan, "Strain-rate-dependent dynamic compression–shear response of alumina," *Ceramics International*, vol. 50, no. 2, pp. 3861–3876, 2024.

[252] G. Ravichandran and G. Subhash, "A micromechanical model for high strain rate behavior of ceramics," *International Journal of Solids and structures*, vol. 32, no. 17-18, pp. 2627–2646, 1995.

[253] N. Alharbi, R. Osman, and D. Wismeijer, "Effects of build direction on the mechanical properties of 3D-printed complete coverage interim dental restorations," *The Journal of prosthetic dentistry*, vol. 115, no. 6, pp. 760–767, 2016.

[254] F Gálvez, J Rodríguez, and V. S. Gálvez, "Influence of the strain rate on the tensile strength in aluminas of different purity," *Le Journal de Physique IV*, vol. 10, no. PR9, Pr9–323, 2000.

[255] Y. Liu *et al.*, "Critical microstructures and defects in heterostructured materials and their effects on mechanical properties," *Acta Materialia*, vol. 189, pp. 129–144, 2020.

[256] Q. Liu and D. Wu, "Machine learning and feature representation approaches to predict stress-strain curves of additively manufactured metamaterials with varying structure and process parameters," *Materials Design*, vol. 241, p. 112 932, 2024.